THE UNIVERSITY OF CHICAGO

TRANSFORMING HYDROXIDES IN METAL-ORGANIC FRAMEWORK NODES FOR CATALYTIC APPLICATIONS

A DISSERTATION SUBMITTED TO

THE FACULTY OF THE DIVISION OF THE PHYSICAL SCIENCES

IN CANDIDACY FOR THE DEGREE OF

DOCTOR OF PHILOSOPHY

DEPARTMENT OF CHEMISTRY

BY

PENGFEI JI

CHICAGO, ILLINOIS

DECEMBER 2018

Table of Contents

List of Figures

List of Schemes

List of Tables

List of Abbreviations

3D	3-dimensional
°C	degrees Celsius
Å	angstrom
ΔR	change in scattering half-path length
σ^2	mean standard relative deviation of a scatter
ANL	Argonne National Laboratory
APS	Advanced Photon Source
B3LYP	Becke 3-parameter, Lee-Yang-Parr (hybrid DFT functional)
BDC	Benzene-1,4-dicarboxylic acid
BET	Brunauer-Emmett-Teller
BNA	1-benzyl-1,4-dihydronicotinamide
BPDC	biphenyl dicarboxylate
Bpin	pinacolborane
Bpy	4,4'-bipyridine
Cp	cyclopentadiene anion
DEF	N,N-diethylformamide
DFT	Density functional theory
DLS	dynamic light scattering
DME	Dimethoxyethane
DMF	N,N-dimethylformamide
DMSO	dimethyl sulfoxide

EDX	energy-dispersive X-ray spectroscopy
EPR	electron paramagnetic resonance
ESI	electrospray ionization
EXAFS	Extended X-ray absorption fine structure
fBDC	2,3,5,6-tetrafluoro-1,4-benzenedicarboxylate
fBPDC	2,2’,3,3’,5,5’,6,6’-octafluoro-4,4’-biphenyldicarboxylate
ESI-MS	electrospray ionization mass spectroscopy
EtOH	ethanol
EXAFS	extended X-ray absorption fine structure
GC	gas chromatography
GC-MS	gas chromatography-mass spectrometry
GPC	gel permeation chromatography
HRTEM	high resolution transmission electron microscopy
HOMO	highest occupied molecular orbital
ICP-MS	inductively coupled plasma-mass spectrometry
I_0	incident beam density
I_t	transmitted beam intensity
I_{ref}	reference beam intensity
ICP-MS	inductively coupled plasma mass spectrometry
IR	infrared spectroscopy
KIE	kinetic isotope effect
LUMO	lowest unoccupied molecular orbital
MD	menadione

MeOH	methanol
MMAO	modified methyl aluminum oxide
MOF	metal-organic framework
MTBC	methane tetraphenylene tetrabenzenecarboxylate
NBO	natural bond orbital
NIS	N-iodosuccinimide
NMR	nuclear magnetic resonance
PBE	Perdew–Burke–Ernzerhof functional
PE	polyethylene
PEG	polyethylene glycol
PH	polyhexene
PP	polypropylene
PXRD	powder X-ray diffraction
QPDCN	4,4’-bis-(carboxyphenyl)-2-nitro-1,1’-biphenyl
R^2	goodness-of-fit metric
R_{eff}	scattering half-path length
r.t.	room temperature
S_0^2	passive electron reduction factor
SBU	secondary building unit
SMSI	strong metal-support interaction
SXRD	single crystal X-ray diffraction
TEM	transmission electron microscopy
TFA	trifluoroacetic acid

TGA	thermogravimetric analysis
THF	tetrahydrofuran
TLC	thin-layer chromatography
TON	turnover number
TON	turnover frequency
TPDC	p,p’-terphenyldicarboxylic acid
UiO	University of Oslo
UV-vis	ultraviolet and visible
XANES	X-ray absorption near-edge structure
XAS	X-ray absorption spectroscopy
XPS	X-ray photoelectron spectroscopy

Abstract

Pengfei Ji: Transforming Hydroxides in Metal-Organic

Framework Nodes for Catalytic Applications

Under Direction of Professor Wenbin Lin

MOFs have provided a highly tunable platform to access site-isolated catalysts that do not undergo multimetallic decomposition. Such site-isolation effect has allowed the design and synthesis of a large variety of novel catalysts that do not have homogeneous or heterogeneous analogues. My research was focused on the hydroxide groups on the MOF nodes, which offer powerful means for introducing catalytic functionalities.

Chapter 1of this thesis discusses general design strategies for MOFs, with specific focus on Zr-based MOFs. This class of MOFs offer an ideal platform to create novel and stable catalysts on the inorganic nodes through different post-synthetic modifications.

Chapter 2 through Chapter 6 of this thesis explore the use of inorganic MOF nodes with bridging hydroxides as binding sites for generating various single-site solid catalysts. For example, the $Zr_3(\mu_3\text{-OH})$ functionality in Zr_6TPDC was metalated with $MgMe_2$ or $CoCl_2$ to afford highly active catalysts for carbonyl hydroboration or C-H bond borylation reactions. To increase the electron-donating ability and open space around the $Zr_3(\mu_3\text{-OH})$ group, three MOFs including Zr_8MTBC, Zr_{12}TPDC and Ti_8BDC with new inorganic nodes were synthesized. These inorganic nodes were shown to provide superior supports for cobalt catalysts.

Chapter 7 through Chapter 10 of this thesis examine the transformation of inorganic nodes

with terminal hydroxides into competent catalysts for a variety of transformations. For example, $Ce_6(OH)_{12}$-BTC has six terminal hydroxides per Ce_6 node which can be activated by pinacol borane to afford terminal hydrides that are active for pyridine hydroboration, alkene hydroboration and alkene hydrophosphination. Other MOFs with terminal hydroxides were similarly activated to generate highly effective catalysts for olefin polymerization and pyridine hydrosilylation reactions.

Acknowledgement

I feel grateful for being surrounded by the most supportive, intelligent and kind people that I can possibility imagine. It is not possible for me to finish my doctoral studies without their help.

The first person I want to thank is Professor Wenbin Lin. I could not have asked for a better research advisor than him. After undergraduate studies, I only know very little about organic chemistry and much less about inorganic chemistry. Wenbin gave me the opportunity to work on metal-organic frameworks. He not only brought me into the door of chemical research, but also guided me through every single step with his critical thinking and attention to fine details. He taught me to examine frontier research wisely, by thinking deeply about the scientific validity of research results as well as their true potential in practical application. I am very grateful for his patience with me over the past four years, because it must have been very difficult to train a budding graduate researcher into a chemist. I will cherish every discussion we had and every advice he gave, and I look forward to any of our future interactions.

I was lucky to come across many senior researchers in the lab. They have been great teachers and close friends. Dr. Takahiro Sawano, a postdoc then at the Lin lab, was my mentor when I just joined the group. I remain grateful to Takahiro for getting me started on ligand synthesis, MOF growth and asymmetric catalysis. I have no doubt that he will have a great career at Chubu University with his diligence, intelligence and kindness. I also want to thank Dr. Zekai Lin, a senior labmate with three years of overlap and a very close friend of mine. Zekai has always been a helpful, passionate, and caring person. Zekai is also an X-ray wizard. He brought me to Argonne National Lab and taught me how to do synchrotron X-ray diffraction and X-ray absorption. I am sure these techniques will remain useful even for my future research on metalloenzymes and heterogeneous catalysts. I also want to thank Dr. Teng Zhang and Dr. Kuangda Lu for helping

me with countless experiments, and for being great friends throughout the years.

I also want to thank my research collaborators who have been crucial to any of my research projects. Dr. Kuntal Manna was a great organometallic chemist; together we have explored the application of MOFs for catalytic hydrogenation and C-H activations. I thank Dr. Nathan Thacker for collaboration, and for enthusiastic discussions over many experimental designs, Dr. Tasha Drake for her efforts on DFT calculations on MOF Lewis acidity and other catalytic systems.

I am also very fortunate to work with many junior lab members. They offered great help in driving the progress of many research projects, for them I'm truly grateful. Also, they constantly bring in fresh views toward different problems. Guangxu Lan is the first junior member that I worked with, who is very hardworking and full of creative ideas. I thank Yang Song and Zhe Li for working together on multiple projects and being a dependable for catalysis and DFT calculations. Yang Song, Zhe Li, and I have also stayed up with me in Argonne for many nights to finish single crystal and EXAFS experiments for the whole group. I also want to thank Xuanyu Feng, a great collaborator and a very close friend. Xuanyu is great to share good chemistry and good dinners with. I also had the privilege to work with three outstanding UChicago undergraduate students, Ania Urban, Sam Veroneau, and Pau Oliveres. They have been indispensable contributors to almost all my projects. I have no doubt about their bright future as great scientists or even lawyers.

I want to specifically thank Kaiyuan Ni, who has been a fun person to work with and an earnest friend to cherish. I have strong resonance with Kaiyuan about his passion in research. From him I learned a great deal about medicinal chemistry through our discussions. Another close friend I need to thank is Wenbo Han. Wenbo is just an ingenious, knowledgeable and forward-looking chemist. I truly wish to have a trip with him to Africa in the future.

I need to thank Christina Chan, for being in the same “boat” with me when pursuing Ph.D degree and doing ordering for the group. I also want to thank (by time joining the lab) Dan Micheroni, Dr. Zhiming Zhang, Dr. Xiangjian Kong, Marek Piechowicz, Dr. Xin Zhou, Dr. Xiaopin Duan, Dr. Ruoyu Xu, Dr. Nining Guo and Dr. Yuanyuan Zhu and others, for all their help with my research experiments and my life in Chicago. I also thank new members to the group, including Theint Aung, Ziwan Xu, Xiaomin Jiang, Taokun Luo, Yunhong Pi, Deyan Gong and others for their help, and wish them great success in UChicago.

I would like to thank my committee members, Professor Guangbin Dong and Professor John Anderson. I am incredibly grateful for the time and effort they devoted and all the suggestions they made.

Finally, I want to thank my family. Without whom I would never have the chance to pursue the career that I love. I must thank my parents, Huaidong Ji and Hongxia Zhang, and my younger sisters, Xiaoqian and Xiaoxuan for their unconditional love and support over the years. I left my hometown Bozhou eight years ago for college and traveled even further to the U.S. four years ago. I truly wish to meet my family more often in the future. I want to thank Min Chen at the other side of the earth. I would not have survived graduate school without her love and support over the past four years. I look forward to our lives together in the near future.

Chapter 1. Introduction

1.1 Metal-Organic Frameworks (MOFs)

The study of a special class of porous materials known as metal-organic frameworks (MOFs) has seen explosive growth over the past two decades. MOFs are constructed by connecting inorganic metal nodes, or secondary building units (SBUs), with bridging organic linkers to create single crystalline frameworks with well-defined porosity. MOFs share a similarity to industrially important zeolites that are characterized by large internal surface areas and uniform pore sizes, but MOFs can be constructed from a variety of organic linkers and inorganic nodes to afford an infinite array of structurally defined solids with interesting properties.

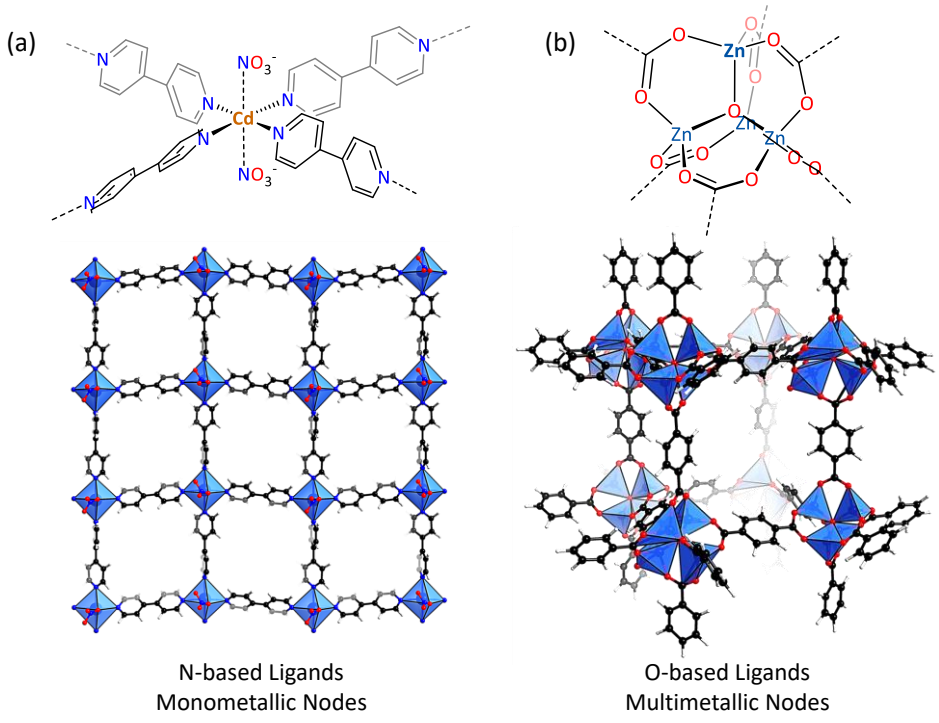

Figure 1-1 (a) Coordination environments of Cd metal centers and the crystal structure of $Cd(Bpy)(NO_3)_2$ lattice. (b) Coordination environments of Zn_4 metal nodes and the crystal structure of MOF-5.

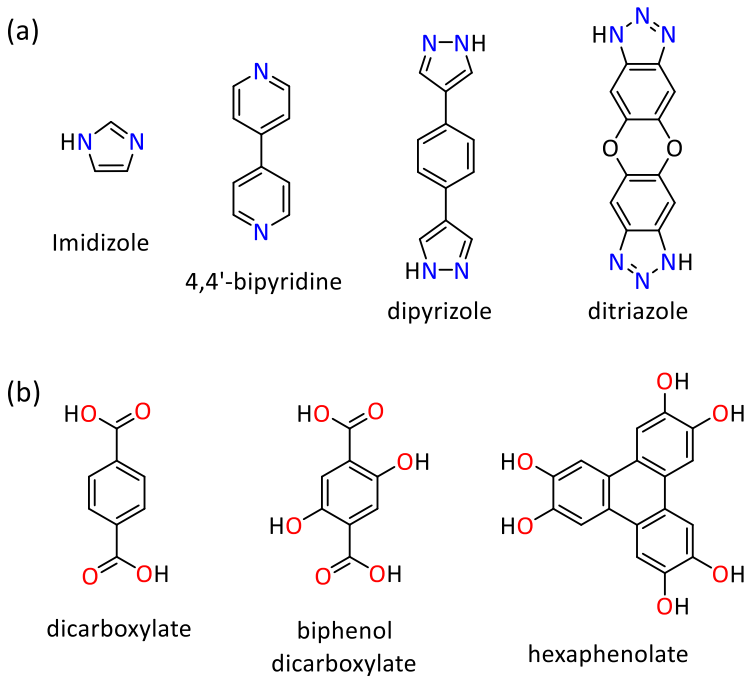

Figure 1-2. Representative examples of (a) N-based linkers and (b) O-based linkers.

The early development of porous coordination polymers was generally limited to N-donor based bridging linkers, to assemble 3-D frameworks by linking d^{10} transition metals (Cu^{I}, Zn^{II}, Cd^{II}). Classical examples are the synthesis of a Cu framework with 4,4',4",4'"-tetracyanotetraphenylmethane by Robson in 1989, and a 2-D $Cd(Bpy)(NO_3)_2$ lattices by linking Cd^{II} with 4,4'-bipyridine (Bpy), reported by Fujita in 1994 (**Figure 1-1**).[1] The two weakly-coordinating nitrates on the axial direction expose the Lewis acidic Cd^{II} metal center for catalysing organic reactions. However, the interations between nitrogen lone pairs and d^{10} metals are not strong enough to maintain the framework porosity upon desolvation. The development of carboxylate coordination-based frameworks has led to the formation of MOFs with permanant porosity. One notable example is MOF-5 constructed from simple terephthalate linkers and $Zn_4O(CO_2)_6$ SBUs, reported by Yaghi in 1999, which shows higher apparent surface area than most zeolites.[2] Follwing these initial discoveries, tens of thousands of MOFs has been developed

in the begining of 21st century. Of particular research interest are those strucutures made from O-based or anionic N-based linkers, with high framework stability and tunability (**Figure 1-2**).

MOFs have became a versitile platform for utilizing MOF components or incorporating molecular functionalities for a broad range of applications. In general, there are three major strategies to exploit MOF components for applications. First, using MOF pores for gas storage, gas seperation, [3-19] enzyme immobilization and drug delivery[20-22]; Second, anchoring functionalities to MOF linkers and inorganic nodes for catalysis,[23-34] imaging and solar energy harvesting[35-36]; Third, using different MOF parts integratively to perform cooperative functions, such as cooperative catalysis[37-38] and synergistic biomedical applications.[20, 39-42]

1.2 Zirconium-based MOFs

A great diversity of inorganic nodes have been used to construct MOFs, including divalent, trivalent, and most importantly, tetravalent metals.[43-45] Among tens of thousands of MOFs synthesized to date, Zr-based MOFs have distinguished themselves with exceptionally high thermal and chemical stability, simple and straightforward linker tunability, and relatively low costs of zirconium precursors.[46-47] Zr nodes with different symmetry and connectivity have been obtained via judicious choice of linkers and synthetic conditions. The best-known example is the UiO-type of MOF first reported by Lillerud and coworkers in 2008, which is composed of $Zr_6O_4(OH)_4(CO_2)_{12}$ type of SBUs.[43] By utilizing different carboxylate linkers that are tritopic or tetratopic, Zr-MOFs with other Zr_6 SBUs, such as $Zr_6O_4(OH)_4(CO_2)_8$ and $Zr_6O_4(OH)_4(CO_2)_6$, have also been synthesized (**Figure 1-3**).[48-49] Part of this thesis explores the possibility of activating the monocarboxylate-capped metal centers in these nodes for catalysis. The straightforward activation

of MOF nodes provides an intriguing opportunity to design single-site solid catalysts that do not have homogeneous counterparts.

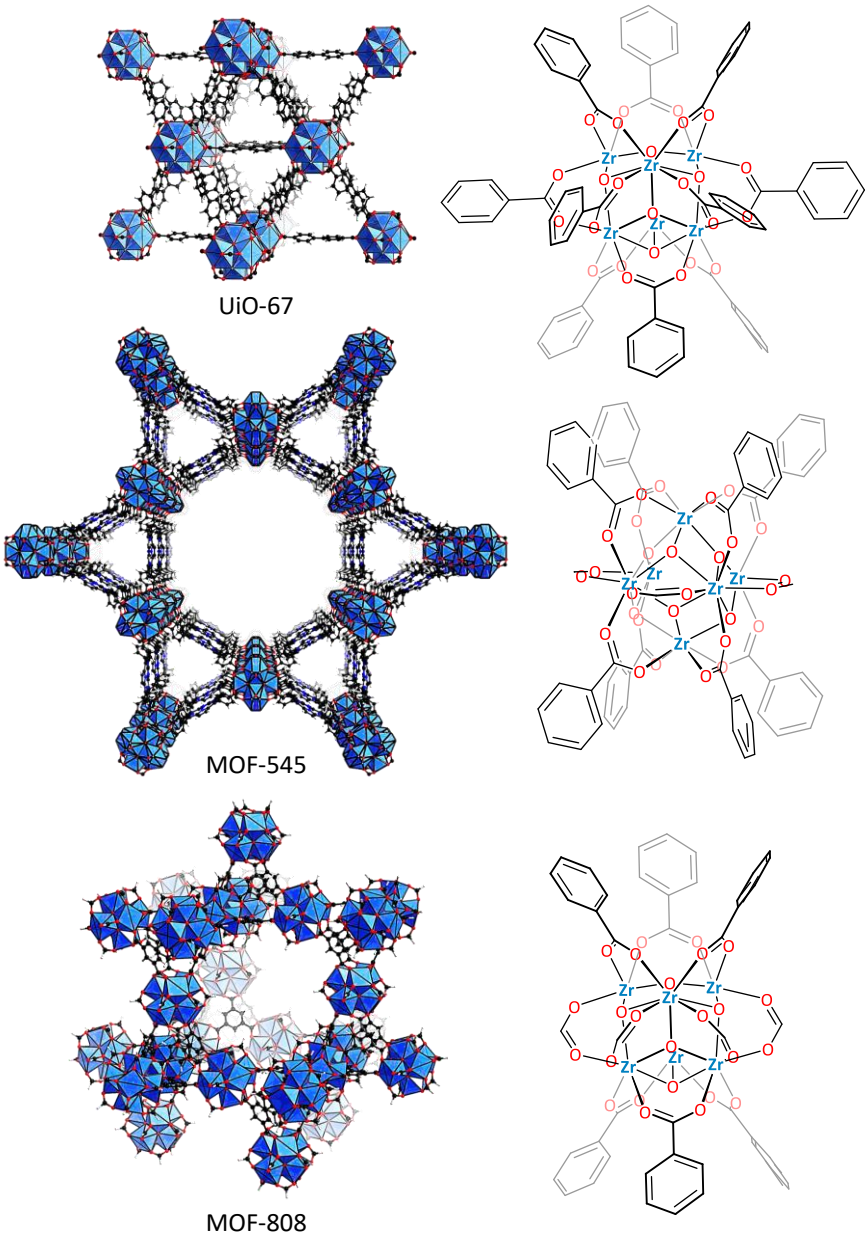

Figure 1-3. Representative examples of Zr_6-based MOFs, including UiO-67, MOF-545 and MOF-808.

Besides Zr_6 SBUs, my work has discovered some other multimetallic Zr-SBUs, including $Zr_8O_8(OH)_4(CO_2)_{12}$ in the Zr_8MTBC MOF,[50] and $Zr_{12}O_8(OH)_{14}(CO_2)_{18}$ SBU in the Zr_{12}TPDC MOF (**Figure 1-4**).[51] These MOFs have expanded the diversity of Zr-MOF families, and provided novel MOF topology and SBU functionalities. Both of these two SBUs provided an excellent ligand platform for discovering single-site base metal catalysts without homogenous analogues.

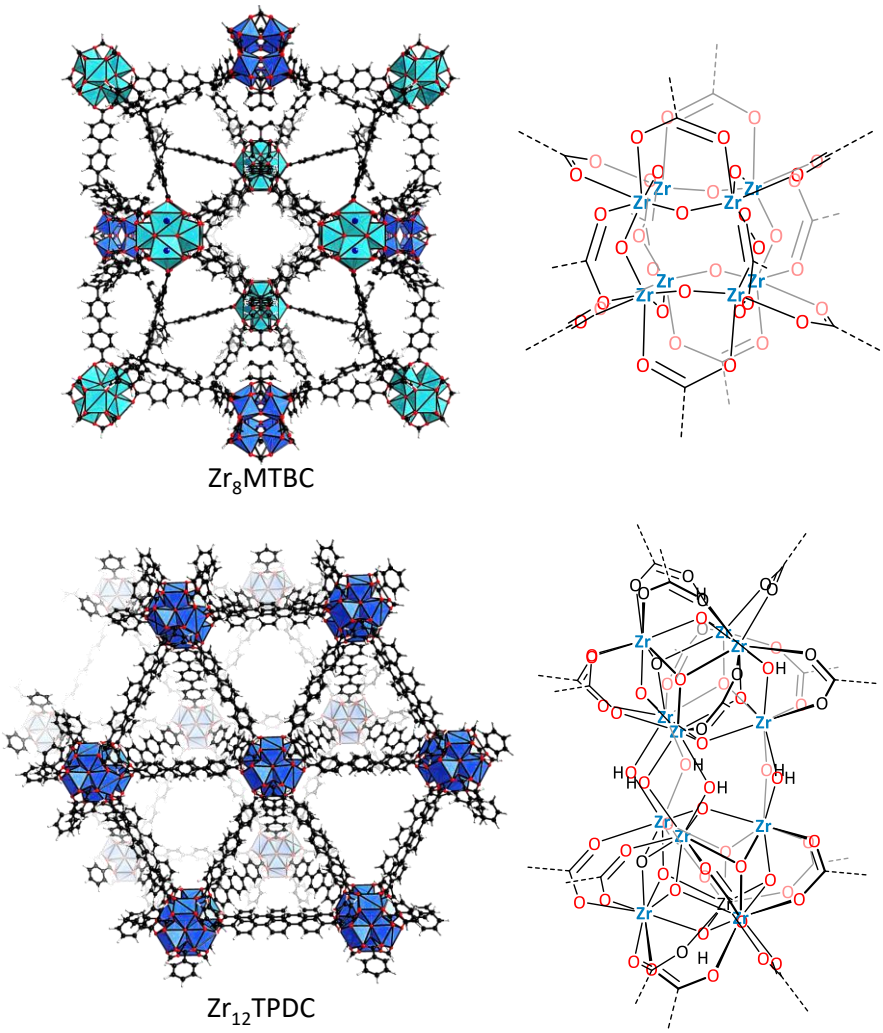

Figure 1-4. Representative examples of Zr_8-based and Zr_{12}-based MOFs.

1.3 Homogeneous versus Heterogeneous Catalysis

Catalysts can be generally divided into homogeneous or heterogeneous types, depending on whether a catalyst exists in the same phase as the substrate. One important example of homogeneous transition metal catalyst is the second generation Grubbs catalyst (Grubbs catalyst II), which is very efficient for olefin metathesis reactions (**Figure 1-5a**). This small molecule Ru complex dissolves in organic solvents before reacting with an olefin substrate. One of the best examples of heterogeneous catalyst is a type of zeolite named Faujasite, which is a common heterogeneous catalyst used in refineries (**Figure 1-5b**). Although Faujasite itself is insoluble in substrates, hydrocarbons can efficiently diffuse through the pores and are converted to products by the surface acidic sites.

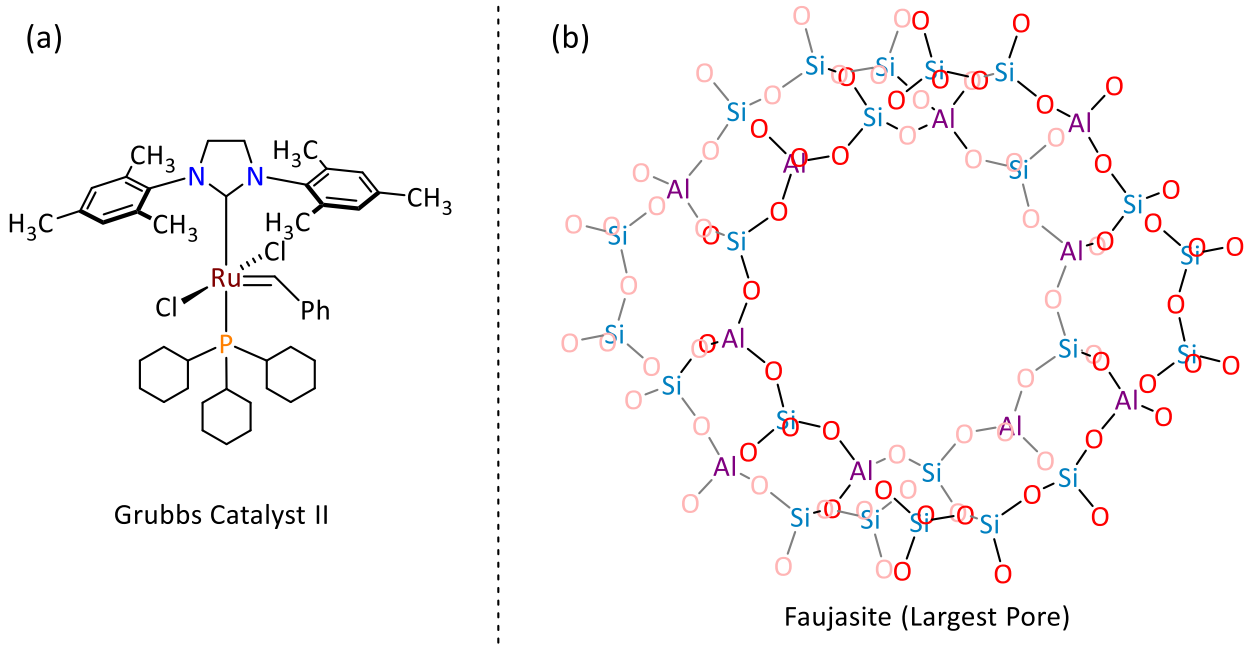

Figure 1-5. (a) Chemical structure of Grubbs catalyst II. **(b)** Structure of the largest pore in Faujasite, highlighting the [SiO_4] and [AlO_4] tetrahedral units.

Homogeneous catalysts have well defined molecular structures and their structures and functions can be easily tuned through molecular modifications. Moreover, their reaction

mechanism can be easily rationalized through kinetic analysis and computational studies. However, homogeneous catalysts generally are more expensive, arising from lengthy synthesis of organic ligands and the inability to reuse the catalyst. On the contrary, heterogeneous catalysts are readily synthesized from abundant precursors, and are easily recycled through solid-liquid or solid-gas separations. This allows for their broad applications in industrial processes, including the Harber-Bosch process for the production of ammonia and the Ziegler-Natta catalyst for olefin polymerizations. However, heterogeneous catalysts contain multiple types of active sites, thus prohibiting the characterization of the active species or the fine-tuning of reaction activity and selectivity. Significant effort has been devoted to address this problem by designing single-site heterogeneous catalysts.

1.4 Site-Isolation Effect in MOF Catalysts

Sterically-hindered chelating ligands are commonly used in homogeneous base-metal catalysts to prevent catalyst decomposition pathways, through metal-ligand disproportionation, oligomerization, or ligand transformation to form deactivated species (**Figure 1-6**). However, such steric protecting groups may weaken the ligand-coordination strength, and even worse, impede the access of substrates to metal centers. These drawbacks are well represented in a homogeneous Co-based catalyst, which displays limited activity toward the hydrogenation of tetra-substituted olefins.

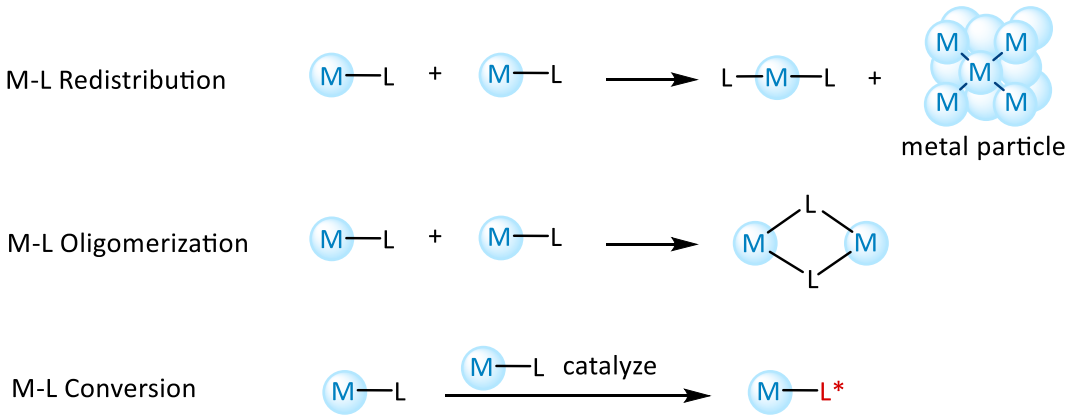

Figure 1-6. Common multimetallic decomposition pathways for homogeneous catalysts.

The major way to prevent catalyst deactivation without using bulky ligands is to immobilize catalysts onto material surface, thus separating the metal centers from direct contact. Solid materials such as silica, alumina and titania are among the most common supports to anchor catalytically active metal centers. However, metal oxide surface often generates non-uniform catalyst species as a result of having multiple kinds of hydroxide functionalities. MOFs provide a highly tunable platform to access site-isolated catalysts with uniform compositions, benefiting from their periodic structure and molecularly well-defined functionalities (**Figure 1-7**). The synthetic versatility of MOFs allows for the fine-tuning of the electronic and steric properties of the active sites, whereas the structure regularity greatly facilitates mechanistic studies of MOF-catalyzed reactions. Prior to my research, many works have been done to generate MOF catalysts by utilizing pre-metalated organic struts or via postsynthetic metalation of functionalized bridging linkers. The first part of this thesis explores the use of metal hydroxide clusters in MOFs as oxo-donor ligands to anchor earth-abundant metal catalysts for organic transformations.

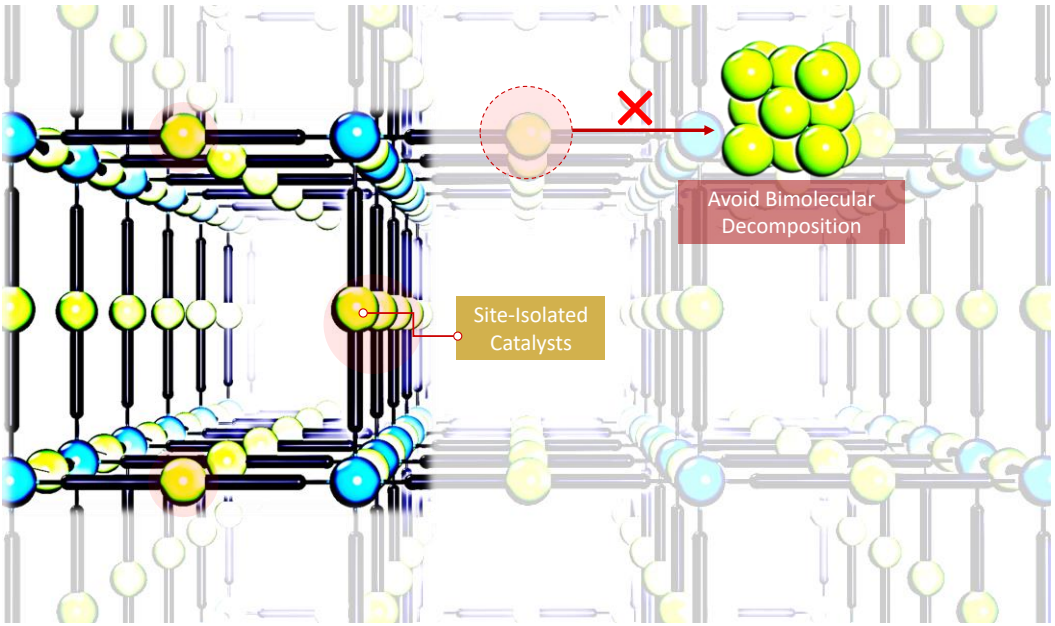

Figure 1-7. Site-isolation of catalysts inside MOF channels avoids bimolecular decomposition pathways.

MOF nodes are not only utilized as catalyst supports, but are also directly activated to open-up coordination around metal centers to generate novel catalysts. Such straightforward activation of MOF nodes provides an intriguing opportunity to design single-site solid catalysts that do not have homogeneous counterparts. There are examples of directly using MOF nodes for catalysis, but these works are limited to Lewis acid or Brønsted acid catalysis. The node-activation part of this thesis demonstrates the generation of unusual organometallic catalysts with the MOF nodes, and their application in much broader range of reactions, including olefin polymerization and hydroelementation reactions.

1.5 Characterization of MOF Catalysts

The uniform composition of MOF active sites facilitates their structural and spectroscopic characterization. Detailed knowledge of the catalyst structure is essential for understanding their

reaction mechanism, and allows for the further optimization of the catalyst performance (**Figure 1-8**). X-ray diffraction (XRD) techniques, ether single crystal X-ray diffractions (SXRD) or powder X-ray diffractions (PXRD), have been essential to the understanding of MOF structures. Monitoring of MOF structure is crucial at all different stages of MOF catalysis, either right upon MOF synthesis, activation, or after catalysis. Spectroscopic methods, particularly electron paramagnetic resonance (EPR), X-ray absorption near-edge spectroscopy (XANES) and X-ray photoelectron spectroscopy (XPS), are very crucial for understanding the oxidation state and spin properties of the metal centers. Moreover, extended X-ray absorption fine-structure is very powerful for determining the metal coordination environment at the active sites.

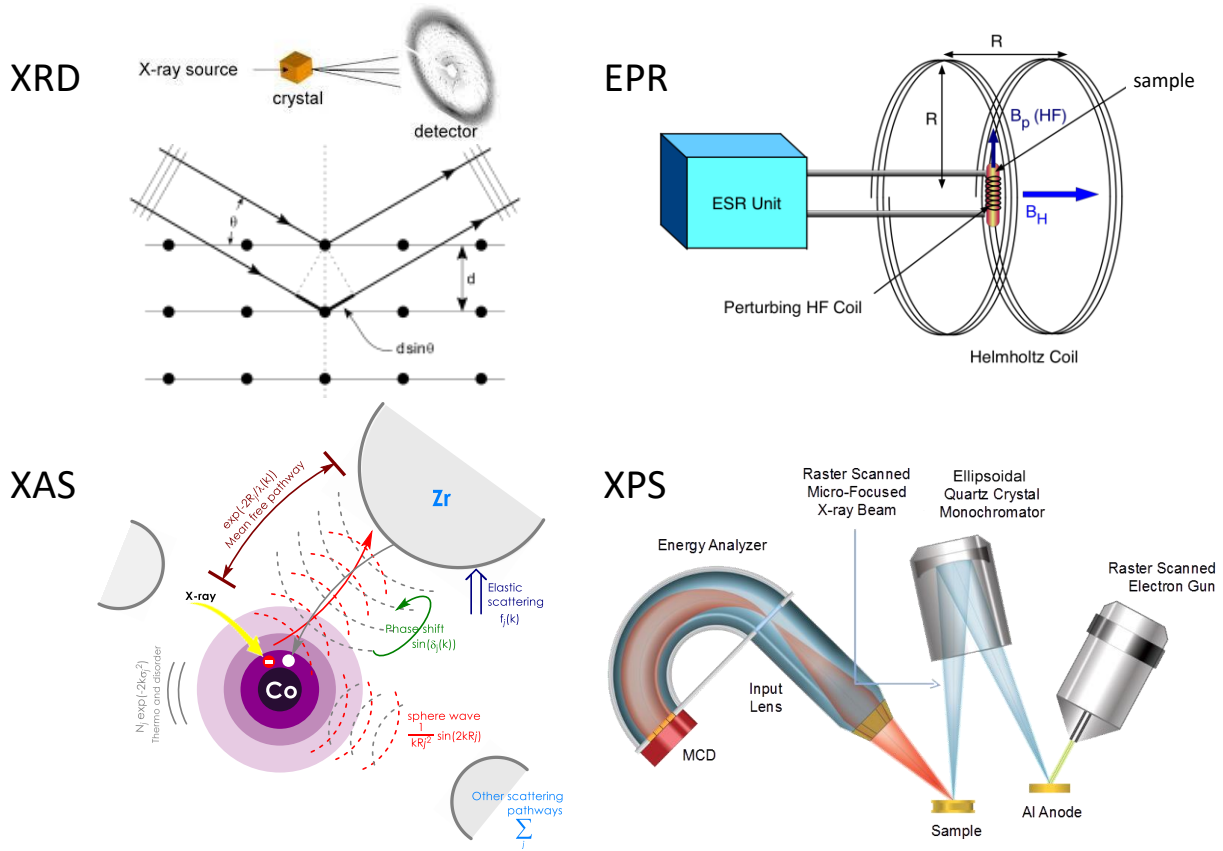

Figure 1-8. Structural and spectroscopic techniques used to characterize MOF catalysts. EPR mechanistic scheme courtesy of Dr. Werner U. Boeglin. XPS mechanistic scheme courtesy of 2018 Physical Electronics, Inc.

1.6 References

1. Fujita, M.; Kwon, Y. J.; Washizu, S.; Ogura, K., Preparation, Clathration Ability, and Catalysis of a Two-Dimensional Square Network Material Composed of Cadmium(II) and 4,4'-Bipyridine. *J. Am. Chem. Soc.* **1994,** 1151-1152.

2. Li, H.; Eddaoudi, M.; O'Keeffe, M.; Yaghi, O. M., Design and synthesis of an exceptionally stable and highly porous metal-organic framework. *Nature* **1999,** 276.

3. Mulfort, K. L.; Hupp, J. T., Chemical Reduction of Metal−Organic Framework Materials as a Method to Enhance Gas Uptake and Binding. *J. Am. Chem. Soc.* **2007,** 9604-9605.

4. Farha, O. K.; Spokoyny, A. M.; Mulfort, K. L.; Hawthorne, M. F.; Mirkin, C. A.; Hupp, J. T., Synthesis and Hydrogen Sorption Properties of Carborane Based Metal−Organic Framework Materials. *J. Am. Chem. Soc.* **2007,** 12680-12681.

5. Chen, B.; Zhao, X.; Putkham, A.; Hong, K.; Lobkovsky, E. B.; Hurtado, E. J.; Fletcher, A. J.; Thomas, K. M., Surface Interactions and Quantum Kinetic Molecular Sieving for H2 and D2 Adsorption on a Mixed Metal−Organic Framework Material. *J. Am. Chem. Soc.* **2008,** 6411-6423.

6. Dincă, M.; Long, J. R., Hydrogen Storage in Microporous Metal–Organic Frameworks with Exposed Metal Sites. *Angew. Chem. Int. Ed.* **2008,** 6766-6779.

7. Murray, L. J.; Dincă, M.; Long, J. R., Hydrogen storage in metal–organic frameworks. *Chem. Soc. Rev.* **2009,** 1294-1314.

8. Rowsell, J. L. C.; Yaghi, O. M., Strategies for Hydrogen Storage in Metal–Organic Frameworks. *Angew. Chem. Int. Ed.* **2005,** 4670-4679.

9. Samanta, A.; Furuta, T.; Li, J., Theoretical assessment of the elastic constants and hydrogen storage capacity of some metal-organic framework materials. *J. Chem. Phys.* **2006,** 084714.

10. Lin, X.; Telepeni, I.; Blake, A. J.; Dailly, A.; Brown, C. M.; Simmons, J. M.; Zoppi, M.; Walker, G. S.; Thomas, K. M.; Mays, T. J.; Hubberstey, P.; Champness, N. R.; Schröder, M., High Capacity Hydrogen Adsorption in Cu(II) Tetracarboxylate Framework Materials: The Role of Pore Size, Ligand Functionalization, and Exposed Metal Sites. *J. Am. Chem. Soc.* **2009,** 2159-2171.

11. Ma, L.; Lee, J. Y.; Li, J.; Lin, W., 3D Metal−Organic Frameworks Based on Elongated Tetracarboxylate Building Blocks for Hydrogen Storage. *Inorg. Chem.* **2008,** 3955-3957.

12. Ma, S.; Sun, D.; Ambrogio, M.; Fillinger, J. A.; Parkin, S.; Zhou, H.-C., Framework-Catenation Isomerism in Metal−Organic Frameworks and Its Impact on Hydrogen Uptake. *J. Am. Chem. Soc.* **2007,** 1858-1859.

13. Matsuda, R.; Kitaura, R.; Kitagawa, S.; Kubota, Y.; Belosludov, R. V.; Kobayashi, T. C.; Sakamoto, H.; Chiba, T.; Takata, M.; Kawazoe, Y.; Mita, Y., Highly controlled acetylene accommodation in a metal–organic microporous material. *Nature* **2005,** 238.

14. Allendorf, M. D.; Houk, R. J. T.; Andruszkiewicz, L.; Talin, A. A.; Pikarsky, J.; Choudhury, A.; Gall, K. A.; Hesketh, P. J., Stress-Induced Chemical Detection Using Flexible Metal−Organic Frameworks. *J. Am. Chem. Soc.* **2008,** 14404-14405.

15. Kapelewski, M. T.; Geier, S. J.; Hudson, M. R.; Stück, D.; Mason, J. A.; Nelson, J. N.; Xiao, D. J.; Hulvey, Z.; Gilmour, E.; FitzGerald, S. A.; Head-Gordon, M.; Brown, C. M.; Long, J. R., M2(m-dobdc) (M = Mg, Mn, Fe, Co, Ni) Metal–Organic Frameworks Exhibiting Increased Charge Density and Enhanced H2 Binding at the Open Metal Sites. *J. Am. Chem. Soc.* **2014,** 12119-12129.

16. Li, B.; Wen, H.-M.; Wang, H.; Wu, H.; Tyagi, M.; Yildirim, T.; Zhou, W.; Chen, B., A Porous Metal–Organic Framework with Dynamic Pyrimidine Groups Exhibiting Record High Methane Storage Working Capacity. *J. Am. Chem. Soc.* **2014,** 6207-6210.

17. Zhao, X.; Wong, M.; Mao, C.; Trieu, T. X.; Zhang, J.; Feng, P.; Bu, X., Size-Selective Crystallization of Homochiral Camphorate Metal–Organic Frameworks for Lanthanide Separation. *J. Am. Chem. Soc.* **2014,** 12572-12575.

18. He, Y.; Zhou, W.; Qian, G.; Chen, B., Methane storage in metal–organic frameworks. *Chem. Soc. Rev.* **2014,** 5657-5678.

19. Wen, H.-M.; Li, B.; Li, L.; Lin, R.-B.; Zhou, W.; Qian, G.; Chen, B., A Metal–Organic Framework with Optimized Porosity and Functional Sites for High Gravimetric and Volumetric Methane Storage Working Capacities. *Adv. Mater.* **2018,** 1704792.

20. Della Rocca, J.; Liu, D.; Lin, W., Nanoscale Metal–Organic Frameworks for Biomedical Imaging and Drug Delivery. *Acc. Chem. Res.* **2011,** 957-968.

21. Horcajada, P.; Serre, C.; Vallet-Regí, M.; Sebban, M.; Taulelle, F.; Férey, G., Metal–Organic Frameworks as Efficient Materials for Drug Delivery. *Angew. Chem. Int. Ed.* **2006,** 5974-5978.

22. Horcajada, P.; Gref, R.; Baati, T.; Allan, P. K.; Maurin, G.; Couvreur, P.; Férey, G.; Morris, R. E.; Serre, C., Metal–Organic Frameworks in Biomedicine. *Chem. Rev.* **2011,** 1232-1268.

23. Huang, Y.-B.; Liang, J.; Wang, X.-S.; Cao, R., Multifunctional metal–organic framework catalysts: synergistic catalysis and tandem reactions. *Chem. Soc. Rev.* **2017,** 126-157.

24. Rogge, S. M. J.; Bavykina, A.; Hajek, J.; Garcia, H.; Olivos-Suarez, A. I.; Sepúlveda-Escribano, A.; Vimont, A.; Clet, G.; Bazin, P.; Kapteijn, F.; Daturi, M.; Ramos-Fernandez, E. V.; Llabrés i Xamena, F. X.; Van Speybroeck, V.; Gascon, J., Metal–organic and covalent organic frameworks as single-site catalysts. *Chem. Soc. Rev.* **2017,** 3134-3184.

25. Zhu, L.; Liu, X.-Q.; Jiang, H.-L.; Sun, L.-B., Metal–Organic Frameworks for Heterogeneous Basic Catalysis. *Chem. Rev.* **2017,** 8129-8176.

26. Farrusseng, D.; Aguado, S.; Pinel, C., Metal–Organic Frameworks: Opportunities for Catalysis. *Angew. Chem. Int. Ed.* **2009,** 7502-7513.

27. Corma, A.; García, H.; Llabrés i Xamena, F. X., Engineering Metal Organic Frameworks for Heterogeneous Catalysis. *Chem. Rev.* **2010,** 4606-4655.

28. Yoon, M.; Srirambalaji, R.; Kim, K., Homochiral Metal–Organic Frameworks for Asymmetric Heterogeneous Catalysis. *Chem. Rev.* **2012,** 1196-1231.

29. Lee, J.; Farha, O. K.; Roberts, J.; Scheidt, K. A.; Nguyen, S. T.; Hupp, J. T., Metal–organic framework materials as catalysts. *Chem. Soc. Rev.* **2009,** 1450-1459.

30. Ma, L.; Abney, C.; Lin, W., Enantioselective catalysis with homochiral metal–organic frameworks. *Chem. Soc. Rev.* **2009,** 1248-1256.

31. Wang, Z.; Cohen, S. M., Postsynthetic modification of metal–organic frameworks. *Chem. Soc. Rev.* **2009,** 1315-1329.

32. Burgess, S. A.; Kassie, A.; Baranowski, S. A.; Fritzsching, K. J.; Schmidt-Rohr, K.; Brown, C. M.; Wade, C. R., Improved Catalytic Activity and Stability of a Palladium Pincer Complex by Incorporation into a Metal–Organic Framework. *J. Am. Chem. Soc.* **2016,** 1780-1783.

33. Nepal, B.; Das, S., Sustained Water Oxidation by a Catalyst Cage-Isolated in a Metal–Organic Framework. *Angew. Chem. Int. Ed.* **2013,** 7365-7368.

34. Logan, M. W.; Ayad, S.; Adamson, J. D.; Dilbeck, T.; Hanson, K.; Uribe-Romo, F. J., Systematic variation of the optical bandgap in titanium based isoreticular metal–organic frameworks for photocatalytic reduction of CO2 under blue light. *J. Mater. Chem. A* **2017,** 11854-11863.

35. Lin, W.; Long, J. R., Preface for the Forum on Metal-Organic Frameworks for Energy Applications. *Inorg. Chem.* **2016,** 7189.

36. Kent, C. A.; Liu, D.; Ma, L.; Papanikolas, J. M.; Meyer, T. J.; Lin, W., Light Harvesting in Microscale Metal–Organic Frameworks by Energy Migration and Interfacial Electron Transfer Quenching. *J. Am. Chem. Soc.* **2011,** 12940-12943.

37. Sun, L.; Campbell, M. G.; Dincă, M., Electrically Conductive Porous Metal–Organic Frameworks. *Angew. Chem. Int. Ed.* **2016,** 3566-3579.

38. Silva, C. G.; Corma, A.; Garcia, H., Metal-organic frameworks as semiconductors. *J. Mat. Chem.* **2010,** 3141-3156.

39. Lin, W.; Rieter, W. J.; Taylor, K. M. L., Modular Synthesis of Functional Nanoscale Coordination Polymers. *Angew. Chem. Int. Ed.* **2009,** 650-658.

40. Horcajada, P.; Chalati, T.; Serre, C.; Gillet, B.; Sebrie, C.; Baati, T.; Eubank, J. F.; Heurtaux, D.; Clayette, P.; Kreuz, C.; Chang, J.-S.; Hwang, Y. K.; Marsaud, V.; Bories, P.-N.; Cynober, L.; Gil, S.; Férey, G.; Couvreur, P.; Gref, R., Porous metal–organic-framework nanoscale carriers as a potential platform for drug delivery and imaging. *Nat. Mater.* **2009,** 172.

41. An, J.; Geib, S. J.; Rosi, N. L., Cation-Triggered Drug Release from a Porous Zinc−Adeninate Metal−Organic Framework. *J. Am. Chem. Soc.* **2009,** 8376-8377.

42. White, K. A.; Chengelis, D. A.; Gogick, K. A.; Stehman, J.; Rosi, N. L.; Petoud, S., Near-Infrared Luminescent Lanthanide MOF Barcodes. *J. Am. Chem. Soc.* **2009,** 18069-18071.

43. Cavka, J. H.; Jakobsen, S.; Olsbye, U.; Guillou, N.; Lamberti, C.; Bordiga, S.; Lillerud, K. P., A New Zirconium Inorganic Building Brick Forming Metal Organic Frameworks with Exceptional Stability. *J. Am. Chem. Soc.* **2008,** 13850-13851.

44. Ji, P.; Sawano, T.; Lin, Z.; Urban, A.; Boures, D.; Lin, W., Cerium-Hydride Secondary Building Units in a Porous Metal-Organic Framework for Catalytic Hydrobo-ration and Hydrophosphination. *J. Am. Chem. Soc.* **2016**.

45. Hendon, C. H.; Tiana, D.; Fontecave, M.; Sanchez, C. m.; D'arras, L.; Sassoye, C.; Rozes, L.; Mellot-Draznieks, C.; Walsh, A., Engineering the optical response of the titanium-MIL-125 metal–organic framework through ligand functionalization. *J. Am. Chem. Soc.* **2013,** 10942-10945.

46. Bai, Y.; Dou, Y.; Xie, L.-H.; Rutledge, W.; Li, J.-R.; Zhou, H.-C., Zr-based metal–organic frameworks: design, synthesis, structure, and applications. *Chem. Soc. Rev.* **2016,** 2327-2367.

47. Devic, T.; Serre, C., High valence 3p and transition metal based MOFs. *Chem. Soc. Rev.* **2014,** 6097-6115.

48. Morris, W.; Volosskiy, B.; Demir, S.; Gándara, F.; McGrier, P. L.; Furukawa, H.; Cascio, D.; Stoddart, J. F.; Yaghi, O. M., Synthesis, Structure, and Metalation of Two New Highly Porous Zirconium Metal–Organic Frameworks. *Inorg. Chem.* **2012,** 6443-6445.

49. Furukawa, H.; Gándara, F.; Zhang, Y.-B.; Jiang, J.; Queen, W. L.; Hudson, M. R.; Yaghi, O. M., Water Adsorption in Porous Metal–Organic Frameworks and Related Materials. *J. Am. Chem. Soc.* **2014,** 4369-4381.

50. Ji, P.; Manna, K.; Lin, Z.; Urban, A.; Greene, F. X.; Lan, G.; Lin, W., Single-Site Cobalt Catalysts at New Zr8(μ2-O)8(μ2-OH)4 Metal-Organic Framework Nodes for Highly Active Hydrogenation of Alkenes, Imines, Carbonyls, and Heterocycles. *J. Am. Chem. Soc.* **2016,** 12234-12242.

51. Ji, P.; Manna, K.; Lin, Z.; Feng, X.; Urban, A.; Song, Y.; Lin, W., Single-Site Cobalt Catalysts at New Zr12(μ3-O)8(μ3-OH)8(μ2-OH)6 Metal–Organic Framework Nodes for Highly Active Hydrogenation of Nitroarenes, Nitriles, and Isocyanides. *J. Am. Chem. Soc.* **2017,** 7004-7011.

Chapter 2. Zr_6 MOF Nodes Support Single-Site Magnesium–Alkyl Catalyst for Hydroboration and Hydroamination Reactions

2.1 Introduction

The $Zr_6O_4(OH)_4(CO_2)_{12}$ SBU in UiO-type of MOF features a unique μ_3-OH functionality. It is possible to anchor organometallic catalysts onto the μ_3-OH site to access supported catalyst with unprecedented electronic and steric properties. Magnesium, one of the most abundant metals on earth, was anchored to the μ_3-OH site for catalytic transformations.

Despite their great abundance, alkaline earth metals such as magnesium and calcium have found limited application in catalytic processes. Developing catalysts that use these metals can be challenging because heteroleptic complexes tend to undergo Schlenk-type and/or irreversible ligand redistribution reactions to form catalytically incompetent homoleptic complexes.[1] To counter such associative intermolecular ligand redistribution reactions, bulky chelating ligands, such as β-diketiminate,[2-4] aminotroponiminates,[5] pybox,[6] silylamido phenolate,[7] and tris(oxazolinyl)borate,[7] have been explored in the preparation of main group catalysts for a range of organic transformations, such as hydroamination,[4-5,8] hydrosilylation,[9] hydroboration,[10] hydrophosphination, [11] and many other reactions. Although sterically encumbered ligands stabilize the heteroleptic species, they slow down the binding and activation of substrates, thus significantly impeding the catalytic activity. In contrast, immobilizing heteroleptic alkaline earth metal species in porous solid supports can provide site isolation without relying on bulky ligands and thus provide an alternative route to obtaining active catalysts.[12]

Zhang et al. recently showed that highly active base-metal catalysts can be stabilized in bipyridyl-based MOFs via active site isolation, while analogous homogeneous catalysts undergo rapid intermolecular deactivation via ligand disproportionation reactions.[13] This chapter explores a simple strategy to stabilize active Mg-alkyl species at SBUs of a UiO-MOF, Zr_6QPDCN (QPDCN is 4,4'-bis-(carboxyphenyl)-2-nitro-1,1'-biphenyl), to afford highly active and reusable single-site solid catalysts for hydroboration of carbonyl and imine compounds and for hydroamination of aminoalkenes. Site isolation within the MOF stabilizes catalytically active heteroleptic Mg-alkyl species by shutting down Schlenk-type intermolecular ligand redistribution reactions (**Figure 2-1**).

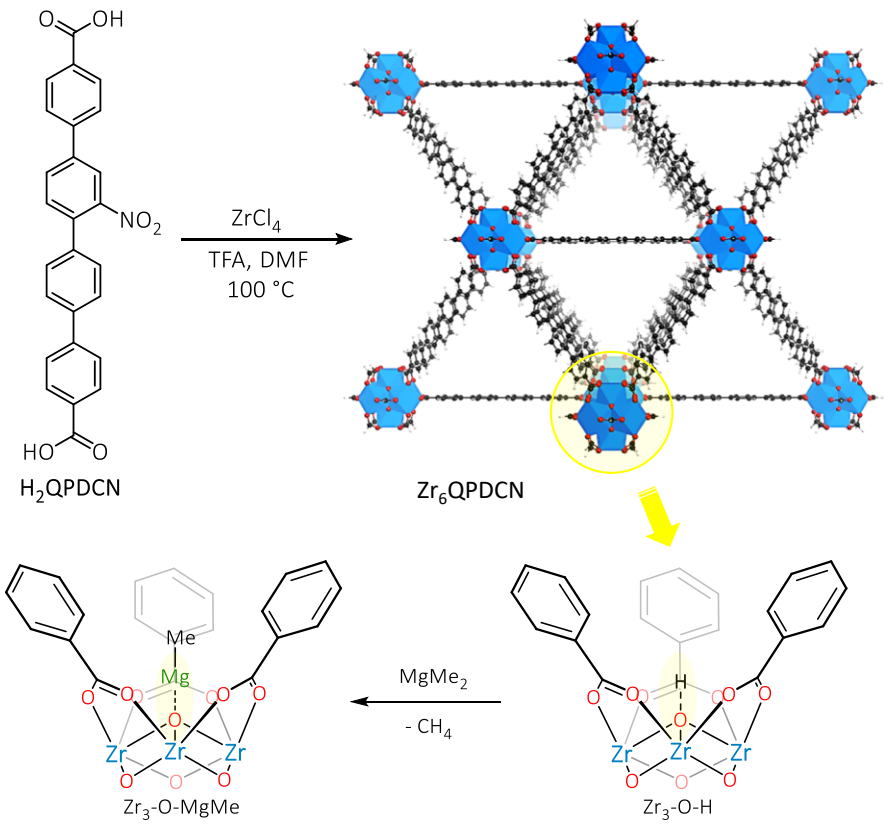

Figure 2-1. The synthesis of Zr_6QPDCN through solvothermal reactions and metalation of its SBUs with $MgMe_2$ to form MgMe-Zr_6QPDCN.

2.2 Results and Discussion

2.2.1 Metalation and characterization of the MgMe-Zr$_6$QPDCN MOF

Scheme 2-1. Active site isolation of $MgMe_2$ on μ_3-OH site of Zr_6 SBU.

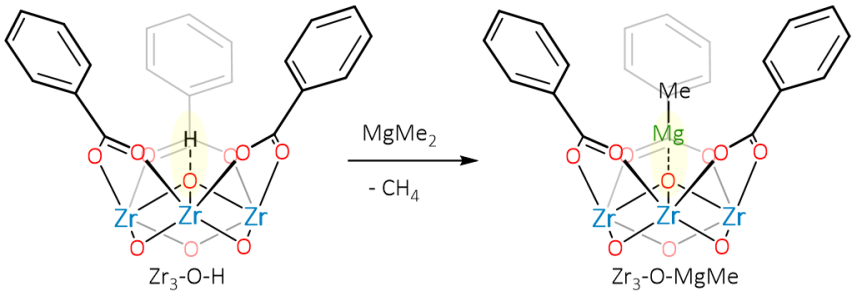

The metalation of $Zr_3(\mu_3$-OH) sites in SBUs of Zr$_6$QPDCN was performed by the protonolysis reaction of Zr$_6$QPDCN with $MgMe_2$ in THF at room temperature to afford Mg-functionalized MOF material (MgMe-Zr$_6$QPDCN) as a yellow solid (**Scheme 2-1**). During the metalation reaction, an equivalent amount of methane was generated, which was identified and quantified by GC analysis. The disappearance of μ_3O-H band (~3629 cm^{-1}, KBr) in the infrared spectrum (IR) of MgMe-Zr$_6$QPDCN indicated that the metalation occurred at $Zr_3(\mu_3$-OH) sites (**Figure 2-2**).

Inductively coupled plasma-mass spectrometry (ICP-MS) analysis of the digested MgMe-Zr$_6$QPDCN revealed four Mg centers per Zr_6 node, indicating 100% metalation at the $Zr_3(\mu_3$-OH) sites. Crystallinity of Zr$_6$QPDCN was maintained upon metalation, as shown by the similarities in the PXRD patterns of Zr$_6$QPDCN and MgMe-Zr$_6$QPDCN (**Figure 2-3**).

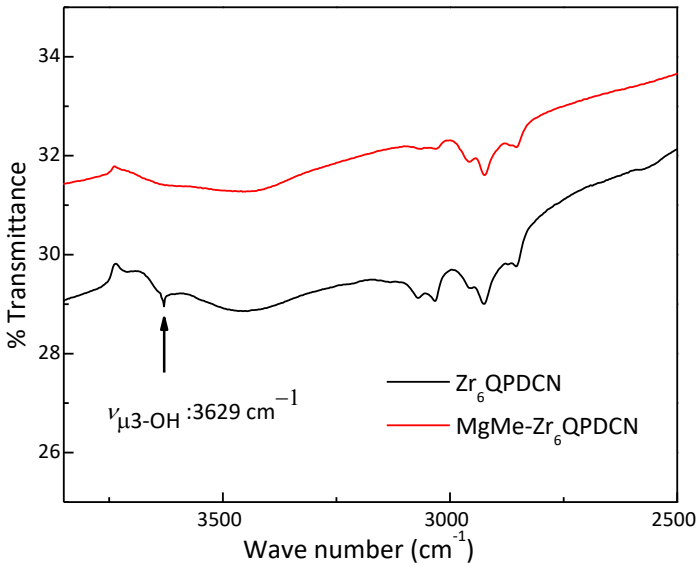

Figure 2-2. IR spectra of Zr_6QPDCN (black) and MgMe-Zr_6QPDCN (red). The disappearance of the $\nu_{\mu 3O\text{-}H}$ band (~3629 cm^{-1}, KBr) suggests postsynthetic metalation at Zr_3-μ_3-OH sites.

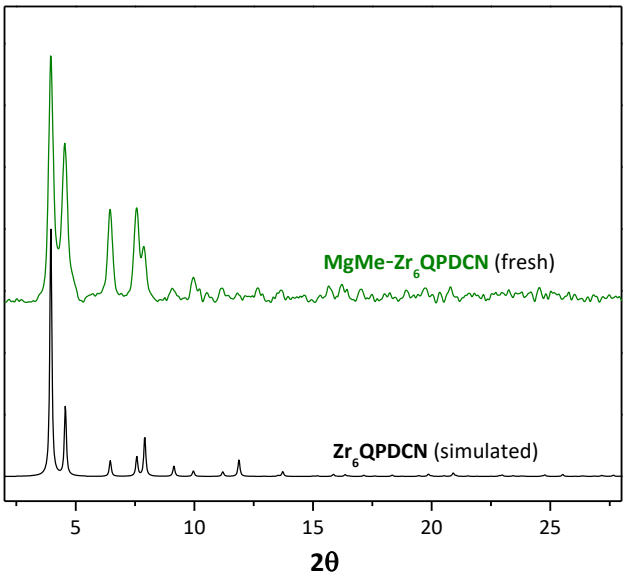

Figure 2-3. PXRD patterns of MgMe-Zr_6QPDCN (green) compared to that of pristine Zr_6QPDCN.

SEM images showed that Zr_6QPDCN has particle sizes of ~2-3 μm. The SXRD study revealed that MgMe-Zr_6QPDCN crystallizes in the $Fm\bar{3}m$ space group, with the $Zr_6(\mu_3\text{-}O)_4(\mu_3\text{-}OH)_4$ SBUs connected by the QPDCN bridging linkers to afford the 12-connected structure of *fcu*

topology. However, due to crystallographic disorder of the MgMe moiety and the low atomic weight of Mg atom, the Mg coordination environments in MgMe-Zr_6QPDCN could not be established by X-ray crystallography. The four MgMe moieties are randomly distributed among the eight μ_3-oxo positions. In addition, every (Zr_3)O-MgMe moiety is in close proximity to six carboxylate oxygen atoms; one or two of the carboxylate oxygen atoms could possibly tilt the Mg atom off the C_3-axis through weak coordination. These disorders lead to low site occupancy of 1/6 for the MgMe moiety if we assume Mg coordinates to two carboxylate groups, thus making Mg atoms impossible to observe in the $Fm\bar{3}m$ space group.

2.2.2 MgMe-Zr_6QPDCN catalyzed hydroboration of ketones.

MgMe-Zr_6QPDCN displayed excellent activity in the hydroboration of a wide range of carbonyl compounds with pinacolborane (**Table 2-1**). The hydroboration reactions were performed by treating ketones or aldehydes with equimolar HBpin in the presence of 0.1 – 0.01 mol % MOF-Mg in hexane or THF at room temperature.

At a 0.05 mol % Mg loading, MOF-Mg afforded borate ester products from a range of carbonyl substrates, including alkyl, halogenated, and alkoxy-functionalized aryl ketones and aldehydes in essentially quantitative yields. Pure hydroboration products were obtained by simply removing the solid catalyst via centrifugation followed by removal of the organic volatiles. Impressively, MgMe-Zr_6QPDCN catalysed the hydroboration of acetophenone with a TON of 84,000. Linear and cyclic aliphatic ketones were efficiently reduced in excellent yields. In addition, α, β-unsaturated carbonyl substrates such as cyclohexenone, trans-crotonophenone, and trans-cinnamaldehyde were reduced selectively at the carbonyl, leaving the C=C bond intact.

Remarkably, at a 0.2 mol% catalyst loading, MgMe-Zr_6QPDCN could be recovered and reused for hydroboration of acetophenone at least 10 times without loss of MOF crystallinity (**Figure 2-4**). Excellent yields (95-100%) of boronate ester were obtained consistently in the reuse experiments with no observation of other byproducts. The PXRD patterns of MOF-Mg recovered from the 1st and 11th runs remained unchanged from that of pristine MOF-Mg, indicating the stability of the MOFs under reaction conditions.

Table 2-1. MgMe-Zr_6QPDCN Catalysed Hydroboration of Ketones and Aldehydes.

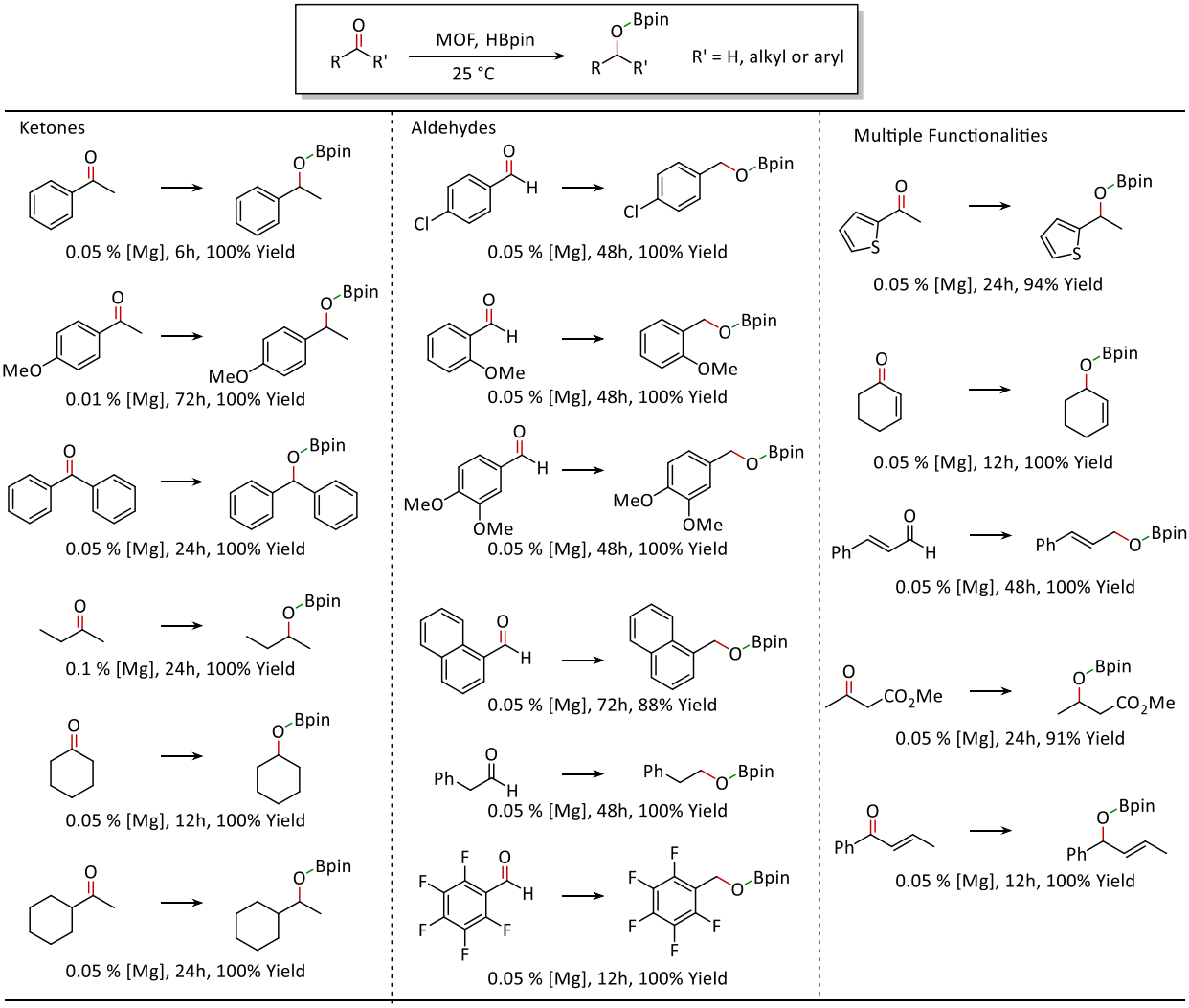

Reaction conditions: 1.0 mg of MgMe-Zr_6QPDCN, carbonyl substrate, hexanes, HBpin (1.1 equiv w.r.t. carbonyl substrate, 23 °C. Yield was determined by 1H NMR with mesitylene as the internal standard. Isolated yields are in parentheses. cTHF was used as the solvent.

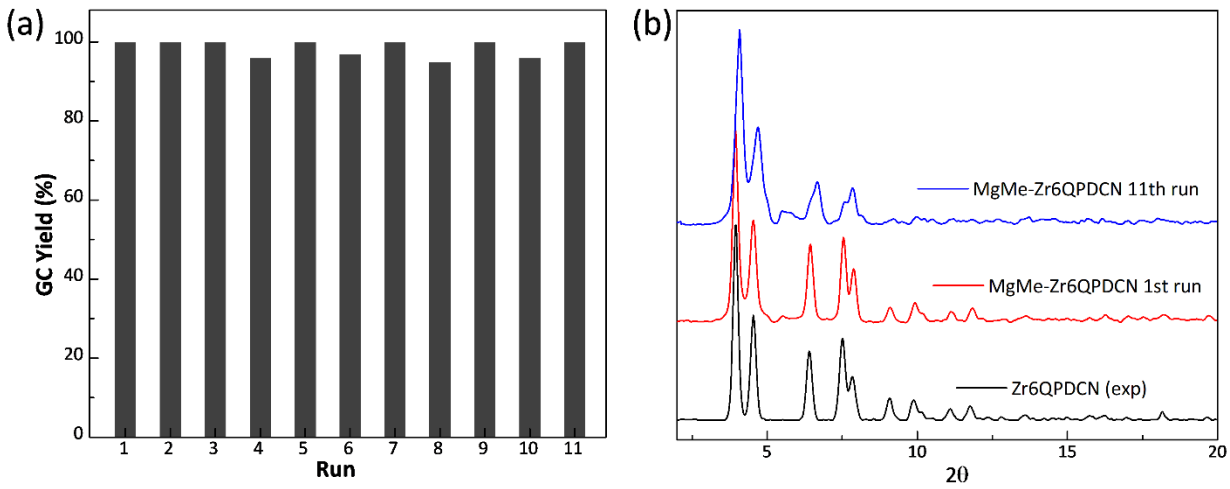

Figure 2-4. (a) Plot of yields (%) of borate ester at different runs in the reuse experiments of MgMe-QPDCN (0.2 mol % Mg) for hydroboration of acetophenone. (b) PXRD patterns of MgMe-Zr_6QPDCN recovered after 1st run (run) and 11th run (blue) of carbonyl hydroboration.

The heterogeneity of MgMe-Zr_6QPDCN was confirmed by the following experiments. ICP-MS analyses showed that the amounts of Mg and Zr leaching into the supernatant after the 1st run were only 1.6% and 0.02%, respectively, and after the 11th run were 1.3% and 0.02%, respectively. Moreover, no further hydroboration was observed after removal of MOF-Mg from the reaction mixture, which rules out the role of the leached Mg species in catalysing hydroboration reactions. An additional control experiment using the unmetalated Zr_6QPDCN did not afford the hydroboration product, indicating that the catalysis occurred at the supported Mg centers at the SBUs.

Two types of pathways were proposed for the Mg-catalysed hydroboration of carbonyls: a) σ-bond metathesis involving insertion of a C=O into a Mg–H bond or b) zwitterionic mechanism without involvement of Mg–H bond species. The mechanism of MgMe-Zr_6QPDCN catalysed hydroboration reactions was investigated by spectroscopic techniques, gas quantification, and kinetic studies. The treatment of MgMe-Zr_6QPDCN (1 mol % Mg) with acetophenone followed

by addition of HBpin (PhCOMe : HBpin = 1.2 : 1.0) in benzene immediately generated MeBpin, and hydroboration reaction occurred without a detectable induction period. After completion of the hydroboration reaction, Zr_3O-Mg(OCHMePh) was identified the intermediate by quenching with D_2O to detect CH(OD)MePh. In addition, Zr_3O-Mg(OMe), prepared by treatment of MgMe-Zr_6QPDCN with 10 equiv. (w.r.t. Mg) of MeOH was also active in catalysing hydroboration of acetophenone. We thus infer that the rapid reaction between Zr_3O-MgMe with one equiv of HBpin afforded the Zr_3O-MgH intermediate, which is likely the active catalyst for hydroboration reactions. The empirical rate law, determined by the method of initial rates (<10% conversion), showed that the hydroboration of acetophenone catalyzed by MgMe-Zr_6QPDCN has a first-order dependence on the Mg and acetophenone concentrations and a zeroth-order dependence on the HBpin concentration. Based on our experimental observations, the proposed pathways for hydroboration of carbonyls likely involved the insertion of C=O into the [Mg]–H bond in the turnover limiting step to give the Zr_3-O-Mg(OCHRR') intermediate. The reaction of Zr_3O-Mg(OCHRR') species with HBpin furnished the boronate ester product and regenerated Zr_3O-MgH in the cycle (**Scheme 2-2**).

Scheme 2-2 Proposed catalytic cycle for MgMe-Zr_6QPDCN catalyzed ketone hydroboration.

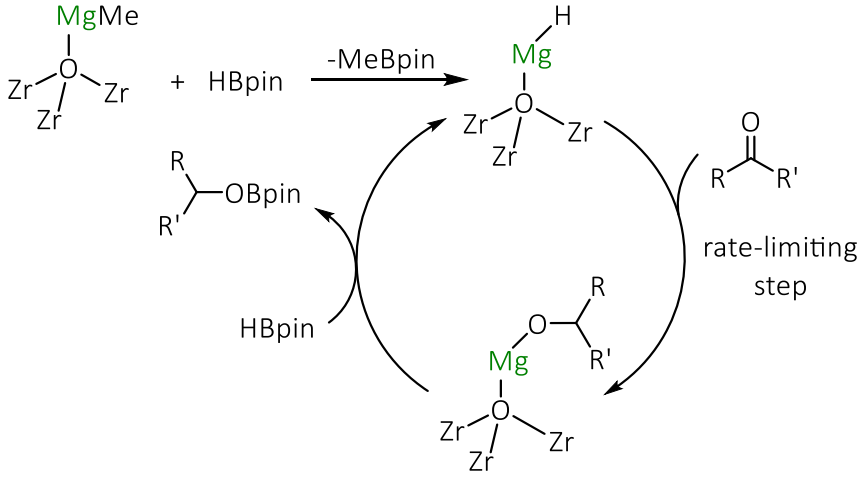

2.2.3 MgMe-Zr_6QPDCN catalyzed hydroboration of imines.

Similar to the hydroboration of carbonyls, MgMe-Zr_6QPDCN is also an active catalyst in the hydroboration of imines to give N-borylamines. At a 0.05 mol % Mg loading, MgMe-Zr_6QPDCN catalyzed hydroboration of N-benzylidene-aniline with HBpin in heptane at 70 °C for less than 12 h afforded N-benzyl-N-pinacolborylaniline in quantitative yield (**Table 2-2**). MOF-Mg recovered after this reaction remained crystalline as shown by PXRD, and the leaching of Mg and Zr into the supernatant was 2.2% and 0.07%, respectively. The hydroboration of substituted imines, however, required higher catalyst loading and longer reaction times, presumably due to the decreased rates of diffusion of the larger substrates and products through the MOF channels.

Table 2-2. MgMe-Zr_6QPDCN Catalyzed Hydroboration of Imines.

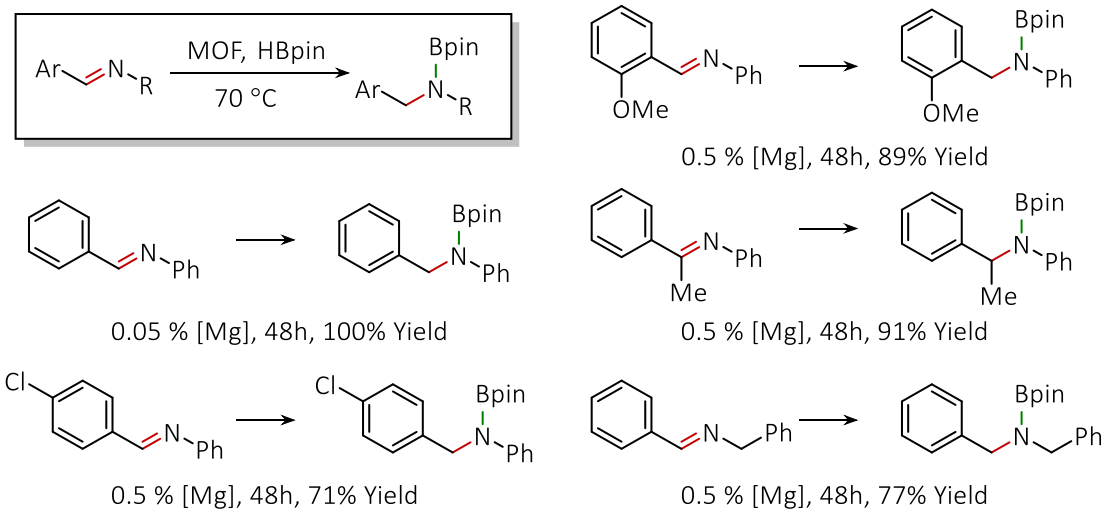

Reaction conditions: 1.0 mg of MgMe-Zr_6QPDCN (0.5 mol % Mg), imine, HBpin, heptane, 70 °C; Yields were determined by ^{1}H NMR with mesitylene as the internal standard. c0.05 mol % Mg was used.

2.2.4 MgMe-Zr_6QPDCN catalyzed intramolecular hydroamination reactions.

MgMe-Zr_6QPDCN is also an active catalyst for hydroamination/cyclization of aminoalkenes. Treatment of MgMe-Zr_6QPDCN with 10 equiv (w.r.t. Mg) of 2,2-bis(2-propenyl)-4-

pentenylamine in benzene at room temperature generated an equivalent amount of CH_4, presumably due to the formation of Mg-amidoalkene species. Upon heating the reaction mixture at 80 °C for 2 d, 4,4-diallyl-2-methylpyrrolidine was obtained in essentially quantitative yield (**Table 2-3**). ICP-MS analyses of the pyrrolidine product showed very low metal leaching (0.82% for Mg and 0.02% for Zr). At a 1.0 mol % Mg loading, MOF-Mg also afforded 4,4-diphenyl-2-methylpyrrolidine and 4-allyl-2-methyl-4-phenyl-pyrrolidine from 2,2-diphenyl-4-penten-1-amine and 2-allyl-2-phenylpent-4-enylamine, respectively, in excellent yields.

Table 2-3. MgMe-Zr_6QPDCN Catalysed Hydroamination of Aminoalkenes.

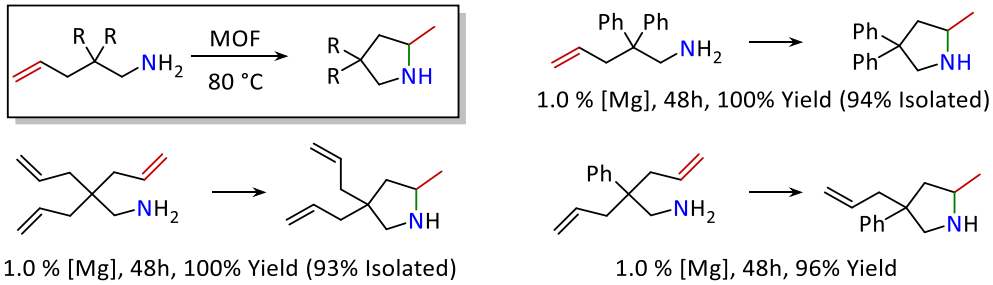

Reaction conditions: 1.0 mg of MgMe-Zr_6QPDCN (1.0 mol % Mg), aminoalkene, benzene, 80 °C; Yields were determined by ^{1}H NMR with mesitylene as the internal standard and isolated yields are in the parenthesis.

2.3 Conclusion

In this chapter, we developed the first MOF-supported single-site main group catalyst for organic transformations. Site isolation of the heteroleptic compounds at MOF-nodes is the key to affording highly active, robust, and reusable alkaline earth metal catalysts. Due to the diversity of metal cluster SBUs and the ease of functionalizing SBUs with metal ions, MOFs may offer a versatile platform for discovering new catalytic transformations and developing earth-abundant metal catalysts for sustainable synthesis of fine and commodity chemicals.

2.4 Experimental

2.4.1 Synthesis of H_2QPDCN ligand

Scheme 2- 3 Suzuki-Miyaura coupling reaction to synthesize Me_2QPDCN.

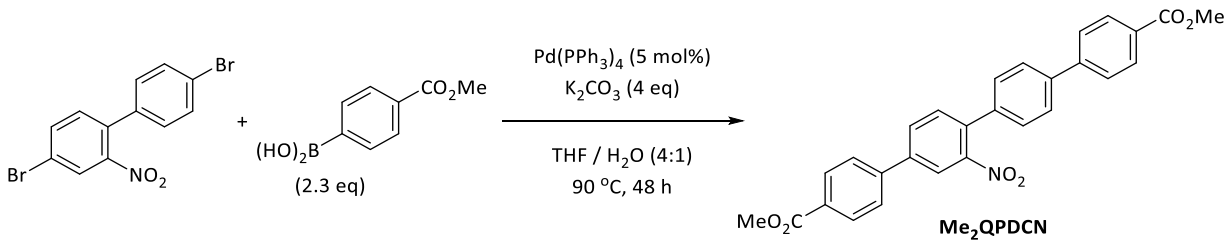

4,4'-dibromo-2-nitro-1,1'-biphenyl (3.00 g, 8.40 mmol) and methyl-4-carboxylphenyl boronic acid (3.48 g, 19.3 mmol) were charged into a 2-neck round bottom flask fitted with a reflux condenser, and then THF (210 mL) was added. The solution was degassed for 30 minutes, and tetrakis(triphenylphosphine)palladium (485 mg, 0.421 mmol) was added. The solution was further degassed for 30 minutes. K_2CO_3 (4.65 g, 33.6 mmol) dissolved in degassed DI water (50 mL) was then added under N_2. The reaction mixture was then heated under N_2 at 90 °C for 48 h. The solution was cooled to room temperature, and the water layer was removed. The volatiles were removed *in vacuo*, and the remaining solids were purified by column chromatography using chloroform as the eluent, affording dimethyl 2''-nitro-[1,1':4',1'':4'',1'''-tetraphenyl]-4,4'''-dicarboxylate (Me_2QPDCN) as a light yellow solid (1.40 g, 3.00 mmol, 36% yield). ^{1}H NMR (500 MHz, Chloroform-*d*): δ 8.18 (d, $^3J_{HH}$ = 8.3 Hz, 2 H), 8.16 – 8.11 (m, 3 H), 7.91 – 7.89 (m, 1 H), 7.77 – 7.68 (m, 6 H), 7.60 (d, $^3J_{HH}$ = 8.0 Hz, 1 H), 7.47 (d, $^3J_{HH}$ = 8.4 Hz, 2 H), 3.97 (s, 3 H), 3.96 (s, 3 H).

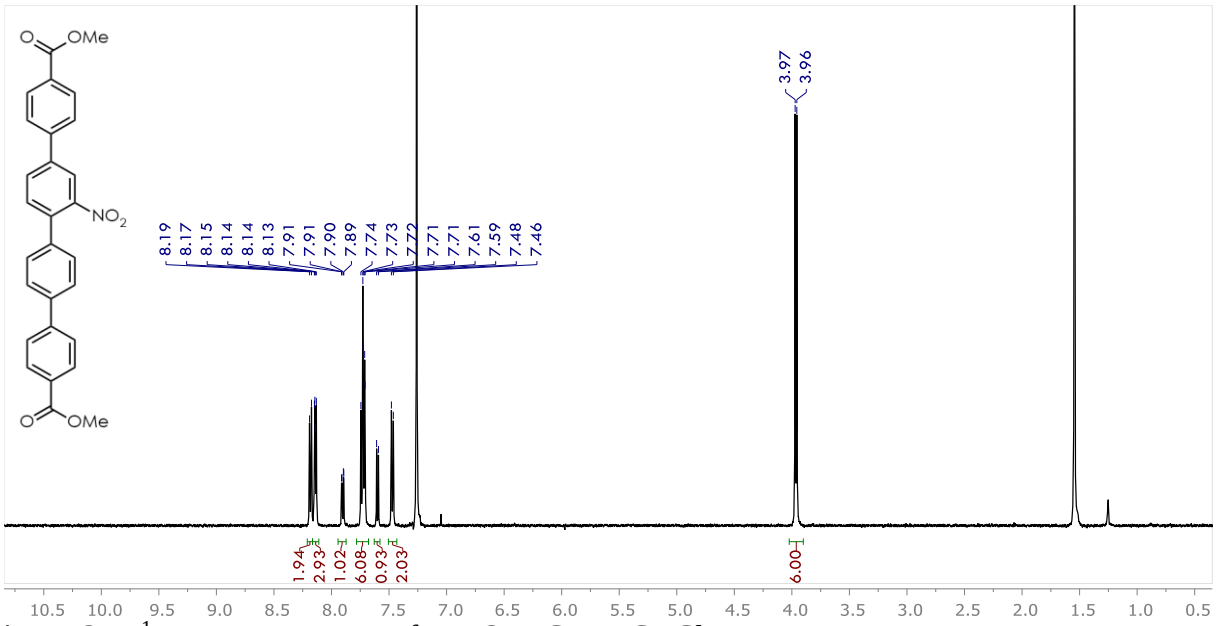

Figure 2-5. ^{1}H-NMR spectrum of Me_2QPDCN in $CDCl_3$.

Scheme 2-4 Hydrolysis of Me_2QPDCN to synthesize H_2QPDCN.

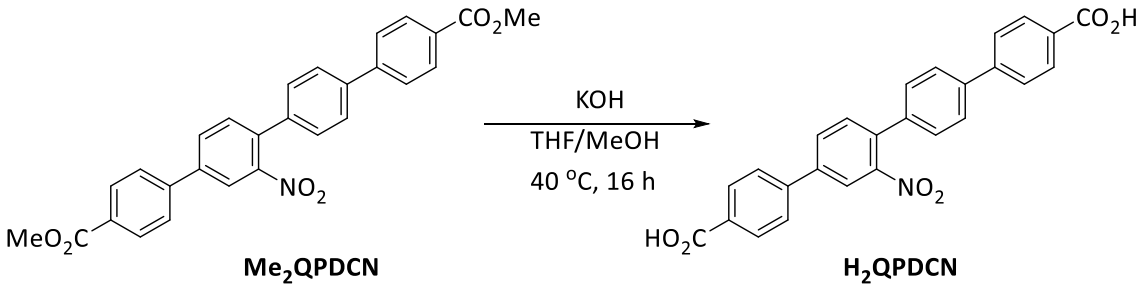

A suspension of dimethyl Me_2QPDCN (400 mg, 0.856 mmol) in THF (65 mL) was heated to 40 ˚C. A solution of KOH (6.17 g, 110 mmol) dissolved in MeOH (20 mL) was then added, and the reaction mixture was stirred at 40 ˚C for 16 h. The suspension was cooled to room temperature, and the resulting precipitate was collected by centrifugation. The solid was washed with dry THF (20 mL) and collected once more by centrifugation. The solid was suspended in THF (20 mL) and trifluoroacetic acid (3 mL) was slowly added and stirred for 1.5 h at room temperature. H_2O (15 mL) was then added, and the yellow solid was isolated by centrifugation. The collected yellow solid was first washed with THF (10 mL), then Et_2O (10 mL), then dried *in*

vacuo to obtain 2"-nitro-[1,1':4',1":4",1"'-quaterphenyl]-4,4"'-dicarboxylic acid (H_2QPDCN) (328 mg, 0.746 mmol, 87% yield) as a light yellow powder. ^{1}H NMR (500 MHz, DMSO-d_6) δ 13.08 (s, 2 H), 8.39 (d, $^4J_{HH}$ = 1.9 Hz, 1 H), 8.17 (dd, $^3J_{HH}$ = 8.0 Hz, $^4J_{HH}$ = 2.0 Hz, 1 H), 8.07 (m, 4 H), 7.98 (d , $^3J_{HH}$ = 8.3 Hz, 2 H), 7.88 (m, 4 H), 7.75 (d, $^3J_{HH}$ = 8.0 Hz, 1 H), 7.53 (d, $^3J_{HH}$ = 8.1 Hz, 2 H). ^{13}C NMR (126 MHz, DMSO-d_6) δ 167.13, 166.99, 149.49, 143.40, 141.35, 139.55, 138.96, 136.28, 133.85, 132.46, 130.92, 130.73, 130.15, 130.06, 129.95, 128.54, 127.41, 127.17, 126.88, 122.39, 39.52. MS (ESI$^-$) exact mass calcd for $C_{26}H_{17}NO_6$: m/z 438.0978 ([(M - H)$^-$]), Found: 438.0985.

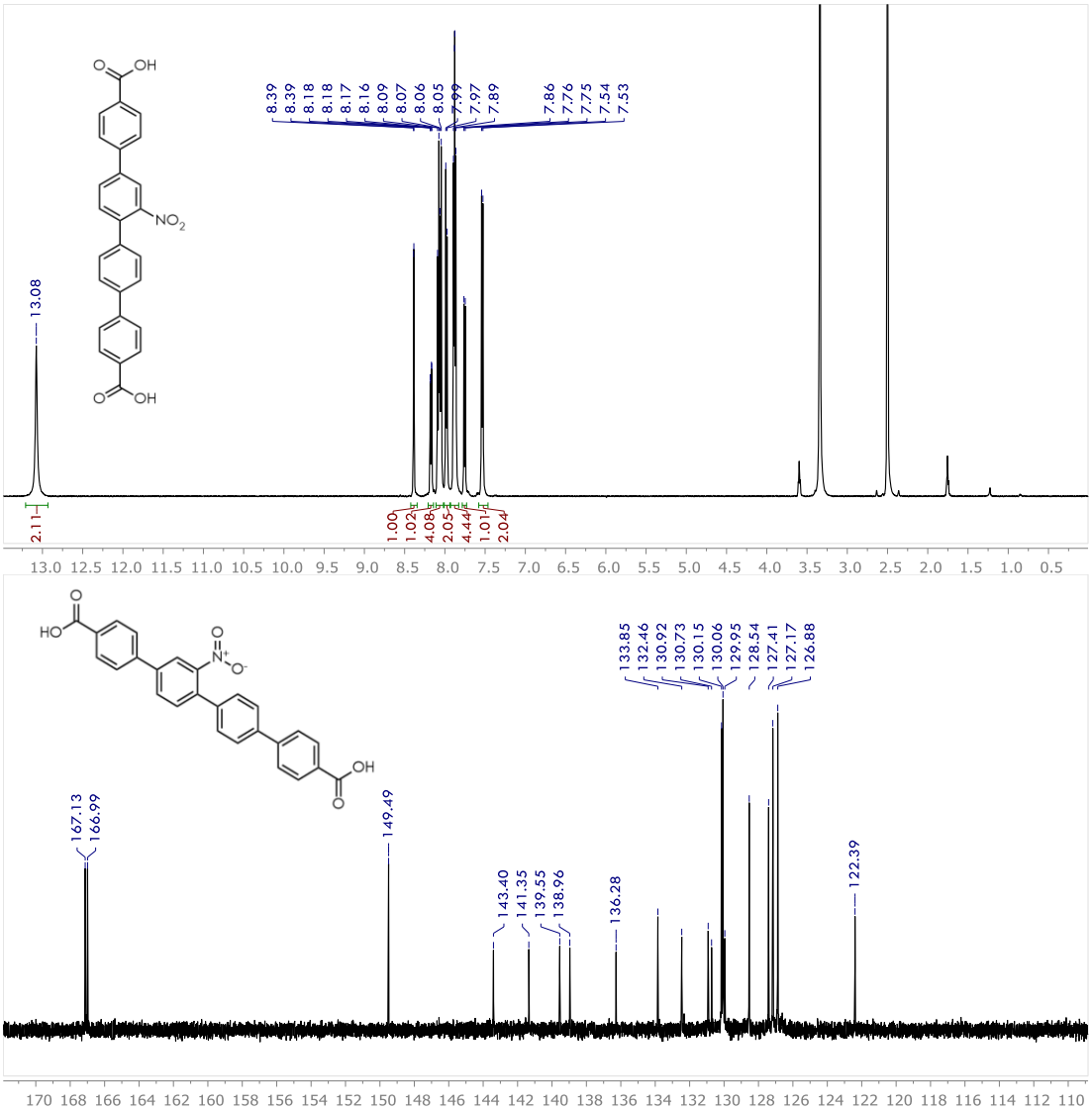

Figure 2-6. ^{1}H NMR (top) and ^{13}C NMR spectra (bottom) of H_2QPDCN in DMSO-d_6.

2.4.2 Synthesis of Zr_6QPDCN MOF

Zr_6QPDCN was synthesized via a solvothermal reaction between $ZrCl_4$ and H_2QPDCN in the presence of DMF and trifluoroacetic acid in 95% yield. $ZrCl_4$ (10 mg) and H_2QPDCN (20 mg) were dissolved in 10 mL of DMF in a 5-dram vial, and 0.1 mL of trifluoroacetic acid was added. The solution was then heated at 100 ºC for 5 days to afford small bright yellow crystals as the MOF product (yield: 21 mg, 84%).

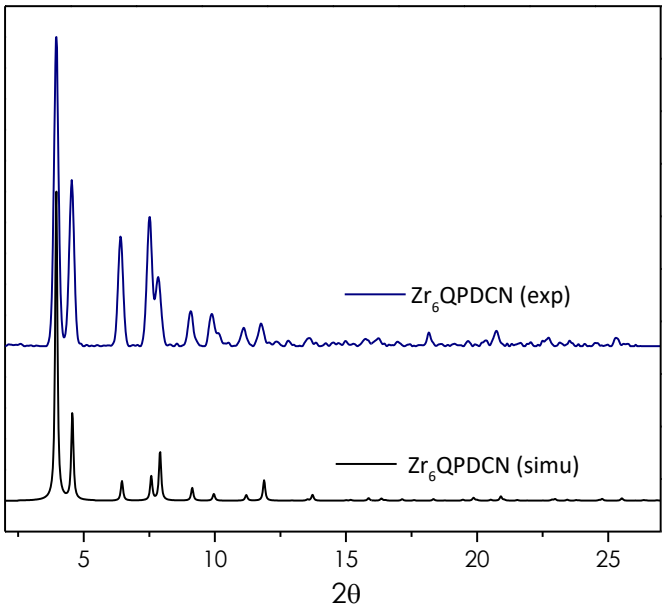

Figure 2-7. PXRD patterns of Zr_6QPDCN simulated from the CIF file (black) and the experimental PXRD patterns as synthesized Zr_6QPDCN (navy).

2.4.3 Quantification of methane evolved during MgMe-Zr_6QPDCN formation.

Quantification of CH_4 production in the reaction of Zr_6QPDCN with Me_2Mg. Preparation of MgMe-Zr_6QPDCN was carried out in THF in a J. Young style NMR tube with a resealable Teflon valve with 0.9 mg of Zr_6QPDCN (1.09 μmol Mg) and 0.12 mg of $MgMe_2$. The headspace gas (total volume 2.8 mL) was analyzed by gas chromatography after 3 h to give a methane content of 0.856% (v/v). The total amount of methane in the headspace was calculated to be:

$$2.8\ \text{mL} \times \frac{0.856}{100} \times 101\ \text{kPa} \div 8.314\ \text{J} \bullet\ \text{Mol}^{-1} \bullet \text{K}^{-1} \div 295\ \text{K} = 0.99\ \mu\text{mol}$$

The amount of CH_4 expected from the reaction of Zr_6QPDCN and HBpin is 1.09 μmol, which is close to the experimental value.

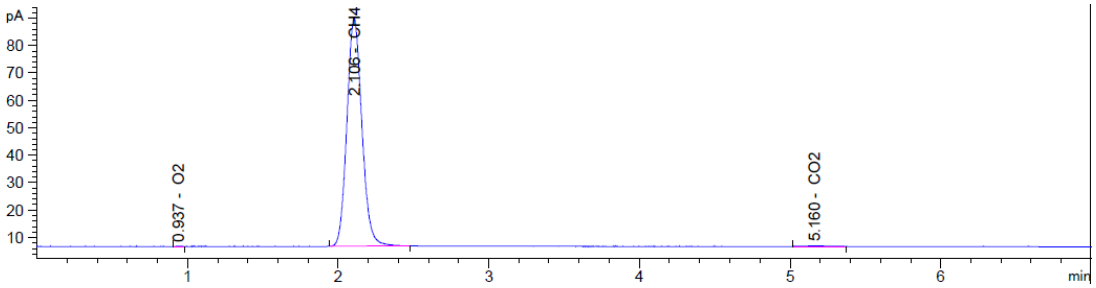

Figure 2-8. GC (FID) trace of CH_4 from the headspace gas.

2.4.4 Quantification of the H_2 production during MgBpin-Zr_6QPDCN formation.

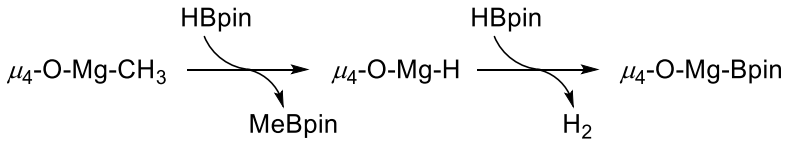

The formation of H_2 was detected upon treatment of HBpin with MgMe-Zr_6QPDCN, or in the catalytic hydroboration reaction if the carbonyl substrate is the limiting reagent. However, no H_2 was formed during the catalytic hydroboration reaction if HBpin is the limiting reagent. The quantification of the H_2 production in the reaction of MgMe-Zr_6QPDCN with HBpin is as follows: A J. Young style NMR tube with a re-sealable Teflon valve was charged with 5.0 mg of MgMe-Zr_6QPDCN (5.7 μmol Mg) in 0.6 mL hexane and an excess of HBpin (9 μL, 57.8 μmol) at room temperature. The headspace gas (total volume 2.8 mL) was analyzed by gas chromatography after 0.5 h to give hydrogen content of 4.6% (v/v). The total amount of H_2 in the headspace was then calculated to be

$$2.8\ \text{mL} \times \frac{4.60}{100} \times 101\ \text{kPa} \div 8.314\ \text{J} \bullet\ \text{Mol}^{-1} \bullet \text{K}^{-1} \div 295\ \text{K} = 5.3\ \mu\text{mol}$$

The amount of H_2 expected from the reaction of Zr_6QPDCN and HBpin is 5.7 μmol, which is close to the experimental value. The hydrogen content in headspace after 4 h was remained same and the formation of B_2pin_2 was not detected as analyzed by GC. A control experiment was performed by addition of HBpin (9 μL, 57.8 μmol) to a J. Young NMR tube containing 0.6 mL of hexane, which showed a negligible amount of H_2 in the headspace after 4 h a room temperature. These experiments suggested that the formation of H_2 was due to the formation of Zr_3O-Mg(Bpin) species via reaction of Zr_3-O-Mg-H with excess HBpin, not due to the decomposition of HBpin or Mg-mediated dehydrogenation reaction of HBpin to form B_2Pin_2.

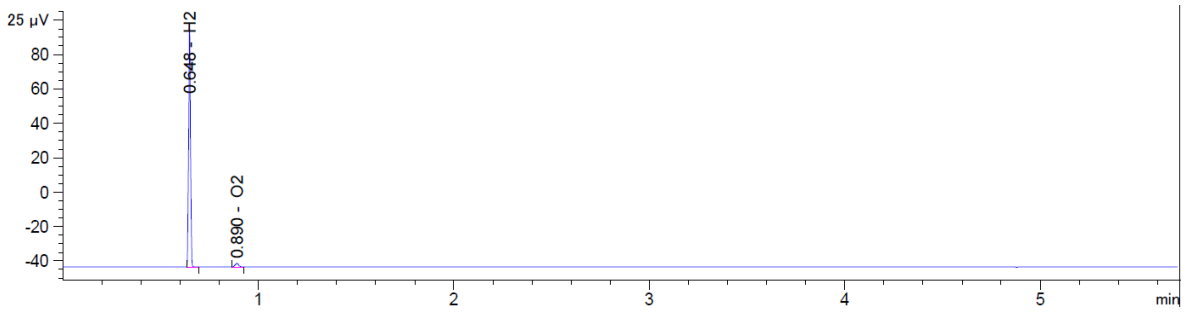

Figure 2-9. GC (TCD) trace of H_2 from the headspace gas.

2.4.5 Typical procedure for MgMe-Zr_6QPDCN catalyzed hydroboration

Scheme 2-5 MgMe-Zr_6QPDCN catalyzed hydroboration of methoxyacetophenone.

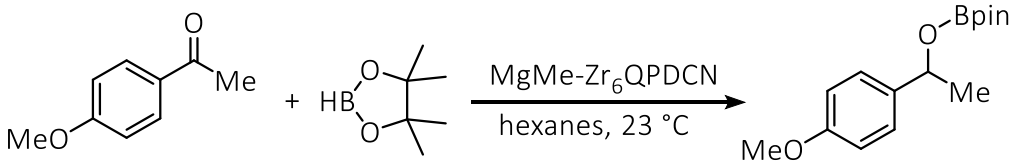

A typical procedure for MgMe-Zr_6QPDCN catalyzed hydroboration of ketones. In a glovebox, MgMe-Zr_6QPDCN (1.0 mg, 0.05 mol % Mg) in 1.0 mL hexanes was charged into a small vial. Then, 3.0 mL solution of 4-methoxyacetophenone (0.174 g, 1.16 mmol) and pinacolborane (0.164 g, 1.28 mmol) was added. The resultant mixture was stirred slowly at room

temperature in the glovebox for 2 d before the solid was centrifuged out of suspension and extracted with hexanes 2-3 times. The combined organic extracts were concentrated *in vacuo* to yield the pure borate ester product (0.317 g, 1.14 mmol, 98.0%).

2.5 References

1. Schlenk, W.; Schlenk, W., Über die Konstitution der Grignardschen Magnesiumverbindungen. *Berichte der deutschen chemischen Gesellschaft (A and B Series)* **1929,** 920-924.

2. Chisholm, M. H.; Huffman, J. C.; Phomphrai, K., Monomeric metal alkoxides and trialkyl siloxides: (BDI)Mg(OtBu)(THF) and (BDI)Zn(OSiPh3)(THF). Comments on single site catalysts for ring-opening polymerization of lactides. *J. Chem. Soc., Dalton Trans.* **2001,** 222-224.

3. Avent, A. G.; Crimmin, M. R.; Hill, M. S.; Hitchcock, P. B., Solution- and solid-state characterisation of a configurationally-stable [small beta]-diketiminato-supported calcium primary amide. *Dalton Trans.* **2004,** 3166-3168.

4. Crimmin, M. R.; Casely, I. J.; Hill, M. S., Calcium-Mediated Intramolecular Hydroamination Catalysis. *J. Am. Chem. Soc.* **2005,** 2042-2043.

5. Datta, S.; Roesky, P. W.; Blechert, S., Aminotroponate and Aminotroponiminate Calcium Amides as Catalysts for the Hydroamination/Cyclization Catalysis. *Organometallics* **2007,** 4392-4394.

6. Wales, S. M.; Walker, M. M.; Johnson, J. S., Asymmetric Synthesis of Indole Homo-Michael Adducts via Dynamic Kinetic Friedel–Crafts Alkylation with Cyclopropanes. *Org. Lett.* **2013,** 2558-2561.

7. Liu, B.; Roisnel, T.; Guégan, J.-P.; Carpentier, J.-F.; Sarazin, Y., Heteroleptic Silylamido Phenolate Complexes of Calcium and the Larger Alkaline Earth Metals: β-Agostic Ae···Si□H Stabilization and Activity in the Ring-Opening Polymerization of L-Lactide. *Chem. Eur. J.* **2012,** 6289-6301.

8. Mukherjee, A.; Nembenna, S.; Sen, T. K.; Sarish, S. P.; Ghorai, P. K.; Ott, H.; Stalke, D.; Mandal, S. K.; Roesky, H. W., Assembling Zirconium and Calcium Moieties through an Oxygen Center for an Intramolecular Hydroamination Reaction: A Single System for Double Activation. *Angew. Chem. Int. Ed.* **2011,** 3968-3972.

9. Buch, F.; Brettar, J.; Harder, S., Hydrosilylation of Alkenes with Early Main-Group Metal Catalysts. *Angew. Chem. Int. Ed.* **2006,** 2741-2745.

10. Arrowsmith, M.; Hadlington, T. J.; Hill, M. S.; Kociok-Kohn, G., Magnesium-catalysed hydroboration of aldehydes and ketones. *Chem. Commun.* **2012,** 4567-4569.

11. Crimmin, M. R.; Barrett, A. G. M.; Hill, M. S.; Hitchcock, P. B.; Procopiou, P. A., Calcium-Catalyzed Intermolecular Hydrophosphination. *Organometallics* **2007,** 2953-2956.

12. Gauvin, R. M.; Buch, F.; Delevoye, L.; Harder, S., Well-Defined Silica-Supported Calcium Reagents: Control of Schlenk Equilibrium by Grafting. *Chem. Eur. J.* **2009,** 4382-4393.

13. Zhang, T.; Manna, K.; Lin, W., Metal–Organic Frameworks Stabilize Solution-Inaccessible Cobalt Catalysts for Highly Efficient Broad-Scope Organic Transformations. *J. Am. Chem. Soc.* **2016,** 3241-3249.

Chapter 3. Single-Site Cobalt Catalyst at Zr_6 MOF Node for C-H Activation and Hydrogenation Reactions

3.1 Introduction

In the previous chapter, we show that the straightforward metalation of MOF SBUs with magnesium afforded highly active catalyst for ketone hydroboration and alkene hydroamination reactions. This chapter discusses the metalation with cobalt to afford highly active and reusable single-site solid catalysts for more challenging organic reactions, including C-H bond borylation, silylation, and amination with benzylic selectivity, as well as the hydrogenation and hydroboration of alkenes and ketones. Our structural, spectroscopic, and kinetic studies suggest that chemoselective organic transformations occur at the site-isolated, electron-deficient, and coordinatively unsaturated metal centers at the SBUs via σ-bond metathesis pathways. The higher reaction selectivity results from the steric control of substrate access around the catalytic site. MOFs thus provide a novel platform for developing highly active and affordable base-metal catalysts for the sustainable synthesis of fine chemicals.

MOFs provide a highly tunable platform to engineer single-site solid catalysts for many organic transformations that cannot be performed by traditional porous inorganic materials. [1-3] This was achieved by utilizing premetalated organic struts as the functionalized bridging linkers, or via postsynthetic metalation of the organic ligands. But the lengthy synthesis of functionalized linkers prohibits the industrial application of these MOFs. The diversity of metal cluster SBUs offers an alternative strategy for the straightforward installation of active catalysts (**Figure 3-1**). MOF SBUs have been only been used as acid catalysts,[4-5] leaving their application in more challenging reactions or as potential supports for catalysis virtually unexplored.[6-7]

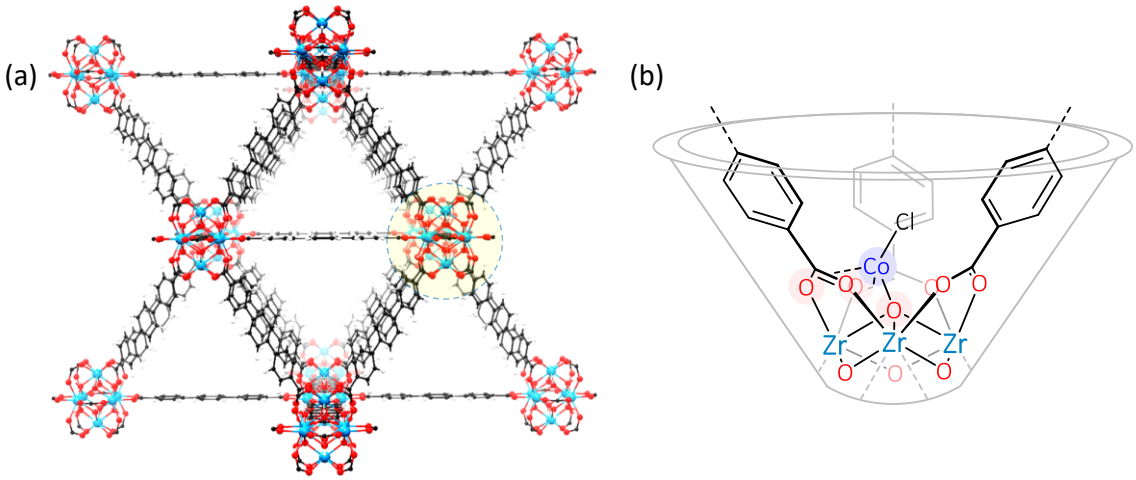

Figure 3-1. (a) Crystal structure of Zr_6TPDC. **(b)** Co coordination environment in the CoCl-Zr_6TPDC catalyst, featuring funnel-like local steric environment.

3.2 Results and Discussion

3.2.1 Synthesis and characterization of CoCl-Zr_6TPDC

CoCl-Zr_6TPDC was synthesized by deprotonation of $Zr_3(\mu_3$-OH) sites in Zr_6TPDC SBUs with *n*BuLi, followed by metalation with $CoCl_2$ solution to afforded the materials as a deep blue solid (**Scheme 3-1**).

Scheme 3-1. Deprotonation and metalation of Zr_6 SBU to form CoCl-Zr_6TPDC.

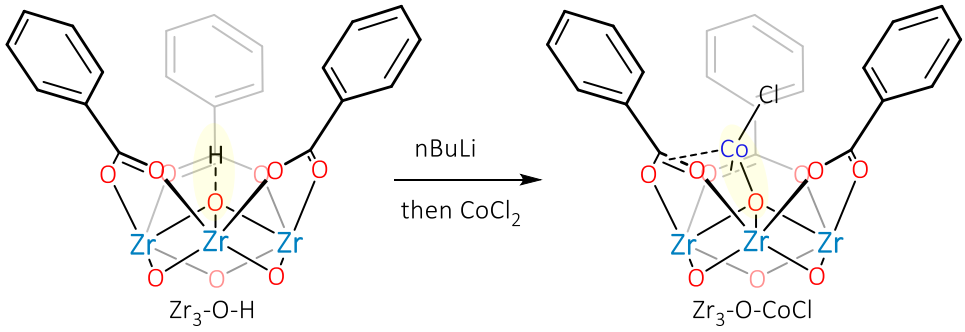

Crystallinity of Zr_6TPDC was maintained upon metalation, as suggested by the similarity of the PXRD patterns of Zr_6TPDC and CoCl-Zr_6TPDC. (**Figure 3-2**). CoCl-Zr_6TPDC has 45% solvent weight based on TGA analysis, and 100% Co-loading with respect to μ_3-OH centers based

on ICP-MS analysis. ICP-MS analysis of the digested CoCl-Zr_6TPDC revealed four Co centers per Zr_6 node, indicating 100% metalation of all the $Zr_3(\mu_3$-OH) sites. The infrared spectrum (IR) of CoCl-Zr_6TPDC showed the disappearance of $\nu_{\mu 3O\text{-}H}$ band (~3640 cm^{-1}, KBr), consistent with the complete metalation of $Zr_3(\mu_3$-OH) sites. In addition, TEM-EDX analysis indicated that cobalt sites are uniformly distributed throughout the particles (**Figure 3-3**).

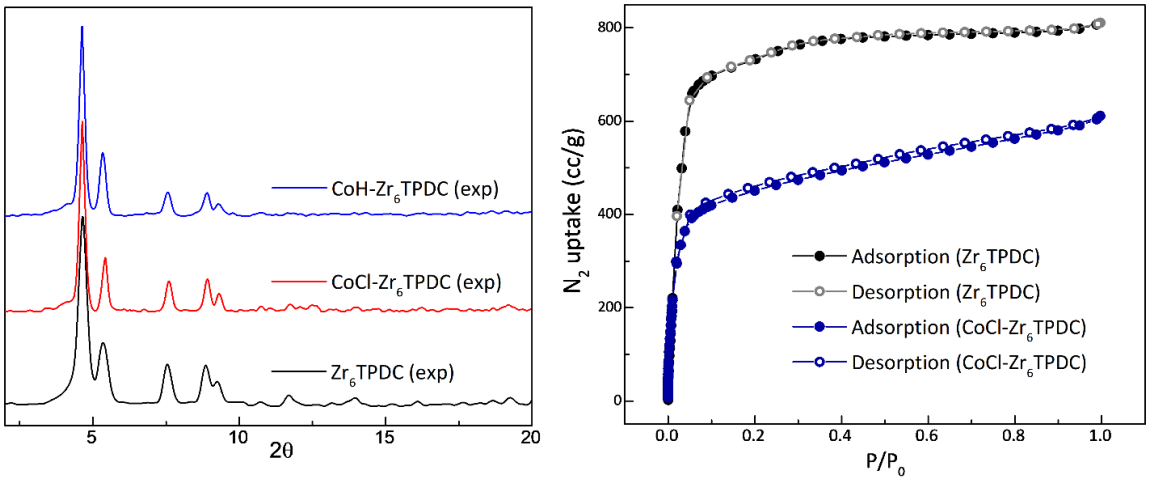

Figure 3-2. (a) PXRD patterns of CoCl-Zr_6TPDC (red) and CoH-Zr_6TPDC (blue). (b) N_2 sorption isotherm of CoCl-Zr_6TPDC (blue) compared to that of pristine Zr_6TPDC (black).

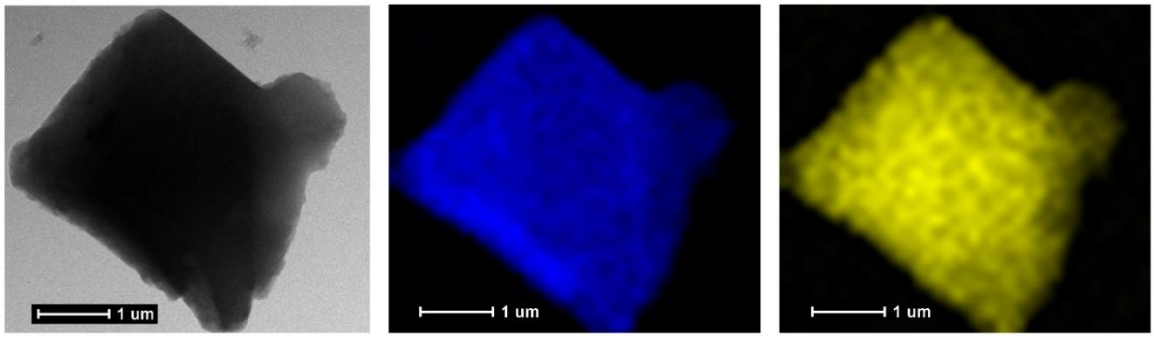

Figure 3-3. TEM-EDX analysis of CoCl-Zr_6TPDC, indicating the uniform distribution of Co (blue color) and Zr (yellow color) throughout the whole particle.

A single-crystal X-ray diffraction study revealed that CoCl-Zr_6TPDC crystallizes in the $Fm\bar{3}m$ space group, with the $Zr_6(\mu_3\text{-}O)_4(\mu_3\text{-}OH)_4$ SBUs connected by the TPDC bridging linkers

to afford the 12-connected fcu topology. The void space was calculated to be 79.6% by PLATON. However, due to the crystallographic disorder of the CoCl moiety, the Co coordination environments in CoCl-Zr_6TPDC could not be established by X-ray crystallography.

Instead, we used X-ray absorption spectroscopy (XAS) to investigate the electronic property and coordination environments of Co. The oxidation states of CoCl-Zr_6TPDC was determined to be divalent by comparing the energies of the pre-edge peaks to the $CoCl_2$ standard (**Figure 3-4**).

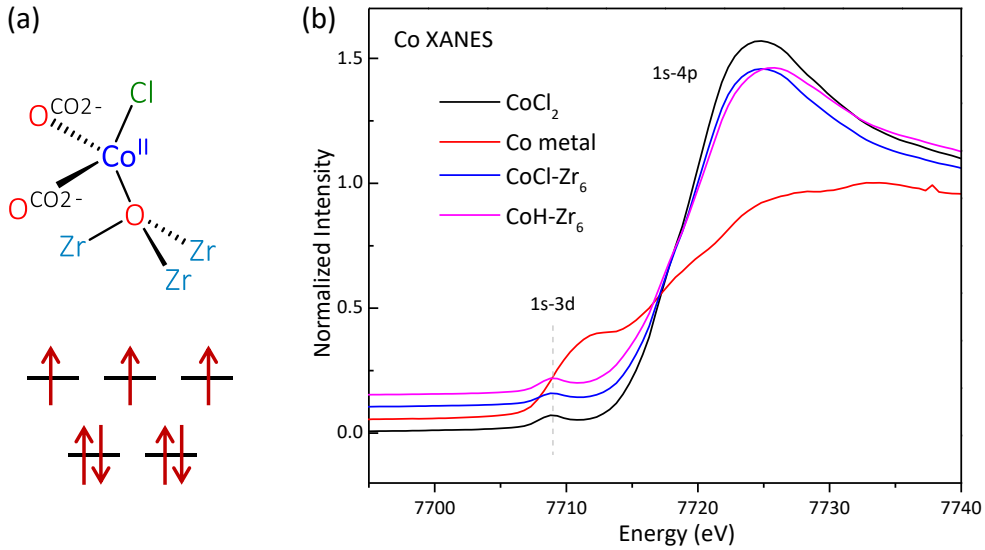

Figure 3-4. (a) Chemical structure and electron configuration of Co^{II} centers in CoCl-Zr_6TPDC. (b) XANES spectra of CoCl-Zr_6TPDC (blue), CoH-Zr_6TPDC compared Co metal (red) and $CoCl_2$ (black) controls.

Since the Co center was not observed with SXRD, we rationalize the crystallographic disorder by proposing a tilting of Co toward the carboxylates. The tilting was validated by DFT calculations, which indicates the Co was anchored to the μ_3-O^- site while weakly coordinating to the π-electron of carboxylate groups. The optimized structure indicates Co-carboxylate oxygen distances of 2.05 Å and Co-carboxylate carbon bond distances of 2.28 Å (**Figure 3-5**).

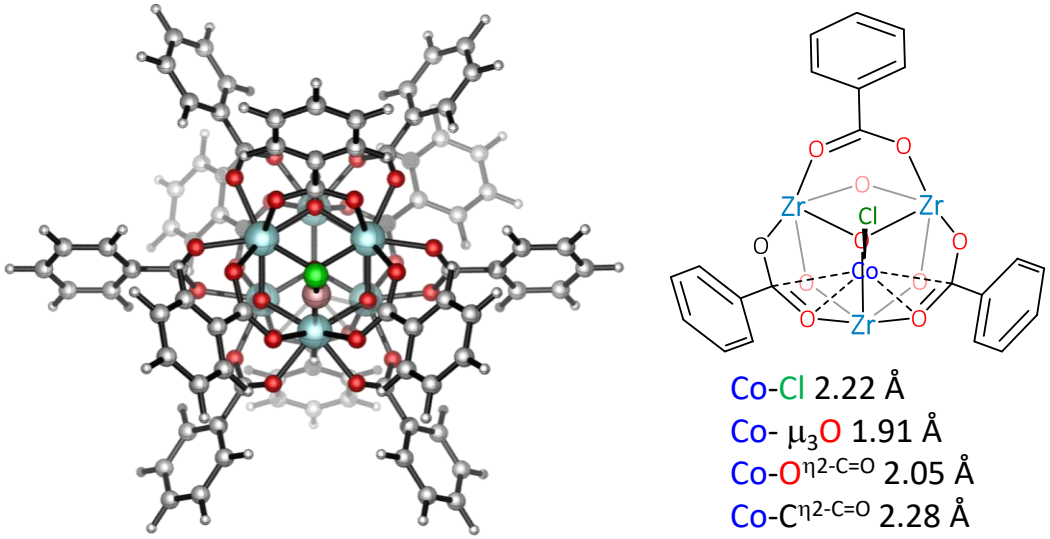

Figure 3-5. DFT calculated structure of CoCl moiety on Zr_6TPDC SBU and the measured bonding distances.

Fitting of the Co Kα EXAFS data of CoCl-Zr_6TPDC validated the DFT optimized structure, indicating the Co center was coordinated to both the μ_3-O^- and the π-electron of carboxylate groups as shown in the model complexes (**Figure 3-6**). The bonding distances are in good agreement with DFT calculated result.

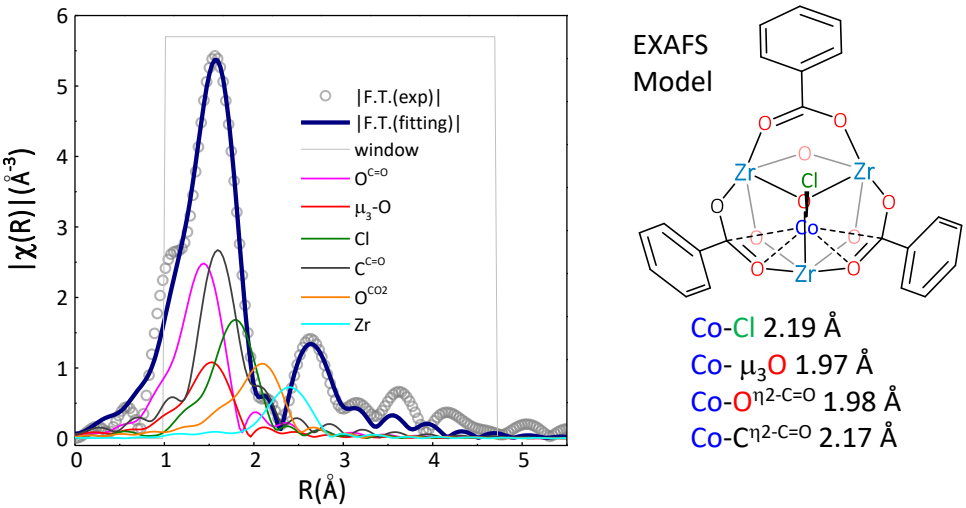

Figure 3-6. EXAFS fitting of Co K-edge X-ray absorption data, and the resulting bond distance parameters.

3.2.2 Synthesis and characterization of CoH-Zr_6TPDC

The CoCl-Zr_6TPDC was activated with $NaBEt_3H$ to cleave the strong Co-Cl bond and generate Co-H active species for catalysis. The resulting black solid was washed with THF and benzene before drying to afford a powder for further characterization. To validate the activation of Co-Cl bond in CoH-Zr_6TPDC, the Co K-edge EXAFS spectrum was plotted against that of CoCl-Zr_6TPDC, which indicates a reduction of peak intensity and lower shift of peak position, matching well with the absence of Co-Cl scattering pathway. The EXAFS data of CoH-Zr_6TPDC was well fitted with a similar CoH coordination environment to CoCl-Zr_6TPDC, where the Co is coordinated to three SBU oxygen atoms and one hydride (**Figure 3-7**). XANES analysis indicates the Co maintained divalency after $NaBEt_3H$ treatment by comparing the pre-edge feature with $CoCl_2$ standard.

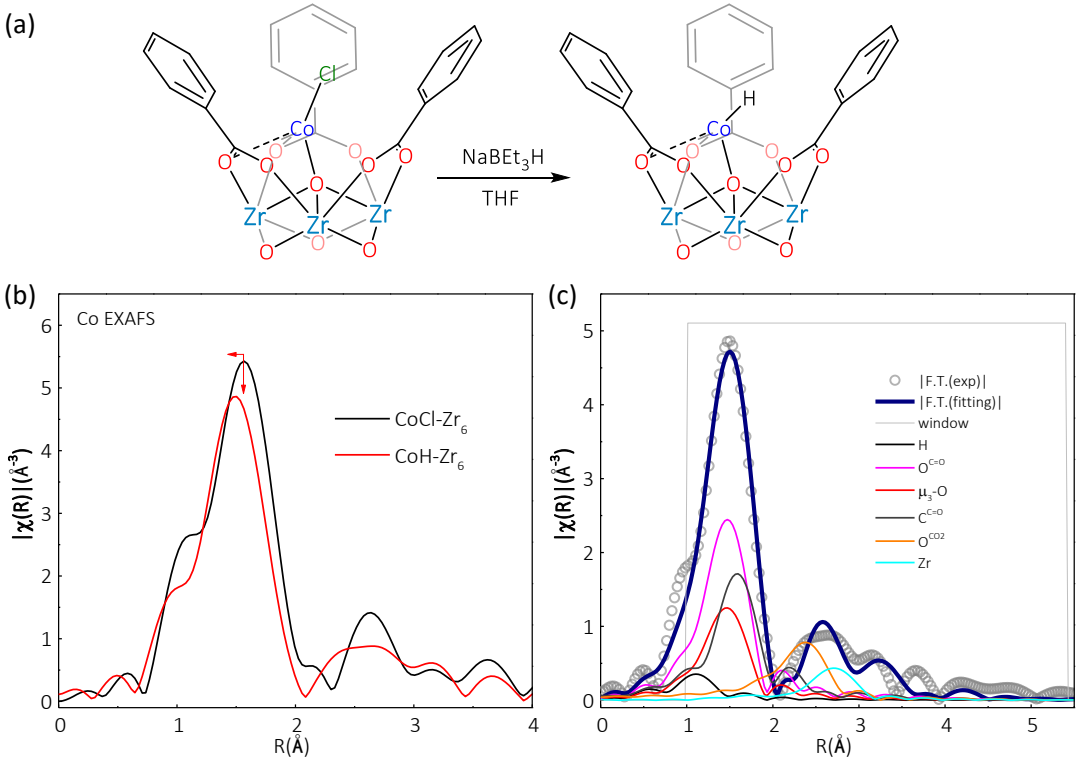

Figure 3-7. **(a)** The activation of CoCl-Zr_6TPDC to form CoH-Zr_6TPDC. **(b)** Comparison of the EXAFS feature of CoCl-Zr_6TPDC with that of CoH-Zr_6TPDC. (c) EXAFS fitting of CoH-Zr_6TPDC K-edge X-ray absorption data with proposed structure model.

3.2.3 CoH-Zr_6TPDC-catalyzed undirected benzylic C−H borylation.

CoH-Zr_6TPDC is a highly active catalyst for undirected borylation of benzylic C−H bonds using B_2pin_2 as the borylation agents. Borylation of alkyl C−H bonds furnishes the formation alkyl boronates, which are versatile reagents in organic synthesis. Although selective borylation of aromatic C−H bonds has been achieved with several homogeneous catalysts, very few examples have reported for benzylic selective borylation. Moreover, most catalysts are based on precious metals (*e.g.* Rh and Ir), while the earth-abundant metal-catalyzed chemoselective C−H borylation is rare. Recently, α-diimine cobalt catalysts were reported for benzylic C-H borylation at high catalyst loadings (5-30 mol%), long reaction time, and with the formation of a mixture of monoborylation and diborylation products. The CoH-Zr_6TPDC was shown to catalyze borylation reactions at much lower catalyst loadings (0.2 mol%) and with exclusive mono-borylation selectivity. Under optimized reaction conditions, CoH-Zr_6TPDC catalyzed the C-H borylation of *m*-xylene to afford benzylic boronate esters in excellent yields at 0.2 mol% loading. The borylation reactions of a broad scope of methylarenes including mesitylene, 3-chlorotolumene and p-xylene were borylated in good yields with excellent benzylic selectivity over aromatic C-H bonds (**Table 3-1**).

The CoH-Zr_6TPDC recovered from the borylation reaction of *m*-xylene maintained the same crystallinity as the freshly prepared CoH-Zr_6TPDC by comparing their PXRD patterns **(Figure 3-8**), indicating that the MOF frameworks are stable under the catalytic conditions. We found that the CoH-Zr_6TPDC catalyst could be used at least five times in the borylation of *p*-xylene at a 1.0 mol% Co loading. This is a significant advantage of using heterogeneous catalysts instead of homogeneous catalysts which cannot be recycled and reused. Furthermore, the boronate ester

was easily isolated in high purity simply by removing the solid catalyst and evaporating the organic volatiles.

Table 3-1. Selected substrate scope for the CoH-Zr_6TPDC catalyzed olefin hydrogenation.

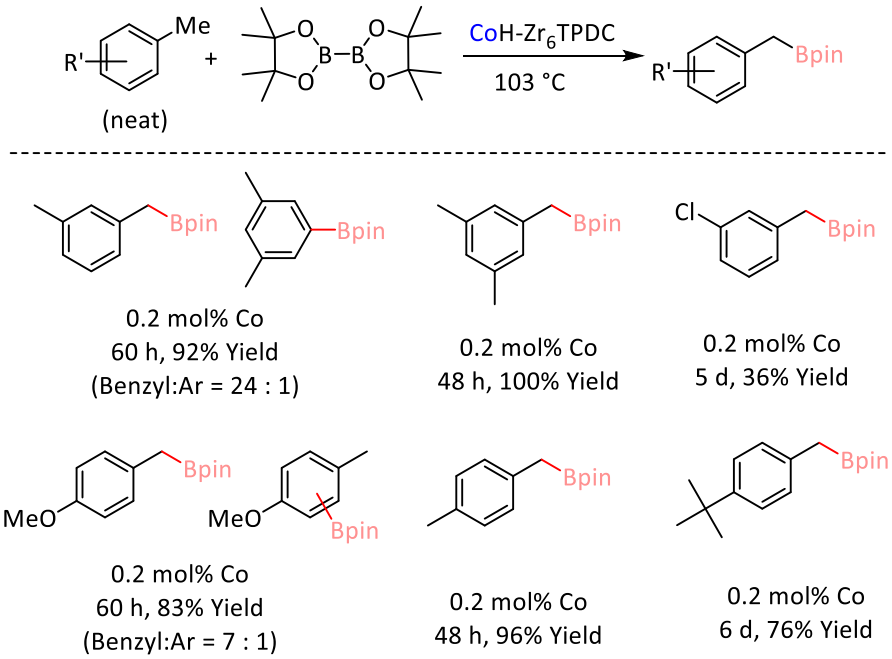

For mesitylene, *p*-xylene, and 4-tert-butyltoluene, benzylic boronates were obtained in good yields and exclusive selectivity, presumably because the steric hindrance at the aryl C−H bonds was much greater than benzylic positions. For the borylation of mesitylene, a high TON of 2300 was obtained for the borylation product. However, reactions with electro-deficient methylarenes (*e.g. m*-chlorobenzene) were rather slow.

The heterogeneity of CoH-Zr_6TPDC was confirmed by several experiments. The leaching of metal into the supernatant during the course of the borylation reaction was very low as shown by ICP-MS analysis, with 0.14% and 0.056% for Co and Zr, respectively. Moreover, no further borylation of p-xylene was detected after the removal of CoH-Zr_6TPDC from the reaction mixture.

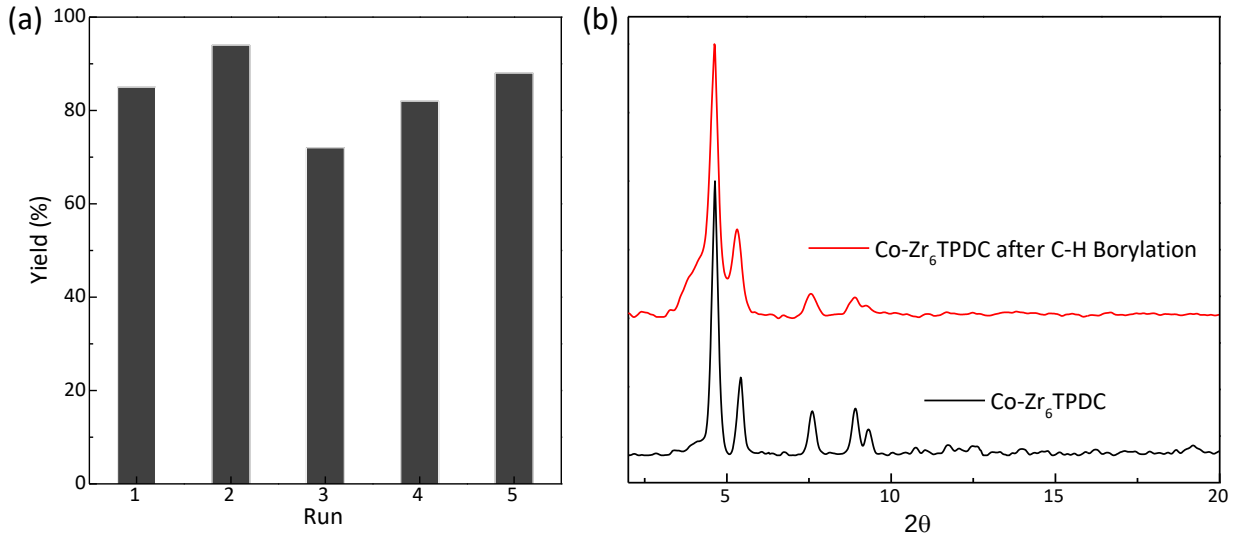

Figure 3-8. **(a)** Recycle experiment of CoH-Zr_6TPDC catalyzed C-H borylation of p-xylene. **(b)** PXRD patterns of CoH-Zr_6TPDC after catalytic reactions (red) compared to that of freshly prepared CoH-Zr_6TPDC (black).

Having shown the highly selective benzylic C−H borylation of alkylarenes with the CoH-Zr_6TPDC catalyst, we sought to investigate the nature of the catalytic species and to reveal their mechanism using structural, kinetic, and spectroscopic techniques. Treatment of CoCl-Zr_6TPDC with $NaEt_3BH$ in THF affords the Zr_3O-Co-H. The reaction of CoH-Zr_6TPDC with HBpin readily generates CoH-Zr_6TPDC-Bpin and one equivalent of H_2 (**Figure 3-9**). The amount of H_2 was detected by GC analysis of the head space of the reaction tube.

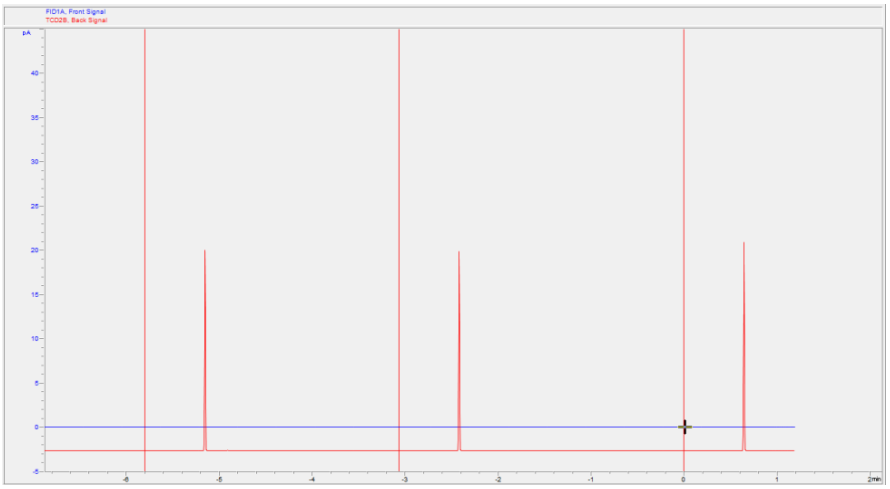

Figure 3-9. GC trace of the headspace gas with constant amount of H_2 in three trials.

The mechanism for the benzylic C-H borylation was proposed based on kinetics study (**Scheme 3-2**). The empirical rate law was determined by the measuring the initial rates (<10% conversion), which showed that the C−H borylation of *p*-xylene catalyzed by CoH-Zr_6TPDC has a first-order dependence on the catalyst and *p*-xylene concentrations and a zeroth-order dependence on the B_2pin_2 concentration. Additionally, the conversion of the deuterated *p*-xylene was slower than the proteo-*p*-xylene. Primary kinetic isotope effects from initial substrate conversion measurements [$k'_{obs}{}^{(H)}/k'_{obs}{}^{(D)}$ = 1.73(9)] indicated that the C−H bond cleavage of *p*-xylene is likely the turnover limiting step. Furthermore, we did not observe any deuterium incorporation into the benzyl boronate, which suggests that the C–H bond activation is irreversible.

Scheme 3-2. Proposed catalytic cycle for CoH-Zr_6TPDC catalyzed benzylic C-H borylation with B_2pin_2.

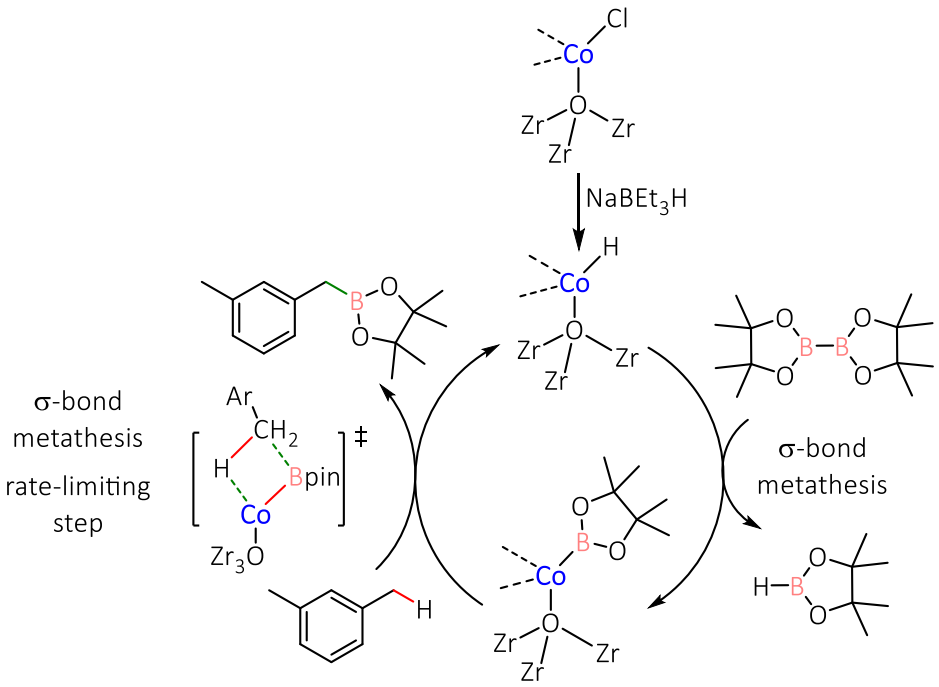

The oxidative addition of C–H bond to the Co-center is unlikely to occur in the turnover limiting step because the Co^{II} center was electron poor and the borylation of the benzylic C−H bonds was faster than that of the more electron-rich aryl C−H bonds of alkylarenes. Instead, CoH-Zr_6TPDC-catalyzed benzylic borylation likely proceeds via σ-bond metathesis pathways. Based on our experimental observations, we propose the following mechanism: The reaction of Zr_3O-Co-Cl moiety in CoCl-Zr_6TPDC with $NaEt_3BH$ generates the Zr_3O-Co-H active species CoH-Zr_6TPDC in the cycle. The σ-bond metathesis between Co-H and B_2pin_2 produces Zr_3O-Co-Bpin species, which then reacts with the alkylarene via a four-centered turnover limiting step involving [2σ + 2σ] cycloaddition of a Co-Bpin bond with the H-CH_2Ar bond of alkylarene to furnish the benzyl boronates and regenerate CoH-Zr_6TPDC.

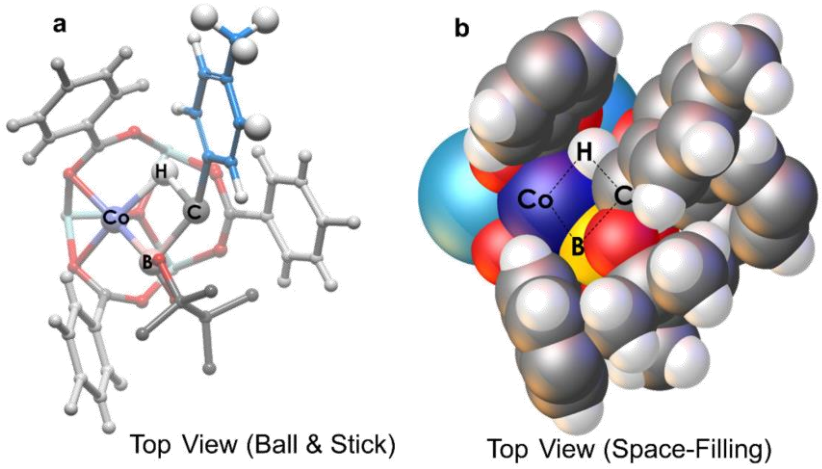

Figure 3-10. Proposed transition state for the rate-limiting σ-bond metathesis step, which involves a sterically-demanding 4-centered structure.

Although the electron-deficient Co catalyst should favor the electron-rich aryl C-H bonds, the steric hindrance from the three phenyl rings surrounding the Co center directs selective binding of less hindered benzylic C-H bonds (**Figure 3-10**). Moreover, the steric hindrance around the Co center prevents the second borylation of the monoborylated product, avoiding the over-borylation problem that was observed in homogeneous Co-diimine system.

3.2.4 CoH-Zr$_6$TPDC-catalyzed hydrogenation and hydroboration.

CoH-Zr$_6$TPDC is also highly active for catalyzing olefin hydrogenation at room temperature. Mono-substituted alkenes, such as 1-octene and styrene, were quantitatively hydrogenated with TONs of over 1.0×10^5. At 0.1-0.01 mol% Co-loading, CoH-Zr$_6$TPDC catalyzed the hydrogenation of 1,1-disubstituted and *cis*-1,2-disubstituted alkenes, *α*-isopropylstyrene and cyclohexene in quantitative yields (**Table 3-2**). Additionally, tri-substituted alkenes (*trans*-α-methylstilbene), and carbonyl-functionalized alkenes (dimethyl itaconate) and dialkenes were readily hydrogenated in excellent yields. Remarkably, CoH-Zr$_6$TPDC displayed a TON of 3.54×10^6 within 66 h in hydrogenation of 1-octene, which is the highest TON that has ever been reported for an earth-abundant metal-catalysed olefin hydrogenation. In addition, the resulting *n*-octane product contains only 3.7 ppm Co and 1.7 ppm Zr after simple filtration. Impressively, at 0.01 mol% Co loading, CoH-Zr$_6$TPDC could be recovered and reused at least sixteen times for the hydrogenation of 1-octene without any loss of catalytic activity.

Table 3- 2. Selected substrate scope for the CoH-Zr$_6$TPDC catalyzed olefin hydrogenation.

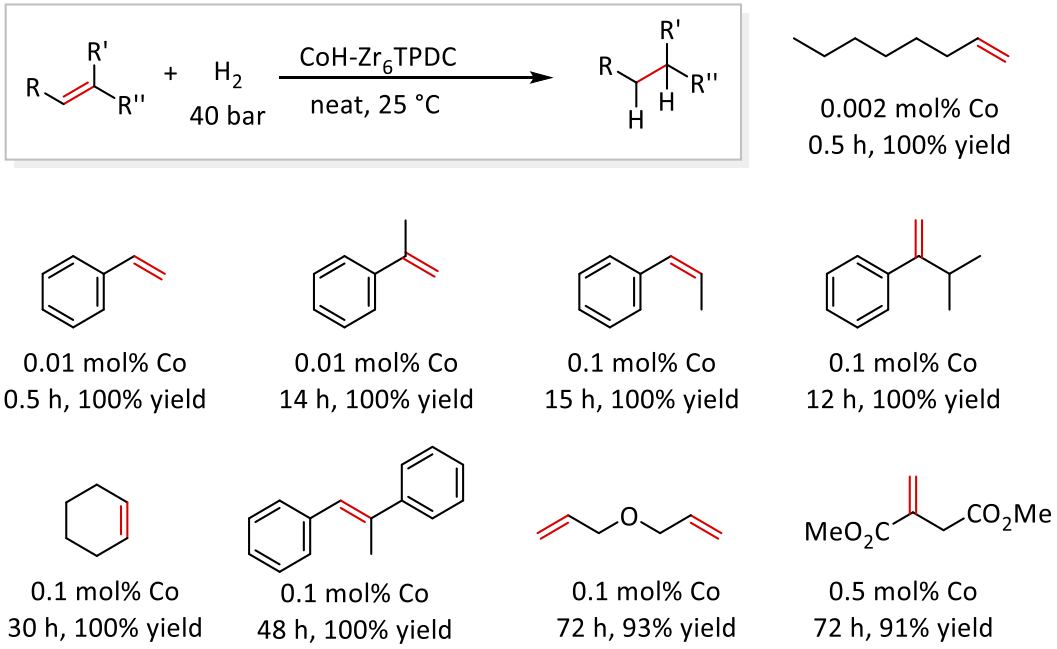

Despite the great activity of CoH-Zr_6TPDC for hydrogenating a broad scope alkene substrates, the catalyst is not active for hydrogenating tetrasubstituted alkenes (*e.g.* tetramethylethylene), even at 1.0% catalyst loading. This is likely a result of having sterically conjested environment around the Co metal center.

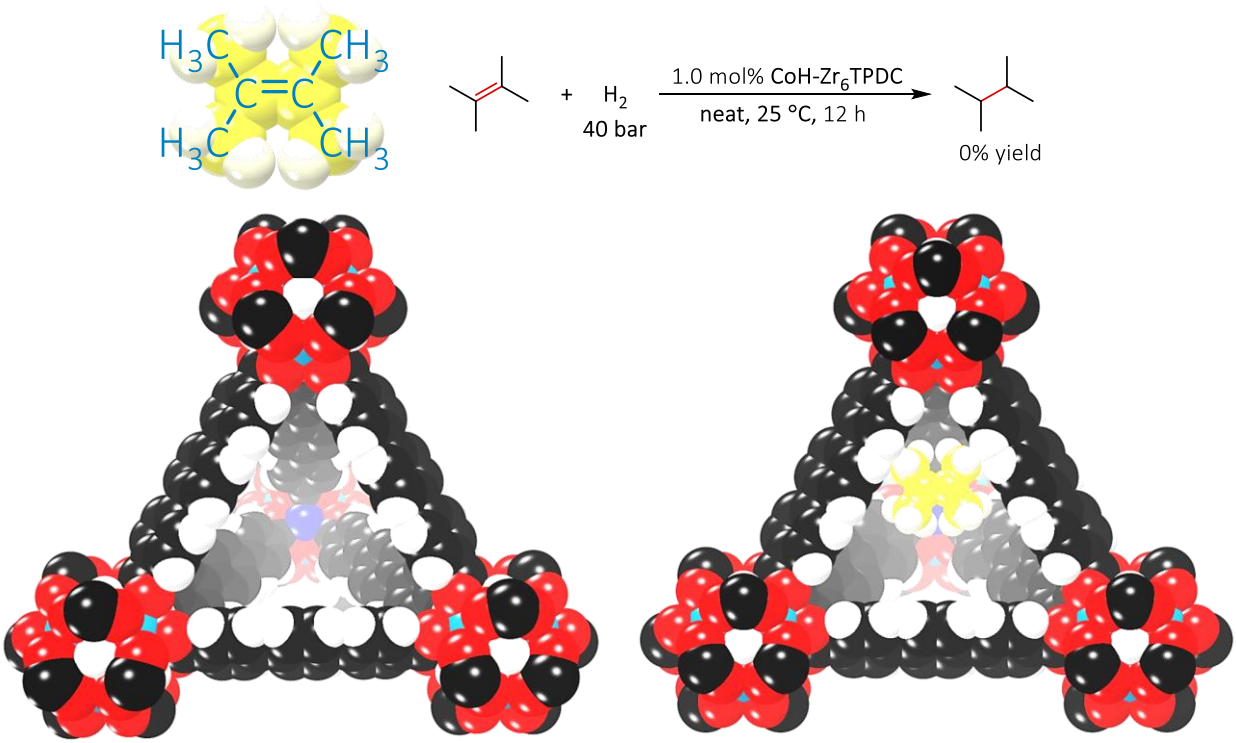

Figure 3-11. Space-filling model of Co binding site within Zr_6TPDC, indicating the space constriction over sterically hindered substrate like tetramethylethylene.

The PXRD patterns of CoH-Zr_6TPDC after hydrogenation were identical to those of the pristine MOF catalysts, indicating the high framework stability under reaction conditions. Additionally, ICP-MS analyses of the organic product showed negligible metal leaching after the first run, with only 0.9% for Co and 1.0% for Zr. Furthermore, no conversion of alkene was observed after the removal of the solid catalyst, demonstrating that the leached-Co species was not responsible for the catalytic activity.

The CoH-Zr_6TPDC was also evaluated for catalysing the hydroboration of alkenes and carbonyl compounds (**Table 3-3**). The hydroboration reactions were performed by treating alkenes, ketones or aldehydes with HBpin in presence of 0.01-0.4 mol% CoH-Zr_6TPDC at 60-100 °C. CoH-Zr_6TPDC catalysed the hydroboration of a range of carbonyl substrates, including alkyl and alkoxy-functionalized aryl ketones and aldehydes in 81-98% yields with TONs up to 5.4×10^4. At 0.1-0.4 mol% catalyst loading, the CoH-Zr_6TPDC effectively catalysed the anti-Markovnikov hydroboration of alkenes, including 1-octene, styrene and α-methylstyrene, to afford the corresponding alkylboronates in excellent yields. Pure hydroboration products were obtained simply by removing the catalyst via centrifugation followed by evaporation of the organic volatiles.

Table 3-3. Selected substrate scope for the CoH-Zr_6TPDC catalyzed hydroboration of carbonyls and alkenes.

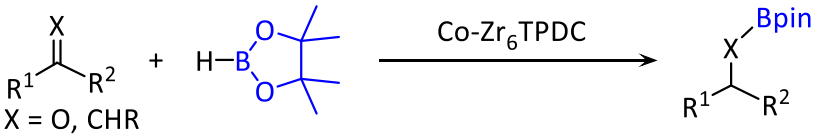

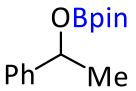	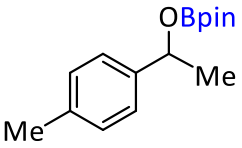	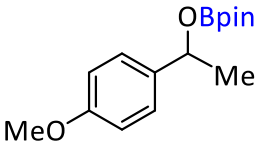	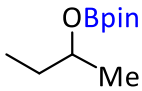
0.01% [Co], 60 °C 2 d, 98% yield	0.01% [Co], 60 °C 2 d, 96% yield	0.01% [Co], 60 °C 2 d, 100% yield	0.01% [Co], 60 °C 2 d, 86% yield
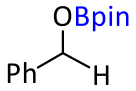	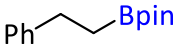	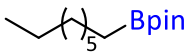	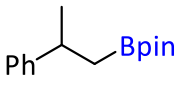
0.01% [Co], 60 °C 1 d, 98% yield	0.1% [Co], 70 °C 3 d, 89% yield	0.2% [Co], 100 °C 3 d, 59% yield	0.4% [Co], 100 °C 3 d, 93% yield

Reaction conditions: CoCl-Zr_6TPDC, 5 equiv of $NaBEt_3H$ (1.0 M in THF) w.r.t. Co, substrate, HBpin (1.4 equiv w.r.t. substarte), 60 - 100 °C. Yields were isolated yields.

3.3 Conclusion

In this chapter, we developed a simple strategy of treating Zr_6 MOF nodes with readily available and cheap earth-abundant metal precursors to afford highly active and selective single-site solid catalysts for a broad scope of organic transformations, including bezylic-selective borylation of sp^3 C-H bonds and the hydrogenation of alkenes. The unique coordination environment of Co centres of the secondary building units as well as the porous frameworks and pore structures of Zr_6TPDC play important roles in controlling the rate and chemoselectivity of these organic reactions. Owing to the high stability of UiO-MOFs and the ease of functionalizing SBUs with metal ions, we anticipate that MOFs may offer a versatile platform for discovering new catalytic transformations and developing earth-abundant metal and other metal catalysts for sustainable synthesis of fine and commodity chemicals. The effective approach of achoring metal catalysts onto MOF SBUs has the potential to promote MOF catalysts from novel discoveries to practical applications.

3.4 Experimental

3.2.1 Synthesis of H_2TPDC Ligand

Scheme 3- 3. Synthesis of Me_2TPDC through Suzuki-Miyaura coupling.

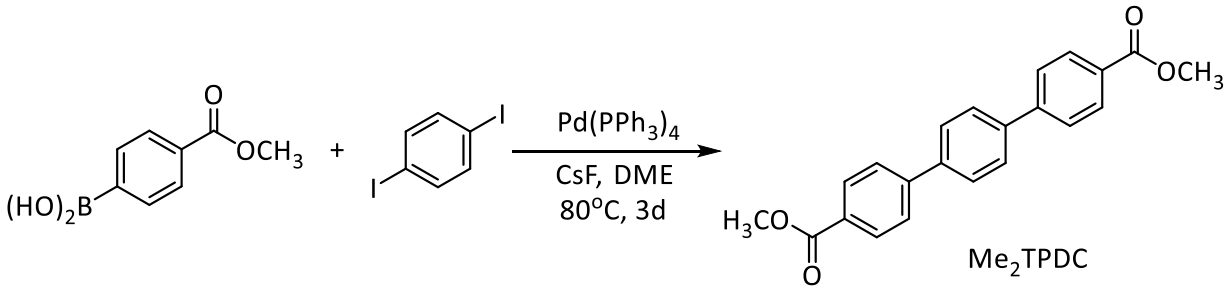

1,4-diiodobenzene (1.00 g, 3.03 mmol) and 4-methoxycarbonylphenylboronic acid (1.64 g, 9.09 mmol) were suspended in 94 mL of 1,2-dimethoxyethane in a glove box. Tetrakis(triphenylphosphine) palladium (175 mg, 0.152 mmol) and cesium fluoride (4.14 g, 27.3 mmol) were then added. The resulting mixture was sealed in a pressure vessel under nitrogen and stirred at 80 °C for 3 days. After cooling to room temperature, the reaction mixture was mixed with H_2O (20 mL) and centrifuged to obtain solid crude compound. The solid was then washed sequentially with H_2O, dimethoxylethane, and THF to remove impurities and dried in vacuo to afford 1,4-bis(4-methoxycarbonylphenyl)benzene as a white solid (420 mg, 1.21 mmol, 40% yield). ^{1}H NMR (500 MHz, $CDCl_3$): δ 8.14 (d, 2 H, $^3J_{HH}$ = 8.4 Hz), 7.74 (s, 4 H), 7.72 (d, 4 H, $^3J_{HH}$ = 8.4 Hz), 3.96 (s, 6 H). HRMS (ESI-TOF, *m/z*), calcd. for $C_{22}H_{18}O_4$ $[M+Na]^+$ 369. 1103, found 369.1079.

Scheme 3-4. Synthesis of H_2TPDC through base-mediated hydrolysis.

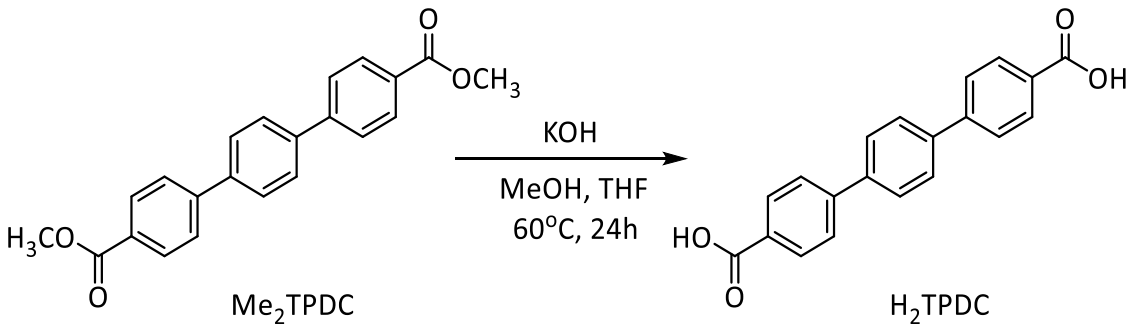

1,4-bis(4-carboxyphenyl)benzene (420 mg, 1.21 mmol) was suspended in THF (65 mL). A solution of KOH (6.17 g, 110 mmol) dissolved in MeOH (20 mL) was then added, and the reaction mixture was stirred at 60 °C for 24 h. The suspension was cooled to room temperature and the resulting precipitate was collected by centrifugation. The solution was washed with dry THF (20 mL) and recollected by centrifugation. The solid was suspended in THF (20 mL) and trifluoroacetic acid (3 mL) was slowly added and stirred for 1.5h at room temperature. H_2O (15

mL) was then added, and the white solid was isolated by centrifugation, washed with THF and Et_2O, and dried in vacuo to obtain 1,4-bis(4-carboxyphenyl)benzene (331.9 mg, 1.04 mmol, 86% yield) as pale-white solid. ^{1}H NMR (500 MHz, DMSO-d_6) δ 13.00 (br s, 2 H), 8.05 (d, 4 H, $^3J_{HH}$ = 8.3 Hz), 7.89 (s, 4H), 7.88 (d, 4 H, $^3J_{HH}$ = 8.3Hz) (**Figure 3-12**).

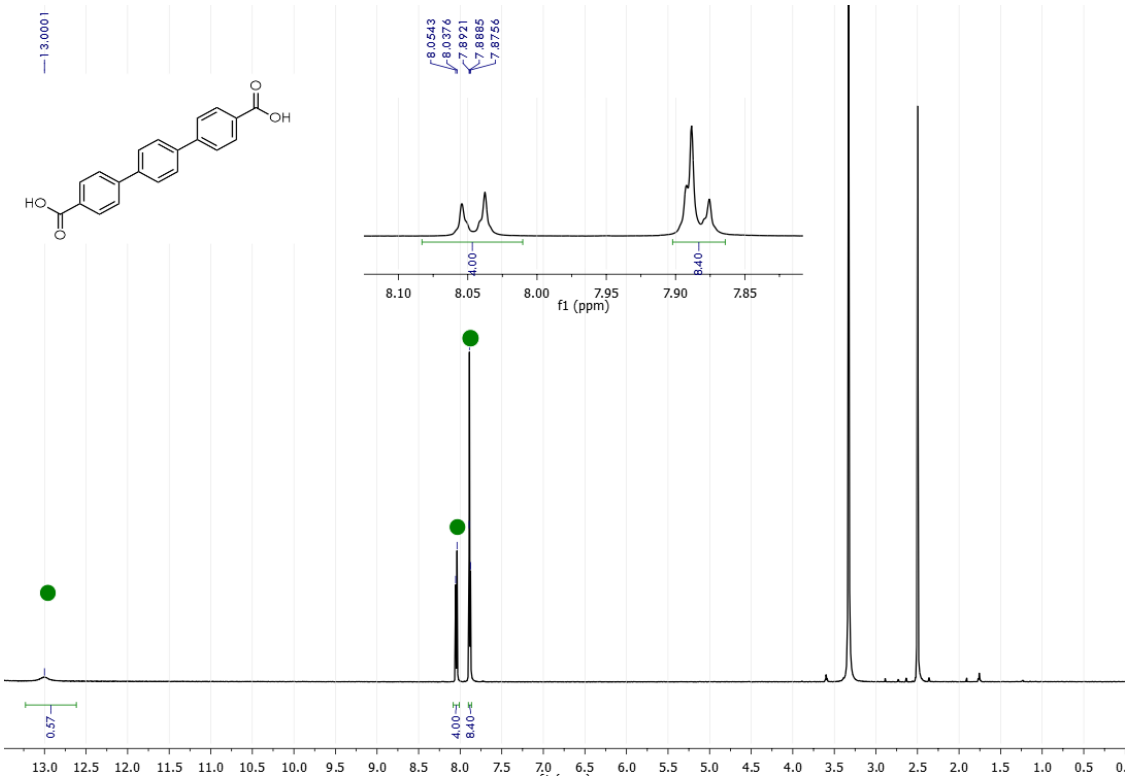

Figure 3-12. ^{1}H NMR of H_2TPDC in DMSO-d_6.

3.2.2 Synthesis of Zr_6TPDC

Zr_6TPDC was synthesized via a solvothermal reaction between $ZrCl_4$ and triphenyldicarboxylic acid (H_2TPDC) in the presence of DMF and trifluoroacetic acid in 95% yield. $ZrCl_4$ (1.30 mg, 5.03 μmol), 1,4-bis(4-carboxyphenyl)benzene (1.6 mg, 5.53 μmol) were dissolved in 0.8 mL of DMF in 1 dram vial, and 15.4 μL of trifluoroacetic acid was then added. The vial was capped and then heated at 120 ºC for 3 days to afford a white solid as the MOF product (2.0 mg,

95% yield). Comparing PXRD pattern of obtained MOF with simulated pattern from single crystal structure shows good crystallinity of the Zr_6TPDC-MOF.

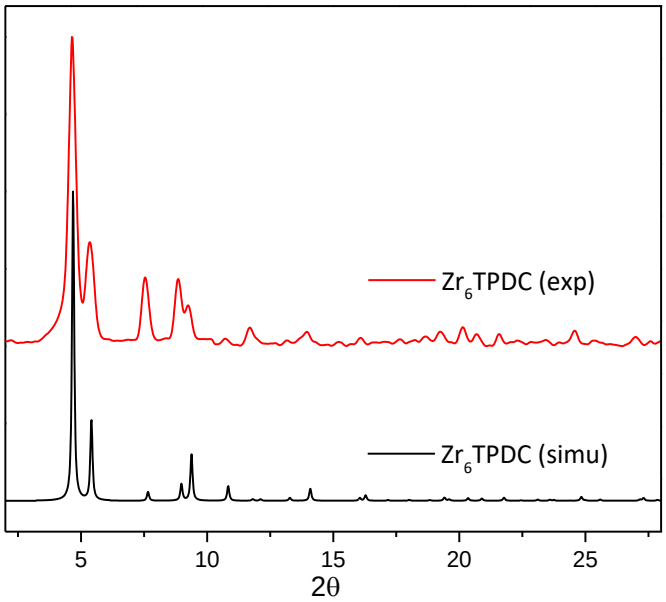

Figure 3-13. PXRD patterns of freshly prepared Zr_6TPDC (red) compared to that simulated from single crystal structure (black).

3.2.3 Synthesis of CoCl-Zr_6TPDC

The experimental procedure for the synthesis and characterization of CoCl-Zr_6TPDC is described as following. In a glovebox, Zr_6TPDC (20.0 mg) in 3 mL THF was cooled to -30 °C for 30 min. To the cold suspension, 33 µL of *n*BuLi (2.5 M in hexanes) was added dropwise and the resultant light yellow mixture was stirred slowly overnight at room temperature. The light yellow solid was centrifuged out and washed with THF 5-6 times over 6 h. Then, the lithiated Zr_6TPDC was transferred to a vial containing 5 mL THF solution of $CoCl_2$ (6.0 mg). The mixture was stirred for 15 h and the deep blue solid was then centrifuged out and washed with THF for 5-8 times. The metalated MOFs were then stored in THF in the glovebox for further uses.

3.2.4 Synthesis of CoH-Zr_6TPDC

The procedure for the CoCl-Zr_6TPDC activation with $NaBEt_3H$ is described as following. In a glovebox, CoCl-Zr_6TPDC (1.0 mg, 0.2 mol % Co) was charged into a small vial and 0.5 mL THF was added. Then, 15 µL $NaBEt_3H$ (1.0 M in THF) was added to the vial and the mixture was stirred slowly for 1 h in the glovebox. The solid was centrifuged out of suspension and washed with THF twice.

3.2.5 EXAFS Analysis of CoCl-Zr_6TPDC

X-ray absorption data were collected at Beamline 9-BM-C at the Advanced Photon Source (APS) at Argonne National Laboratory. Spectra were collected at the cobalt K-edge in transmission mode. The X-ray beam was monochromatized by a Si(111) monochromater and detuned by 25% to minimize harmonics. A metallic cobalt foil standard was used as the reference for energy calibration and was measured simultaneously with experimental samples. The incident beam intensity (I_0) was measured by an ionization chamber with 30% N_2 and 70% He gas composition. Data was collected in three regions: a pre-edge region –150 to –20 eV (5 eV step size, dwell time 1.0 s), XANES region –20 to 50 eV (0.5 eV step size, dwell time 1.0 s), and EXAFS region 3.62 $Å^{-1}$ to 13.93 $Å^{-1}$ (0.05 $Å^{-1}$ step size, dwell time increased linearly from 1.0 to 3.9 seconds over the region to facilitate higher k-weighted data processing). All energies are listed relative to the elemental Co K-edge (7709 eV). Multiple X-ray absorption spectra were collected at room temperature for each sample. Samples were ground and mixed with polyethyleneglycol (PEG) and packed into a 6-shooter sample holder to achieve adequate absorption length.

Data were processed using the Athena and Artemis programs of the IFEFFIT package based on FEFF 6.[8-9] Prior to merging, spectra were calibrated against the reference spectra (metallic Co or Fe) and aligned to the first peak in the smoothed first derivative of the absorption spectrum, background removed, and spectra processed to obtain a normalized unit edge step.

3.2.6 CoH-Zr$_6$TPDC catalyzed C-H borylation.

Scheme 3-5. Benzylic C-H borylation with B_2pin_2 catalyzed with CoH-Zr$_6$TPDC.

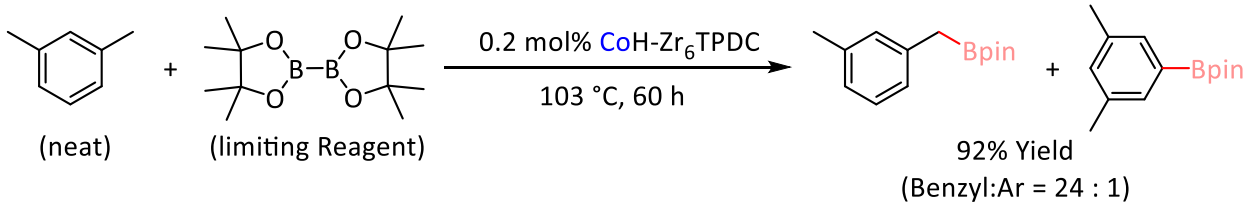

In a glovebox, UiO-CoCl (1.0 mg, 0.2 mol % Co) was charged into a small vial and 0.5 mL THF was added. Then, 15 µL $NaBEt_3H$ (1.0 M in THF) was added to the vial and the mixture was stirred slowly for 1 h in the glovebox. The solid was centrifuged out of suspension and washed twice with THF and then once with *m*-xylene. B_2pin_2 (43.0 mg, 0.169 mmol) in 2.0 mL *m*-xylene was added to the vial and the resultant mixture was transferred to a Schlenk tube. The tube was heated under nitrogen at 103 °C for 48 h to obtain the alkyl boronate ester in 92% yield as determined by GC analysis.

3.5 References

1. Zhang, T.; Manna, K.; Lin, W., Metal–Organic Frameworks Stabilize Solution-Inaccessible Cobalt Catalysts for Highly Efficient Broad-Scope Organic Transformations. *J. Am. Chem. Soc.* **2016,** 3241-3249.

2. Thacker, N. C.; Lin, Z.; Zhang, T.; Gilhula, J. C.; Abney, C. W.; Lin, W., Robust and Porous β-Diketiminate-Functionalized Metal–Organic Frameworks for Earth-Abundant-Metal-Catalyzed C–H Amination and Hydrogenation. *J. Am. Chem. Soc.* **2016,** 3501-3509.

3. Manna, K.; Zhang, T.; Greene, F. X.; Lin, W., Bipyridine- and Phenanthroline-Based Metal–Organic Frameworks for Highly Efficient and Tandem Catalytic Organic Transformations via Directed C–H Activation. *J. Am. Chem. Soc.* **2015,** 2665-2673.

4. Jiang, J.; Gándara, F.; Zhang, Y.-B.; Na, K.; Yaghi, O. M.; Klemperer, W. G., Superacidity in Sulfated Metal–Organic Framework-808. *J. Am. Chem. Soc.* **2014,** 12844-12847.

5. Jiang, J.; Yaghi, O. M., Brønsted Acidity in Metal–Organic Frameworks. *Chem. Rev.* **2015,** 6966-6997.

6. Yang, D.; Odoh, S. O.; Wang, T. C.; Farha, O. K.; Hupp, J. T.; Cramer, C. J.; Gagliardi, L.; Gates, B. C., Metal–Organic Framework Nodes as Nearly Ideal Supports for Molecular Catalysts: NU-1000- and UiO-66-Supported Iridium Complexes. *J. Am. Chem. Soc.* **2015,** 7391-7396.

7. Nguyen, H. G. T.; Schweitzer, N. M.; Chang, C.-Y.; Drake, T. L.; So, M. C.; Stair, P. C.; Farha, O. K.; Hupp, J. T.; Nguyen, S. T., Vanadium-Node-Functionalized UiO-66: A Thermally Stable MOF-Supported Catalyst for the Gas-Phase Oxidative Dehydrogenation of Cyclohexene. *ACS Catal.* **2014,** 2496-2500.

8. Rehr, J. J.; Albers, R. C., Theoretical approaches to x-ray absorption fine structure. *Rev. Mod. Phys.* **2000,** 621-654.

9. Ravel, B.; Newville, M., ATHENA, ARTEMIS, HEPHAESTUS: data analysis for X-ray absorption spectroscopy using IFEFFIT. *J. Synchrotron Radiat.* **2005,** 537-541.

Chapter 4. Site-Isolated Cobalt Catalysts at New $Zr_8(\mu_2\text{-}O)_8(\mu_2\text{-}OH)_4$ MOF Nodes for Highly Active Hydrogenation

4.1 Introduction

The last chapter discussed the design of a highly active and chemoselective cobalt-hydride catalyst supported on the $Zr_6(\mu_3\text{-}O)_4(\mu_3\text{-}OH)_4$ node of Zr_6TPDC MOF for benzylic C-H activation and olefin hydrogenation. Although the Zr_3OH site was shown as an excellent ligand for supporting various catalysts, the site is sterically encumbered by three phenyl rings groups which prohibits the Zr_3O-CoH catalyst from hydrogenating challenging substrates including tetrasubstituted olefins and heterocycles. Design and synthesis of analogous Zr-MOFs containing sterically-open bridging hydroxides would facilitate the discovery of more active node-supported cobalt catalysts for the hydrogenation of challenging substrates, and enable their application in industrial hydrogenation. This chapter describes a new $Zr_8(\mu_2\text{-}O)_8(\mu_2\text{-}OH)_4$ node with electron-rich and sterically-open Zr_2OH ligand sites to anchor Co catalysts for hydrogenation of a broad range of unsaturated compounds, including olefins, imines, carbonyls, and heterocycles. The Zr_8 SBU features much more open space around the bridging hydroxide as indicated by the space-filling model (**Figure 4-1**).

Hydrogenation of unsaturated organic compounds is one of the most widely practiced catalytic reactions in organic synthesis and chemical industry, with pivotal role in producing commodity chemicals, pharmaceuticals, and agrochemicals.[1-3] For decades, hydrogenation reactions have relied on precious metal catalysts supported either on solid surfaces or by strong field ligands to enable two-electron redox chemistry, including oxidative addition and reductive elimination, that constitutes key bond breaking and forming steps in the catalytic cycle.[4-6] However,

the low abundance, high price, and inherent toxicity of precious metals have stimulated intense interest in developing earth-abundant metal catalysts.[7] Significant progress has been made in recent years to develop iron, cobalt, nickel, and copper-based hydrogenation catalysts, by coordinating with sterically encumbered nitrogen- or phosphorus-donor ligands with strong ligand fields.[8-16] However, each of these catalyst only hydrogenates typically a narrow class of substrates with limited turnover numbers. Furthermore, only scarce examples of Earth-abundant metal catalyzed hydrogenation of imines and heterocycles were reported, and all of them require harsh reaction conditions.[17-18] The MOF-derived catalyst, CoH-Zr_8MTBC, is one of the few Earth-abundant metal-based hydrogenation catalysts with very high activities.

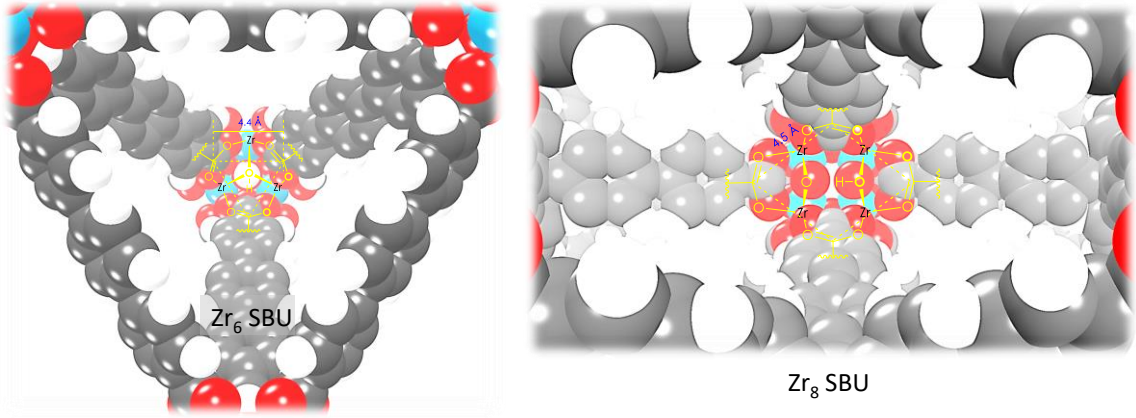

Figure 4-1. Space-filling model comparison of the steric environments of Zr_6 SBU and Zr_8 SBU.

4.2 Results and Discussion

4.2.1 Synthesis and characterizations of CoCl-Zr_8MTBC

The detailed synthesis and characterization of Zr_8MTBC was described in the experimental section of this chapter. The Hf-based isostructural MOF, Hf_8MTBC, was also synthesized and characterized via a similar protocol. The crystal structure of the MOFs was determined by SXRD. Zr_8MTBC was metalated with Co analogously to that for Zr_6TPDC. Zr_8MTBC was treated with

10 equiv. of ^{n}BuLi to deprotonate both the μ_2-OH in Zr_8-SBU and the μ_3-OH in Zr_6-SBU, then reacted with a $CoCl_2$ solution in THF to afford CoCl-Zr_8MTBC as a deep-blue solid (**Scheme 4-1**).

Scheme 4-1. Metalation of Zr_2OH sites in Zr_8 SBU with $CoCl_2$ through sequential deprotonation and metalation.

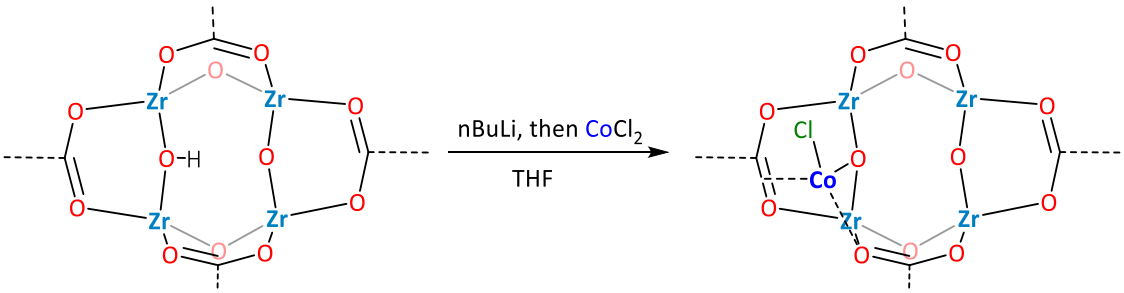

Only the inorganic node was transformed during lithiation and metalation without modifying the carboxylate groups of the organic linker, evidenced by the ^{1}H NMR spectrum of recovered MTBC from the acid-digested CoCl-Zr_8MTBC. The ligand was intact also by the IR spectrum of CoCl-Zr_8MTBC, which displayed characteristic carboxylate carbonyl stretching bands (**Figure 4-2**). ICP-MS analysis of the digested CoCl-Zr_8MTBC revealed complete metalation of all Zr_8 and Zr_6 clusters, corresponding to four Co centers per Zr_8 or Zr_6 node. The complete metalation of both nodes was also evidenced by the disappearance of both the μ_2O-H stretching band (3737 cm^{-1}) and μ_3O-H stretching band (3639 cm^{-1}) in the IR spectrum.

The crystallinity of the MOF was maintained after metalation as evidenced by the similar PXRD patterns of Zr_8MTBC and CoCl-Zr_8MTBC (**Figure 4-3**). The porosity of CoCl-Zr_8MTBC was characterized by N_2 sorption isotherms (**Figure 4-4**). The BET surface area was lower than that of Zr_8MTBC as a result of the increased higher molecular weight.

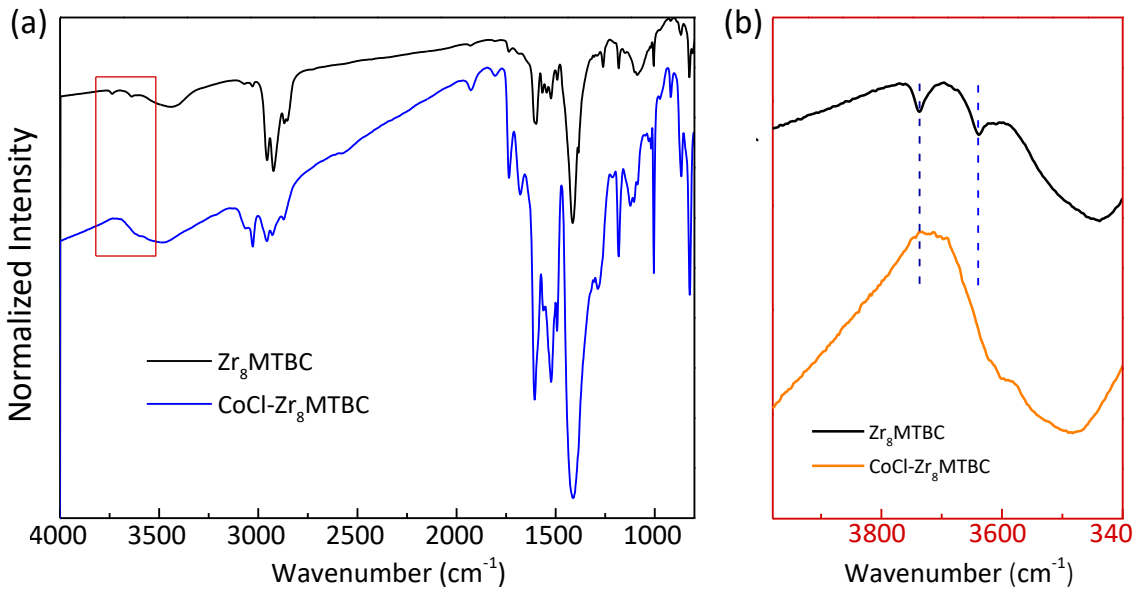

Figure 4-2. IR spectra of freshly prepared CoCl-Zr_8MTBC in comparison with non-metalated Zr_8MTBC. The Zr_6 cluster Zr_3OH stretching at 3639 cm^{-1} and the Zr_8 cluster Zr_2OH stretching at 3737 cm^{-1} disappeared after metalation, indicating the metalation at both sites.

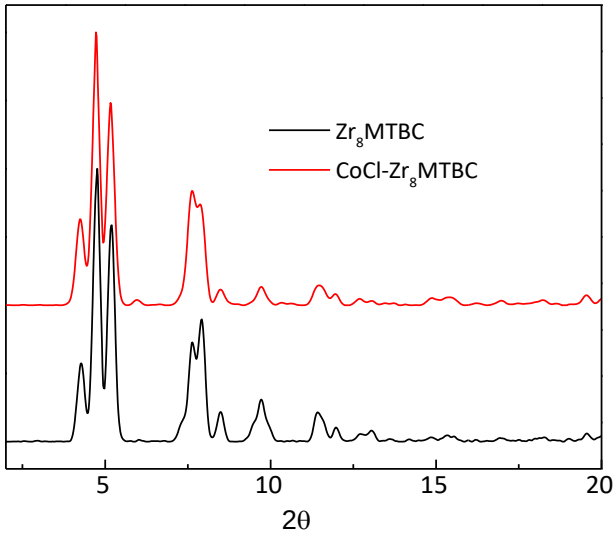

Figure 4-3. PXRD of CoCl-Zr_8MTBC (red) compared with that of Zr_8MTBC (black).

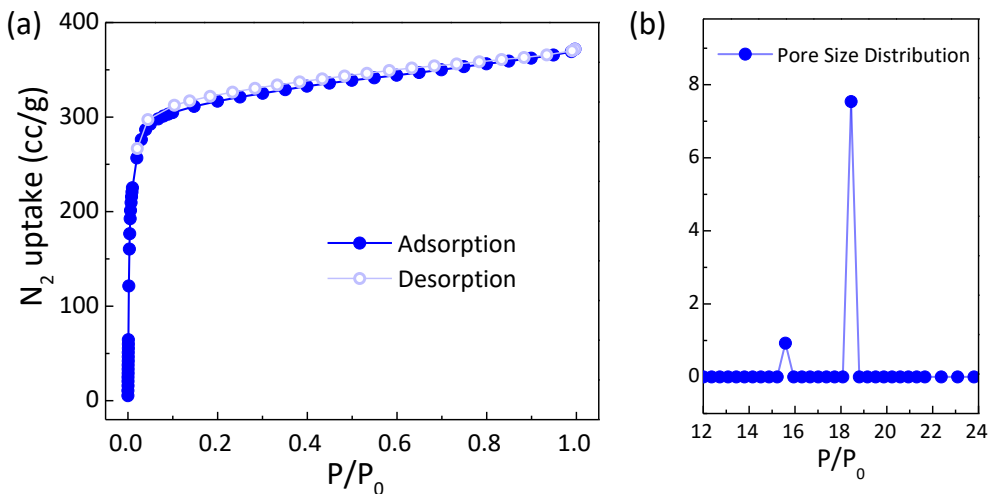

Figure 4-4. N_2 sorption isotherms (a) and pore size distributions (b) of CoCl-Zr_8MTBC.

The coordination environment of the Co centers in CoCl-Zr_8MTBC could not be established by SXRD due to their location disorder. We instead utilized XAS to investigate the Co coordination environments and electronic properties. Four out of six facets of the $Zr_8(\mu_2\text{-}O)_8(\mu_2\text{-}OH)_4$ cubic node have the μ_2-OH groups to bind Co. We envisioned two different Co coordination modes on the Zr_8 node, either the μ_2-oxide/μ_2-oxo chelation or the μ_2-oxide/(μ_2-carboxylate)$_2$ tridentate chelation. We noticed that the μ_2-oxide/μ_2-oxo chelation mode is disfavored because the μ_2-oxide to μ_2-oxo distance was only 2.35 Å, too short for chelating with Co. Such a structural model was also ruled out by the misfit of the Co EXAFS data. In contrast, the μ_2-oxide and two μ_2-carboxylate groups could coordinate to the same Co center in a more stable conformation, with Co to μ_2-oxide distance of 1.83 Å and Co to η_2-carboxylate distance of 1.94 Å, as indicated by the EXAFS fitting result (**Figure 4-5**). Cobalt coordination on Zr_6 node also adopts a μ_2-oxide/ η_2-carboxylate)$_2$ tridentate mode, analogous to that proposed in the CoCl-Zr_6TPDC system described in the last chapter.[22]

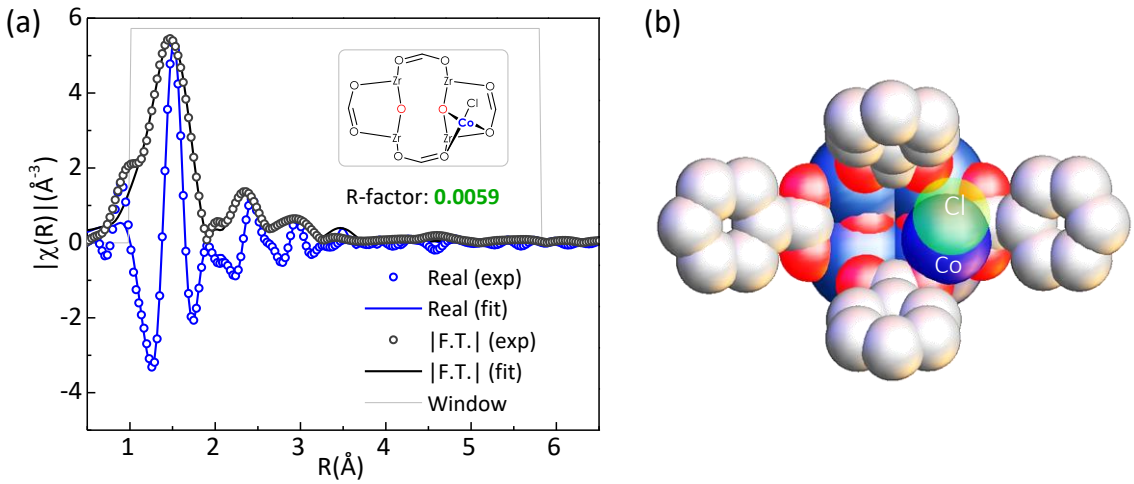

Figure 4-5. EXAFS fitting of CoCl-Zr_8MTBC with proposed Zr_2O-CoCl binding model.

4.2.2 Synthesis and characterizations of CoH-Zr_8MTBC

Activation of CoCl-Zr_8MTBC with $NaBEt_3H$ is necessary for generating CoH-Zr_8MTBC as the active catalyst for olefin hydrogenation. Upon treatment with with 5 equiv. of $NaBEt_3H$, the CoH-Zr_8MTBC catalyst was generated as a black solid. No hydrogen gas was detected by GC analysis, indicating a simple H/Cl metathesis during the activation step without involving any redox pathway (*e.g.* the formation of Co nanoparticle). The Co centers in CoH-Zr_8MTBC maintained a divalent oxidation state through XANES analysis, by comparing its pre-edge feature with that of $CoCl_2$ standard (**Figure 4-6**).

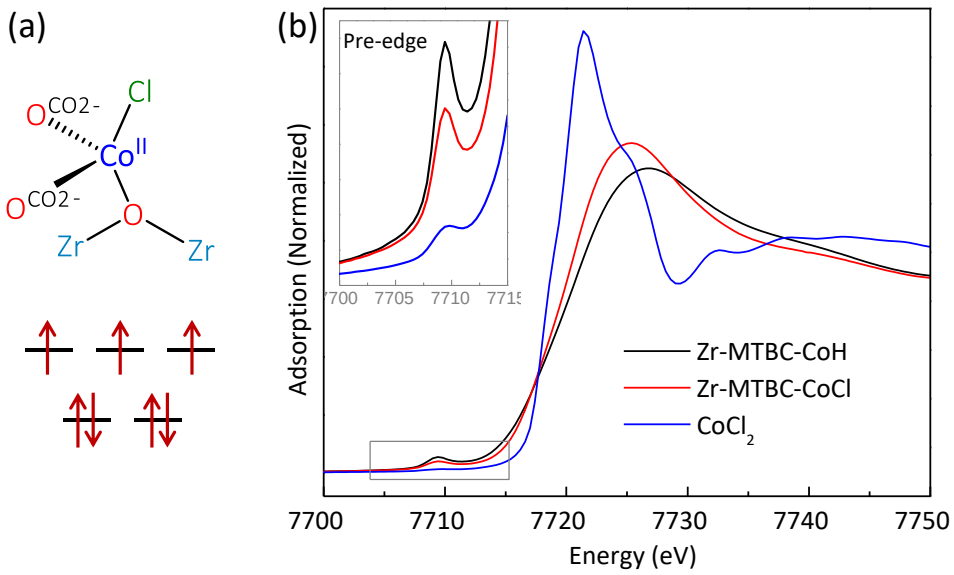

Figure 4-6. (a) The coordination environment and electron configuration of Co^{II} centers in CoCl-Zr_8MTBC. (b) XANE spectra of CoCl-Zr_8MTBC (red), CoH-Zr_8MTBC (black) compared to that of $CoCl_2$ reference (blue).

4.2.3 CoH-Zr_8MTBC catalyzed hydrogenation of alkenes

CoH-Zr_8MTBC is a highly active catalyst for hydrogenating a broad scope of alkenes at room temperature. At a 0.05 mol % Co loading, terminal alkenes containing polar functionalities, such as allyl ether, allyl acetate, dimethyl itaconate and 2-vinyl pyridine, were selectively hydrogenated to afford the corresponding products in quantitative yields (**Table 4-1**). At a 0.05-0.1 mol % Co loading, CoH-Zr_8MTBC was also very active for hydrogenating trisubstituted alkenes, including ethyl-3,3- dimethylacrylate, α-terpinene, trans-α-methylstilbene and 1-methyl-1-cyclohexene, in excellent yields. The hydrogenated products were obtained in high purity simply by filtration of reaction mixtures followed by evaporation of the organic volatiles.

Table 4-1. Substrate scope for the CoH-Zr_8MTBC catalyzed alkene hydrogenation.

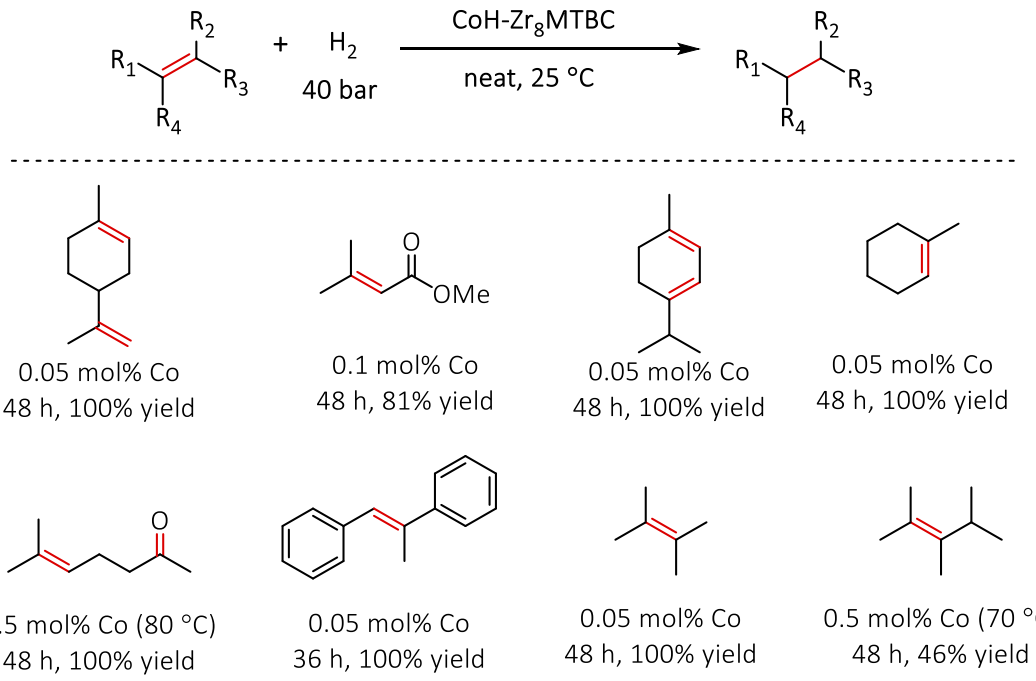

The hydrogenation of tetrasubstituted alkene is vey challenging because the C=C bond is sterically conjescted. Even the Wilkinson's catalyst, a common Rh-based hydrogenation catalyst, is inactive for tetrasubstituted substrates. Impressively, CoH-Zr_8MTBC quantitatively hydrogenates tetrasubstituted alkenes (*e.g.* 2,3-dimethyl-2-butene) at room temperature within 48 h with a TON of 8000. Hydrogenation of even bulkier tetrasubstituted alkenes such as 2,3,4-trimethylpent-2-ene could also be achieved at elevated temperatures. In the case of CoH-Zr_6TPDC, the Zr_3O-Co site was shown to be inactive for hydrogenating of bulky and rigid trisubstituted alkenes (*e.g.* 1-methyl-1-cyclohexene and tetrasubstituted alkenes. Therefore, we believe the hydrogenation of these bulky alkenes only occured at the Zr_2O-Co sites in Zr_8-SBUs of CoH-Zr_8MTBC.

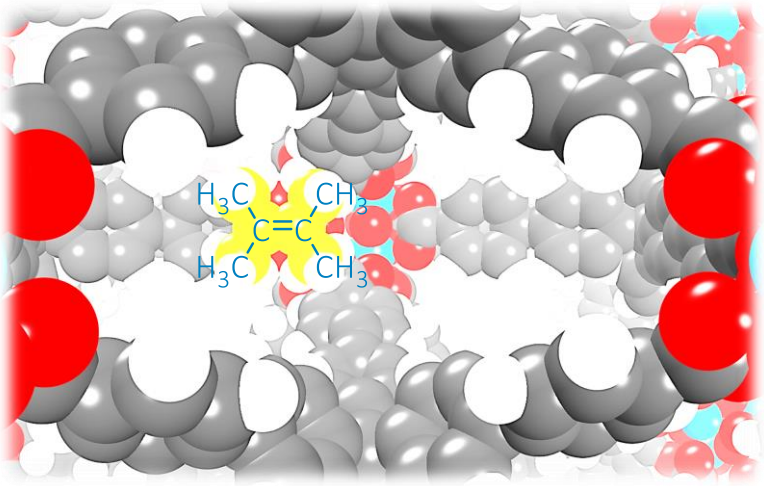

Figure 4-7. Space-filling model showing the coordination of tetramethylethylene to the Co centers in CoH-Zr_8MTBC.

The hydrogenation of methylheptenone to methylheptanone is a key step to synthesizing dimethyloctenol (DMOE), an important aroma compound. This reaction is generally catalyzed with precious metal catalysts including Pd/C and Pd/Al_2O_3. At a 0.5 mol% Co loading, CoH-Zr_8MTBC selectively hydrogenates methylheptenone to afford methylheptanone at 40 °C in quantitative yield without reducing the carbonyl group. At elevated temperature of 80 °C, both the alkene and carbonyl groups are hydrogenated to afford 6-methyl-2-heptanol in quantitative yield.

Importantly, at a 0.1 mol% Co loading, CoH-Zr_8MTBC was recovered and reused at least 5 times for the hydrogenation of 1-methylcyclohexene without lossing MOF crystallinity (**Figure 4-8**). Excellent yields (92-100%) of methylcyclohexane were obtained consistently in the reuse experiments. The CoH-Zr_8MTBC recovered from the 1st and 6th runs maintained good crystalinity by comparing their PXRD patterns with pristine CoH-Zr_8MTBC, indicating the high stability of the MOF under reaction conditions.

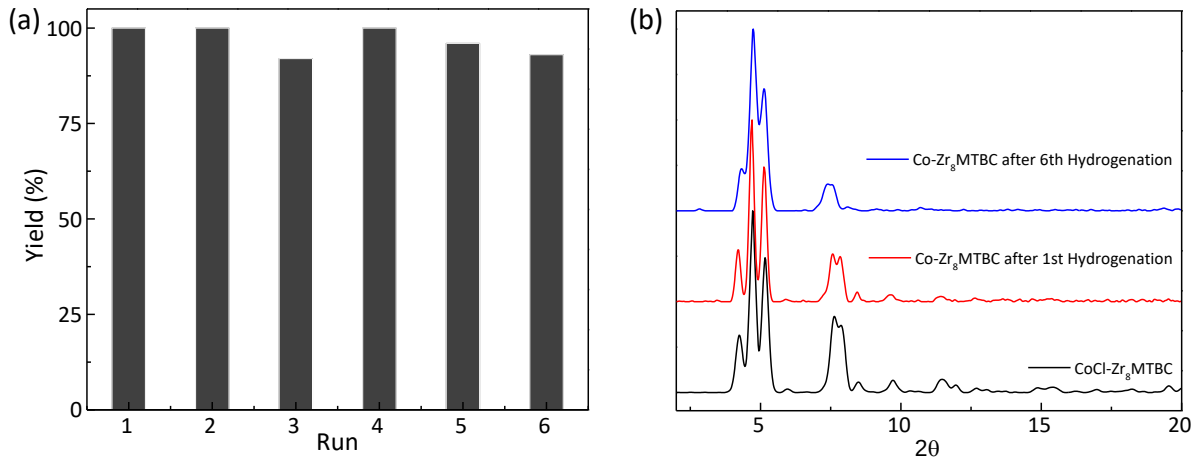

Figure 4-8. (a) Plot of yields (%) of methylcyclohexane at different runs in the reuse experiments of Co-Zr_8MTBC for hydrogenation of 1-methylcyclohexene. The Co loadings were 0.1 mol %. (b) PXRD patterns of CoH-Zr_8MTBC after the 1st run of hydrogenation and after the 6th run of hydrogenation, similar to that of untreated CoCl-Zr_8MTBC.

The heterogeneity of CoH-Zr_8MTBC was confirmed by several experiments. ICP-MS analyses showed that the amounts of leached Co and Zr into the supernatant after the first run were only 1.6% and 0.02%, respectively. Moreover, no further hydrogenation was observed after removal of CoH-Zr_8MTBC from the reaction mixture, which ruled out the role of the leached Co-nanoparticles or other Co-species in catalyzing hydrogenation reactions. The EXAFS spectrum of freshly prepared CoH-Zr_8MTBC or that recovered from 1-methylcyclohexene hydrogenation showed no contribution from Co-Co scattering, ruling out the formation of Co-nanoparticles during the catalysis (**Figure 4-9**).

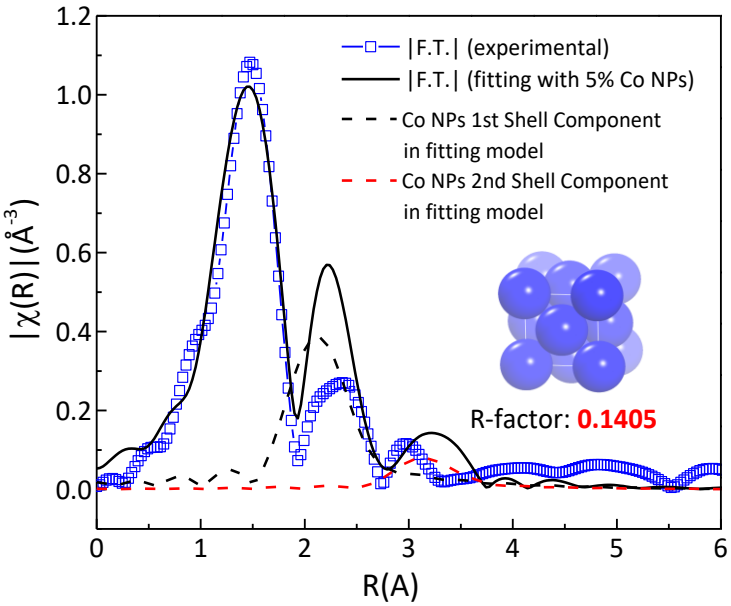

Figure 4-9. Fitting of the CoH-Zr_8MTBC catalyst after hydrogenation with inclusion of 5% Co nanoparticles. Scattering paths attributed from first shell (black dash line) and second shell (red dash line) of Co NPs in R space showing the magnitude of Fourier transform. Bad fitting was because the misfit in the 2.1 Å and 3.1 Å region, which are characteristic features of Co-Co scattering.

We further investigated the reaction mechanism of CoH-Zr_8MTBC catalyzed hydrogenation of 1-methylcyclohexene through kinetics study. The rate law of the reaction was determined by the initial rates method (<15% conversion) in THF at room temperature. In order to avoid complications caused by the presence of two kinds of Co-centers in CoH-Zr_8MTBC, the initial rates were measured for hydrogenation of 1-methylcyclohexene catalyzed by only Zr_2O-CoH sites, since Zr_3O-CoH at the SBUs of Zr_6TPDC was inactive in hydrogenation of 1-methylcyclohexene. The empirical rate law showed that the initial rates had a first-order dependence on the cobalt concentrations and pressure of H_2 and a zeroth-order dependence on the alkene concentration. The activation of H_2 at the electron deficient Co^{II}-center via oxidative addition is unlikely. Our kinetic and spectroscopic data thus suggest that the insertion of the C=C bond of the alkene into the Co-H bond generates a Co-alkyl intermediate, which undergoes σ-bond

metathesis with H_2 in the turnover limiting step to give an alkane product, simultaneously regenerating the cobalt-hydride species (**Scheme 4-2**).

Scheme 4-2. Proposed catalytic cycle for the CoH-Zr_8MTBC catalyzed alkene hydrogenation, which involves the insertion of alkene into the Co-H bond gives a Co-alkyl species, followed by turnover limiting σ-bond metathesis with H_2 to generate the alkane product.

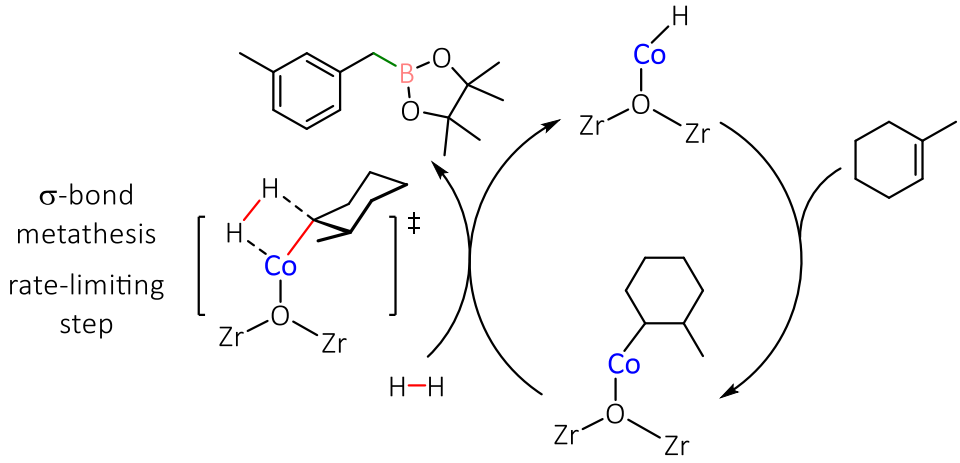

4.2.4 CoH-Zr_8MTBC catalyzed hydrogenation of carbonyls and imines

Prompted by the hydrogenation of the carbonyl group of methylheptenone at elevated temperatures, we sought to investigate the hydrogenation of imines and carbonyls. CoH-Zr_8MTBC also displayed excellent activity in catalytic hydrogenation of imines (**Table 4-2**). Though hydrogenation of imines is an important synthetic route to amines, examples of base metal catalysts for imine hydrogenation are rare. The imine hydrogenation reactions were performed in toluene at 80 °C under 40 bar of H_2 in presence of 0.5 mol % CoH-Zr_8MTBC. N-benzylideneaniline was completely hydrogenated to N-benzylaniline in 5 h. The pure product was isolated in 98% yield after simple filtration followed by removal of the volatiles in vacuo.

Table 4-2. CoH-Zr_8MTBC-catalyzed hydrogenation of imines.

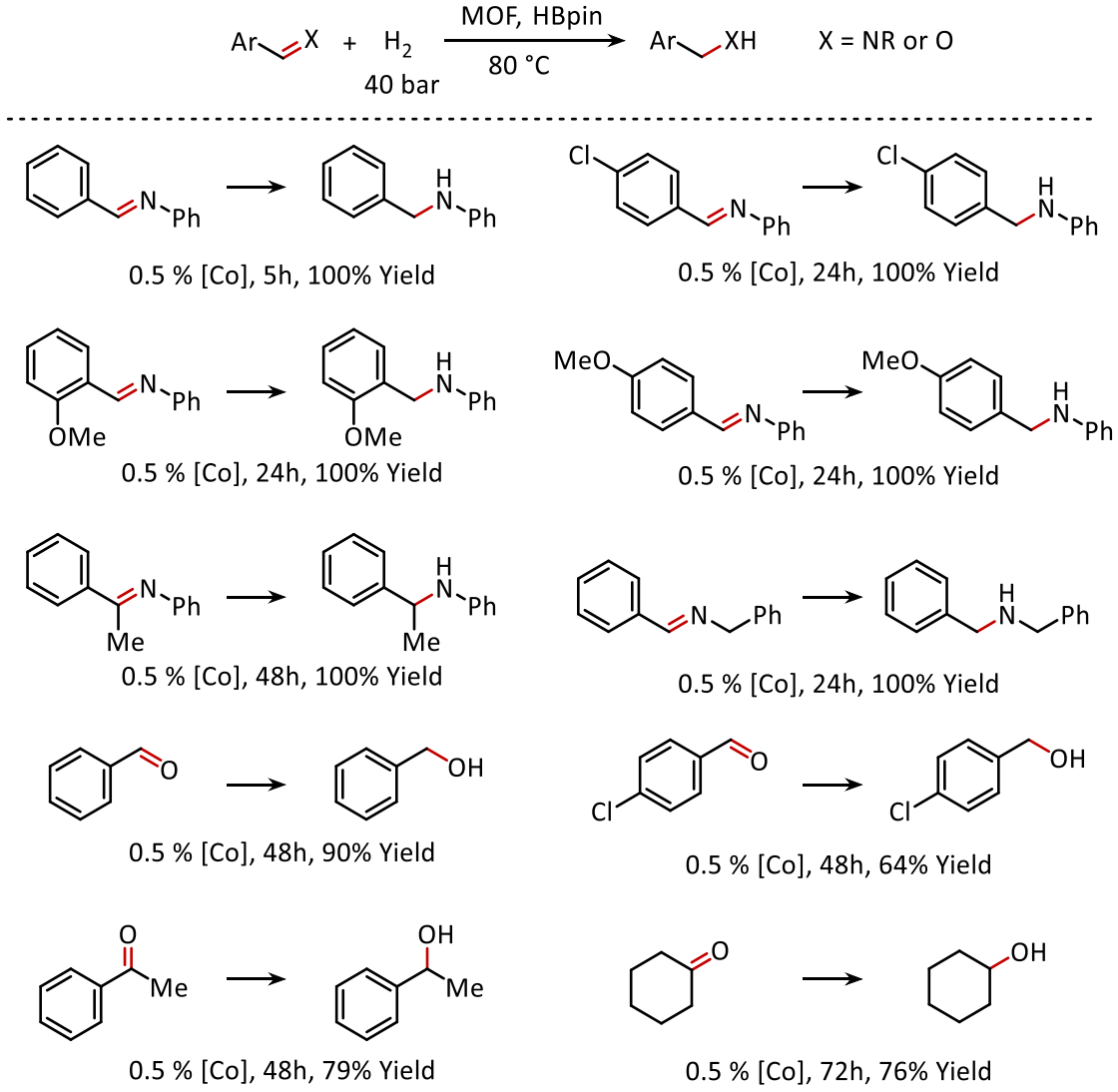

Reaction conditions: 0.25 mg of CoCl-Zr_8MTBC (0.5 mol % Co), 5 equiv of $NaBEt_3H$ (1.0 M in THF) w.r.t. Co, alkene, toluene, 40 bar H_2, 80 °C; Yields were deter-mined by ^1H NMR with mesitylene as the internal standard. Isolated yield in the parenthesis.

The CoH-Zr_8MTBC recovered after this reaction remained crystalline, as shown by PXRD (**Figure 4-10**). The leaching of Co and Zr into the supernatant was 0.23% and 0.08%, respectively. A broad scope of aldimines were readily hydrogenated within 24 h to afford corresponding N-benzylanilines in excellent yields. The hydrogenation of ketimine (*e.g.* (E)-N-(1-

phenylethylidene)aniline) requires longer reaction times, presumably due to the less facile binding and activation of the ketimine substrate.

CoH-Zr_8MTBC is also active in hydrogenating a broad scope of carbonyl compounds to their corresponding alcohols in toluene at 90 °C. At a 0.5 mol % Co loading, CoH-Zr_8MTBC efficiently hydrogenates both aromatic and aliphatic ketones and aldehydes to the corresponding alcohol prodcuts in good yields.

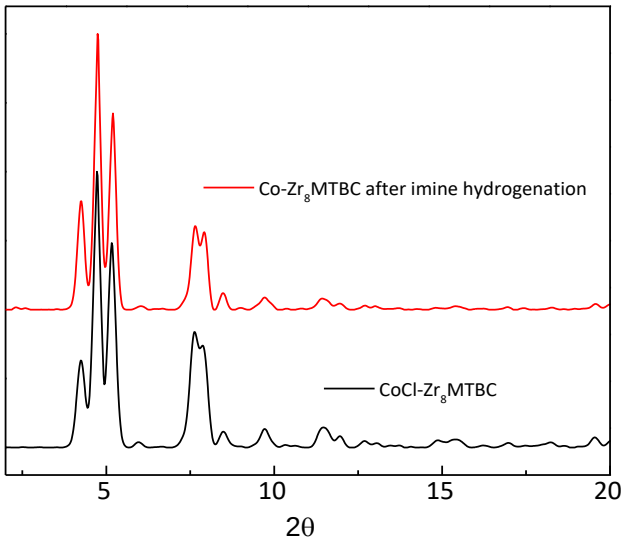

Figure 4-10. PXRD patterns of CoCl-Zr_8MTBC (blue) and CoH-Zr_8MTBC after the hydrogenation of N-benzylidenebenzenamine (red), showing the retention of MOF crystallinity after catalysis.

4.2.5 CoH-Zr_8MTBC catalyzed hydrogenation of arenes

The hydrogenation of heterocycles is challenging for the aromaticity and the catalyst inhibition by both the substrates and hydrogenation products. Most heteroarene hdyrogenation processes suffer from harsh reaction conditions, high catalyst loadings, and requirement of excess additives. Although significant progress has been made in developing precious metal-based molecular and heterogeneous catalysts for selective hydrogenation of N-heteoarenes including

indoles and quinolines, the advancement of the analogous earth abundant-metal catalysts has lagged behind.

Table 4-3. CoH-Zr_8MTBC-catalyzed hydrogenation of heterocycles.

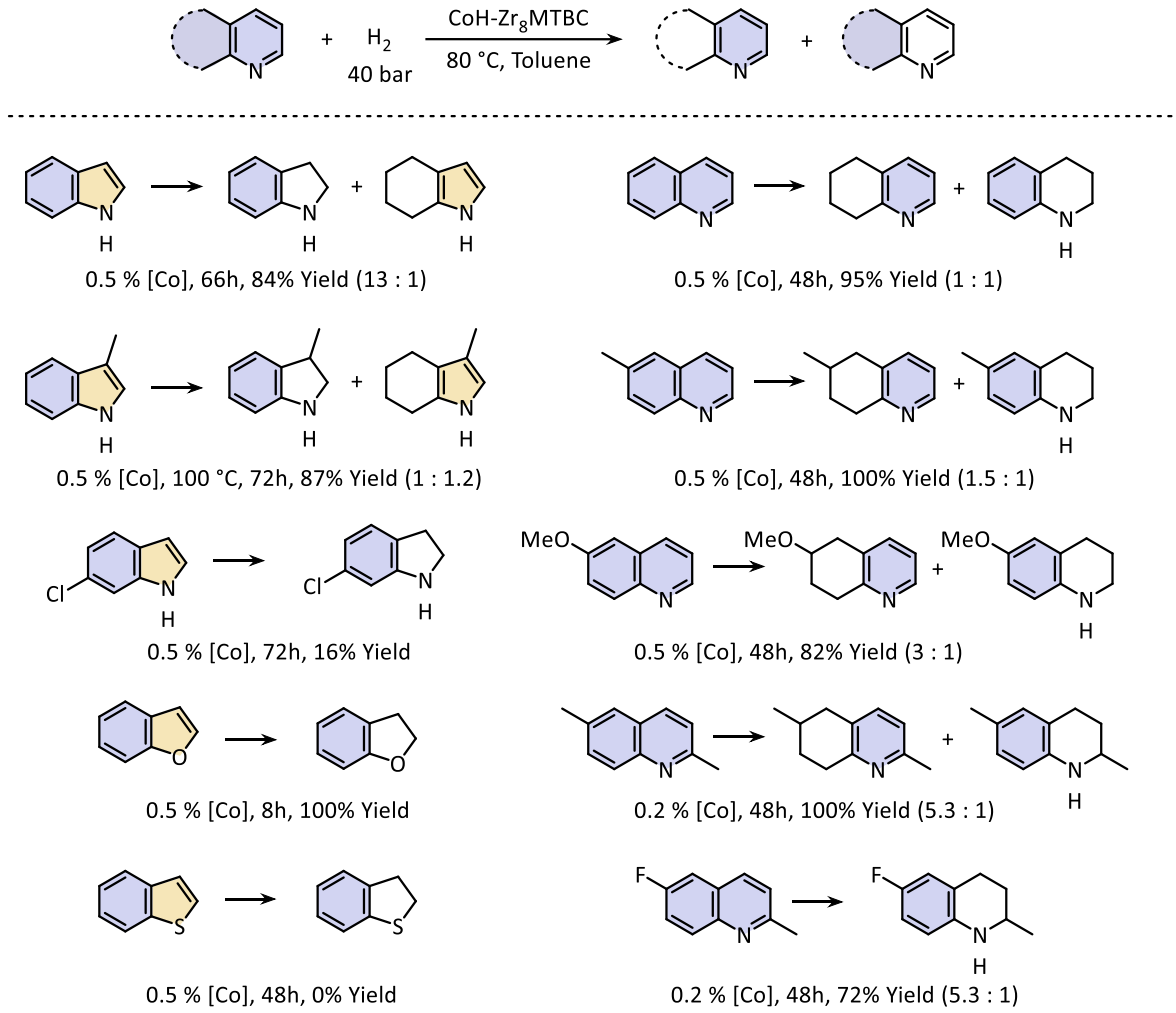

Reaction conditions: 0.25 mg of CoCl-Zr_8MTBC, 5 equiv of $NaBEt_3H$ (1.0 M in THF) w.r.t. Co, alkene, toluene (2 mL), 40 bar H_2, 80 °C; Yields were determined by ^1H NMR with mesitylene as the internal standard.

CoH-Zr_8MTBC is a very active catlayst for hydrogenting various heterocycles (**Table 4-3**). At a 0.5 mol % Co loading, CoH-Zr_8MTBC hydrogenates indole to afford a mixture of indoline and 4,5,6,7-tetrahydroindole at 80 °C. Indoline was obtained in 84% isolated yield after

preparative TLC. Interestingly, hydrogenation of 3-methylindole gave 3-methylindoline and 3-methyl-4,5,6,7-tetrahydroindole in 1:1.2 ratio, which indicates that reduction of the phenyl ring is also possible. The selectivity for the quinoline hydrogenation is highly dependent on the substitution patterns. Quinolines was hydrogenated to afford a mixture of two products, 1,2,3,4-tetrahydroquinoline and 5,6,7,8-tetrahydro-quinoline in a 1:1 ratio. However, the hydrogenation favors the phenyl rings for quinolines with electron-donating substituents at the 6-position. For example, the 6-methylquinoline, 6-methoxyquinoline and 2,6-dimethylquinoline were hydrogenated to give corresponding tetrahydroquinoline with high arene selectivity. In contrast, strong electron-withdrawing substituents disfavor the reduction of the phenyl ring. The 2-methyl-6-fluoro-quinoline was hydrogenated to afford 2-methyl-6-fluoro-1,2,3,4,-tetrahydro-quinoline exclusively in 72% yield. Moreover, CoH-Zr_8MTBC was also a very active catalyst for hydrogenation of benzofuran. At a 0.2 mol % Co loading, benzofuran was completely hydrogenated to 2,3-dihydrobenzofuran in qualitative yield.

4.3 Conclusion

This chapter reports the synthesis of two new Zr_8- and Hf_8-based MOFs featuring previously unknown $M_8(\mu_2\text{-}O)_8(\mu_2\text{-}OH)_4$ SBUs. Benefiting from the unique Zr_2O-Co coordination, open space around the Co center and the site-isolation effect, the MOF node-anchored cobalt-hydride catalyst was highly active in catalyzing the hydrogenation of a broad scope of substrates. Challenging substrates including hindered alkenes, imines, carbonyls, and heterocycles were all hdyrogenated in high yields. The high stability, low cost, and exceptional activity of metal node-supported MOF catalysts make them promising candidates for for industrial application in the synthesis of commodity chemicals, phamaceuticals, and agrochemicals. Our straightforward yet

effective strategy of metalating MOF SBUs with readily available base-metal precursors could be used for the discovery of novel single-site catalysts with unprecedented activity and selectivity.

4.4 Experimental

4.4.1 Synthesis of H_4MTBC ligand

Scheme 4-3. Synthesis of the Me_4MTBC through Suzuki-Miyaura coupling.

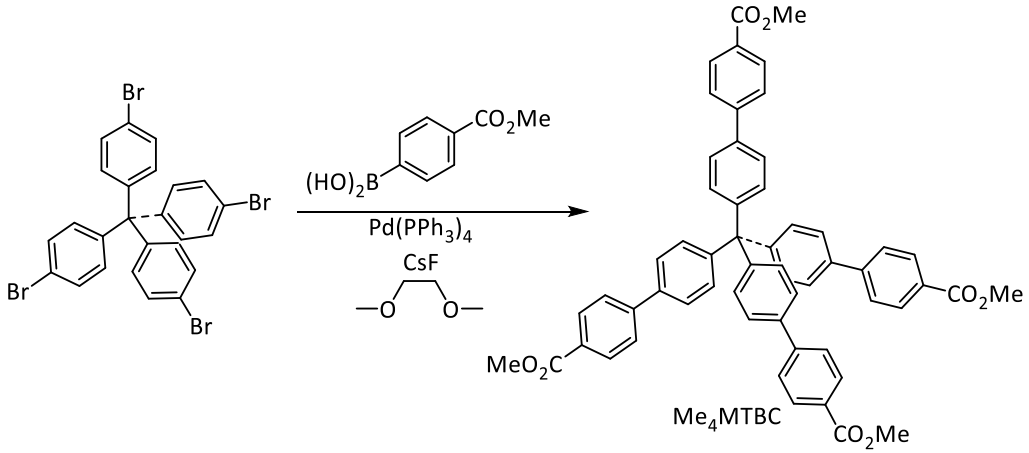

Tetramethyl 4',4''',4'''',4'''''-methanetetrayltetrakis([1,1'-biphenyl]-4-carboxylate) (Me_4-MTBC) was synthesized using a modified procedure from the literature. Tetrakis(4-bromophenyl)methane (723 mg, 1.14 mmol, 1 equiv.), $Pd(PPh_3)_4$ (132 mg, 0.114 mmol, 0.1 equiv.), 4-(methoxycarbonyl)phenylboronic acid (1.23 g, 6.82 mmol, 6 equiv.) and CsF (3.11 g, 20.46 mmol, 18 equiv.) were charged in a 120 mL high-pressure reaction tube and pumped into an N_2 glove box. To the reaction tube was added 60 mL of degassed dimethoxyethane, and the tube was capped and stirred at 85 °C for 3 days. Progress of the reaction was monitored by TLC (1% EtOAc/$CHCl_3$). After cooling to room temperature, the reaction mixture was transferred to a round-bottom flask and evaporated with a rotavap. The resulting solid was dissolved with $CHCl_3$ and filtered through celite to remove CsF and Pd nanoparticles. The filtrate was evaporated with a rotavap, then purified by flash column chromatography on silica gel using 1% EtOAc/Hexane as

eluent to give white solid as pure product (572 mg, 59% yield). ^{1}H NMR (500 MHz, $CDCl_3$): δ 8.10 (d, $^{3}J_{HH}$ = 8.3 Hz, 8 H), 7.68 (d, $^{3}J_{HH}$ = 8.3 Hz, 8 H), 7.59 (d, $^{3}J_{HH}$ = 8.4 Hz, 8 H), 7.44 (d, $^{3}J_{HH}$ = 8.5 Hz, 8 H), 3.94 (s, 12 H).

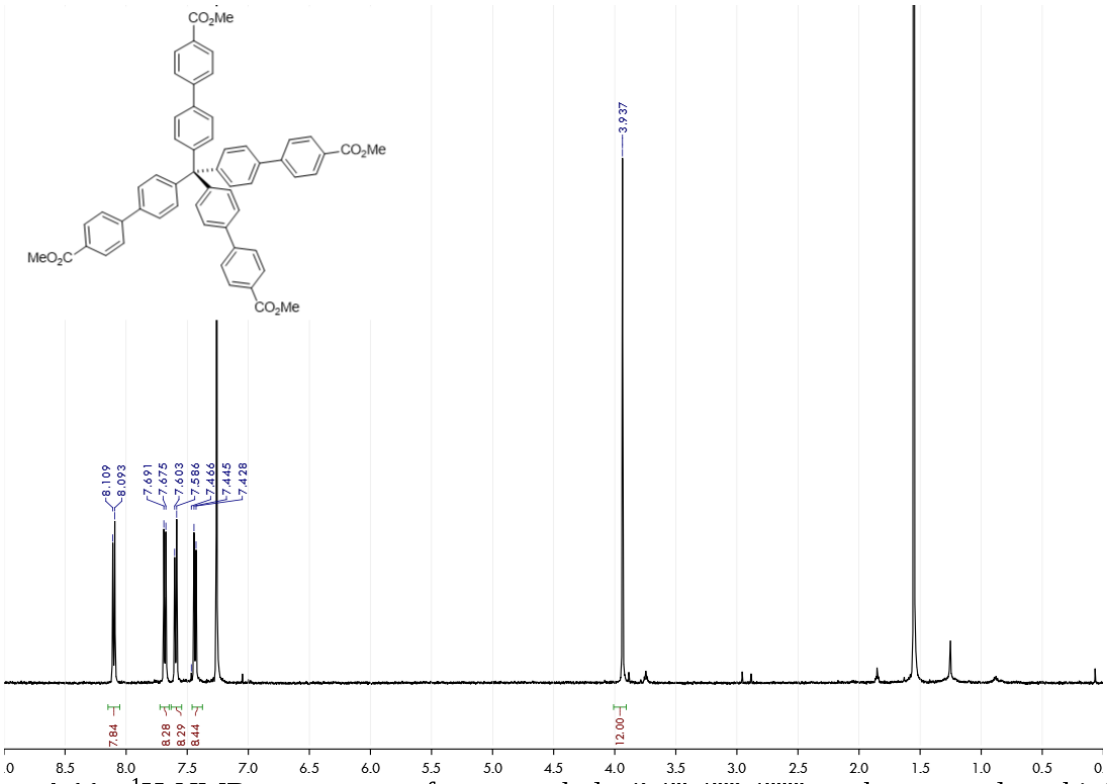

Figure 4-11. ^{1}H-NMR spectrum of tetramethyl 4',4''',4'''''',4''''''''-methanetetrayltetrakis([1,1'-biphenyl]-4-carboxylate) in $CDCl_3$.

Scheme 4-4. Synthesis of the H_4MTBC through base-mediated hydrolysis.

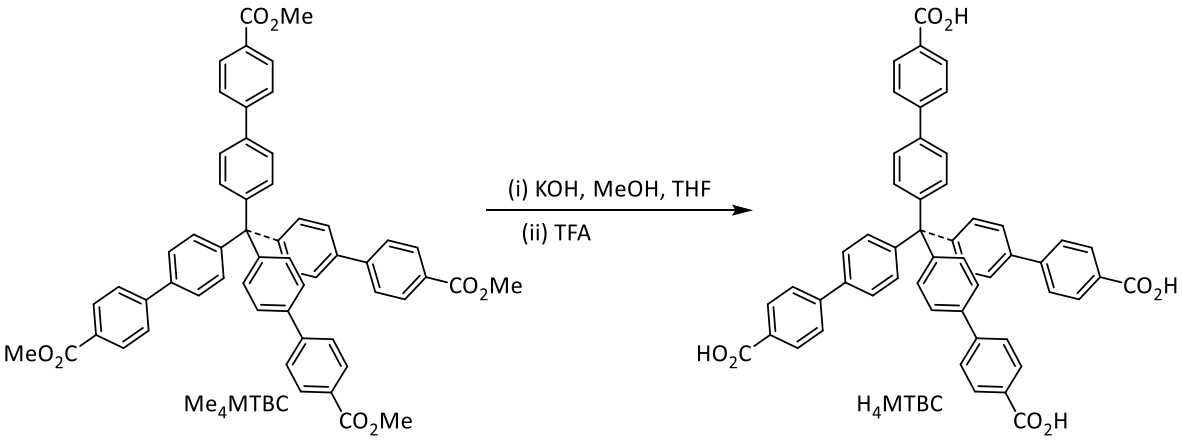

Me_4MTBC (367 mg, 0.428 mmol) was suspended in THF (65 mL). A solution of KOH (6.17 g, 110 mmol) dissolved in MeOH (20 mL) was then added, and the reaction mixture was stirred at 60 ºC for 24 h. The suspension was cooled to room temperature and the resulting precipitate was collected by centrifugation. The solution was washed with dry THF (20 mL) and recollected by centrifugation. The solid was suspended in THF (20 mL) and trifluoroacetic acid (3 mL) was slowly added and stirred for 1.5 h at room temperature. H_2O (15 mL) was then added, and the white solid was isolated by centrifugation, subsequently washed with THF and Et_2O, and dried in vacuo to obtain 4',4''',4'''',4'''''-methanetetrayltetrakis(([1,1'-biphenyl]-4-carboxylic acid)) (H_4MTBC, 331.9 mg, 1.04 mmol, 86% yield) as a pale-white solid. ^{1}H NMR (500 MHz, DMSO-d_6): δ 12.98 (s, 4 H), 8.02 (dd, $^3J_{HH}$ = 12.6, $^4J_{HH}$ = 8.4 Hz, 8 H), 7.84 (dd, $^3J_{HH}$ = 16.9, $^4J_{HH}$ = 8.3 Hz, 8 H), 7.78 (dd, $^3J_{HH}$ = 8.5, $^4J_{HH}$ = 4.3 Hz, 8 H), 7.43 (d, $^3J_{HH}$ = 7.9 Hz, 8 H).

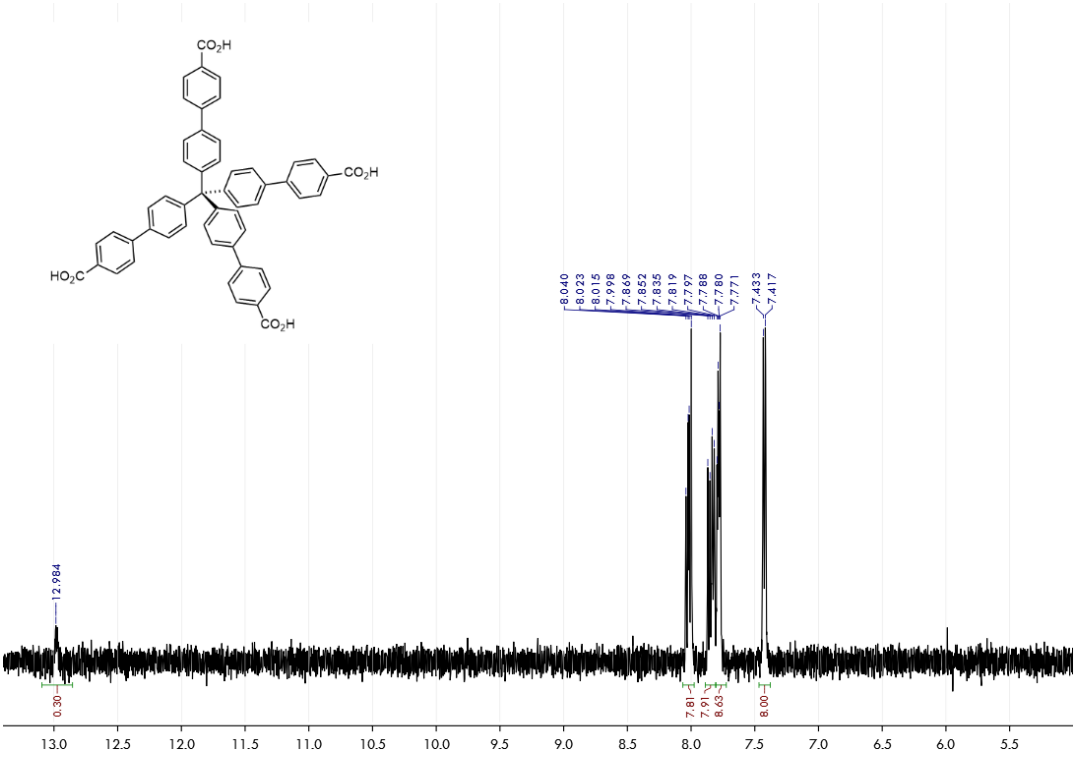

Figure 4-12. ^{1}H-NMR spectrum of H_4MTBC in DMSO-d_6.

4.4.2 Synthesis and characterization of Zr_8MTBC

Zr_8MTBC was synthesized in 54% yield via a solvothermal reaction between $ZrCl_4$ and H_4MTBC in DEF using benzoic acid as modulator. The detailed experimental procedure was described below:

To a 50 mL flask was added $ZrCl_4$ (91.0 mg, 0.390 mmol), H_4MTBC (80 mg, 0.1 mmol), benzoic acid (2.77 g, 22.7 mmol), and DEF (16 mL, 6.25 mM to H_4MTBC). The mixture was sonificated for 5 min until all solids were dissolved. The 16 mL solution obtained was heated at 120 ^oC on a hotplate and stirred at 250 rpm for 24 h. The amount of Zr_8MTBC (90 mg, 87% yield) was determined after drying MOF on a filter paper. PXRD pattern of the obtained MOF was compared to that of a simulated pattern from a single crystal structure to show the good crystallinity of the Zr_8MTBC. Hf_8MTBC was also obtained using analogous method.

SXRD study of Zr_8MTBC indicated that Zr_8MTBC crystallizes in the cubic pm-3n space group and revealed the presence of two types of SBUs, $Zr_8(\mu_2\text{-}O)_8(\mu_2\text{-}OH)_4$ and the $Zr_6(\mu_3\text{-}O)_4(\mu_3\text{-}OH)_4$ in 1:3 ratio (**Figure 4-13**). The void space was calculated to be 73.53% by PLATON. The MOF possessed two kinds of trigonal-bipyramid cavities of dimensions 24.9 Å × 21.6 Å × 35.9 Å and 20.8 Å × 20.8 Å × 13.1 Å, respectively.

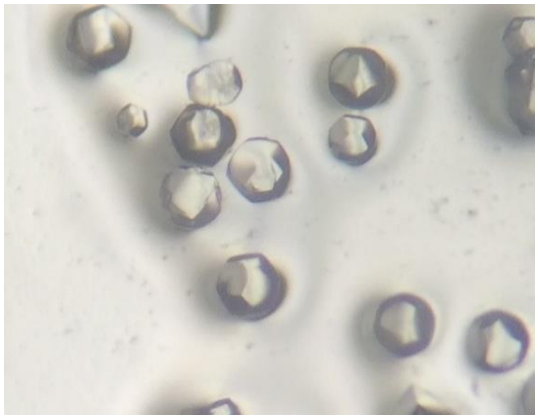

Figure 4-13. Zr_8MTBC Single crystal used for determining crystal structure under optical microscope.

Table 4-4. Crystallographic information of Zr_8MTBC and Hf_8MTBC.

Name	**Zr_8MTBC**	**Hf_8MTBC**
Formula	$C_{318}H_{144}O_{66}Zr_{13}$	$C_{318}O_{66}Hf_{13}$
Fw	6206.19	7195.55
Temperature (K)	100	100
Wavelength (Å)	0.41328	0.668
Crystal system	Cubic	Cubic
Space group	$Pm\bar{3}n$	$Pm\bar{3}n$
***a*, Å**	41.512(4)	41.516(2)
***b*, Å**	41.512(4)	41.516(2)
***c*, Å**	41.512(4)	41.516(2)
α, °	90	90
β, °	90	90
γ, °	90	90
***V*, Å^3**	71535.21	71556.10
Z	4	4
Density (calcd. g/cm^3)	0.576	0.668
Absorption coeff. (mm^{-1})	0.287	0.460
F(000)	12400.0	13488.0
θ range data collection	1.097 – 26.396	0.638 – 13.369
Limiting indices	-44<=h<=50 -36<=k<=51 -50<=l<=50	-43<=h<=46 -34<=k<=46 -46<=l<=45
Reflection collected	12692	9175
Independent reflections	6116	7375
R(int)	0.257	0.169
Data/restraints/parameters	12692/621/298	9175/623/310
Goodness-of-fit on F^2	1.122	1.244
Final R indices [I>2σ(I)]	R1=0.1276, wR2=0.3136	R1=0.1145, wR2=0.2758
R indices (all data)	R1=0.2586, wR2=0.3628	R1=0.1540, wR2=0.3046

Single crystal X-ray diffraction of M_8MTBC was performed with a Bruker APEX II CCD-based detector at ChemMatCARS (Sector 15), Advanced Photon Source (APS), Argonne National Laboratory. Data were scaled and corrected for absorption effects using the multi-scan procedure as implemented in SADABS (Bruker AXS, version 2014/5, 2015, part of Bruker APEX3 software

package). The structure was solved by SHELXT (Version 2014/5)[19] and refined by a full-matrix least-squares procedure using OLEX2[20] software packages (XL refinement program version 2014/7)[21]. Crystallographic data and details of the data collection and structure refinement are listed in **Table 4-4**.

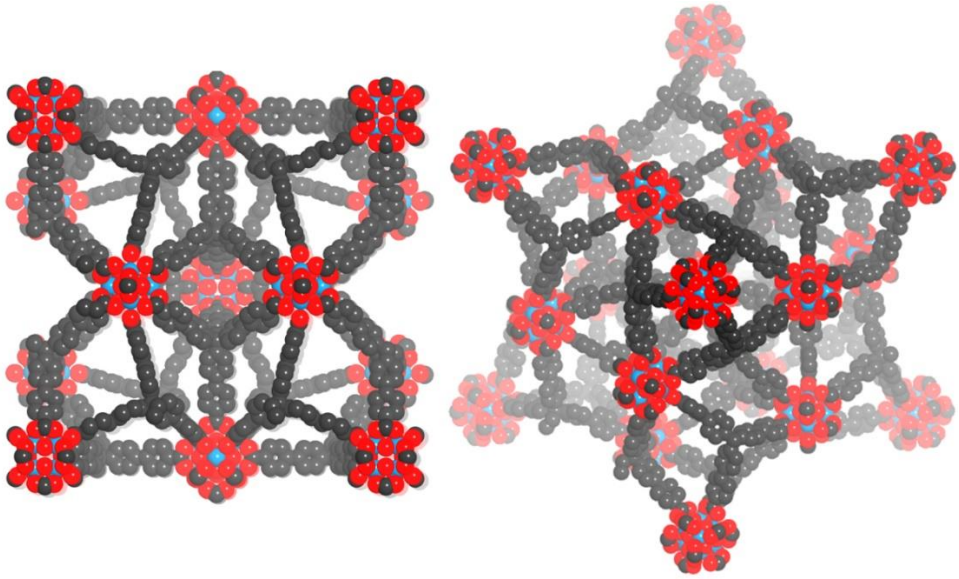

Figure 4-14. Space-filling models of Zr_8MTBC, as viewed along [100] (left), [111] (right). Zr_8-SBUs occupy corners and body center of unit cell; Zr_6 SBUs occupy faces of unit cell.

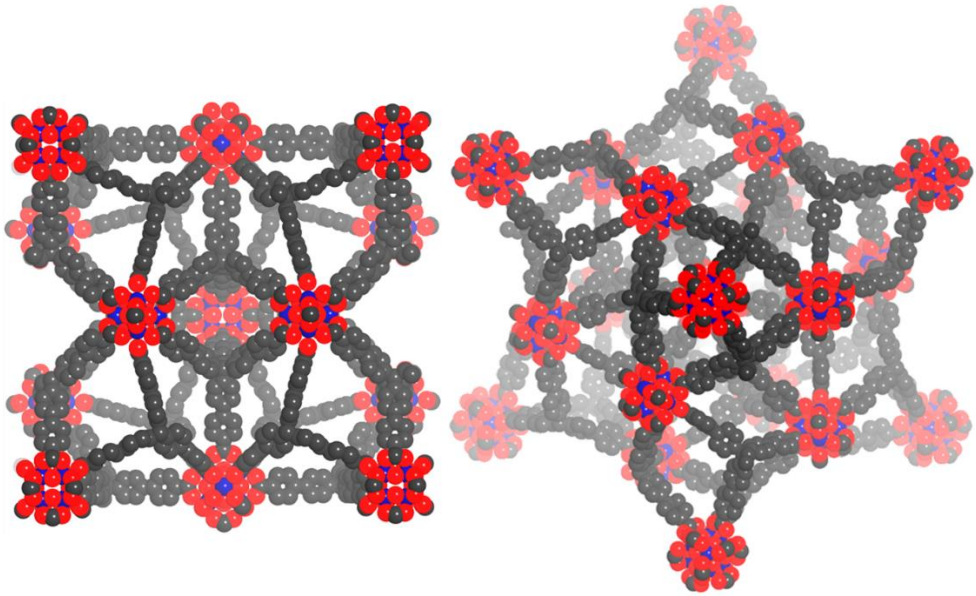

Figure 4-15. Space-filling models of Hf_8MTBC. The structure is identical to Zr_6MTBC except minor difference in SBU bond distances.

To our knowledge, the octameric $Zr_8(\mu_2\text{-}O)_8(\mu_2\text{-}OH)_4$ SBU has not been synthesized before as a discrete cluster or as a structural unit in a MOF. In the $Zr_8(\mu_2\text{-}O)_8(\mu_2\text{-}OH)_4$ SBU, eight Zr^{IV} ions occupy the eight corners of the cube, while eight μ_2-oxo and four μ_2-OH occupy the twelve edges of the cube. The $Zr_6(\mu_3\text{-}O)_4(\mu_3\text{-}OH)_4$ unit is isostructural to the SBU of UiO-type MOFs, with six Zr^{IV} ions occupying six corners of an octahedron that are held together by four μ_3-oxo and four μ_3-OH groups at eight faces of the octahedron (**Figure 4-16**).

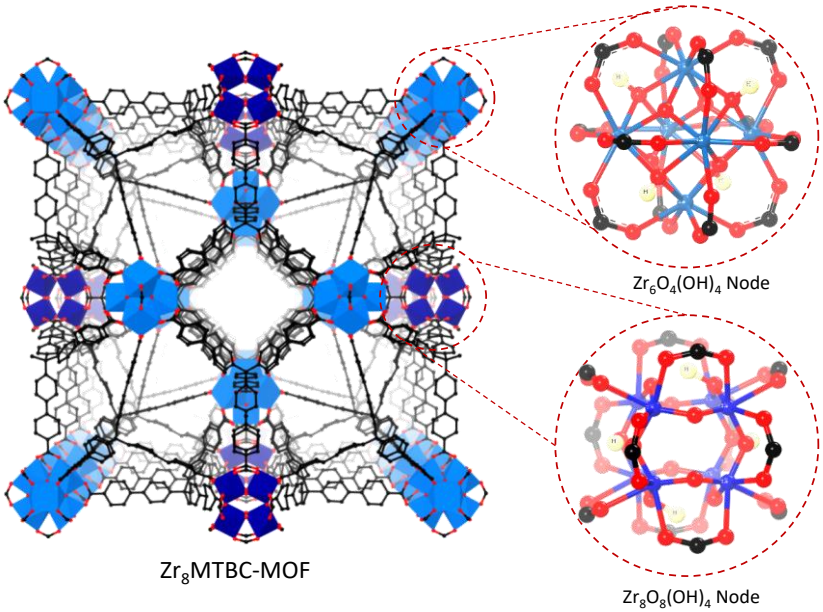

Figure 4-16. SBU composition of Zr_8MTBC and the detailed coordination environment of $Zr_8O_8(OH)_4$ node.

IR spectrum of the solid MOF sample showed the presence of both the μ_2O-H stretching band at 3737 cm^{-1} and μ_3O-H stretching band at 3639 cm^{-1} (**Figure 4-17**). N_2 sorption isotherm of Zr_8MTBC showed a type I adsorption with BET surface area of 3700 m^2/g (**Figure 4-18**).

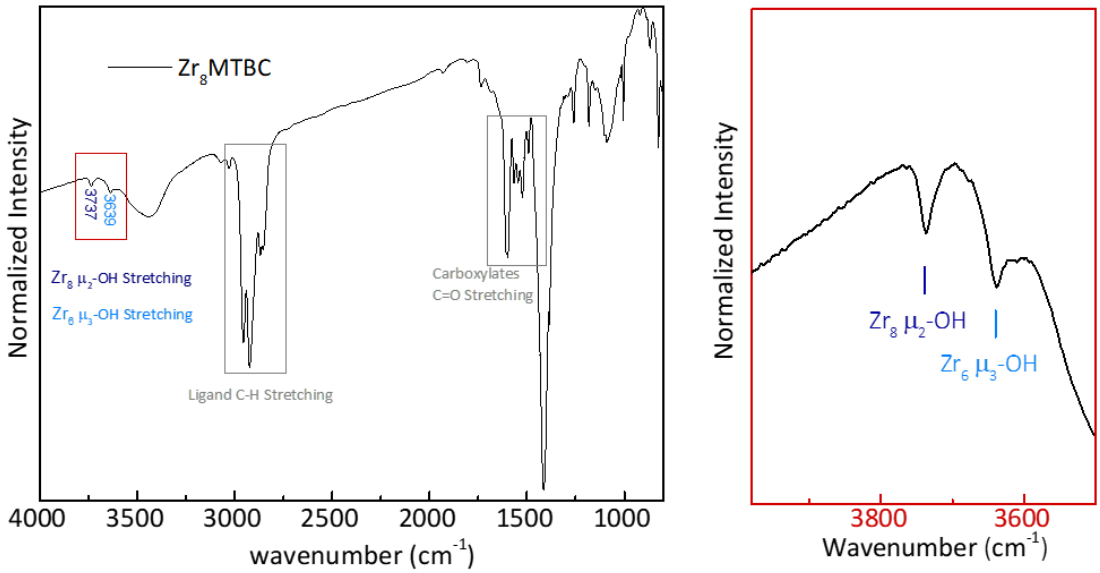

Figure 4-17. IR spectrum of freshly prepared Zr_8MTBC. Peaks of O-H stretching from MOF SBU was clearly observed, including the Zr_6 cluster μ_3-OH stretching at 3639 cm^{-1}, and the Zr_8 cluster μ_2-OH stretching at 3737 cm^{-1}. The expected ligand C-H peak and coordinated carboxylate peaks were also observed.

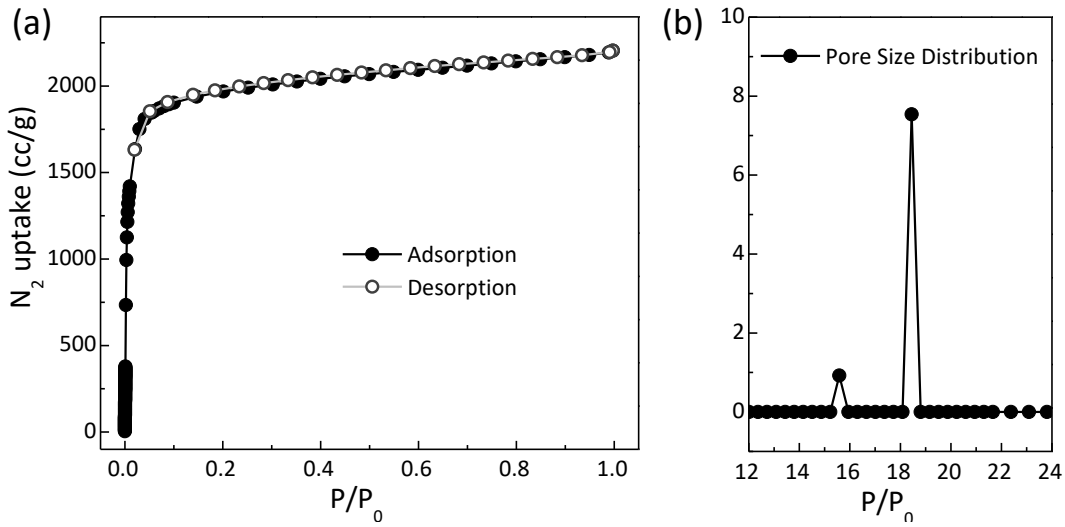

Figure 4-18. N_2 sorption isotherm (a) and pore size distribution (b) of Zr_8MTBC.

SEM and TEM images showed cubic particles of 1-3 μm in length (**Figure 4-19**). The Hf_8MTBC analog was synthesized similarly and characterized by single-crystal X-ray diffraction.

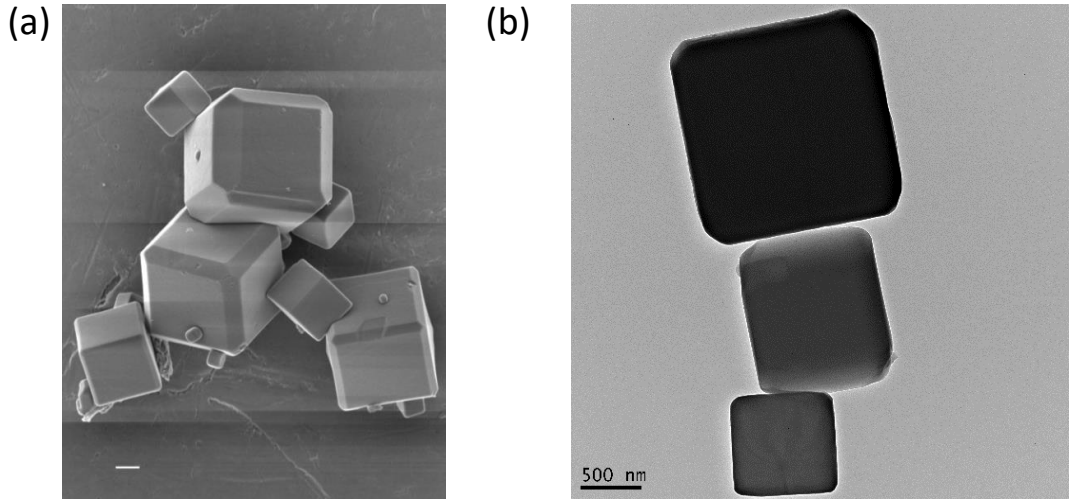

Figure 4-19. SEM image (a) and TEM image (b) of Zr_8MTBC synthesized from stirring method. The scale bar is 1 μm and 500 nm for SEM and TEM respectively.

TGA was used to study the thermal stability and validate the chemical composition of Zr_8MTBC (**Figure 4-20**). The first weight loss (57.4%) in the 25 - 420 °C temperature range corresponds to removal of adsorbed solvents in the pores. The second weight loss (74.7%) in the 420 - 800 °C temperature range corresponds to decomposition of the MOF to ZrO_2, consistent with a calculated weight loss of 74.5% based on $[Zr_6O_4(OH)_4(L)_3]_6[Zr_8O_8(OH)_4(L)_3]_2$ to $(ZrO_2)_{52}$.

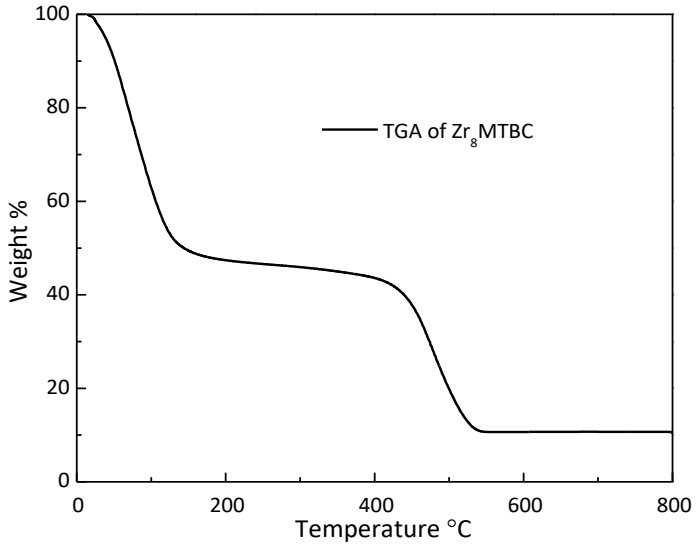

Figure 4-20. TGA curves of freshly prepared Zr_8MTBC in the 25 ~ 800 °C range.

4.4.3 Synthesis and characterization of Zr_8MTBC

In a glovebox, Zr-MTBC (45 mg) in 4 mL THF was cooled to -30 °C for 30 min. To the cold suspension, *n*BuLi (2.5 M in hexanes, 0.2 mL, 10 equiv. to μ_2-OH) was added dropwise and the resultant light green-yellow mixture was stirred slowly overnight at room temperature. The light-yellow solid was collected after centrifugation, and washed with THF 5-6 times over 6 h. Then, the lithiated Zr-MTBC was transferred to a vial containing 4 mL THF solution of $CoCl_2$ (10.1 mg, 1.5 equiv. to μ_2-OLi). The mixture was stirred for 15 h and the deep blue solid was then centrifuged and washed with THF 5-8 times. The metalated MOFs were stored in THF in the glovebox for further use.

4.4.4 CoH-Zr_8MTBC catalyzed alkene hydrogenation

In a glovebox, a vial was charged with Zr-MTBC-CoCl (0.5 mg, 0.1 mol % Co) in 1 mL THF. 14 µL $NaBEt_3H$ (1.0 M in THF) was added to the vial and the mixture was stirred slowly for 1 h in the glovebox. The solid was centrifuged out of suspension and washed with THF two times. Then, the solid in 1.0 mL THF was transferred to a vial and 1-cyclohexene (59 µL, 0.50 mmol) was added. The vial was placed into a Parr pressure reactor in a nitrogen-filled glovebox. The reactor was then pressurized to 40 bar. After 2 d, hydrogen was released and the solid was centrifuged out of suspension and extracted two times with THF in the glovebox. Quantitative yield of methylcyclohexane was obtained as determined by ^{1}H NMR with mesitylene as the internal standard.

4.5 References

1. Johnson, N. B.; Lennon, I. C.; Moran, P. H.; Ramsden, J. A., Industrial-Scale Synthesis and Applications of Asymmetric Hydrogenation Catalysts. *Acc. Chem. Res.* **2007,** 1291-1299.

2. Knowles, W. S.; Noyori, R., Pioneering Perspectives on Asymmetric Hydrogenation. *Acc. Chem. Res.* **2007,** 1238-1239.

3. Saudan, L. A., Hydrogenation Processes in the Synthesis of Perfumery Ingredients. *Acc. Chem. Res* **2007,** 1309-1319.

4. Mallat, T.; Orglmeister, E.; Baiker, A., Asymmetric Catalysis at Chiral Metal Surfaces. *Chem. Rev.* **2007,** 4863-4890.

5. Zhang, W.; Chi, Y.; Zhang, X., Developing Chiral Ligands for Asymmetric Hydrogenation. *Acc. Chem. Res.* **2007,** 1278-1290.

6. Wang, D.-S.; Chen, Q.-A.; Lu, S.-M.; Zhou, Y.-G., Asymmetric Hydrogenation of Heteroarenes and Arenes. *Chem. Rev.* **2012,** 2557-2590.

7. Chirik, P.; Morris, R., Getting Down to Earth: The Renaissance of Catalysis with Abundant Metals. *Acc. Chem. Res.* **2015,** 2495-2495.

8. Bart, S. C.; Lobkovsky, E.; Chirik, P. J., Preparation and Molecular and Electronic Structures of Iron(0) Dinitrogen and Silane Complexes and Their Application to Catalytic Hydrogenation and Hydrosilation. *J. Am. Chem. Soc.* **2004,** 13794-13807.

9. Casey, C. P.; Guan, H., An Efficient and Chemoselective Iron Catalyst for the Hydrogenation of Ketones. *J. Am. Chem. Soc.* **2007,** 5816-5817.

10. Mikhailine, A.; Lough, A. J.; Morris, R. H., Efficient Asymmetric Transfer Hydrogenation of Ketones Catalyzed by an Iron Complex Containing a P−N−N−P Tetradentate Ligand Formed by Template Synthesis. *J. Am. Chem. Soc.* **2009,** 1394-1395.

11. Nakazawa, H.; Itazaki, M., Fe–H Complexes in Catalysis. In *Iron Catalysis: Fundamentals and Applications*, Plietker, B., Ed. Springer Berlin Heidelberg: Berlin, Heidelberg, 2011; pp 27-81.

12. Chakraborty, S.; Dai, H.; Bhattacharya, P.; Fairweather, N. T.; Gibson, M. S.; Krause, J. A.; Guan, H., Iron-Based Catalysts for the Hydrogenation of Esters to Alcohols. *J. Am. Chem. Soc.* **2014,** 7869-7872.

13. Chakraborty, S.; Bhattacharya, P.; Dai, H.; Guan, H., Nickel and Iron Pincer Complexes as Catalysts for the Reduction of Carbonyl Compounds. *Acc. Chem. Res* **2015,** 1995-2003.

14. Li, Y.-Y.; Yu, S.-L.; Shen, W.-Y.; Gao, J.-X., Iron-, Cobalt-, and Nickel-Catalyzed Asymmetric Transfer Hydrogenation and Asymmetric Hydrogenation of Ketones. *Acc. Chem. Res* **2015,** 2587-2598.

15. Morris, R. H., Exploiting Metal–Ligand Bifunctional Reactions in the Design of Iron Asymmetric Hydrogenation Catalysts. *Acc. Chem. Res* **2015,** 1494-1502.

16. Stalzer, M. M.; Nicholas, C. P.; Bhattacharyya, A.; Motta, A.; Delferro, M.; Marks, T. J., Single-Face/All-cis Arene Hydrogenation by a Supported Single-Site d0 Organozirconium Catalyst. *Angew. Chem. Int. Ed.* **2016,** 5263-5267.

17. Chen, F.; Surkus, A.-E.; He, L.; Pohl, M.-M.; Radnik, J.; Topf, C.; Junge, K.; Beller, M., Selective Catalytic Hydrogenation of Heteroarenes with N-Graphene-Modified Cobalt Nanoparticles (Co3O4–Co/NGr@α-Al2O3). *J. Am. Chem. Soc.* **2015,** 11718-11724.

18. Zhang, G.; Scott, B. L.; Hanson, S. K., Mild and Homogeneous Cobalt-Catalyzed Hydrogenation of C□C, C□O, and C□N Bonds. *Angew. Chem. Int. Ed.* **2012,** 12102-12106.

19. Sheldrick, G., Crystal structure refinement with SHELXL. *Acta Cryst. C* **2015,** 3-8.

20. Dolomanov, O. V.; Bourhis, L. J.; Gildea, R. J.; Howard, J. A. K.; Puschmann, H., OLEX2: a complete structure solution, refinement and analysis program. *J. Appl. Crystallogr.* **2009,** 339-341.

21. Sheldrick, G., A short history of SHELX. *Acta Cryst. A* **2008,** 112-122.

22. Manna, K.; Eedugurala, N.; Sadow, A. D., Zirconium-Catalyzed Desymmetrization of Aminodialkenes and Aminodialkynes through Enantioselective Hydroamination. *J. Am. Chem. Soc.* **2015,** 425-435.

Chapter 5. Site-Isolated Cobalt Catalysts at New $Zr_{12}(\mu_3\text{-}O)_8(\mu_3\text{-}OH)_8(\mu_2\text{-}OH)_6$ MOF Nodes for Highly Active Hydrogenation

5.1 Introduction

This chapter will discuss the synthesis of Zr_{12}-TPDC, a robust and porous MOF constructed from H_2TPDC and an unprecedented SBU with the formula of $Zr_{12}(\mu_3\text{-}O)_8(\mu_3\text{-}OH)_8(\mu_2\text{-}OH)_6$. The Zr_{12} SBU can be viewed as an inorganic node dimerized from a pair of common Zr_6 clusters via six bridging μ_2-OH groups. The metalation of Zr_{12}-TPDC SBUs with $CoCl_2$ followed by $NaBEt_3H$ treatment afforded CoH-Zr_{12}TPDC as a highly active and reusable solid catalyst for hydrogenating nitroarenes, nitriles, and isocyanides to the corresponding amines in excellent activity and selectivity.

Compared to MOFs constructed from other metals, Zr-based MOFs have distinguished themselves with exceptional stability, modular linkers, and high abundance of the zirconium precursors.[1-8] The last two chapters discussed the $Zr_6O_4(\mu_3\text{-}OH)_4$ and $Zr_8O_8(\mu_2\text{-}OH)_4$ SBUs as excellent sites for anchoring uniform catalysts that do not have homogenous analogues. The Zr_6TPDC SBUs supported a unique cone-shaped secondary environment around the metal centers that cannot be easily enforced in molecular catalysts. Furthermore, we discovered that the activity and selectivity of the anchored catalysts were exquisitely sensitive to the subtle steric and electronic changes in Zr-SBUs. For example, the CoH-Zr_8 catalyst is more effective than CoH-Zr_6 in hydrogenating hindered alkenes, imines, and heterocycles, as a result of having a more electron-rich and sterically open Co catalyst. This chapter highlights a novel $Zr_{12}O_8(\mu_3\text{-}OH)_8(\mu_2\text{-}OH)_6$ node

which features unique pair-site bridging-hydroxide structure as an effective catalyst support (**Figure 5-1**).

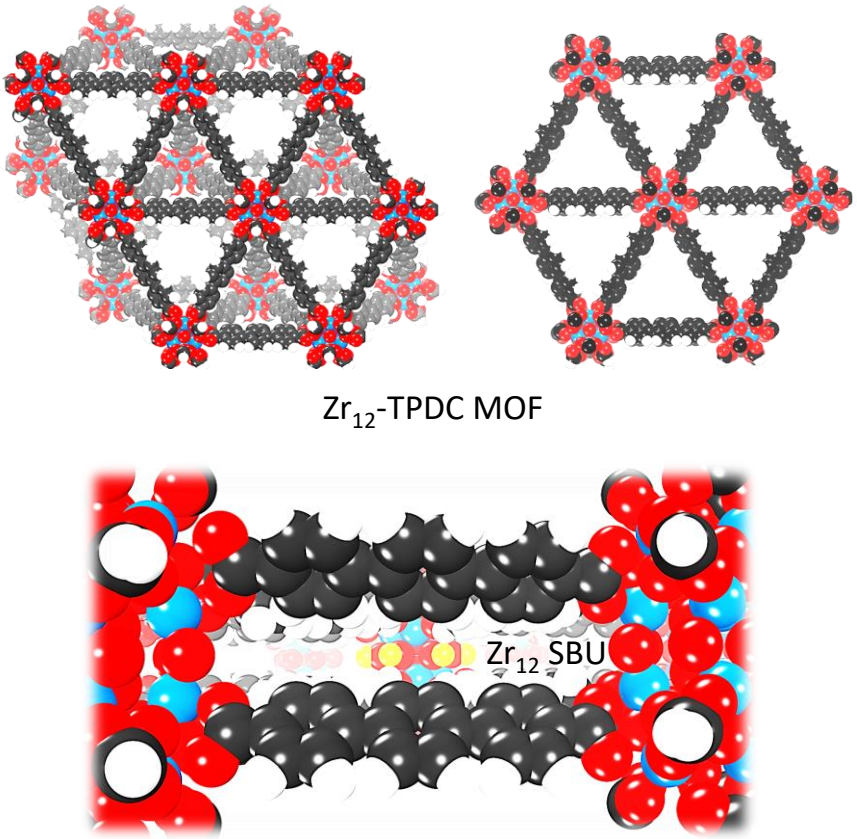

Figure 5-1. (a) Depiction of the structure of Zr_{12}TPDC MOF. (b) Space-filling model of the bridging hydroxide sites in Zr_{12} SBU.

The Zr_3OH group in Zr_6 SBU or the Zr_2OH group in Zr_8 SBUs only function as monoanionic ligands with one strongly-coordinating hydroxide. In contrast, the Zr_{12} SBU contains a pair of proximal Zr_2OH sites with mutual distance of around 3.0 Å. This pair-site Zr_2OH functionality in Zr_{12} SBU allows for the chelation of a metal species to form a more stable and electron-rich catalyst (**Figure 5-2**).

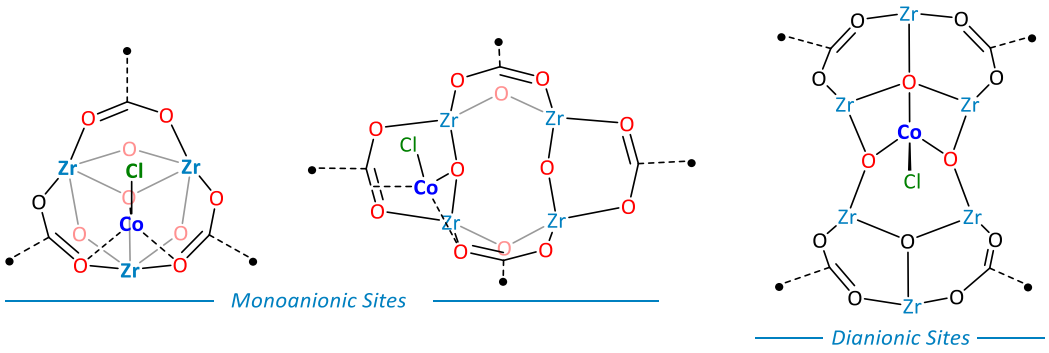

Figure 5-2. Chemical structures of the Co coordination environments in Zr_6 SBU, Zr_8 SBU and Zr_{12} SBU.

5.2 Results and Discussion

5.2.1 Synthesis and characterization of Zr_{12}TPDC

Zr_{12}-TPDC was synthesized from a solvothermal reaction of $ZrCl_4$ with H_2TPDC in DMF and water at 90 °C using acetic acid as the modulator. Detailed synthetic procedure and characterization are discussed in the experimental section. Crystal structure of the Zr_{12}-MOF was simulated based on a combination of the crystal structures of the small molecular Zr_{12} cluster and Zr_6TPDC. The space group was selected to be the hexagonal *P6₃/mmc*, which is the space group of highest symmetry based on the systematic absences. This structural assignment was supported by the similarity between the simulated PXRD with the experimental one (**Figure 5-3**). The Zr coordination environment in the Zr_{12} SBU was also studied by EXAFS. A good fit with an R-factor of 0.008 was obtained based on the Zr_{12} cluster crystal structure.

TGA analysis showed a weight loss of 65.5% in the 240 °C to 800 °C range, corresponding well to the decomposition of $Zr_{12}O_8(\mu_3\text{-}OH)_8(\mu_2\text{-}OH)_6(TPDC)_9$ to $(ZrO_2)_{12}$ (65.7% expected). The observed weight loss is much smaller than that of Zr_6TPDC (71.3%) due to the increased Zr weight percentage in Zr_{12}TPDC (**Figure 5-17**). The first weight loss (20.0%) in the 20 to 240 °C

temperature range corresponds to removal of adsorbed solvents in the pores. The second weight loss (65.5%) in the 240 - 800 °C temperature range corresponds to the decomposition of the MOF to ZrO_2, consistent with a calculated weight loss of 65.7% based on the conversion of $Zr_{12}O_8(\mu_3\text{-}OH)_8(\mu_2\text{-}OH)_6(TPDC)_9$ to $(ZrO_2)_{12}$.

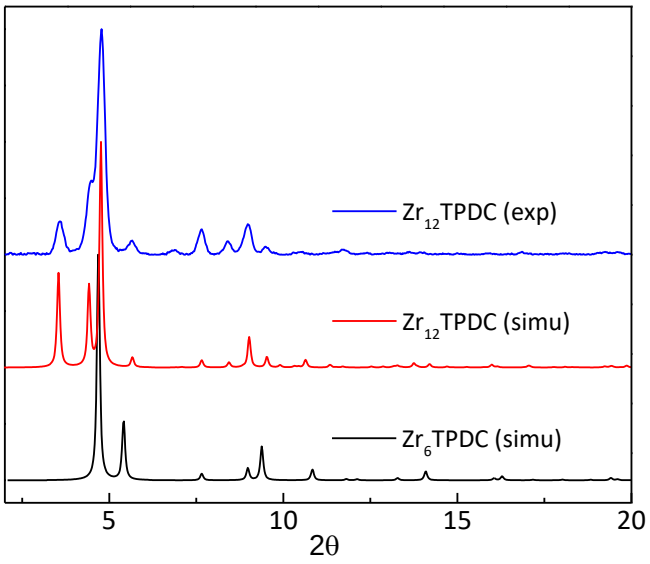

Figure 5-3. The experimental PXRD pattern of Zr_{12}TPDC (blue) is similar to the simulated PXRD of Zr_{12}TPDC (red), but very different from the simulated PXRD of Zr_6TPDC (black).

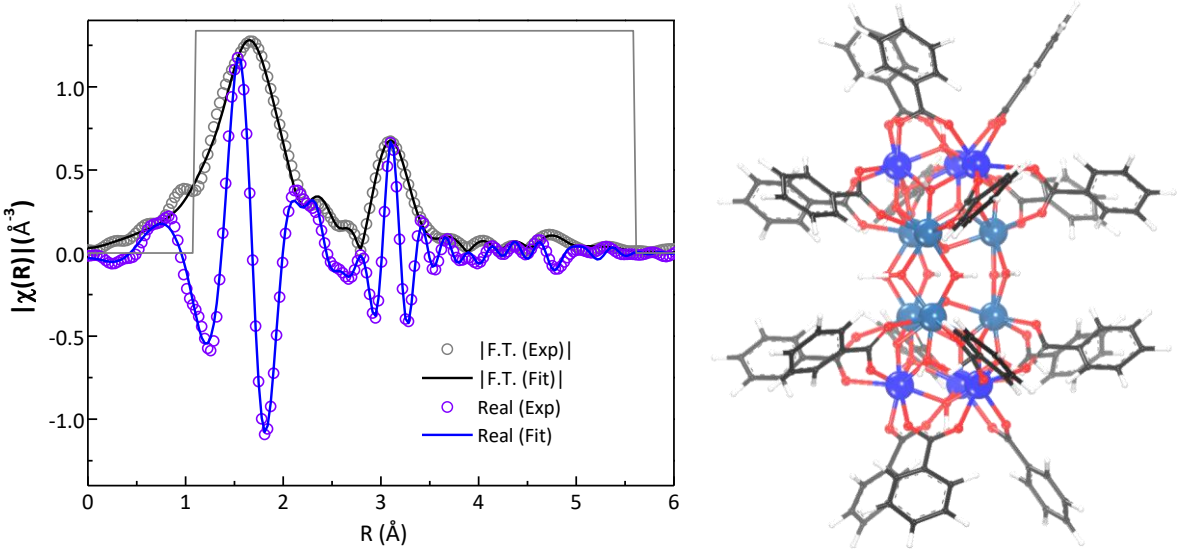

Figure 5- 4. EXAFS fitting of Zr coordination environment in Zr_{12}TPDC. Two types of Zr centers coexist in this structure.

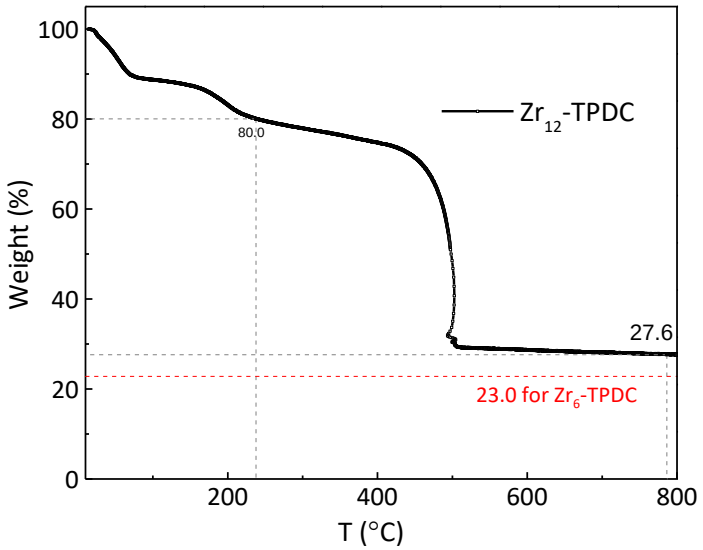

Figure 5-5. TGA curve of freshly prepared Zr_{12}TPDC in the 25 ~ 800 °C range. The red line shows the remaining ZrO_2 weight percentage expected for Zr_{12}TPDC.

N_2 sorption isotherm of Zr_{12}TPDC showed a type I adsorption (77K, 1 bar) with BET surface area of 1967 m^2/g (**Figure 5-6**). The surface area of Zr_{12}TPDC is smaller than that of Zr_6TPDC (2815 m^2/g) due to the increased molecular weight of SBUs and similar pore shape and size.

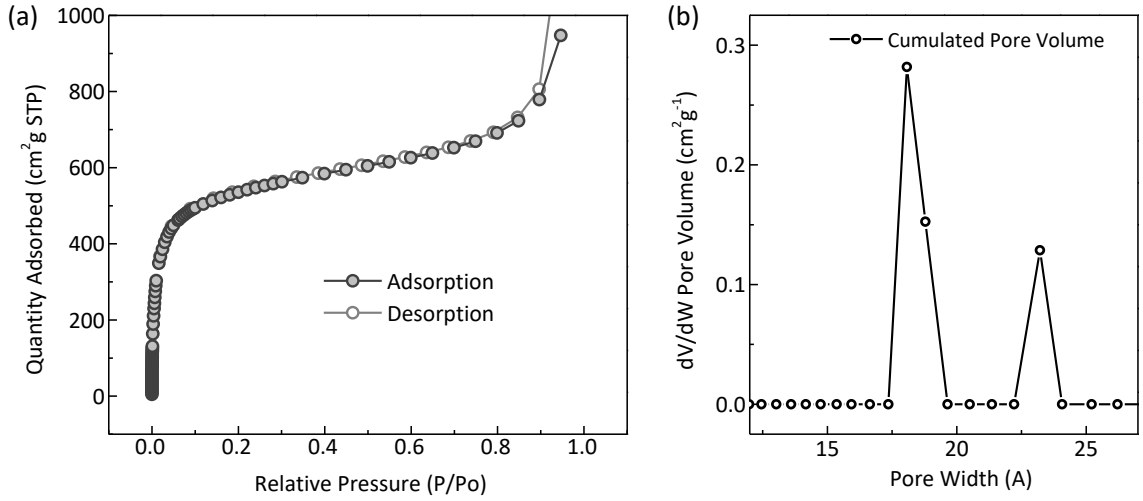

Figure 5-6. (a) Nitrogen sorption isotherms of Zr_{12}TPDC (77 K). Zr_{12}-TPDC has a BET surface areas of 1967 m^2/g. (b) Pore size distributions of Zr_{12}TPDC showing existence of two kinds of pores of 18 Å and 23 Å in diameters.

5.2.2 Synthesis and characterization of CoCl-Zr_{12}TPDC

Zr_{12}TPDC was metalated with $CoCl_2$ by first treating with 5 equiv. of $LiCH_2SiMe_3$ to deprotonate both the μ_2-OH and μ_3-OH groups in the Zr_{12} SBU, then reacting with $CoCl_2$ in THF to afford CoCl-Zr_{12}TPDC as a deep-blue solid (**Figure 5-7**).

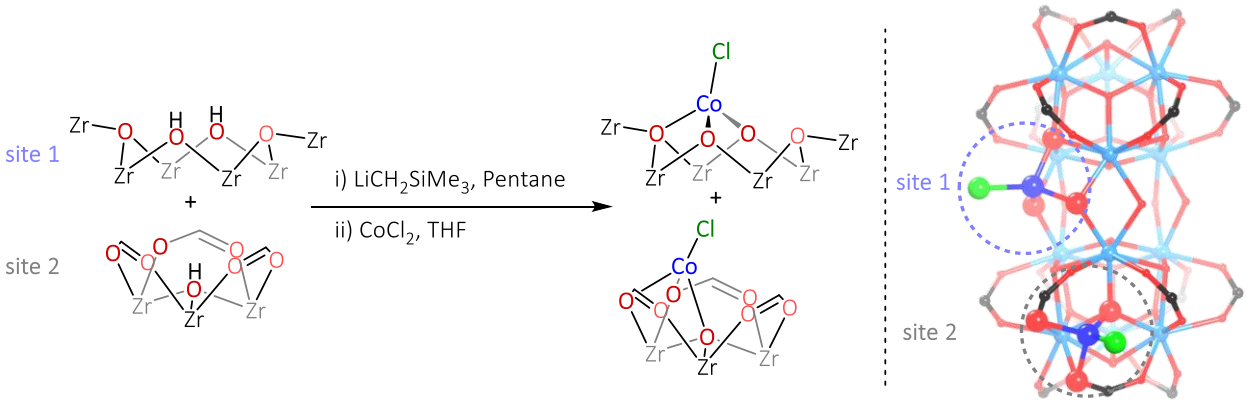

Figure 5-7. Metalation of Zr_{12} SBU in Zr_{12}TPDC through sequential deprotonation and metalation.

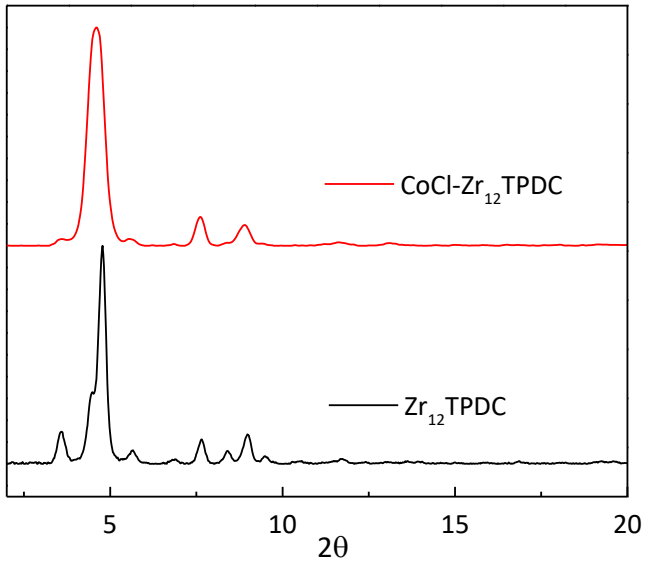

Figure 5-8. The PXRD pattern of CoCl-Zr_{12}TPDC (red) compared to that of Zr_{12}TPDC (black).

The CoCl-Zr_{12}TPDC MOF maintained crystallinity through the metalation, indicated by the similar PXRD patterns between the Zr_{12}TPDC and CoCl-Zr_{12}TPDC (**Figure 5-8**). ICP-MS analysis of the digested MOF revealed the presence of 11.2±0.6 Co per Zr_{12} cluster, corresponding to complete metalation of all the eight μ_3-OLi sites to form eight (Zr_3O^-)CoCl species, and all six μ_2-OLi sites to form three [(Zr_2O^-)$_2$(Zr_3O)CoCl]Li species, to give the overall formula of Zr_{12}(μ_3-O)$_5$[(μ_3-O^-)CoCl]$_8$[(μ_2-O^-)$_2$(μ_3-O)CoCl]$_3$$Li_3$(TPDC)$_9$.

The coordination environments of the Co centers in CoCl-Zr_{12}TPDC were studied by Co K-edge EXAFS. The six μ_2-OH sites are very close to each other, with a mutual distance of ~3.0 Å. Based on the reported structures of Co complexes with oxide ligands, we envisioned three different Co coordination modes on the μ_2-OH sites: [(μ_2-O^-)$_2$(μ_3-O)CoCl]$^-$, [(μ_2-O^-)$_2$$CoCl_2$]$^{2-}$ and (μ_2-O^-)(μ_3-O)(μ-CO_2^-)CoCl. EXAFS fitting with the [(μ_2-O^-)$_2$$CoCl_2$]$_2^-$ and (μ_2-O^-)(μ_3-O)(μ-CO_2^-)CoCl structure models gave large R-factors of 0.023 and 0.027, respectively, as a result of misfits in the second shells (R = 2.2-3.2 Å), which is mainly due to the Co-Zr scattering pathway. The [(μ_2-O^-)$_2$(μ_3-O)CoCl]$^-$ model gives the best fit to the Co EXAFS data, with a R-factor of 0.020 and fitted Co-(μ_2-O^-) distance of 1.90 Å (**Figure 5-9**). The Co centers on the μ_3-OH sites adopt a (μ_3-O)(μ-CO_2^-)$_2$CoCl mode, similar to the structures proposed in CoCl-Zr_6TPDC. We further propose the exchange between the μ_3-O and μ_3-OLi sites in Zr_{12} SBUs after lithiation in order to avoid the steric clash between the μ_3-OCoCl and [(μ_2-O^-)$_2$(μ_3-O)CoCl]$^-$ moieties that are installed on the adjacent Zr_3(μ_3-OH) and (μ_2-OH)$_2$ binding sites.

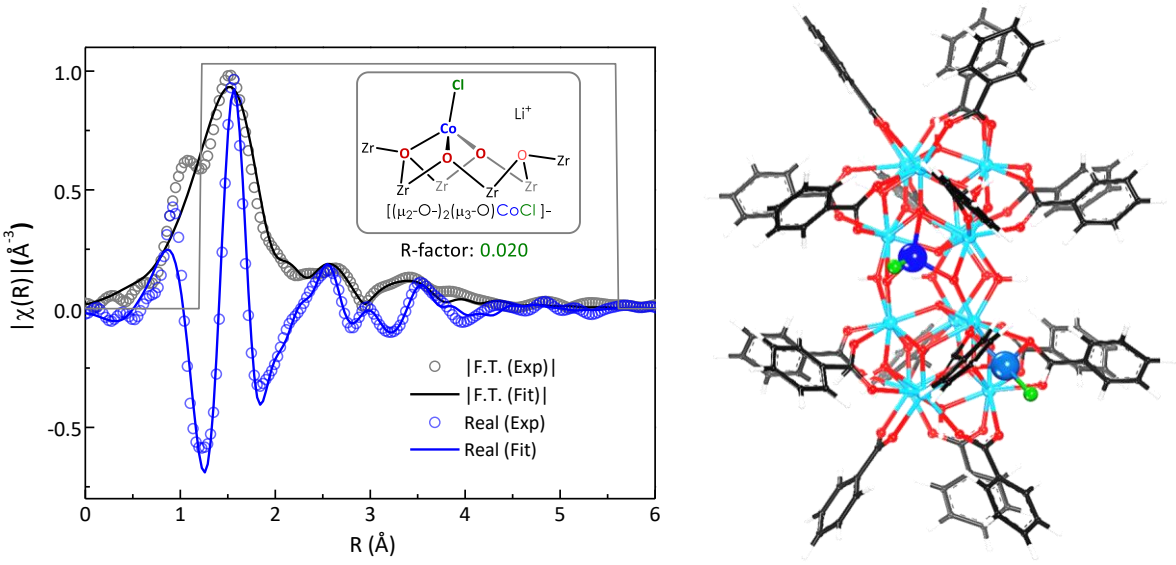

Figure 5-9. EXAFS spectra and fits in R-space at the Co K-edge of CoCl-Zr_{12}TPDC showing the magnitude (hollow squares, black) and real component (hollow squares, blue) of the Fourier transformation. The fitting range is 1.2-5.6 Å in R space (within the grey lines). The structural model used for fitting is shown on the right, and the parameters are listed in **Table 5-2**.

TGA of the CoCl-Zr_{12}TPDC showed a weight loss of 55.3% from 180 °C to 800 °C, corresponding well to the decomposition of $Zr_{12}O_5(OCoCl)_8(O_3CoCl)_3Li_3(TPDC)_9$ to $(ZrO_2)_{12}(CoO_{1.5})_{11}(LiO_{0.5})_3$ (54.5% expected). The BET surface area of CoCl-Zr_{12}TPDC was calculated to be 810 m^2/g based on N_2 sorption isotherm. In contrast to Zr_{12}TPDC which exhibits a Type I adsorption isotherm, CoCl-Zr_{12}TPDC adopts a type II adsorption isotherm (**Figure 5-10**), likely due to severe distortion of the CoCl-Zr_{12}TPDC framework upon desolvation. The severe framework distortion was also indicated by the loss of PXRD pattern for the dried CoCl-Zr_{12}TPDC sample. The CoCl-Zr_{12}TPDC MOF remains high crystalline as long as it was soaked in solvents.

Upon treatment with 5 equiv. of $NaBEt_3H$, CoCl-Zr_{12}TPDC was converted to CoH-Zr_{12}TPDC as a black solid. The CoH-Zr_{12}TPDC material is a highly active catalyst for the hydrogenation of Nitroarenes. XANES analysis of CoH-Zr_{12}TPDC suggested the divalent oxidation state of the Co centers (**Figure 5-11**).

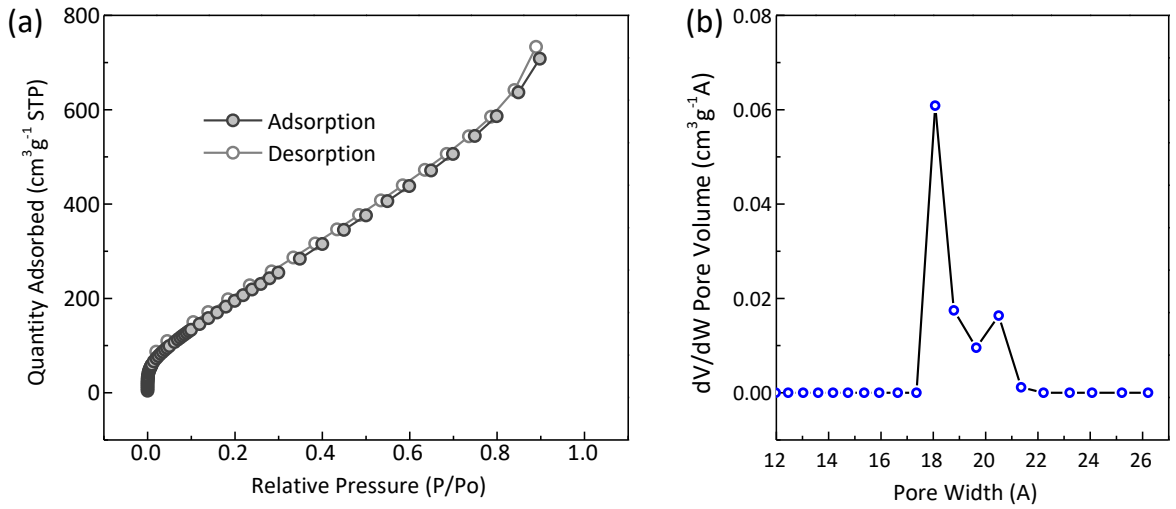

Figure 5-10. (a) Nitrogen sorption isotherms of CoCl-Zr_{12}TPDC (77 K). CoCl-Zr_{12}TPDC has a BET surface areas of 1967 m^2/g. (b) Pore size distributions of CoCl-Zr_{12}TPDC showing existence of two kinds of pores of 18 Å and 23 Å in diameters.

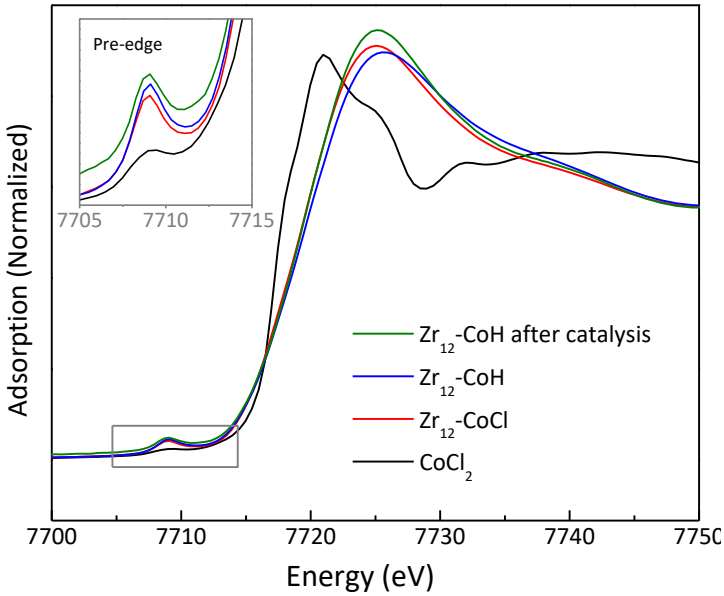

Figure 5-11. XANES spectra of CoCl-Zr_{12}TPDC (red), CoH-Zr_{12}TPDC (blue) and post-catalysis CoH-Zr_{12}TPDC after nitrobenzene hydrogenation (green); all three spectra are similar to that of $CoCl_2$ (black), indicating a divalent oxidation state of the Co centers in all of the species.

5.2.3 CoH-Zr_{12}TPDC catalyzed hydrogenation of nitroarene

Anilines are important building blocks for the synthesis of pharmaceuticals, fine chemicals, and commodities.[10-11] Among the various known procedures for synthesizing anilines, the catalytic hydrogenation of nitroarenes represents one of the most efficient and environmental-benign synthetic routes. To date, most chemoselective and efficient catalysts for nitroarene hydrogenation are based on precious metals, which are toxic and unsustainable.[12-14] Only a handful of Earth-abundant metal catalysts were recently reported for this reaction.[15-18] CoH-Zr_{12}TPDC was an active catalyst for hydrogenating a broad scope of nitroarenes to the corresponding anilines. The optimal condition for performing CoH-Zr_{12}TPDC catalyzed nitroarene hydrogenation (evaluated by reaction TOF) was screened to be 110 °C using toluene as solvent. At a 0.5 mol % Co loading, 4-nitroanisole was quantitatively hydrogenated in toluene at 110 °C under 40 bar of H_2 in 42 h to form 4-aminoanisole.

Under the same reaction condition, nitroarenes containing oxygen and halogens were also selectively hydrogenated to the corresponding anilines in 70-100% yields (**Table 5-1**). Pure aniline products were isolated by simple filtration of the reaction mixtures followed by evaporating of the organic solvent. Both electron-withdrawing substituents (*e.g.* trifluoromethyl), and electron-donating groups (*e.g.* methoxy and amines) were well tolerated under the same reaction conditions.

Impressively, CoH-Zr_{12}TPDC selectively reduced nitro groups in presence of more reactive substituents, including iodine and ketone functionalities. For example, at 0.5 – 2.0 mol % Co loading, 1-iodo-4-nitrobenzene, 4-nitrobenzophenone, and 4-nitroacetophenone were selectively hydrogenated to corresponding anilines without converting other sensitive substituents. We also tested the hydrogenation of nitroindole compounds to produce heteroaromatic amines, which are important building blocks for a variety of pharmaceuticals and biologically-active

compounds. Without further optimization, 4-nitroindole and 5-nitroindole were hydrogenated to 4-aminoindole and 5-aminoindole in 55% and 92% yields, respectively, without forming any by-products.

Table 5-1. CoH-Zr_{12}TPDC catalysed hydrogenation of nitroarenes.

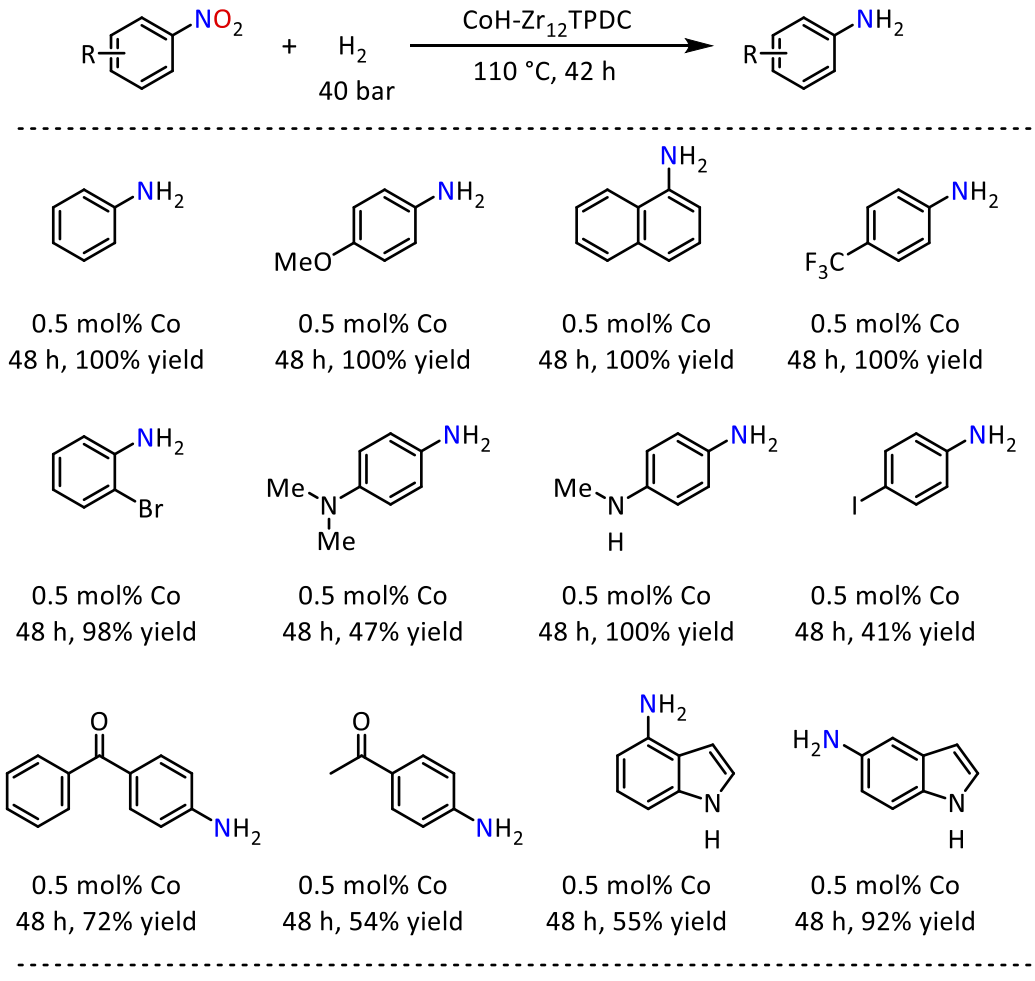

Reaction conditions: 0.50 mg of CoCl-Zr_{12}TPDC, 5 equiv of $NaBEt_3H$ (1.0 M in toluene) w.r.t. Co, nitroarene, toluene, 40 bar H_2, 110 °C, 42 h; Yield was determined by ^1H NMR with mesitylene as the internal standard. Isolated yields are in parentheses. cReaction was performed for 72 h.

Furthermore, at a 1.0 mol% Co-loading, CoH-Zr_{12}TPDC was recovered and reused at least 7 times for the hydrogenation of 4-nitroanisole without losing the catalytic activity (**Figure 5-12**).

Excellent yields (86-100%) of 4-aminoanisole were obtained consistently without formation of any by-product in the reuse experiments.

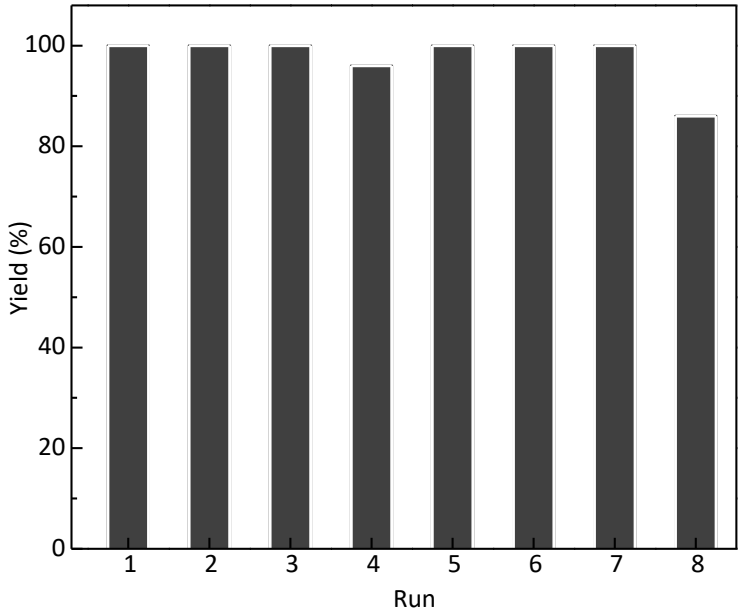

Figure 5-12. Plots of yields (%) of 4-aminoanisole at different runs in the recycle experiments of CoH-Zr_{12}TPDC for the hydrogenation of 4-nitroanisole. The Co-loadings were 1.0 mol %.

CoH-Zr_{12}TPDC recovered from the first run of catalysis maintained high crystallinity, indicated by its similar PXRD pattern to pristine CoH-Zr_{12}TPDC. This experiment proved the MOF stability under the reaction conditions. The heterogeneity of CoH-Zr_{12}TPDC was confirmed by several experiments. ICP-MS analyses showed that the amounts of Co and Zr that leached into the supernatant after the first run were only 0.4% and 0.03%, respectively. Moreover, no additional hydrogenation was observed after removal of the solid catalyst from the reaction mixture (**Scheme 5-1**). These experiments rule out the role of any leached Co-nanoparticles or other Co-species in catalyzing the hydrogenation reactions.

Scheme 5-1. Heterogeneity test experimental for CoH-Zr$_{12}$TPDC catalyzed nitroarene hydrogenation.

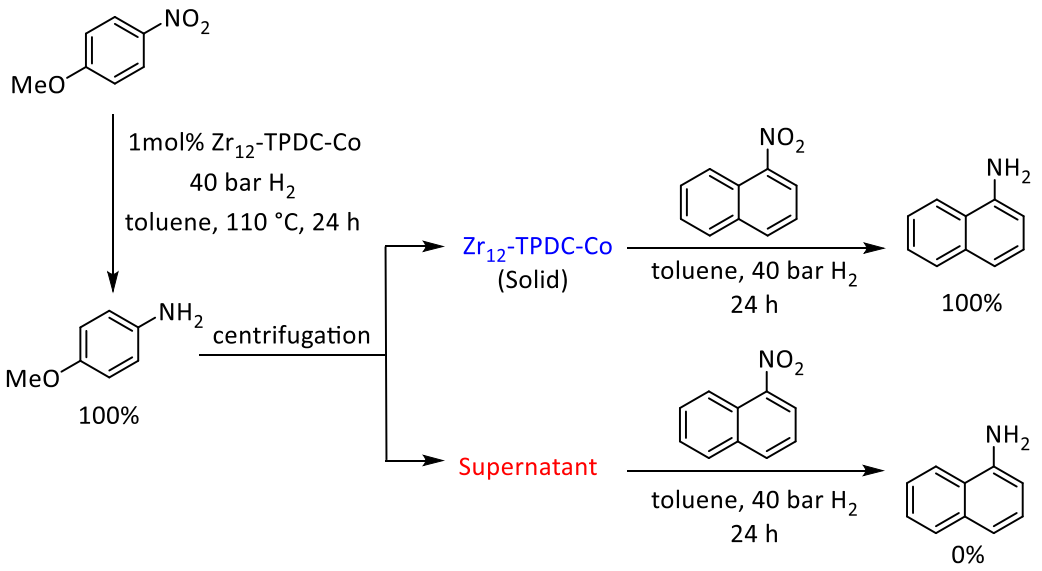

To elucidate the multistep hydrogenation pathways, all possible intermediates in nitrobenzene hydrogenation reactions were tested for their activity. Two possible reaction pathways have been proposed in the literature for nitrobenzene hydrogenation, including the monomeric pathway and dimeric pathway.[19] The monomeric pathway proceeds *via* stepwise hydrogenation of nitrobenzene to nitrosobenzene, to phenyhydroxyamine, and then to aniline. The dimeric pathway initiates with the azoxybenzene formation from the nitrosobenzene reacting with phenylhydroxyamine. The nitrosobenzene was subsequently hydrogenated to azobenzene, to hydrazobenzene, and then to aniline. While azobenzene and hydrazobenzene were readily hydrogenated to aniline by CoH-Zr$_{12}$TPDC, azoxybenzene only gave 2% yield of aniline under identical reaction conditions, indicating that the azoxybenzene hydrogenation is the slowest step in the dimeric pathway (**Table 5-2**).

Table 5-2. CoH-Zr_{12}TPDC-catalyzed hydrogenation of intermediates in proposed pathways of nitroarene hydrogenation.

Entry	Substrate	Products and Yields			Conversion
1	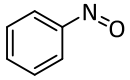	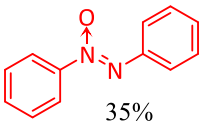 35%	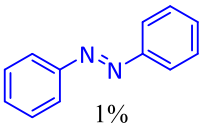 1%	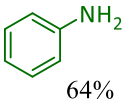 64%	100%
2	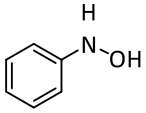	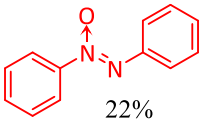 22%	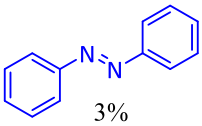 3%	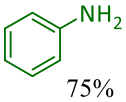 75%	100%
3	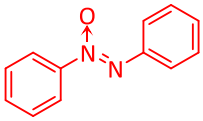	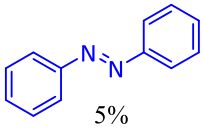 5%	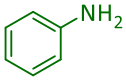 2%		7%
4	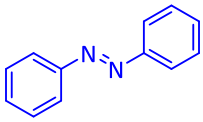	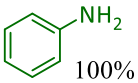 100%			100%
5	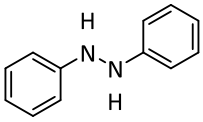	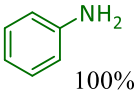 100%			100%

Reaction conditions: 0.50 mg of CoH-Zr_{12}TPDC (0.5 mol % Co), substrate, toluene, 40 bar H_2, 110 °C, 42 h; Yields were determined by GC-MS analysis.

In addition, the rate of hydrogenation of 4-nitroanisole was greatly suppressed in presence of azoxybenzene, indicating that azoxybenzene acts as a catalyst inhibitor. In comparison, hydrogenation of nitrosobenzene and phenylhydroxyamine gave 64-75% yield of aniline together with 22-35% of azoxybenzene side product formed through substrate dimerization. No azoxybenzene intermediate was observed during hydrogenation of nitrobenzene, presumably because very little nitrosobenzene or phenylhydroxyamine accumulated during the reaction process. With these results, we propose that CoH-Zr_{12}TPDC catalyzed nitroarene hydrogenation mainly via the monomeric pathway as shown in the green dotted box in **Scheme 5-2**.

Scheme 5-2. Two possible pathways for CoH-Zr_{12}TPDC-catalyzed hydrogenation of nitroarenes. Based on our mechanistic studies, we propose that CoH-Zr_{12}TPDC catalyzes nitroarene hydrogenation mainly via the monomeric pathway as shown in the dotted box.

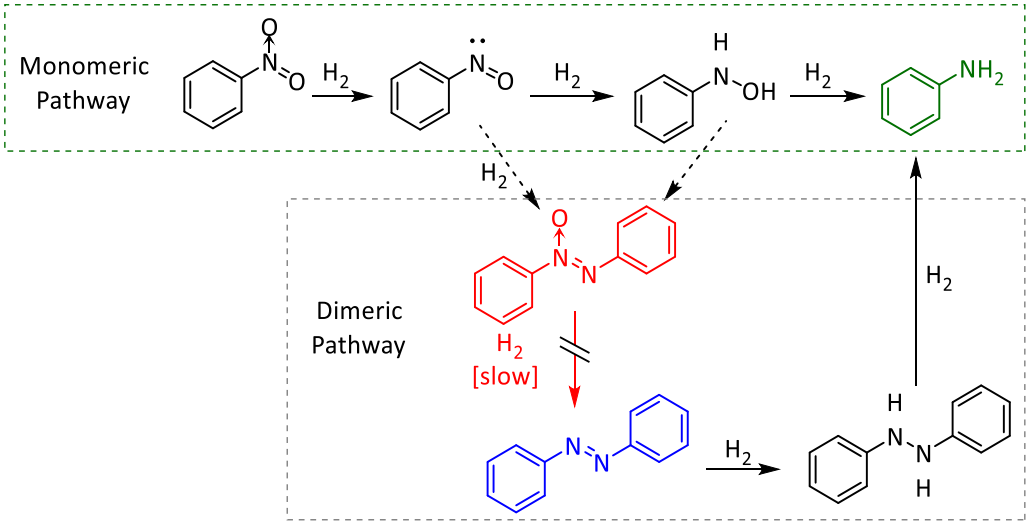

5.2.4 CoH-Zr_{12}TPDC catalyzed hydrogenation of nitriles

CoH-Zr_{12}TPDC is also active for the hydrogenation of nitrile compounds. Nitrile groups are typically reduced to amino groups using stoichiometric amounts of metal hydrides or hydrosilanes in the presence of metal complexes or organocatalysts. However, these methods suffer from poor atom economy and low functional group tolerance. In contrast, catalytic hydrogenation of nitrile compounds is a highly atom-efficient and sustainable route to prepare amines. Typical catalysts for nitrile hydrogenation are based on precious metals, with only a handful of iron or cobalt-based homogeneous catalysts that were recently reported. Catalytic hydrogenation of nitriles was performed under identical conditions to the nitroarene hydrogenation reactions. At a 0.5 mol % Co-loading, CoH-Zr_{12}TPDC efficiently reduced a range of nitrile compounds to afford corresponding benzylamines in quantitative yields (**Table 5-3**). Substrates bearing bromine or amine functionalities were also well tolerated. Pure benzylamine products were

isolated in 94-100% yields through simple filtration followed by evaporation of the volatiles *in vacuo*.

Table 5-3. CoH-Zr_{12}TPDC catalyzed hydrogenation of nitriles.

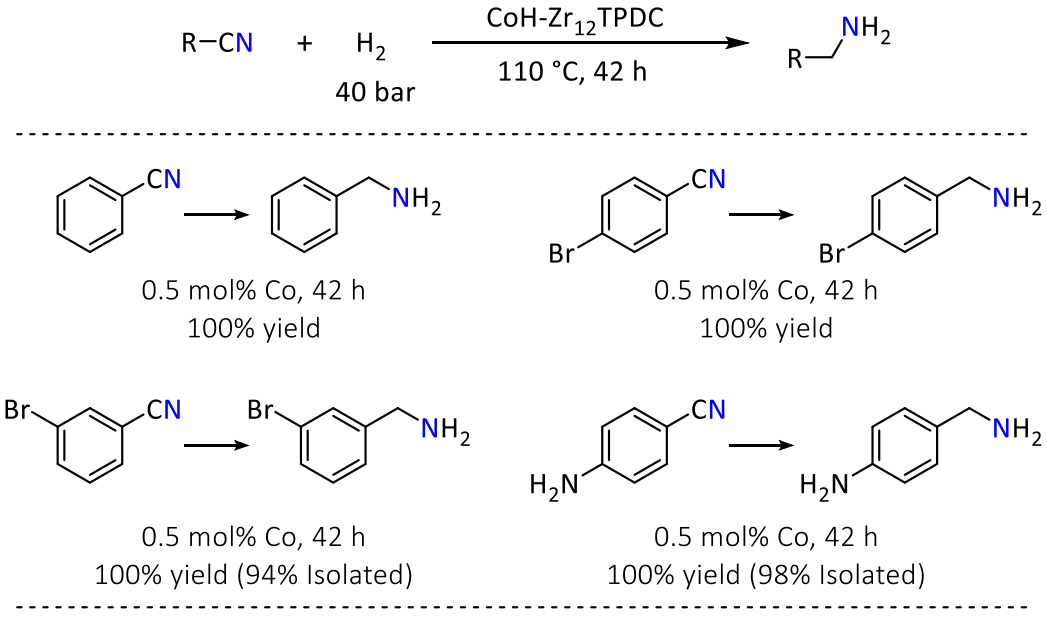

Reaction conditions: 0.50 mg of CoH-Zr_{12}TPDC for nitrile substrates, 2.0 mg of CoH-Zr_{12}TPDC for isocyanide substrates, nitrile or isocyanide, toluene, 40 bar H_2, 110 °C, 42 h; Yield was determined by ^{1}H NMR with mesitylene as the internal standard. Isolated yields are in parentheses.

The MOF recovered from the hydrogenation of benzonitrile maintained high crystallinity, as shown by PXRD analysis (Figure 3b). The leaching of Co and Zr into the supernatant were only 0.2% and 0.03%, respectively, further proving the high MOF stability under the reaction condition. CoH-Zr_{12}TPDC was recovered and reused at least 7 times for the hydrogenation of benzonitrile to afford pure benzylamine without any loss of catalytic activity (**Figure 5-13**).

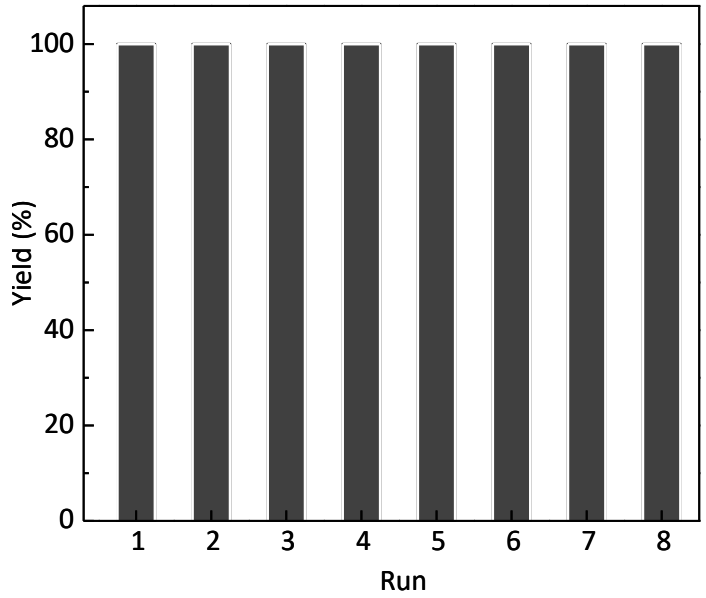

Figure 5-13. Plots of yields (%) of benzylamine at different runs in the recycle experiments of CoH-Zr_{12}TPDC catalyzed nitrile hydrogenation.

5.2.5 CoH-Zr_{12}TPDC catalyzed hydrogenation of isocyanides

The catalytic hydrogenation of isocyanides into N-methylamines is very rare and challenging reaction, as a result of the strong isocyanide inhibition to transition metal catalysts. Impressively, CoH-Zr_{12}TPDC is an effective catalyst for hydrogenating isocyanides to corresponding N-methylamines at 110 °C under 40 bar H_2. At a 0.5-2.0 mol % Co loading, benzyl isocyanide, 2-naphthyl isocyanide, cyclohexyl isocyanide, and α-methylbenzyl isocyanide were effectively hydrogenated. Pure secondary amines were isolated in 82-96% yields (**Table 5-4**). The leaching of Co and Zr into the supernatant after hydrogenation of 2-naphthyl isocyanide was determined to be only 0.2% and 0.08%, respectively, indicating the strong cobalt coordination on to the pair-site bridging hydroxides of the Zr_{12}-SBU.

Table 5-4. Substrate scope for the CoH-Zr_{12}TPDC catalyzed hydrogenation of benzonitriles.

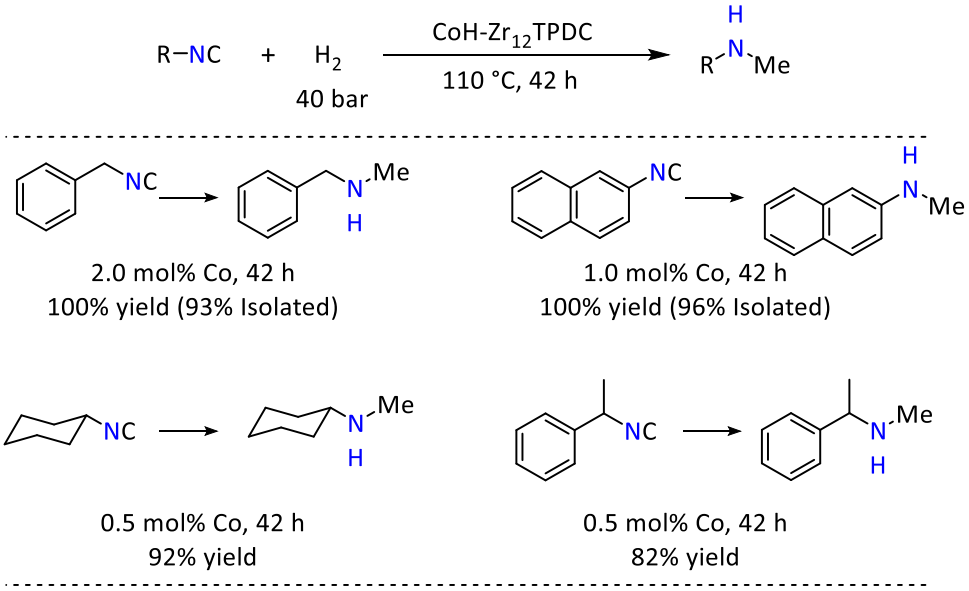

Reaction conditions: 0.50 mg of CoH-Zr_{12}TPDC for nitrile substrates, 2.0 mg of CoH-Zr_{12}TPDC for isocyanide substrates, nitrile or isocyanide, toluene, 40 bar H_2, 110 °C, 42 h; Yields were determined by 1H NMR with mesitylene as the internal standard. Isolated yields are in parentheses.

5.2.6 Catalytic performance comparison of CoH-Zr_{12}TPDC versus other CoH-SBU catalysts

To highlight the advantage of having electron-rich and strongly coordinating Co centers in CoH-Zr_{12}TPDC, the previously reported CoH-Zr_6TPDC and CoH-Zr_8MTBC were tested for the three types of challenging hydrogenations under identical conditions. For the hydrogenation of 1-nitronaphthalene, CoH-Zr_{12}TPDC gave complete yield of 1-aminonaphthalene, while CoH-Zr_6TPDC and CoH-Zr_8MTBC were completely inactive for this substrate (**Table 5-5**). For hydrogenation of benzonitrile, CoH-Zr_{12}TPDC afforded benzylamine in a quantitative yield while CoH-Zr_6TPDC and CoH-Zr_8MTBC produced benzylamine in 0% and 4% yields, respectively. CoH-Zr_{12}TPDC is also significantly more active than CoH-Zr_6TPDC and CoH-Zr_8MTBC in isocyanide hydrogenation. For example, CoH-Zr_{12}TPDC catalyzed the hydrogenation of sterically

hindered (S)-(−)-α-methylbenzyl isocyanide to afford the secondary amine product in 82% yield, while CoH-Zr_6TPDC was totally inactive and CoH-Zr_8MTBC gave only 7% of the hydrogenation product.

Table 5-5. Hydrogenation of nitroarene, nitrile and isocyanide compounds with different SBU-supported Co-catalysts.

Entry	Reactions	CoH-Zr_6TPDC	CoH-Zr_8MTBC	CoH-Zr_{12}TPDC
1	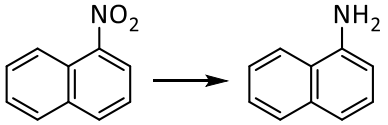	0%	0%	100%
2	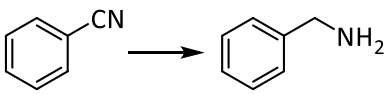	0%	4%	100%
3	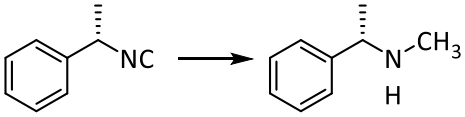	0%	7%	82%

[a]Reaction conditions: 0.5 mol% of CoH-Zr_{12}TPDC, 1-nitronaphthalene (69 mg, 0.4 mmol), toluene, 40 bar H_2, 110 °C, 42 h. [b]Reaction conditions: 0.5 mol% of CoH-Zr_{12}TPDC catalyst, benzonitrile (42 μL, 0.4 mmol), toluene, 40 bar H_2, 110 °C, 42 h. [c]Reaction conditions: 0.5 mol% of CoH-Zr_{12}TPDC catalyst, (S)-(−)-α-methylbenzyl isocyanide (54 μL, 0.4 mmol), toluene, 40 bar H_2, 110 °C, 42 h.

The drastically different activities of the three CoH-SBU catalysts can be rationalized by considering both the electronic and steric effects of different Zr-SBUs. The steric difference among the three SBUs are very significant. The Co-binding site in Zr_{12}-SBU is featured by a sterically open 4.6 Å×6.9 Å rectangle space, while the Zr_6-SBU site is an equilateral triangle with edge length of 4.4 Å and the Zr_8-SBU site is a rhombus with an edge length of 4.5 Å (**Figure 5-14**).

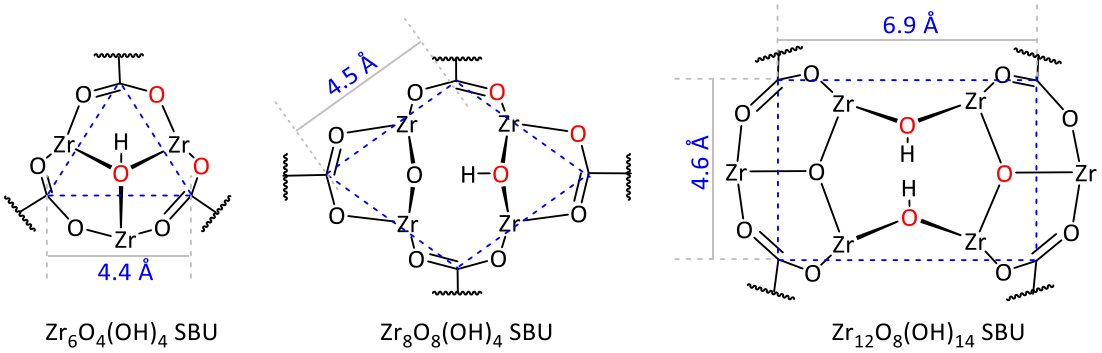

Figure 5-14. Comparison of the electronic and steric properties of Co binding sites in Zr_6, Zr_8, and Zr_{12} SBUs. The oxygen atoms highlighted in red are involved in cobalt binding after lithiation and metalation.

The electronic properties for Co species supported on different SBUs are also significantly different. The Zr_{12} SBU in Zr_{12}TPDC features a pair of μ_2-OH sites that efficiently chelates to the Co center to afford a much more electron-rich and stable catalytic center. As a result, the hydride in CoH-Zr_{12}TPDC could more easily undergo migratory insertion to the nitrile triple bond. The significantly higher activity of CoH-Zr_{12}TPDC for isocyanide hydrogenation could be partially attributed to the much higher catalyst stability.

To prove the high catalytic activity of CoH-Zr_{12}TPDC originates from the unique steric/electronic properties of Zr_{12} SBU instead of the nanoscale particle size of Zr_{12}-TPDC, a nanosized Zr_6-TPDC (160 nm) has been metalated and tested for catalytic reactions. The nano-sized CoH-Zr_6TPDC was synthesized through solvothermal reactions of $ZrCl_4$ with H_2TPDC in DMF using TFA as the modulator (**Figure 5-15**).

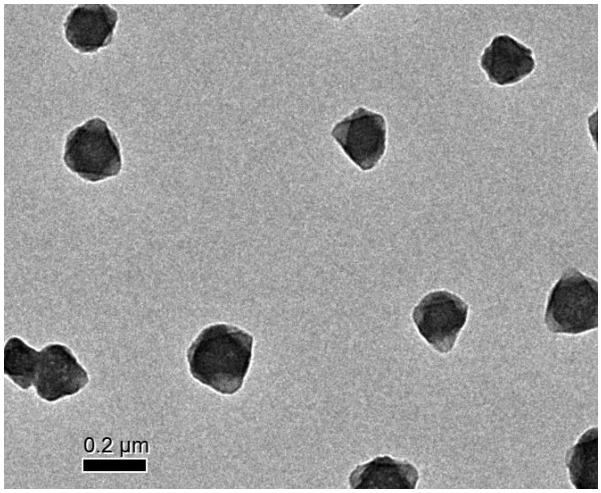

Figure 5-15. TEM image of nano Zr_6-TPDC octahedrons showing size distribution of 160 ± 19.7 nm.

The nano-sized CoH-Zr_6TPDC was tested for the hydrogenation reaction of nitroarene, nitrile and isocyanides under identical reaction conditions as the CoH-Zr_{12}TPDC catalyst. However, the downsized CoH-Zr_6TPDC was still not active for any of the hydrogenation reactions, ruling out the possibility of MOF size as major contributor to the catalytic activity enhancement (**Table 5-6**).

Table 5-6. Effect of size on catalytic hydrogenation**.**

Entry	Reactions	CoH-Zr_6TPDC (5 µm)	CoH-Zr_6TPDC (16 µm)	CoH-Zr_{12}TPDC (40 nm)
1	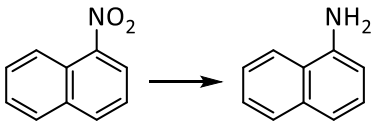	0%	0%	100%
2	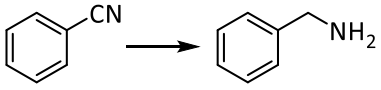	0%	4%	100%
3	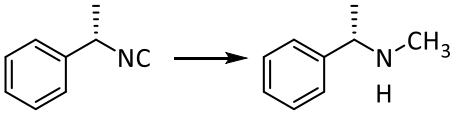	0%	7%	82%

Reaction conditions: 0.5 mol% of Zr-MOF-Co catalyst, 0.4 mmol of substrates, 2mL toluene, 40 bar H_2, 110 °C, 42 h.

5.3 Conclusion

This chapter reports the first MOF based on a novel $Zr_{12}(\mu_3\text{-}O)_8(\mu_3\text{-}OH)_8(\mu_2\text{-}OH)_6$ node. The Zr_{12} SBU provide a unique binding site for Co species to afford a highly effective single-site solid catalyst for the hydrogenation of nitroarenes, nitriles, and isocyanides. The monomeric pathway was proposed for the nitroarene hydrogenation reaction by comparing hydrogenation reactivities of all possible intermediates. The CoH-Zr_{12}TPDC catalyst displayed much higher catalytic performance than the previously described CoH-Zr_6TPDC and CoH-Zr_8MTDC for the three challenging hydrogenation reactions. The straightforward SBU functionalization and the exceptional catalytic activity of CoH-Zr_{12}TPDC indicate that MOF nodes can provide an unprecedented ligand platform to design reusable Earth-abundant metal catalysts for sustainable synthesis of fine and commodity chemicals.

5.4 Experimental

5.4.1 Synthesis of a Zr_{12} cluster and structure simulation of Zr_{12}TPDC

In an attempt to synthesis a chiral MOF using formic acid as the modulator, I ended up getting a molecular cluster with the composition of $Zr_{12}O_8(\mu_3\text{-}OH)_8(\mu_2\text{-}OH)_6(HCO_2)_{18}(DMF)_4$. Then I sought to synthesize a MOF with the Zr_{12} cluster as the constructing SBU. Interesting, this Zr_{12} cluster is exactly the SBU for a nanosized MOF we have in the group for a few years, yet the exact structure remained unknown.

The synthesis of Zr_{12}-formate cluster was done through solvothermal reactions. To an 8 mL vial was charged 60 mg of $ZrCl_4$, 50 mg of D-(+)-Camphoric acid, 4 mL DMF, and 1 mL of

formic acid (88% solution in water). The mixture was sonicated to form a clear solution, and then kept in a preheated 100 °C oven for 10 days. Plate-like crystal was obtained and analyzed by single-crystal X-ray diffraction (**Figure 5-16**).

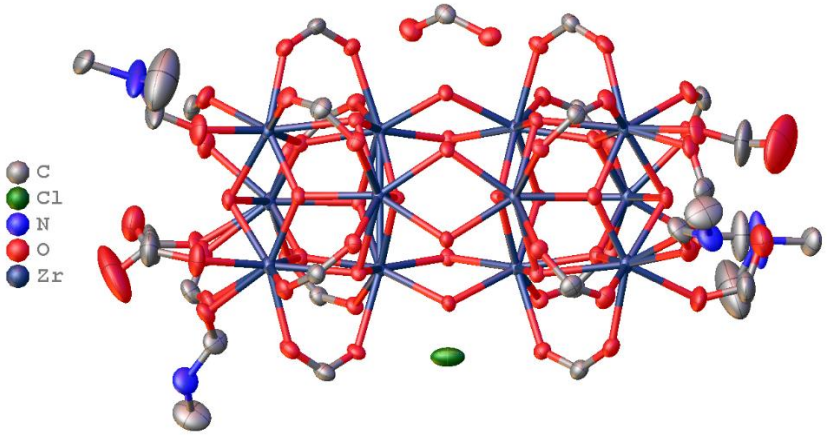

Figure 5-16. Crystal Structure of Zr_{12}-formate cluster.

Table 5-7. Crystallographic information

Name	**Zr_{12}-Form**
Formula	$C_{15.21}Cl_{0.5}N_{1.4}O_{33.9}Zr_6$
Fw	1309.79
Temperature (K)	100
Wavelength (Å)	0.41328
Crystal system	Monoclinic
Space group	*C*2/*c*
***a*, Å**	11.4489(5)
***b*, Å**	20.7494(9)
***c*, Å**	30.7865(14)
α, °	90
β, °	91.1600(10)
γ, °	90
***V*, Å^3**	7312.1(6)
Z	8
Density (calcd. g/cm^3)	2.380
Absorption coeff. (mm^{-1})	2.432
F(000)	4966.0

2θ range data collection	2.282 – 40.158
Index Ranges	$-17 \leq h \leq 11$ $-34 \leq k \leq 28$ $-49 \leq l \leq 46$
Reflections collected	39218
Independent reflections	13490
R(int)	0.0494
Data/restraints/parameters	13490/455/570
Goodness-of-fit on F^2	1.046
Final R indices [I>2σ(I)]	R1=0.0527, wR2=0.1295
R indices (all data)	R1=0.0862, wR2=0.1428

Crystal structure of the Zr_{12}-MOF was simulated based on a combination of the crystal structures of the $Zr_{12}O_8(OH)_8(OH)_6(HCO_2)_{18}$ cluster and Zr_6TPDC.[9] The space group was selected to be the hexagonal P63/mmc, which is the group of highest symmetry based on the systematic absences. This structural assignment was supported by the similarity between the simulated PXRD with the experimental (**Figure 5-17**). The 2θ peak at 3.56° corresponds to the (002) diffraction with a d spacing of 2.49 nm, which is characteristic of Zr_{12}TPDC and results from diffraction between neighboring Zr_{12} SBUs along the c axis. This d spacing is larger than the SBU distance of Zr_6TPDC (1.88 nm) along the [111] direction. The d spacing of 2.49 nm between Zr_{12} SBUs is also evidenced in high resolution TEM images of Zr_{12}TPDC.

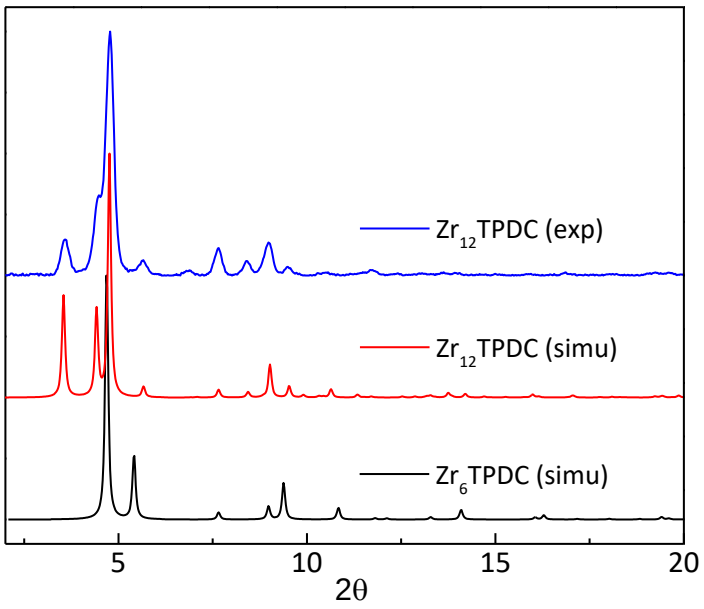

Figure 5-17. The experimental PXRD pattern of Zr_{12}TPDC (blue) is similar to the simulated PXRD of Zr_{12}TPDC (red), but very different from the simulated PXRD of Zr_6TPDC (black).

5.4.2 Synthesis and Characterization of Zr_{12}-TPDC

Detailed synthetic procedure for Zr_{12}TPDC was discussed as below. To a 20 mL vial was added $ZrCl_4$ (4.2 mg, 18 μmol), H_2TPDC (5.7 mg, 18 μmol), acetic acid (0.75 mL), and DMF (10 mL). The mixture was sonicated for 5 min until all solids were dispersed and then kept in a 90 °C oven for 3 d. The MOF was separated through centrifugation (13,000 rpm), then washed sequentially with DMF three times (5 mL each), THF three times (5 mL each), and benzene three times (5 mL each) before freeze drying in a salt-ice bath. 3.0 mg of Zr_{12}TPDC (45% yield) was obtained as light gray powder. The Zr_{12}TPDC has the formula of $Zr_{12}O_8(\mu_3\text{-}OH)_8(\mu_2\text{-}OH)_6(TPDC)_9$.

Transmission electron microscopy (TEM) showed a disk-like morphology of approximately 40 nm in diameter and 10 nm in thickness (**Figure 5-18**, **5-19**). The small particle

size is advantageous for MOF catalysts due to shorter diffusion distances for both reaction substrates and products, which increases reaction rates.

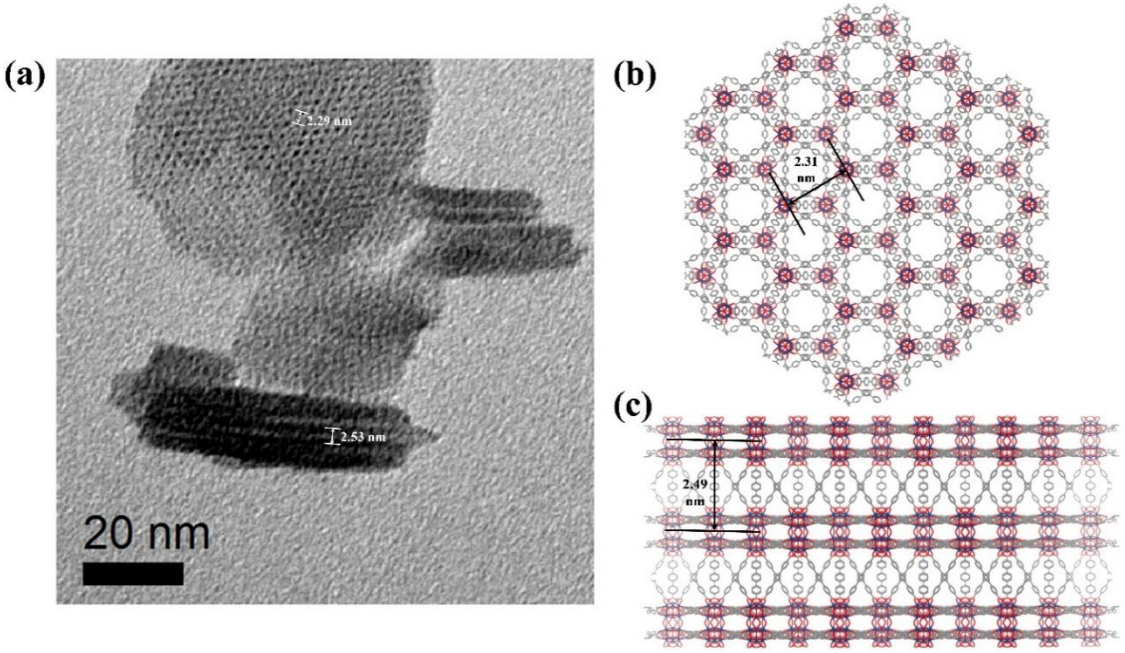

Figure 5-18. (a) Top-view high-resolution TEM showing the lattice fringes of Zr_{12}-TPDC along the [002] and [100] direction. The Measured lattice distance matched well with calculated distance based on the simulated structure. (b) Along the [002] direction, the distance between two side-by-side connected Zr_{12} SBU was calculated to be 2.31 nm, matching to the measured distance of 2.29 nm well. (c) Along the [100] direction, the distance between two Zr_{12} SBU planes was calculated to be 2.49 nm, matching the measured distance of 2.53 nm well.

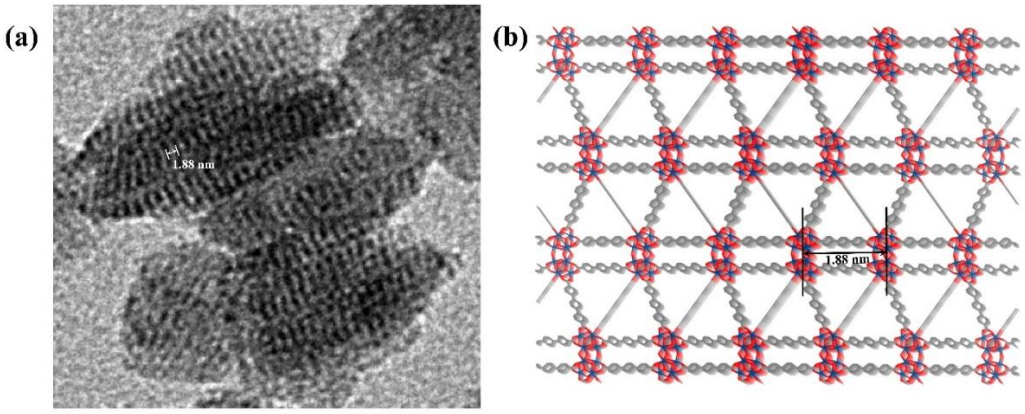

Figure 5-19. (a) Side-view high resolution TEM showing the wavy lattice fringes of Zr_{12}TPDC along the [2,-1,0] direction. (b) The distance between two neighboring wavy Zr_{12} SBU planes is calculated to be 1.88 nm, exactly matching the measured distance of 1.88 nm.

5.4.3 Procedure of CoH-Zr_{12}TPDC-catalyzed nitro hydrogenation

X-ray absorption data were collected at Beamline 10-BM-A, B at the Advanced Photon Source (APS) at Argonne National Laboratory. Spectra were collected at the cobalt K-edge (7709 eV) in transmission mode. The X-ray beam was monochromatized by a Si(111) monochromater and detuned by 50% to reduce the contribution of higher-order harmonics below the level of noise. A metallic cobalt foil standard was used as a reference for energy calibration and was measured simultaneously with experimental samples. The incident beam intensity (I_0), transmitted beam intensity (I_t), and reference (I_r) were measured by 20 cm ionization chambers with gas compositions of 63% N_2 and 37% He, 73% N_2 and 27% Ar, and 100% N_2, respectively. Data were collected over six regions: -250 to -30 eV (10 eV step size, dwell time of 0.25 s), -30 to -12 eV (5 eV step size, dwell time of 0.5 s), -12 to 30 eV (0.4 eV step size, dwell time of 1 s), 30 eV to 6 $Å^{-1}$, (0.05 $Å^{-1}$ step size, dwell time of 2 s), 6 $Å^{-1}$ to 12 $Å^{-1}$, (0.05 $Å^{-1}$ step size, dwell time of 4 s), 12 $Å^{-1}$ to 15 $Å^{-1}$, (0.05 $Å^{-1}$ step size, dwell time of 8 s). Multiple X-ray absorption spectra were collected at room temperature for each sample. Samples were ground and mixed with PEG and packed in a 6-shooter sample holder to achieve adequate absorption length.

Data were processed using the Athena and Artemis programs of the IFEFFIT package based on FEFF 6. Prior to merging, spectra were calibrated against the reference spectra (metallic Co) and aligned to the first peak in the smoothed first derivative of the absorption spectrum, background removed, and spectra processed to obtain a normalized unit edge step.

Table 5-8. Summary of EXAFS fitting parameters for CoCl-Zr_{12}TPDC

$(\mu_2\text{-O})_2$-CoCl site (27%)	μ_3-O-CoCl site (73%)
Fitting range	k 2.80 – 11.50 $Å^{-1}$ R 1.2– 5.6 Å

Independent points		24	
Variables		15	
Reduced chi-square		654.1	
R-factor		0.020	
ΔE_0(eV)		-7.43±0.90	
S_0^2		1.000	
Percentage	0.27	Percentage-	0.73
R (Co-μ_2-O9) (2)	1.90±0.04 Å	R (Co-μ_4-O) (1)	1.97±0.27 Å
R (Co-μ_3-O8) (1)	1.97±0.01 Å	R (Co-O^{CO2-}) (2)	1.98±0.14 Å
R (Co-Cl) (1)	2.18±0.01 Å	R (Co-C^{CO2-}) (2)	2.17±0.08 Å
R (Co-μ_3-O25) (1)	3.17±0.01 Å	R (Co-Cl) (1)	2.19±0.05 Å
R (Co-Zr1) (2)	3.16±0.14 Å	R (Co- O^{CO2-}) (2)	2.62±0.04 Å
R (Co-$O14^{CO2-}$) (2)	3.20±0.01 Å	R (Co-Zr1) (1)	2.90±0.06 Å
R (Co-μ_3-O4) (1)	3.20±0.01 Å	R (Co-C^{Ph}) (2)	3.36±0.04 Å
R (Co-$C16^{CO2-}$) (2)	3.39±0.14 Å	R (Co-$O^{CO2\text{-}distal}$) (2)	3.42±0.05 Å
R (Co-$O12^{CO2-}$) (2)	3.75±0.56 Å	R (Co-$C^{CO2\text{-}distal}$) (2)	3.45±0.05 Å
R (Co-Zr19) (2)	3.78±0.18 Å	R (Co-Zr2) (2)	3.77±0.06 Å
R (Co-μ_2-O7) (2)	3.78±0.61 Å	R (Co-$C^{Ph\text{-}distal}$) (2)	4.26±0.04 Å
σ^2 (Co-O)	0.008±0.005 $Å^2$	σ^2 (Co-O)	0.010±0.002 $Å^2$
σ^2 (Co-Cl)	0.010±0.001 $Å^2$	σ^2 (Co-Cl)	0.009±0.008 $Å^2$
σ^2 (Co-C)	0.001±0.001 $Å^2$	σ^2 (Co-C)	0.006±0.006 $Å^2$
σ^2 (Co-Zr)	0.016±0.020 $Å^2$	σ^2 (Co-Zr)	0.016±0.006 $Å^2$

5.4.4 Procedure of CoH-Zr_{12}TPDC-catalyzed nitro hydrogenation

Scheme 5-3. CoH-Zr_{12}TPDC catalyzed hydrogenation of nitroarenes.

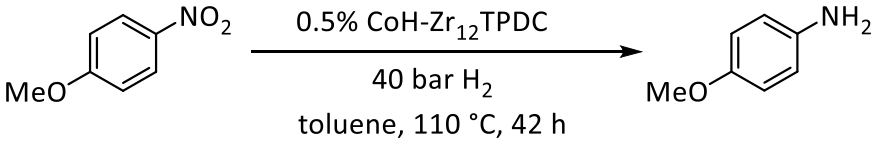

In a glovebox, CoCl-Zr_{12}TPDC in THF (0.50 mg, 0.5 mol % Co) was charged into a small vial and 0.5 mL THF was added. Then, 4.4 µL $NaBEt_3H$ (1.0 M in THF) was added to the vial and the mixture was stirred for 1 h in the glovebox. The solid was centrifuged out of suspension and then washed with THF twice. Then, the black solid in 1.0 mL toluene was transferred to a vial

containing 4-nitroanisole. The vial was placed into a Parr pressure reactor in a nitrogen-filled glovebox, then pressurized to 40 bar. After stirring at 110 °C for 42 h, the solid was centrifuged out of suspension and extracted three times with toluene. The combined organic extracts were concentrated *in vacuo* to afford crude 4-methoxyaniline in quantitative yield, which was sufficiently pure as analyzed by ^{1}H NMR spectrum (**Figure 5-20**).

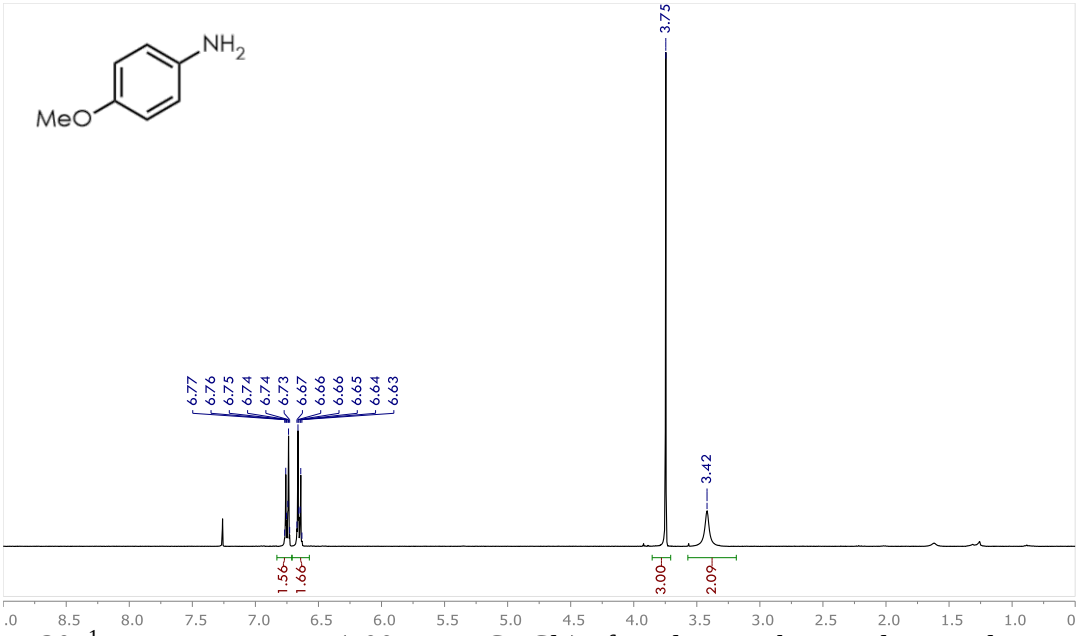

Figure 5-20. ^{1}H NMR spectrum (400 MHz, $CDCl_3$) of crude 4-methoxyaniline product.

5.4.5 Procedure of CoH-Zr$_{12}$TPDC-catalyzed Nitrile Hydrogenation

Scheme 5-4. CoH-Zr$_{12}$TPDC catalyzed hydrogenation of nitroarenes.

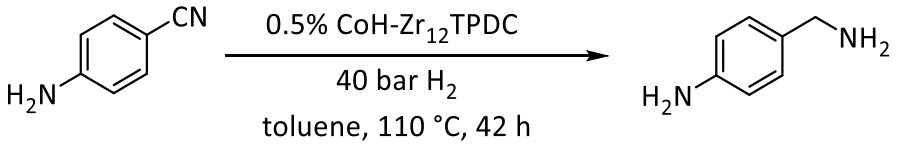

A typical procedure for CoH-Zr$_{12}$TPDC catalyzed hydrogenation of nitriles.In a glovebox, CoCl-Zr$_{12}$TPDC in THF (0.50 mg, 0.5 mol % Co) was charged into a small vial and 0.5 mL THF was added. Then, 4.4 µL $NaBEt_3H$ (1.0 M in THF) was added to the vial and the mixture was

stirred for 1 h in the glovebox. The solid was centrifuged out of suspension and then washed with THF twice. Then, the black solid in 1.0 mL toluene was transferred to a vial containing 4-aminobenzoitrile (21 mg, 0.178 mmol). The vial was placed into a Parr pressure reactor in a nitrogen-filled glovebox, then pressurized to 40 bars. After stirring at 110 °C for 42 h, the solid was centrifuged out of suspension and extracted three times with toluene. The combined organic extracts were concentrated *in vacuo* to afford crude 4-aminobenzylamine in quantitative yield, which was sufficiently pure as analyzed by ^{1}H NMR (**Figure 5-21**).

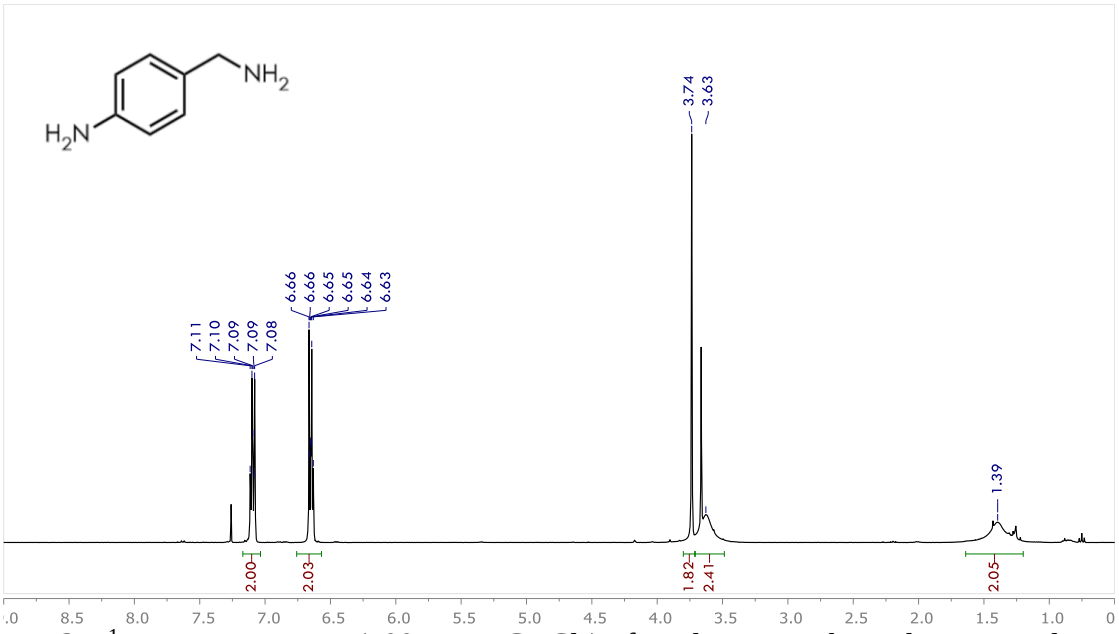

Figure 5-21. ^{1}H NMR spectrum (400 MHz, $CDCl_3$) of crude 4-aminobenzylamine product.

5.4.6 Procedure of CoH-Zr$_{12}$TPDC-catalyzed Isocyanide hydrogenation

Scheme 5-5. CoH-Zr$_{12}$TPDC catalyzed hydrogenation of isocyanide.

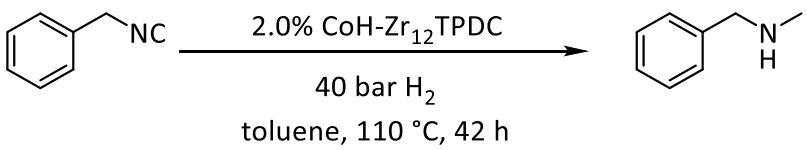

In a glovebox, CoCl-Zr_{12}TPDC in THF (2.0 mg, 2.0 mol % Co) was charged into a small vial and 0.5 mL THF was added. Then, 17.6 µL $NaBEt_3H$ (1.0 M in THF) was added to the vial and the mixture was stirred for 1 h in the glovebox. The solid was centrifuged out of suspension and then washed with THF twice. Then, the black solid in 1.0 mL toluene was transferred to a vial containing benzylisocyanide (20 mg, 0.171 mmol). The vial was placed into a Parr pressure reactor in a nitrogen-filled glovebox, then pressurized to 40 bar. After stirring at 110 °C for 42 h, the solid was centrifuged out of suspension and extracted three times with toluene. The combined organic extracts were concentrated *in vacuo* to afford crude *N*-benzylmethylamine in 93% isolated yield, which was sufficiently pure as analyzed by ^{1}H NMR spectrum (**Figure 5-22**).

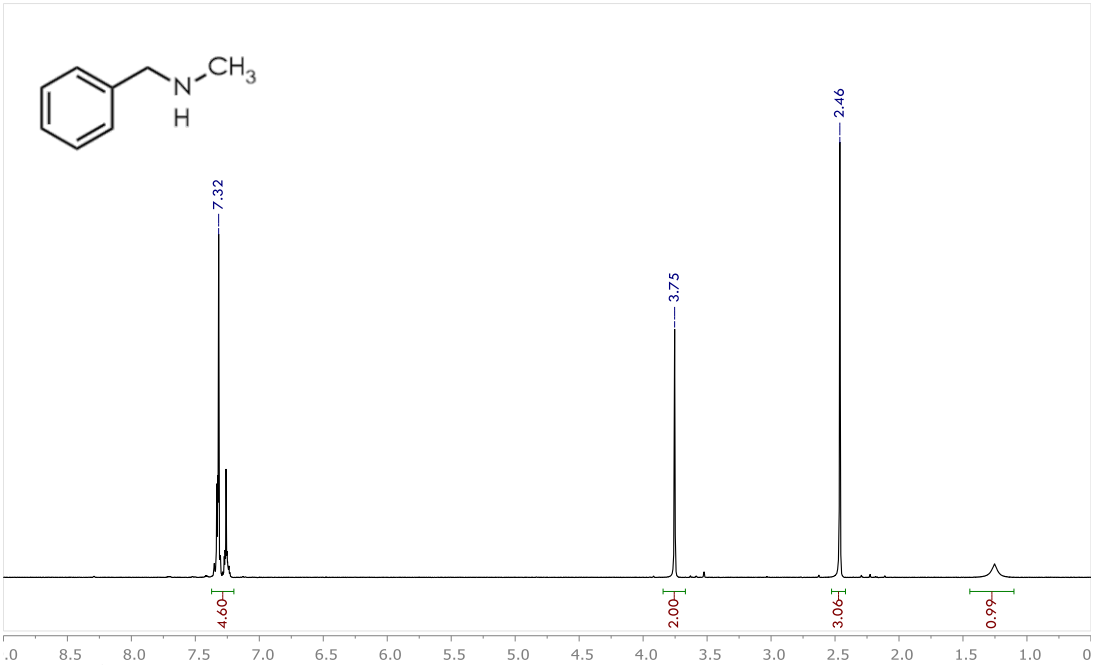

Figure 5-22. ^{1}H NMR spectrum (400 MHz, $CDCl_3$) of crude *N*-benzylmethylamine.

5.5 References

1. Bai, Y.; Dou, Y.; Xie, L.-H.; Rutledge, W.; Li, J.-R.; Zhou, H.-C., Zr-based metal–organic frameworks: design, synthesis, structure, and applications. *Chem. Soc. Rev.* **2016,** 2327-2367.

2. Devic, T.; Serre, C., High valence 3p and transition metal based MOFs. *Chem. Soc. Rev.* **2014,** 6097-6115.

3. Mouchaham, G.; Cooper, L.; Guillou, N.; Martineau, C.; Elkaïm, E.; Bourrelly, S.; Llewellyn, P. L.; Allain, C.; Clavier, G.; Serre, C., A robust infinite zirconium phenolate building unit to enhance the chemical stability of Zr MOFs. *Angew. Chem. Int. Ed.* **2015,** 13495-13499.

4. Guillerm, V.; Ragon, F.; Dan-Hardi, M.; Devic, T.; Vishnuvarthan, M.; Campo, B.; Vimont, A.; Clet, G.; Yang, Q.; Maurin, G., A series of isoreticular, highly stable, porous zirconium oxide based metal–organic frameworks. *Angew. Chem. Int. Ed.* **2012,** 9267-9271.

5. Cavka, J. H.; Jakobsen, S.; Olsbye, U.; Guillou, N.; Lamberti, C.; Bordiga, S.; Lillerud, K. P., A new zirconium inorganic building brick forming metal organic frameworks with exceptional stability. *J. Am. Chem. Soc.* **2008,** 13850-13851.

6. Furukawa, H.; Gándara, F.; Zhang, Y.-B.; Jiang, J.; Queen, W. L.; Hudson, M. R.; Yaghi, O. M., Water adsorption in porous metal–organic frameworks and related materials. *J. Am. Chem. Soc.* **2014,** 4369-4381.

7. Ji, P.; Manna, K.; Lin, Z.; Urban, A.; Greene, F. X.; Lan, G.; Lin, W., Single-Site Cobalt Catalysts at New Zr8 (μ2-O) 8 (μ2-OH) 4 Metal-Organic Framework Nodes for Highly Active Hydrogenation of Alkenes, Imines, Carbonyls, and Heterocycles. *J. Am. Chem. Soc.* **2016,** 12234-12242.

8. Zhang, X.; Zhang, X.; Johnson, J. A.; Chen, Y.-S.; Zhang, J., Highly Porous Zirconium Metal–Organic Frameworks with β-UH3-like Topology Based on Elongated Tetrahedral Linkers. *J. Am. Chem. Soc.* **2016,** 8380-8383.

9. Manna, K.; Ji, P.; Lin, Z.; Greene, F. X.; Urban, A.; Thacker, N. C.; Lin, W., Chemoselective single-site Earth-abundant metal catalysts at metal-organic framework nodes. *Nat. Commun.* **2016**.

10. Ono, N., *The nitro group in organic synthesis*. John Wiley & Sons: 2003; Vol. 9.

11. Sheldon, R. A.; Van Bekkum, H., *Fine chemicals through heterogeneous catalysis*. John Wiley & Sons: 2008.

12. Blaser, H.-U.; Steiner, H.; Studer, M., Selective Catalytic Hydrogenation of Functionalized Nitroarenes: An Update. *ChemCatChem* **2009,** 210-221.

13. Li, J.; Shi, X.-Y.; Bi, Y.-Y.; Wei, J.-F.; Chen, Z.-G., Pd Nanoparticles in Ionic Liquid Brush: A Highly Active and Reusable Heterogeneous Catalytic Assembly for Solvent-Free or On-Water Hydrogenation of Nitroarene under Mild Conditions. *ACS Catal.* **2011,** 657-664.

14. Corma, A.; Serna, P., Chemoselective Hydrogenation of Nitro Compounds with Supported Gold Catalysts. *Science* **2006,** 332-334.

15. Westerhaus, F. A.; Jagadeesh, R. V.; Wienhöfer, G.; Pohl, M.-M.; Radnik, J.; Surkus, A.-E.; Rabeah, J.; Junge, K.; Junge, H.; Nielsen, M.; Brückner, A.; Beller, M., Heterogenized cobalt oxide catalysts for nitroarene reduction by pyrolysis of molecularly defined complexes. *Nat Chem* **2013,** 537-543.

16. Wienhöfer, G.; Sorribes, I.; Boddien, A.; Westerhaus, F.; Junge, K.; Junge, H.; Llusar, R.; Beller, M., General and Selective Iron-Catalyzed Transfer Hydrogenation of Nitroarenes without Base. *J. Am. Chem. Soc.* **2011,** 12875-12879.

17. Jagadeesh, R. V.; Surkus, A.-E.; Junge, H.; Pohl, M.-M.; Radnik, J.; Rabeah, J.; Huan, H.; Schünemann, V.; Brückner, A.; Beller, M., Nanoscale Fe2O3-Based Catalysts for Selective Hydrogenation of Nitroarenes to Anilines. *Science* **2013,** 1073-1076.

18. Schwob, T.; Kempe, R., A Reusable Co Catalyst for the Selective Hydrogenation of Functionalized Nitroarenes and the Direct Synthesis of Imines and Benzimidazoles from Nitroarenes and Aldehydes. *Angew. Chem. Int. Ed.* **2016,** 15175-15179.

19. Wienhöfer, G.; Sorribes, I.; Boddien, A.; Westerhaus, F.; Junge, K.; Junge, H.; Llusar, R.; Beller, M., General and selective iron-catalyzed transfer hydrogenation of nitroarenes without base. *J. Am. Chem. Soc.* **2011,** 12875-12879.

20. Hermannsdörfer, J.; Friedrich, M.; Kempe, R., Colloidal Size Effect and Metal-Particle Migration in M@ MOF/PCP Catalysis. *Chem. Eur. J.* **2013,** 13652-13657.

Chapter 6. Single-site Co Catalysts at A Titanium (III)-oxo MOF Nodes for Arene Hydrogenation

6.1 Introduction

Metal oxides have found broad applications in the chemical industry by using surface oxo/hydroxo groups to support catalytic metal centers. The surface oxo/hydroxo ligands are readily available, thermally robust, and chemically stable, but lack the electronic and steric tunability when compared to small molecular organic ligands. In this context, TiO_2 is one of the most efficacious metal oxide catalyst supports for its negligible toxicity, low price, high stability, and most interestingly, the titanium redox activity that tunes the electronic properties of supported catalysts.[1-2] Previous research into TiO_2-supported catalysts has uncovered the strong metal-support interaction (SMSI) effect, which occurs when metallic or metal oxide catalysts are immobilized on TiO_2 support followed by thermal treatment.[3-5] The SMSI effect significantly impacts the activity and selectivity of supported catalysts. Many macroscopic processes have been proposed to explain this effect, including TiO_2 migration,[6] local Ti^{IV} reduction to Ti^{III},[5,7] or substrate activation with the surface O-vacancies, [8-9] but there is still not a clear understanding of the SMSI effect at the molecular level. [10-12] The effect of metal oxide supports is difficult to rationalize due to the presence of multiple species that bind to different crystal facets and different binding modes to each crystal facet as well as the pervasive defects leading to complex chemical compositions (**Figure 6-1**). Therefore, it is highly desirable to design structurally well-defined Ti-oxo/hydroxo sites to support uniform catalytic metal centers to precisely pinpoint the effects of the Ti-oxo support on the catalytic activity and selectivity.

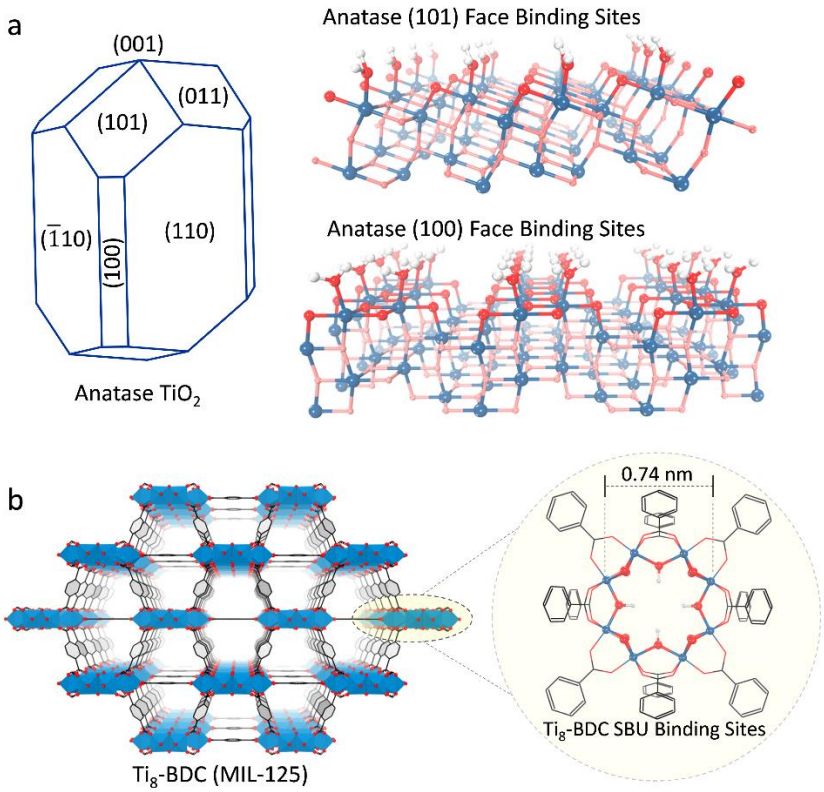

Figure 6-1. (a) Schematic representation of possible faces on the anatase phase of TiO_2 (left) and surface structures of the (101) face (top right) and (100) face (bottom right). The first layer of oxygen atoms on each of the faces are highlighted in red. All of these faces can undergo surface metalation leading to multiple catalytic sites. (b) Ti_8 SBUs in the Ti_8BDC MOF have one possible binding site only and support the formation of single-site catalysts.

In this work, we used Ti-oxo/hydroxo SBU of a titanium-based MOF, MIL-125 (Ti_8BDC, BDC is 1,4-benzenedicarboxylate), to support Co^{II}-H catalysts for highly effective arene hydrogenation.[13] Ti_8BDC features a nanosized octatitanium cluster with structurally-defined bridging hydroxides and oxides that serve as precise molecular model to study the electronic effects of Ti-O donor ligand on the catalytic performance of supported catalysts. We observed Co-mediated dihydride reductive elimination to form H_2 and the electron spillover to reduce Ti^{IV} to Ti^{III} on Ti-oxo SBUs.[14] The reduction of Ti-O donor ligand on Ti_8-SBUs significantly enhances

the electronic density of Co^{II}-H catalysts to effect arene and heteroarene hydrogenation with exceptional activities.

6.2 Results and Discussion

6.2.1 Synthesis and Structure of CoCl-Ti_8BDC

The Ti_8BDC MOF, with the formula of $Ti_8O_8(OH)_4(BDC)_6$, was prepared from solvothermal reactions of $Ti(O^iPr)_4$ and H_2BDC in methanol and DMF according to the literature procedure.[13] Ti_8BDC was deprotonated with $LiCH_2SiMe_3$ to generate a $Ti_8O_8(OLi)_4(BDC)_6$ intermediate, then metalated with 1 equiv. of $CoCl_2$ to afford CoCl-Ti_8BDC as a turquoise solid (**Figure 6-2**). $CoCl_2$ was only added in an equivalent amount to avoid over-coordination that leads to non-uniform species. The Co content in the metalated MOF was determined to be 0.7 Co per Ti_8 node by ICP-MS.

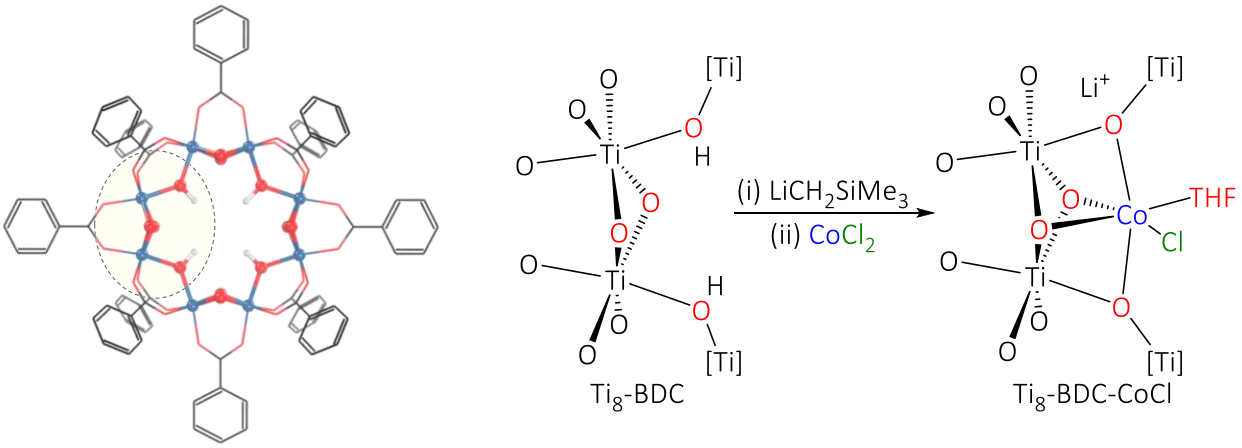

Figure 6-2. Depiction of the tetradentate binding pocket of the Ti_8 node and the cobalt coordination environment within the binding pocket.

The CoCl-Ti_8BDC particles maintained the plate-like morphology of Ti_8BDC by TEM imaging (**Figure 6-3a**). The BET surface area of CoCl-Ti_8BDC was evaluated by nitrogen sorption

isotherms to be 1479 m^2/g, indicating the CoCl-Ti_8BDC maintained similar porosity to Ti_8BDC precursor, which has a BET surface area of 1552 m^2/g (**Figure 6-3b**).

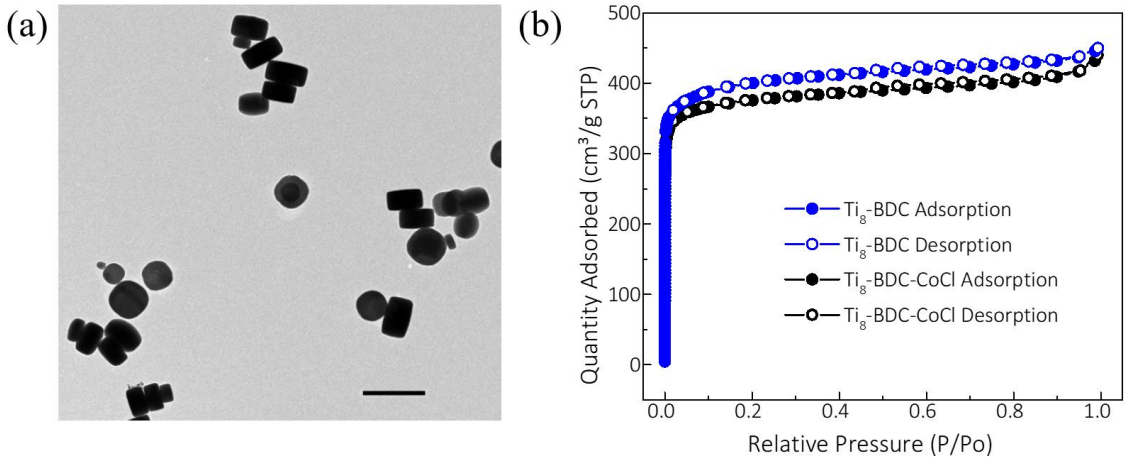

Figure 6-3. (a) TEM image of CoCl-Ti_8BDC, showing the same morphology as pristine Ti_8BDC. The scale bar is 1 μm. (b) Nitrogen sorption isotherms of Ti_8BDC and CoCl-Ti_8BDC.

The crystallinity of CoCl-Ti_8BDC was characterized by PXRD analysis (**Figure 6-4**). The PXRD patterns of CoCl-Ti_8BDC (blue) is identical to that of pristine Ti_8BDC, indicating the high framework stability toward metalation.

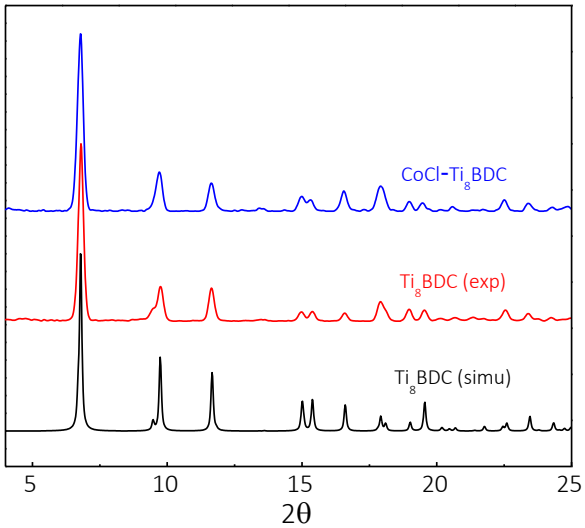

Figure 6-4. PXRD pattern of CoCl-Ti_8BDC compared to that of non-metalated MOF.

The Co coordination environment of CoCl-Ti_8BDC was first optimized by DFT calculation using the Perdew–Burke–Ernzerhof (PBE) functional.[15-16] DFT optimization converged at a geometry where the octahedral cobalt ion was docked into the tetraoxo binding pocket within Ti_8 octagonal plane, by coordinating to two anionic bridging-oxo (μ_2-O^-) groups in the axial positions and two neutral bridging-oxo (μ_2-O) groups in the equatorial positions (**Figure 6-5**). The other two coordination moieties from chloride and THF are located above and below the Ti_8 plane. The Ti_8 node thus acts as a tetradentate oxide ligand to form the $[(\mu_2\text{-O})_2(\mu_2\text{-O}^-)_2\text{CoCl(THF)}]^-$ species. The average calculated distances for Co-(μ_2-O^-) is 2.05 Å and Co-(μ_2-O) distance is 2.27 Å, consistent with the general trend that anionic oxide ligands form shorter M-O bonds than the neutral oxo ligand. Spin density plot from DFT calculation indicates the spin-localization around Co center, as a result of having divalent Co with three unpaired electrons (**Figure 6-6**).[17]

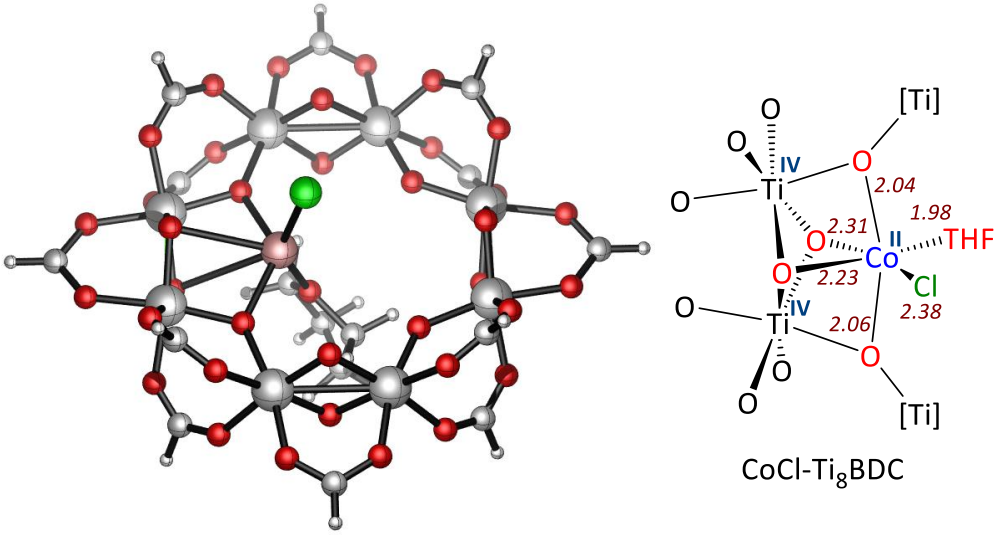

Figure 6-5. Optimized structure and measured bond distances of CoCl-Ti_8BDC fragment.

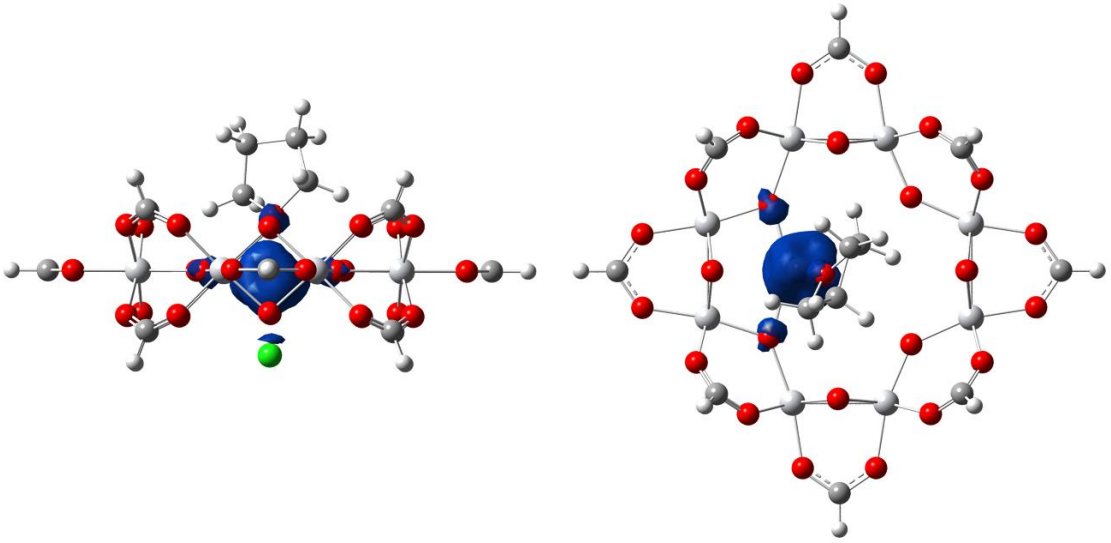

Figure 6-6. Spin density plot of CoCl-Ti$_8$BDC fragment, side view (left) and top view (right). The Co center have a spin density of 2.79.

The calculated structural model well fitted the Co K-edge EXAFS of CoCl-Ti$_8$BDC, with average fitted distances for Co-(μ_2-O$^-$) of 2.03 Å and Co-(μ_2-O) of 2.25 Å (**Figure 6-7**). These Co-(OTi) experimental bond distances are consistent with that calculated from DFT and those reported in the literature.

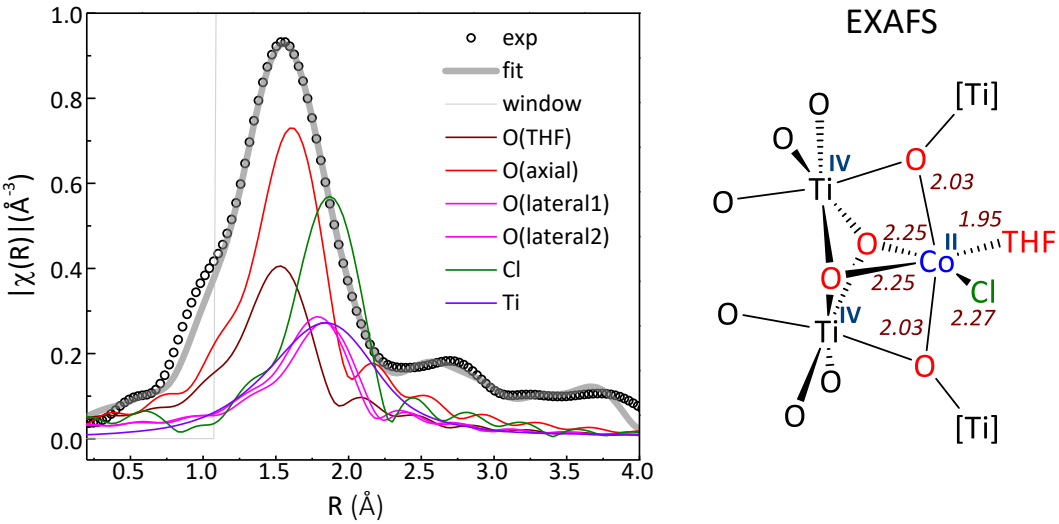

Figure 6-7. EXAFS spectra (gray circles) and fits (black solid line) in R-space at the Co K-edge adsorption of CoCl-Ti$_8$BDC.

6.2.2 Co^{II} center in CoH-$Ti^{III}_2Ti^{IV}_6$BDC

The CoCl-Ti_8BDC material was treated with $NaBEt_3H$ to activate the Co-Cl bond. The MOF color immediately changed from turquoise to navy and then to black with concomitant evolution of H_2 to afford "CoH-Ti_8BDC" as a black solid. This process was proposed to proceed via Co-mediated reductive elimination of H_2 from two Co-H groups, while the electron from the hydrides were spillover to the Ti^{IV} centers (**Figure 6-8**). Several reactivity and spectroscopic studies were performed to validate the structure and electronic properties of the proposed CoH-$Ti^{III}_2Ti^{IV}_6$BDC species.

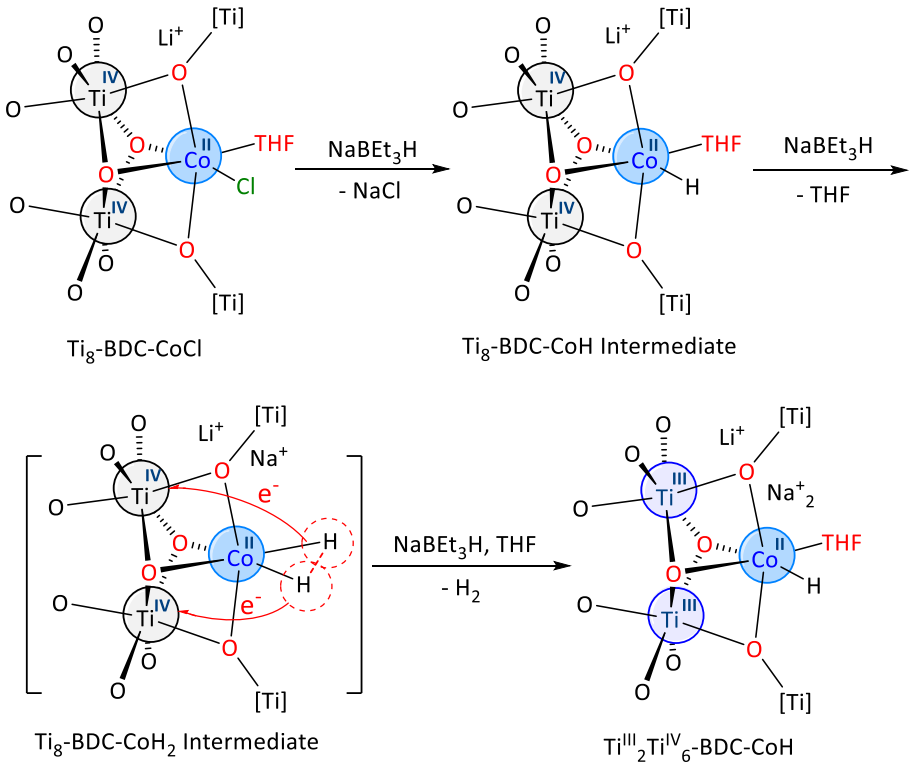

Figure 6-8. (a) Proposed reduction of CoCl-Ti_8BDC to $Ti^{III}_2Ti^{IV}_6$-BDC-CoH with $NaBEt_3H$ via electron spill-over from Co to Ti through reductive elimination of H_2.

The Co K-edge EXAFS spectra significantly changed after the $NaBEt_3H$ activation (**Figure 6-9**). The peak intensity has decreased and the peak position has shifted to lower R,

indicating the absence of Co-Cl scattering pathway. This experiment suggests the successful activation of strong Co-Cl bond through $NaBEt_3H$ treatment.

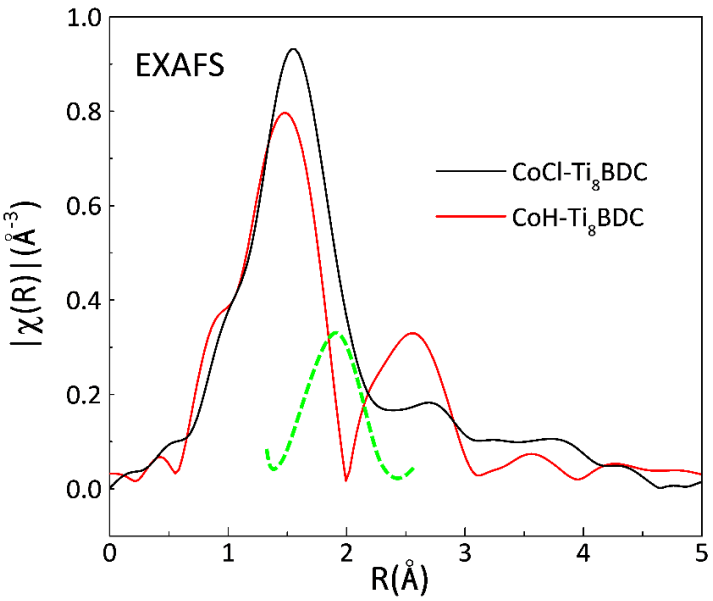

Figure 6-9. Comparison of EXAFS spectra of CoH-Ti_8BDC and the CoCl-Ti_8BDC precursor.

EPR, XPS, and XANES were employed to determine the Co oxidation state after the $NaBEt_3H$ reduction process. The EPR spectra of the reduced sample in toluene clearly displayed two sets of intense signals (**Figure 6-10**). The first sharp isotropic signal, with a g-value of 1.94, agrees with those of Ti^{III} species reported in the literature.[18-20] The second set of broad signals, with an average g-value of 2.32, is consistent with the high-spin state of a divalent octahedron Co species reported in the literature.[21] High-spin Co^{II} centers indicate the weak field nature of the oxo ligands, which is different from those of the widely investigated C-, N-, or P-based pincer ligands.[22-23] Such oxo-based ligands are difficult to access in molecular systems for their tendency to bridge multiple metal centers, highlighting the unique advantage of anchoring catalysts onto MOF nodes.

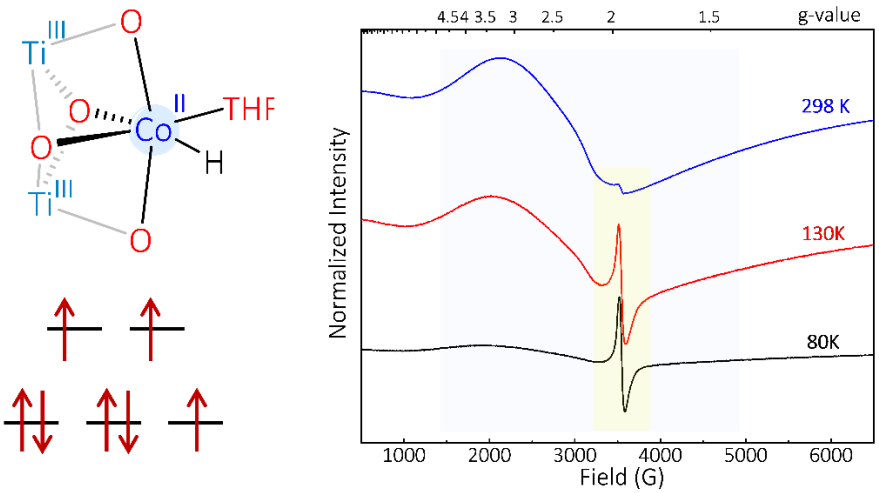

Figure 6-10. Proposed Co electron configuration in CoH-$Ti^{III}_2Ti^{IV}_6$BDC and the EPR spectra at 80 K (black), 130 K (red), and 293 K (blue). The signal from Ti^{III} is shaded in yellow, and the signals from CoII are shaded in blue.

Co 2p XPS data of the reduced MOF displayed strong $2p_{3/2}$ and $2p_{1/2}$ peaks at 781.4 eV and 797.4 eV along with strong $2p_{3/2}$ and $2p_{1/2}$ shake-up peaks at 786.8 eV and 803.4 eV, which are characteristic of a Co^{II} species (**Figure 6-11**). The Co K-edge XANES spectra of CoH-$Ti^{III}_2Ti^{IV}_6$BDC was compared against that of $CoCl_2$ standard, which shows identical pre-edge feature at 7709 eV, further proving the divalency of Co centers in CoH-$Ti^{III}_2Ti^{IV}_6$BDC. Both the EPR, XPS, and XANES spectra indicated Co^{II} centers were maintained during the treatment with $NaBEt_3H$, we thus inferred the reduction occurred exclusively at the Ti centers.

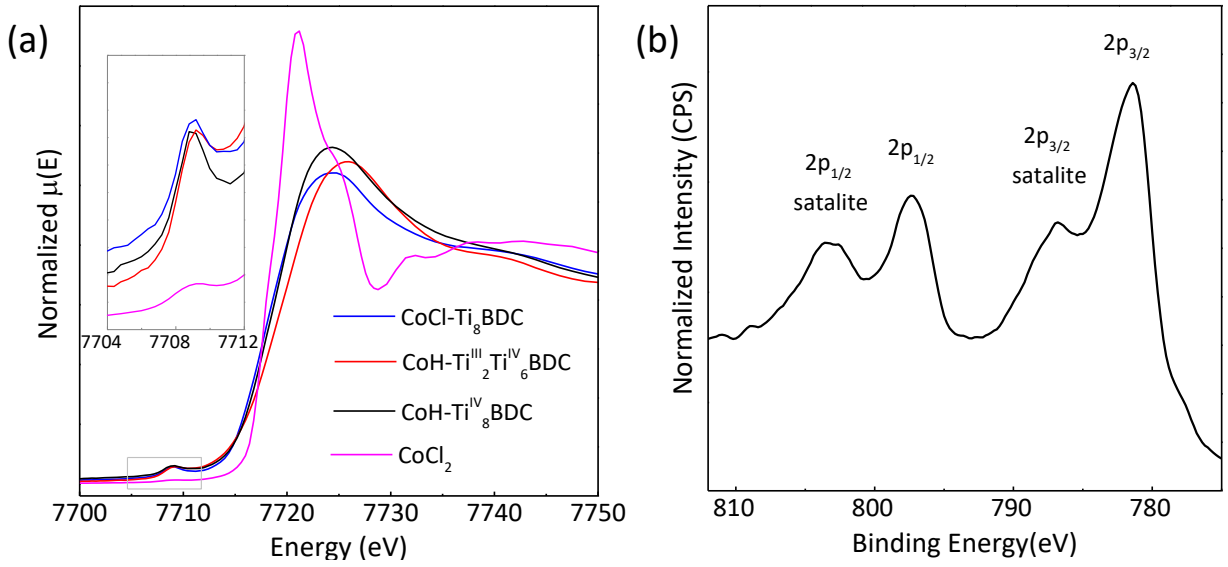

Figure 6-11. (a) Co K-edge XANES spectra of CoCl-Ti_8BDC (blue), $Ti^{III}_2Ti^{IV}_6$-BDC-CoH (red) and Ti^{IV}_8BDC-CoH (black) compared against $CoCl_2$ (magenta). The pre-edge of the three MOFs aligned well to that of $CoCl_2$, showing Co^{II} centers in all three MOFs. (b) Co 2p XPS spectra of $Ti^{III}_2Ti^{IV}_6$-BDC-CoH displayed 4 peaks at 781.4 eV ($2p_{3/2}$), 786.8 eV ($2p_{3/2}$ shake-up), 797.4 eV ($2p_{1/2}$) and 803.4 eV ($2p_{1/2}$ shake-up).

6.2.3 Ti^{III} center in CoH-Ti_8BDC

Besides the Ti^{III} EPR features at g-value of 1.94, the partial reduction of Ti^{IV} to Ti^{III} was also evidenced by XPS and XANES analysis. The Ti_8BDC was used as a standard for analysing Ti 2p XPS data, which displayed $2p_{3/2}$ peaks at 458.8 eV and $2p_{1/2}$ at 464.6 eV. For the CoH-$Ti^{III}_2Ti^{IV}_6$BDC, The Ti overall $2p_{3/2}$ and $2p_{1/2}$ binding energies shifted lower to 458.4 eV and 464.3 eV, respectively, consistent with partial reduction of Ti^{IV} centers (**Figure 6-12**). Fitting of the $2p_{3/2}$ peak with Ti^{III} and Ti^{IV} components converged at 1:3 ratio, with binding energy of 458.0 eV for Ti^{III} and 458.5 eV for Ti^{IV}. The two additional signals at 461.2 eV and 466.9 eV are likely the Ti^{III} shake-up satellites, which are characteristic features of the unpaired d electrons of Ti^{III} centers.[26-27]

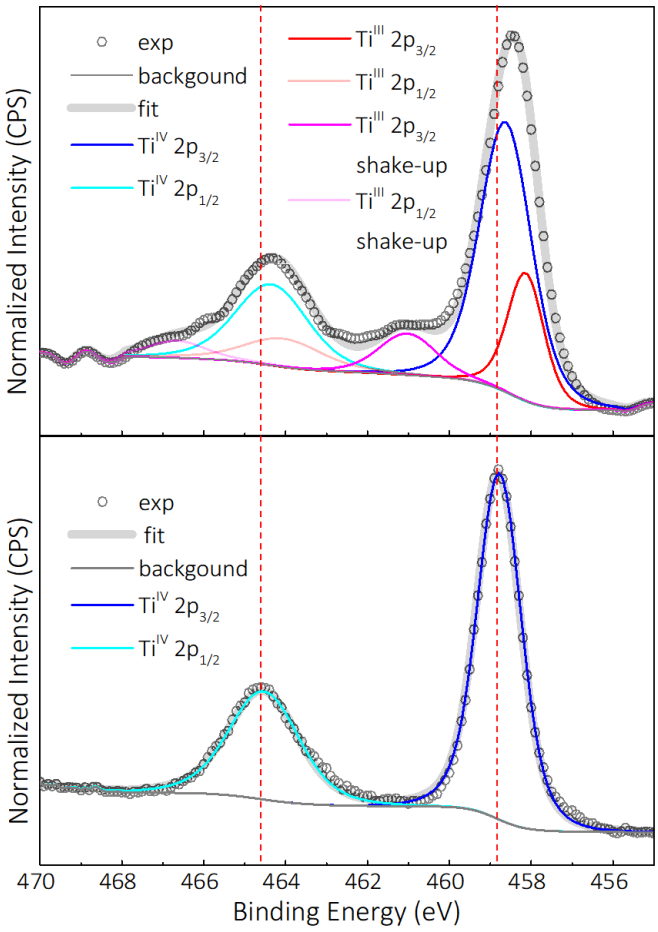

Figure 6-12. Ti 2p XPS spectra of Ti^{IV}_8BDC (bottom) and CoH-$Ti^{III}_2Ti^{IV}_6$BDC (top). The experimental data (gray circles) fit well (gray bold line) with a 3:1 ratio of Ti^{IV} and Ti^{III} species.

The Ti pre-edge feature of CoH-$Ti^{III}_2Ti^{IV}_6$BDC showed an overall 0.3 eV shift to lower energy than that of CoCl-Ti^{IV}_8BDC, due to the presence of Ti^{III} centers which enables the lower energy $1s \rightarrow 3d^1$ transition in addition to the Ti^{IV} centered $1s \rightarrow 3d^0$ transition (**Figure 6-13**). Furthermore, the pre-edge region of CoH-Ti_8BDC has higher overall intensity than that of the CoCl-Ti_8BDC, presumably due to the distortion of $[Ti^{III}O_6]^{3-}$ or $[Ti^{IV}O_6]^{2-}$ octahedra caused by the partial reduction, which leads to higher probability of spin-forbidden 1s-3d transitions. In contrast, a CoH-Ti^{IV}_8BDC control (described later) displays identical pre-edge features as CoCl-Ti_8BDC, validating the XANES features changes result from the Ti^{III} centers.[27-28]

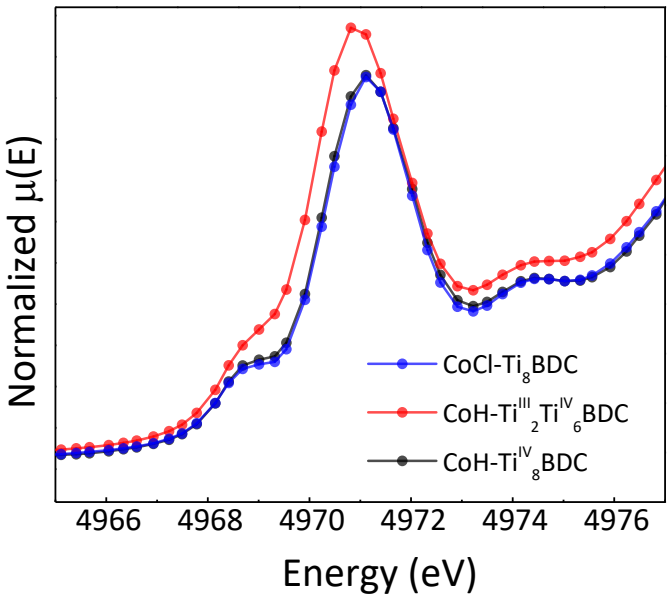

Figure 6-13. XANES analysis of CoCl-Ti^{IV}_8BDC (blue), CoH-$Ti^{III}_2Ti^{IV}_6$BDC (red), and CoH-Ti^{IV}_8BDC (black) at the Ti K-edge pre-edge region.

To quantify the amount of Ti^{III} species per Ti_8 cluster, the reduced MOF was titrated with ferrocenium hexafluorophosphate ($FcPF_6$, 1 mM in CH_2Cl_2) to determine the amount of ferrocene product.[24] GC quantification indicated the formation of 2.07±0.11 equiv. of ferrocene w.r.t. Co. The Co^{II} centers were not oxidized by Co XANES analysis. The hydride groups in Co-H were known to be poor reductants through electron transfer pathway.[25] We thus conclude that the Fc^+ oxidation reaction only occurs at Ti^{III} centers, suggesting a $Ti^{III}_2Ti^{IV}_6$ composition of the Ti_8 node, giving the overall formula of Co^{II}H-$Ti^{III}_2Ti^{IV}_6$BDC. EXAFS fitting revealed that the Co centers in the oxidized MOF maintained identical coordination environment (**Figure 6-14**). CoH-Ti^{IV}_8BDC was used as a control for both spectroscopic analyses and catalytic reactions in subsequent studies.

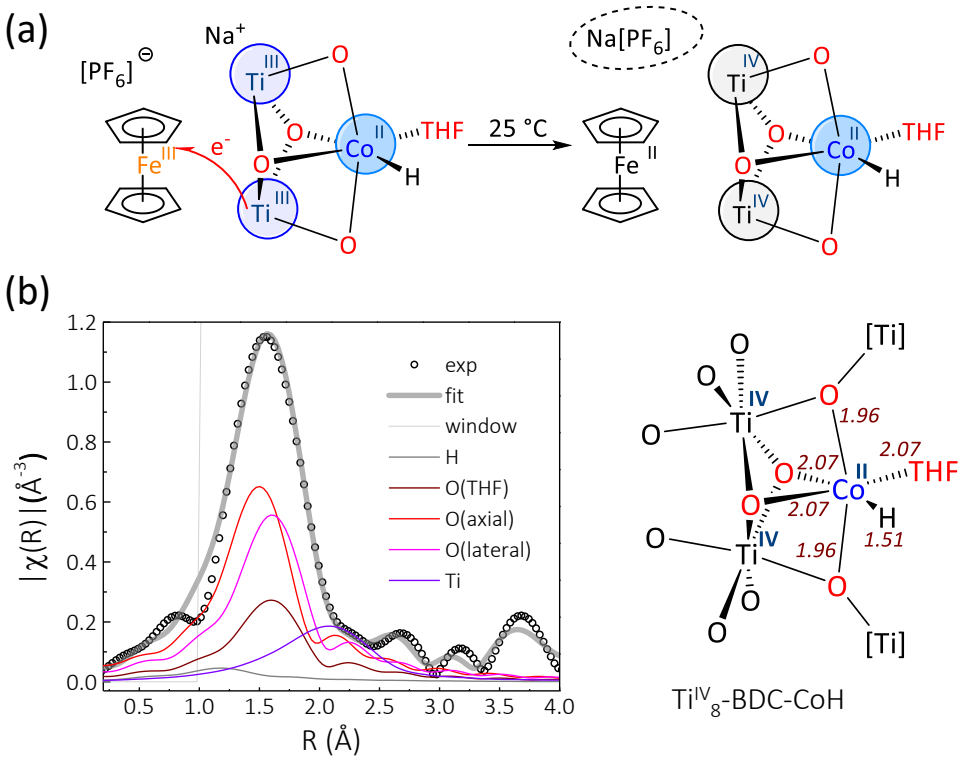

Figure 6-14. (a) Oxidation of Ti^{III} to Ti^{IV} with $FcPF_6$ through an electron transfer reaction. (b) EXAFS spectrum (gray circles) and fit (black solid line) in R-space at the Co K-edge adsorption of CoH-Ti^{IV}_8BDC. The scattering paths of Co to THF-oxygen (wine), axial oxo (red), equatorial oxo (pink), hydride (gray), and titanium (purple) are shown in dashed lines.

The Co coordination environment and electronic structure in $Ti^{III}_2Ti^{IV}_6$-BDC-CoH were studied through DFT calculation using the PBE functional. The DFT optimized structure was shown in **Figure 6-15**. The Co centers in CoH-$Ti^{III}_2Ti^{IV}_6$BDC maintained a similar coordination geometry to that in CoCl-Ti_8BDC. The calculated Co-(μ_2-O^-) distance is 1.94 Å and the Co-(μ_2-O) distances are 2.10/2.41 Å. The spin density of the system was calculated to determine the electronic configuration of this system with five net spins (two on the Ti^{III} pair and three on Co^{II}). The spin calculation indicates the spin density is localized both on the Co^{II} center and the neighbouring Ti^{III} centers, matching well with the assigned oxidation states for these metals. The overall doublet spin state, which features ferromagnetic coupling between the two Ti^{III} centers and

antiferromagnetic coupling between the Ti^{III} and Co^{II} centers, has lower energy than the quartet and sextet spin states. Interestingly, other than the two proximal Ti^{III} centers to Co^{II}, the remote Ti^{IV} centers also displayed small amount of spin density, possibility due to spin-delocalization through different Ti centers (**Figure 6-16**). The fine details regarding the energy profile and interconversion of different spin states require further study.

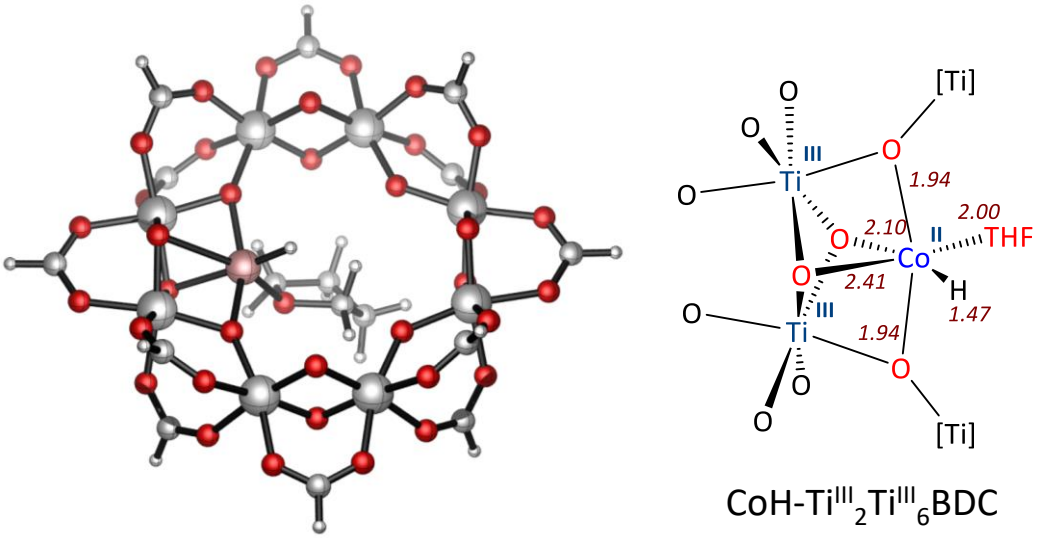

Figure 6-15. DFT optimized geometry of CoH-$Ti^{III}_2Ti^{IV}_6$BDC and the bond distances around Co center.

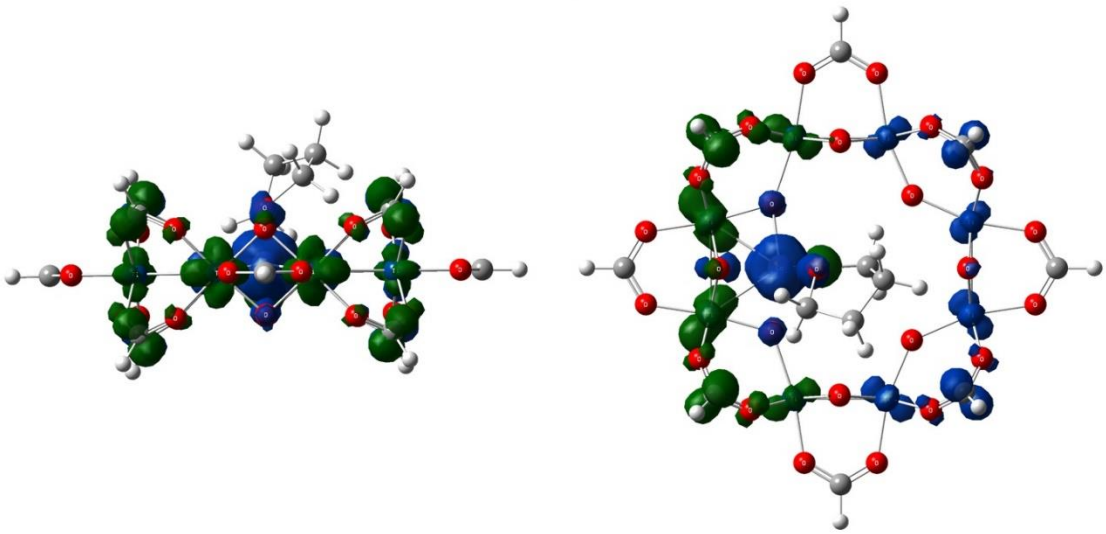

Figure 6-16. Spin density plot of $Ti^{III}_2Ti^{IV}_6$-BDC-CoH fragment with doublet spin state, side view (left) and top (view).

The calculated structure of CoH-$Ti^{III}_2Ti^{IV}_6$BDC is a very good model to fit the Co K-edge EXAFS data, with the fitted Co-(μ_2-O^-) distance of 2.00 Å and the Co-(μ_2-O) distance of 2.17/2.48 Å. The bond distances from EXAFS fitting are given in **Figure 6-17**.

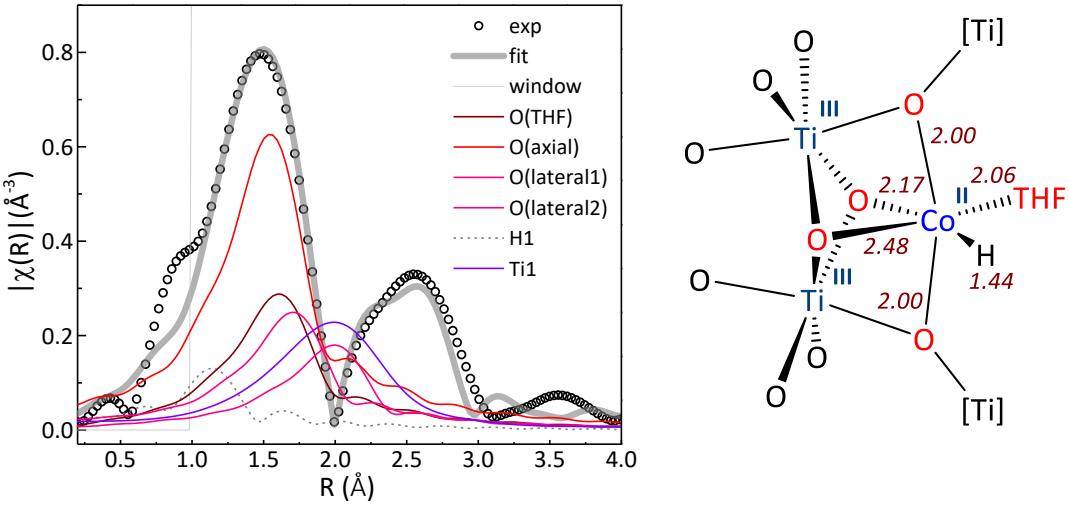

Figure 6-17. EXAFS spectrum (gray circles) and fit (black solid line) in R-space at the Co K-edge adsorption of CoH-$Ti^{IV}_6Ti^{III}_2$BDC. The scattering paths of Co to THF-oxygen (wine), axial oxo (red), equatorial oxo (pink), hydride (gray), and titanium (purple) are shown in dashed lines.

6.2.4 CoH-$Ti^{III}_2Ti^{IV}_6$BDC catalyzed arene hydrogenation

Arene hydrogenation is an important industrial process to produce of a large diversity of commodities and fine chemicals, including cyclohexane analogues, polyester monomers, and plasticizers. With the ever stringent environmental and health regulations over carcinogenic aromatic compounds, dearomatization reactions like arene hydrogenation are playing a bigger role in diesel fuel refining/upgrading and polymer productions. Conventional arene hydrogenation catalysts are based on Ni, Ru, Pd, or Pt nanoparticles supported on metal oxides or carbon materials. However, the exact structures and reaction mechanisms of these catalysts remain elusive due to

the complication from the multiple catalytic species and involvement of multimetallic catalytic pathways.

Although many small-molecule complexes were reported to hydrogenate arenes, most of them were later shown to be simply precursors to nanoparticle catalysts, evidenced by their long induction periods, short life times, and mercury deactivation. Arenes are very inert and only weakly coordinate to single metal center, so they are very difficult to hydrogenate with a monometallic catalyst. To date, there are very few examples of single-site arene hydrogenation catalysts, either for late transition metals or early transition metals. CoH-$Ti^{IV}_6Ti^{III}_2$BDC is a unique MOF-based single-site solid catalyst which represents a unique platform to study non-nanoparticle catalyzed arene hydrogenation.

Benzene was chosen as the model compounds to optimize reaction conditions. Even at room temperature, CoH-$Ti^{IV}_6Ti^{III}_2$BDC catalyzed the hydrogenation of benzene to cyclohexane in 66% yield, with a TON of 330. At elevated temperature of 120 °C under 50 bar H_2, only 0.05 mol% of CoH-$Ti^{IV}_6Ti^{III}_2$BDC catalyst was needed to quantitatively hydrogenate benzene in 1.5 h, affording a TOF of 1333 h^{-1} (**Table 6-1**). At 140 °C and 120 bar H_2, an impressive TOF of 7017 h^{-1} was obtained with a catalyst loading of 0.005 mol%. To our knowledge, this is one of the highest TOFs reported for a benzene hydrogenation catalyst, and one of the very few catalysts to hydrogenate benzene under room temperature. Exceptionally high TOFs were also obtained with substituted arenes. At 160 °C and 50 bar H_2, toluene was hydrogenated to methylcyclohexane in 42% yield in 1.5 h, with a TOF of 5600 h^{-1}.

Table 6-1. Optimization of CoH-$Ti^{III}_2Ti^{IV}_6$BDC catalyzed arene hydrogenation.[a]

	Reaction	Catalyst (mol % Loading)	T (°C)	Time	Yield	TON	TOF (h^{-1})
1	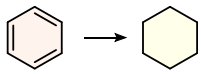	CoH-$Ti^{III}_2Ti^{IV}_6$BDC (0.05 %)	120	1.5 h	100 %	≥2000	1333
2[b]		CoH-$Ti^{III}_2Ti^{IV}_6$BDC (0.005 %)	140	1.5 h	53 %	10526	7017
3		CoH-$Ti^{III}_2Ti^{IV}_6$BDC (0.05 %)	80	18 h	100 %	≥2000	111
4		CoH-$Ti^{III}_2Ti^{IV}_6$BDC (0.2 %)	25	18 h	66 %	330	18
5	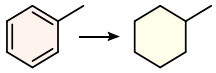	CoH-$Ti^{III}_2Ti^{IV}_6$BDC (0.005 %)	160	1.5 h	42 %	8400	5600
6		CoH-$Ti^{III}_2Ti^{IV}_6$BDC (0.05 %)	120	1.5 h	76 %	1520	1013
7		CoH-Ti^{IV}_8BDC (0.05 %)	120	1.5 h	0 %	0	0

[a]Reaction conditions: Parr high pressure reactor, freshly prepared CoH-$Ti^{III}_2Ti^{IV}_6$BDC, neat arene substrate, 50 bar H_2 unless specified. [b]120 bar H_2.

CoH-$Ti^{III}_2Ti^{IV}_6$BDC was reused for at least 6 times for benzene hydrogenation without any drop in yields, highlighting the robustness and recyclability of this catalyst (**Figure 6-18**). The amount of Co and Ti leached into the reaction mixture is less than 0.1%, indicating the high catalyst stability under reaction condition, even at very high temperature of 160 °C.

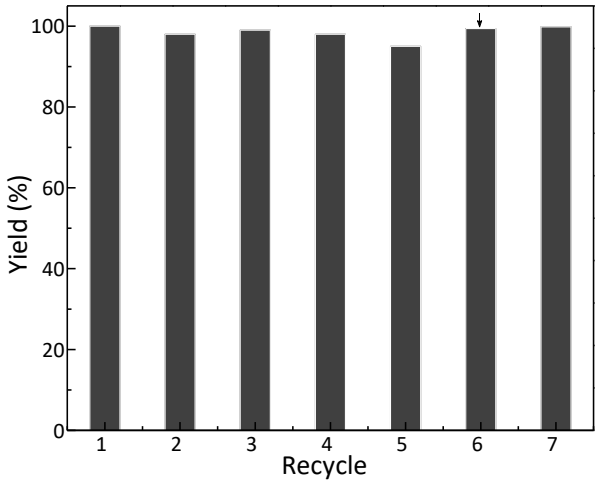

Figure 6-18. Recycle experiment for $Ti^{III}_2Ti^{IV}_6$-BDC-CoH catalyzed benzene hydrogenation. Arrow indicates catalysts reactivation with $NaBEt_3H$ before that run.

Mercury test on the CoH-$Ti^{III}_2Ti^{IV}_6$BDC catalyzed benzene hydrogenation ruled out the role of Co nanoparticles. The high thermal stability of CoH-$Ti^{III}_2Ti^{IV}_6$BDC is crucial in terms of potential industrial application considering the exothermic nature of arene hydrogenation reactions.

To investigate the impact of metal-support interactions on the catalyst performance, the CoH-Ti^{IV}_8BDC generated from $FcPF_6$ oxidation was also tested for toluene hydrogenation. At 0.05 mol% catalyst loading and under identical reaction conditions, Ti^{IV}_8BDC-CoH displayed no catalytic activity while CoH-$Ti^{III}_2Ti^{IV}_6$BDC converted toluene to cyclohexane in 76 % yield (**Table 6-1**, entries 6-7). This experiment indicates that the reduction of Ti^{IV}_8 support to $Ti^{III}_2Ti^{IV}_6$ is crucial for the catalytic activity, by providing a more electron-donating Ti^{III}-oxo ligand to afford electron-rich high-spin Co^{II} centers which efficiently dearomatize arenes. This result offers a molecular understanding for the role of reduced Ti in the SMSI effect, which is often observed in TiO_2-supported catalysts but never validated with a model system.

CoH-$Ti^{III}_2Ti^{IV}_6$BDC catalyzed arene hydrogenation exhibited an exceptionally broad substrate scope (**Table 6-2**). Mono-substituted benzenes, including toluene, ethylbenzene, cumene, and *n*-propylbenzene, were readily hydrogenated to corresponding saturated hydrocarbons in almost quantitative yields and TONs. Disubstituted benzenes, including *p*-, *m*-, and *o*-xylenes, were quantitatively hydrogenated to corresponding dimethylcyclohexanes with TONs of 2000. Mesitylene was hydrogenated to 1,3,5-trimethylcyclohexane in 84% yield at 160 °C. Impressively, at 0.2 mol% catalyst loading, polyarenes, including naphthalene and fluorene, were perhydrogenated in 100% and 85% yields, respectively. One unique feature of MOF catalysts is the size-exclusion effect, originating from the uniform shape and size of MOF channels/cages. In contrast to fluorene, anthracene was hydrogenated in only 2% conversion under identical reaction

conditions. $Ti^{III}_2Ti^{IV}_6$-BDC-CoH is thus potentially useful in industrially relevant size-selective arene hydrogenation.

Table 6-2. CoH-$Ti^{III}_2Ti^{IV}_6$BDC Catalyzed Hydrogenation of Nonpolar Arenes.

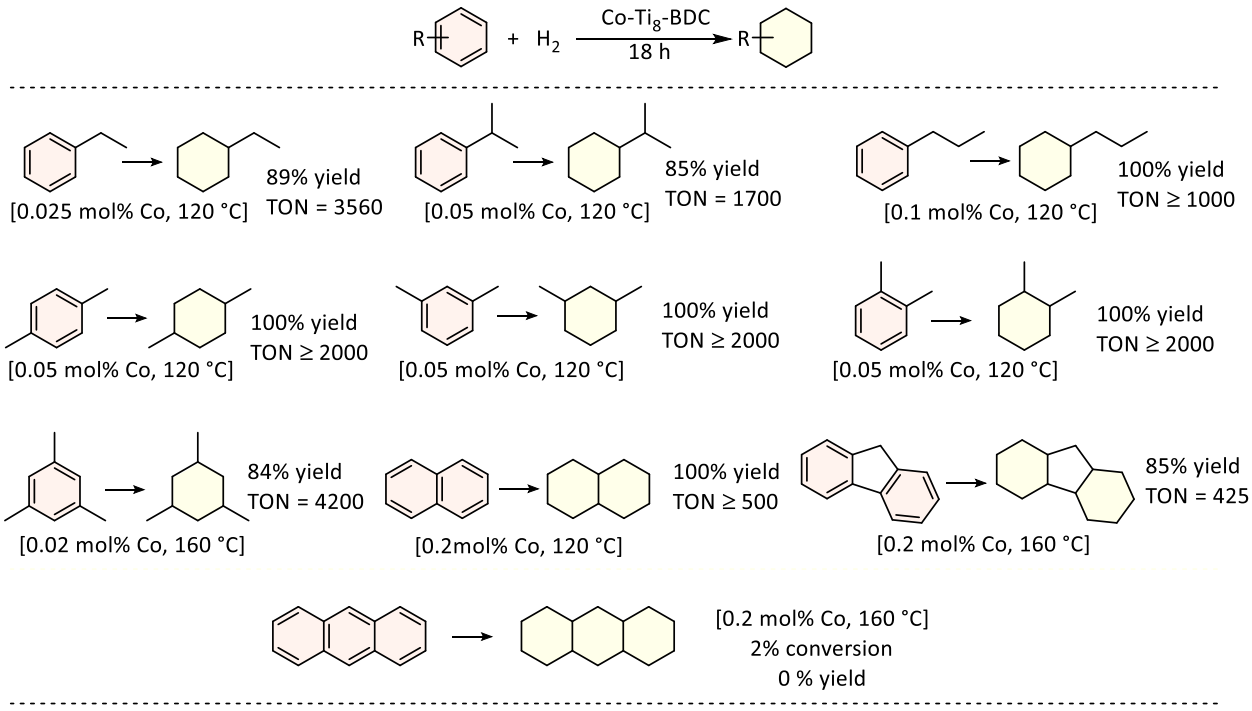

Reaction conditions: Parr high pressure reactor, freshly prepared CoH-$Ti^{III}_2Ti^{IV}_6$BDC, neat arene substrate, 50 bar H_2.

CoH-$Ti^{III}_2Ti^{IV}_6$BDC also tolerates a variety of polar substituents on arenes (**Table 6-3**). Arenes with amino groups, including aniline, α-methylbenzylamine, and N-methylbenzylamine, were all hydrogenated in high yields without substrate/product inhibition. Aryl ethers, such as anisole and 1,4-dimethoxybenzene, and benzylic ethers, such as dibenzyl ether, were all hydrogenated to corresponding cyclohexyl ethers in good yields without ether hydrogenolysis. The hydrogenation of dialkyl phthalates and terephthalates to corresponding aliphatic esters models an important industrial process for producing green plasticizers, which cannot be achieved with other reported arene hydrogenation catalysts due to electron deficiency and steric hindrance. CoH-

$Ti^{III}_2Ti^{IV}_6$BDC hydrogenated diethyl phthalate to produce diethyl cyclohexane-1,2-dicarboxylate in 31% yield at 160 °C.

Table 6-3. CoH-$Ti^{III}_2Ti^{IV}_6$BDC Catalyzed Hydrogenation of Polar Arenes.

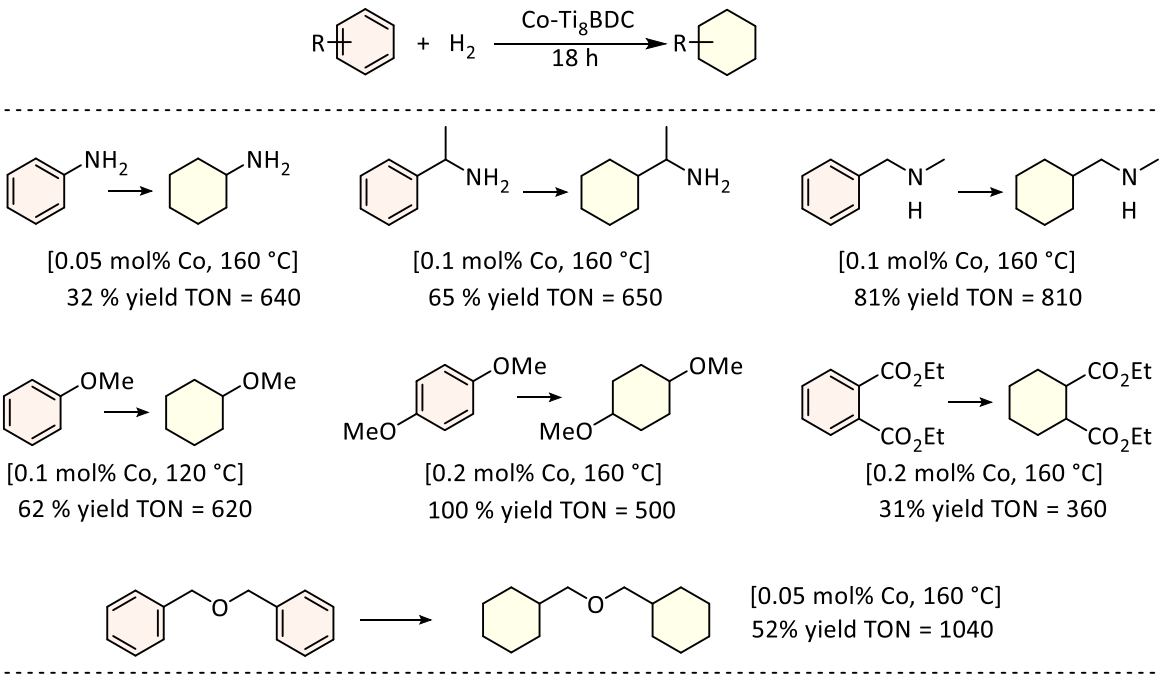

Reaction conditions: Parr high pressure reactor, freshly prepared CoH-$Ti^{III}_2Ti^{IV}_6$BDC, neat arene substrate, 50 bar H_2.

6.2.5 CoH-$Ti^{III}_2Ti^{IV}_6$BDC catalyzed heteroarene hydrogenation

Heteroarene hydrogenation is an efficient method to generate saturated heterocycles, which are very common structural motifs in pharmaceuticals and biologically active natural products. However, heteroarenes are generally more difficult to hydrogenate than other unsaturated compounds due to the aromaticity-stabilization and the heteroatom inhibition. Impressively, CoH-$Ti^{III}_2Ti^{IV}_6$BDC is highly active for hydrogenating a broad scope of heteroarenes (**Table 6-4**). At 0.05 mol% loading, CoH-$Ti^{III}_2Ti^{IV}_6$BDC hydrogenated pyridine to piperidine in 94% yield without forming any ring-cleavage side-products, making it one of the most active and selective catalysts

for pyridine reduction. More hindered pyridines including 2,6-lutidine and 2,4,6-collidine were also hydrogenated in almost quantitative yields to the corresponding piperidines.

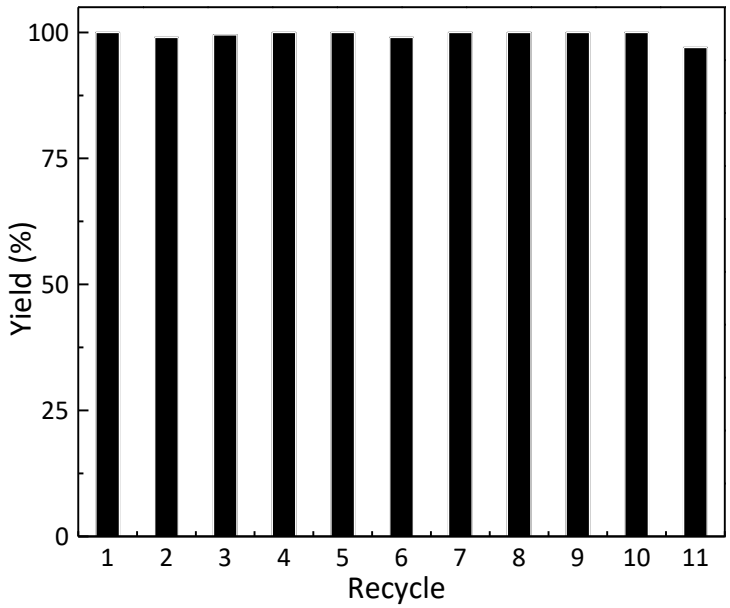

Figure 6-19. Recycle experiment for CoH-$Ti^{III}_2Ti^{IV}_6$BDC catalyzed 2,6-lutidine hydrogenation.

Furthermore, the catalyst was recycled 10 times for the hydrogenation of 2,6-lutidine without any decrease in yields, supporting the heterogeneity and robustness of the MOF catalyst (**Figure 6-19**). Quinoline derivatives including 3-methylquinoline and 2,6-dimethylquinoline were also perhydrogenated to the corresponding decahydroquinolines in over 90% yields. For substrates with a strong electron withdrawing group (*e.g.* 6-chloroquinoline), the hydrogenation only occurred at the non-substituted rings. Other heterocyclic systems including indole and benzofuran, were also semi-hydrogenated to indoline and dihydrobenzofuran in good yields.

Table 6-4. CoH-Ti_8BDC Catalyzed Heteroarene Hydrogenation.

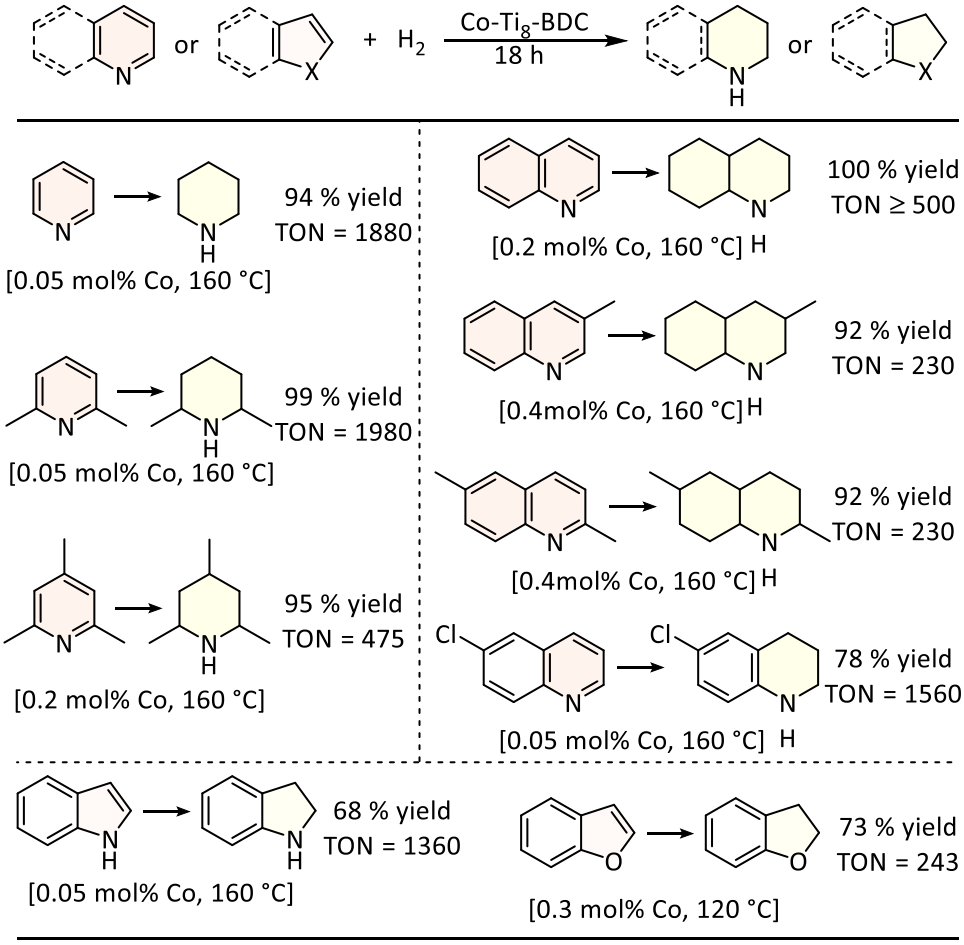

Reaction condition: Parr high pressure reactor, freshly pre-pared $Ti^{III}_2Ti^{IV}_6$-BDC-CoH, neat heteroarene substrate, 50 bar H_2.

6.3 Conclusion

This chapter reports the use of the $Ti_8(\mu_2\text{-}O)_8(\mu_2\text{-}OH)_4$ node of the Ti_8BDC MOF as an excellent molecular model of TiO_2 to support a single-site Co^{II}-hydride catalyst for arene hydrogenation. Upon deprotonation, the Ti-oxo clusters of Ti_8BDC coordinated to Co^{II} centers as a tetradentate ligand to afford CoCl-Ti_8BDC with well-defined coordination environment. Treatment of CoCl-Ti_8BDC with $NaBEt_3H$ leads to partial reduction of the Ti-oxo support through reductive elimination of H_2 followed by electron spillover to Ti. The electronic property of Co^{II}H-

$Ti^{III}_2Ti^{IV}_6$BDC was established based on EPR, XPS, XANES, DFT, and ferrocenium titration studies. The CoH-$Ti^{III}_2Ti^{IV}_6$BDC MOF features electron-donating Ti^{III}-oxo ligands which leads to electron-rich high spin Co^{II} centers. CoH-$Ti^{III}_2Ti^{IV}_6$BDC is one of few highly active structurally well-defined, non-nanoparticle catalysts for arene and heteroarene hydrogenation. Interestingly, the oxidized form of the catalyst (Co^{II}H-Ti^{IV}_8BDC) is totally inactive for arene hydrogenation, therefore proving the crucial role of Ti^{III}-oxo cluster on the catalytic activity of Co^{II}H species. The Ti_8BDC MOF thus provides a molecularly precise model of metal oxo clusters for understanding the SMSI effect of TiO_2-supported heterogeneous catalysts. In general, the uniform structure of MOF node-anchored catalysts allows for the spectroscopic and computational investigations of catalyst structure and reaction pathways, thus promising deeper understanding of the key parameters that modulate catalytic performances and guide the rational design of effective arene hydrogenation catalysts to meet the ever increasing environmental and health regulations for the chemical industry.

6.4 Experimental

6.4.1 Material and Methods

All of the reactions and manipulations were carried out under N_2 with the use of stand-ard inert atmosphere and Schlenk technique unless otherwise indicated. All solvents used were dry and oxygen-free. All of the arene and heteroarene substrates were purchased from Fisher or Aldrich. Solid substrates were used as received while liquid substrates were distilled and dried over 4 Å molecular sieves prior to use. Toluene and tetrahydrofuran were degassed by sparging with N2, filtered through activated alumina columns, and stored under N_2.

Powder X-ray diffraction (PXRD) data was collected on a Bruker D8 Venture diffractometer using a Cu Kα radiation source (l = 1.54178 Å). N_2 sorption experiments were per-formed on a Micrometrics TriStar II 3020 instrument. Thermogravimetric analysis (TGA) was performed in air using a Shimadzu TGA-50 equipped with a platinum pan and heated at a rate of 1.5 °C per min. Electron paramagnetic resonance (EPR) spectra were collected with a Bruker Elexsys 500 X-band EPR spectrometer at 20 K. X-ray photoelectron spectroscopy (XPS) data was collected using an AXIS Nova spectrometer (Kratos Analytical) with monochromatic Al Kα X-ray source. For this instrument, the Al anode was powered at 10 mA and 15 kV, and the instrument work function was calibrated to give an Au $4f_{7/2}$ metallic gold binding energy (BE) of 83.95 eV. Instrument base pressure was ca. 1×10^{-9} Torr, and the analysis area size was 0.3 × 0.7 mm^2. For calibration purposes, the binding energies were referenced to the C 1s peak at 284.8 eV. Survey spectra were collected with a step size of 1 eV and a pass energy of 160 eV. ICP-MS data was obtained with an Agilent 7700x ICP-MS and analyzed using ICP-MS Mas-sHunter version B01.03. Samples were diluted in a 2% HNO_3 matrix and analyzed with a 159Tb internal standard against a 12-point standard curve over the range from 0.1 ppb to 500 ppb. The correlation was >0.9997 for all analyses of interest. Data collection was performed in Spectrum Mode with five replicates per sample and 100 sweeps per replicate. A Shimadzu GC-2010 Plus gas chromatograph equipped with a flame ionization detector (FID) was used for gas chromato-graphic analysis (GC). Column: SH-Rxi-5Sil MS column, 30.0 m in length, 0.25 mm in diame-ter, 0.25 μm in thickness. GC conditions: Injection temperature, 220 °C; Column temperature program, 30 °C hold for 5 min, followed by a ramp of 5 °C/min to 60 °C then a ramp of 10 °C/min to 300 °C; Column flow, 1.21 mL/min. ^1H NMR spectra were recorded on a Bruker NMR 500 DRX spectrometer at 500 MHz,

and referenced to the proton resonance resulting from incomplete deuteration of $CDCl_3$ (δ 7.26) or C_6D_6 (δ 7.16).

6.4.2 Synthesis of Ti_8BDC

Ti_8BDC was synthesized from a modified literature procedure. 1,4-Benzenedicarboxylic acid (500 mg, 3.0 mmol) and titanium isoproproxide (0.6 mL, 2 mmol) were charged to a solution of 9.0 mL of dry dimethylformamide and 1.0 mL of dry methanol. The mixture was stirred gently for 5 minutes at room temperature and then further inserted into a Teflon liner and put into a metallic Parr bomb at 150 °C for 24 hours. After cooling to room temperature, the white solid was recovered by centrifugation and then sequentially washed three times with DMF, three times with THF, and three times with benzene. This solid was then freeze-dried in benzene and stored within an N_2-filled glove box.

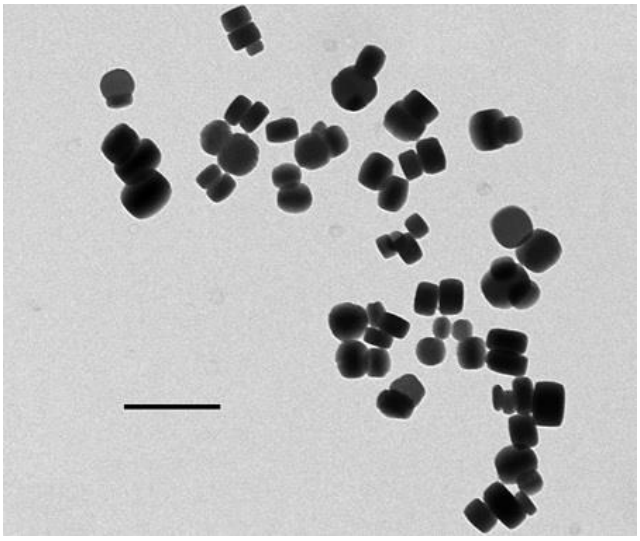

Figure 6-20. TEM image of the Ti_8BDC MOF, showing thick-plate morphology. Scale bar is 1 μm.

6.4.3 Synthesis of CoCl-Ti_8BDC

In an N_2-filled glovebox, $LiCH_2SiMe_3$ (1.0 M in pentane, 2.3 mL, 10 equiv. to Ti_8 node) was added dropwise to a suspension of Ti_8-BDC (500 mg, 29% solvent content by TGA, 0.23 mmol Ti_8 node) in 15 mL hexanes, and the resultant light-yellow mixture was stirred at 25 °C for 6 h. The resulting light-yellow solid was collected through centrifugation, and washed with hexanes six times. The lithiated Ti_8-BDC was then transferred to a vial containing 11.5 mL of a $CoCl_2$ solution in THF (20 mM). This mixture was stirred for 12 h at 25 °C and the turquoise solid was then centrifuged and washed with THF five times. The Ti_8-BDC-CoCl was freeze-dried in benzene and stored in the glovebox for further use. ICP-MS analysis showed a Ti/Co ratio of 11.4, indicating 0.7 Co per Ti_8 node. PXRD, TEM and BET showed the crystallinity of MOF was maintained after metalation.

6.4.4 Typical Procedure for CoH-$Ti^{III}_2Ti^{IV}_6$BDC Catalyzed Arene Hydrogenation

Scheme 6-1. Hydrogenation of benzene to cyclohexane.

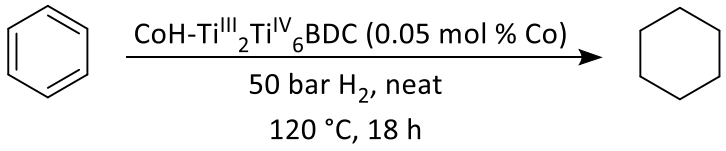

The $Ti^{III}_2Ti^{IV}_6$-BDC-CoH catalyzed hydrogenation of arenes was set up in Parr reactor. Typically, in an N_2-filled glove box, CoCl-Ti_8BDC (5 μmol of Co) in 1.0 mL heptane was charged into a glass vial. $NaBEt_3H$ (10 equiv. to Co, 50 μL, 1.0 M in toluene) was then added to the vial and the mixture was reacted for 30 min. The solid was then centrifuged, washed with heptane three times, and transferred to a Parr reactor with a glass liner using benzene (0.89 mL, 10 mmol). The reactor was sealed in the glovebox, and then charged with hydrogen to 50 bar. After stirring at 120 °C for 18 h, the pressure was released and the MOF catalyst was removed from the reaction

mixture via centrifugation. The supernatant was then analyzed by ^{1}H NMR, revealing a 100% yield of cyclohexane. ICP-MS analysis of the supernatant showed <0.1% leaching of Co from the CoH-$Ti^{III}_{2}Ti^{IV}_{6}$BDC catalyst.

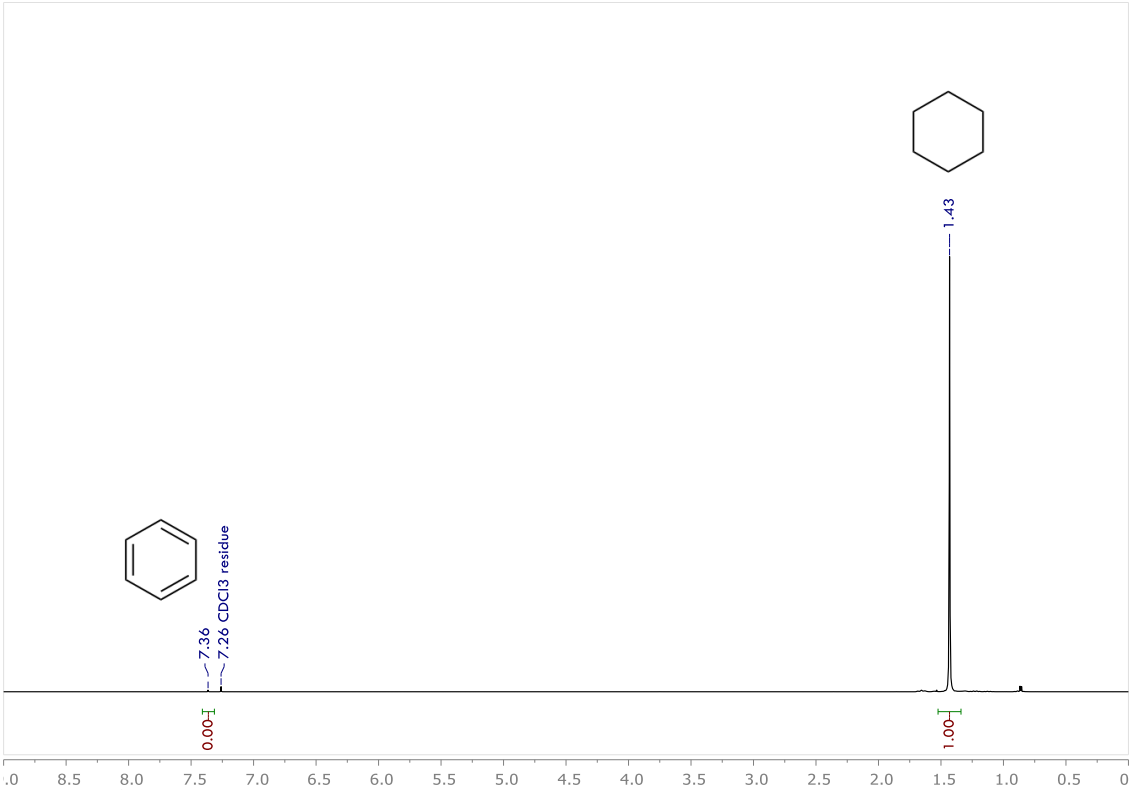

Figure 6-21. ^{1}H NMR spectrum (500 MHz, $CDCl_3$) of crude reaction product, showing complete hydrogenation of benzene to cyclohexane.

6.5 References

1. Bourikas, K.; Kordulis, C.; Lycourghiotis, A., Titanium Dioxide (Anatase and Rutile): Surface Chemistry, Liquid–Solid Interface Chemistry, and Scientific Synthesis of Supported Catalysts. *Chem. Rev.* **2014,** 9754-9823.

2. Siddiqi, G.; Mougel, V.; Copéret, C., Highly Active Subnanometer Au Particles Supported on TiO2 for Photocatalytic Hydrogen Evolution from a Well-Defined Organogold Precursor, [Au5(mesityl)5]. *Inorg. Chem.* **2016,** 4026-4033.

3. Matsubu, J. C.; Zhang, S.; DeRita, L.; Marinkovic, N. S.; Chen, J. G.; Graham, G. W.; Pan, X.; Christopher, P., Adsorbate-mediated strong metal–support interactions in oxide-supported Rh catalysts. *Nat. Chem.* **2017,** 120-127.

4. Tauster, S., Strong metal-support interactions. *Acc. Chem. Res.* **1987,** 389-394.

5. Park, J. Y.; Baker, L. R.; Somorjai, G. A., Role of Hot Electrons and Metal–Oxide Interfaces in Surface Chemistry and Catalytic Reactions. *Chem. Rev.* **2015,** 2781-2817.

6. Dulub, O.; Hebenstreit, W.; Diebold, U., Imaging Cluster Surfaces with Atomic Resolution: The Strong Metal-Support Interaction State of Pt Supported on TiO2 (110). *Phys. Rev. Lett.* **2000,** 3646-3649.

7. Chen, M. S.; Goodman, D. W., The Structure of Catalytically Active Gold on Titania. *Science* **2004,** 252-255.

8. Baker, L. R.; Kennedy, G.; Van Spronsen, M.; Hervier, A.; Cai, X.; Chen, S.; Wang, L.-W.; Somorjai, G. A., Furfuraldehyde Hydrogenation on Titanium Oxide-Supported Platinum Nanoparticles Studied by Sum Frequency Generation Vibrational Spectroscopy: Acid–Base Catalysis Explains the Molecular Origin of Strong Metal–Support Interactions. *J. Am. Chem. Soc.* **2012,** 14208-14216.

9. Shi, F.; Baker, L. R.; Hervier, A.; Somorjai, G. A.; Komvopoulos, K., Tuning the Electronic Structure of Titanium Oxide Support to Enhance the Electrochemical Activity of Platinum Nanoparticles. *Nano Lett.* **2013,** 4469-4474.

10. Lazzeri, M.; Selloni, A., Stress-Driven Reconstruction of an Oxide Surface: The Anatase TiO2(001)-(1×4) Surface. *Phys. Rev. Lett.* **2001,** 266105.

11. Yang, H. G.; Sun, C. H.; Qiao, S. Z.; Zou, J.; Liu, G.; Smith, S. C.; Cheng, H. M.; Lu, G. Q., Anatase TiO2 single crystals with a large percentage of reactive facets. *Nature* **2008,** 638-641.

12. Morgan, B. J.; Watson, G. W., A Density Functional Theory + U Study of Oxygen Vacancy Formation at the (110), (100), (101), and (001) Surfaces of Rutile TiO2. *J. Phys. Chem. C* **2009,** 7322-7328.

13. Dan-Hardi, M.; Serre, C.; Frot, T.; Rozes, L.; Maurin, G.; Sanchez, C.; Férey, G., A New Photoactive Crystalline Highly Porous Titanium(IV) Dicarboxylate. *J. Am. Chem. Soc.* **2009,** 10857-10859.

14. Conner Jr, W. C.; Falconer, J. L., Spillover in heterogeneous catalysis. *Chem. Rev.* **1995,** 759-788.

15. Frisch, M.; Trucks, G.; Schlegel, H.; Scuseria, G.; Robb, M.; Cheeseman, J.; Zakrzewski, V.; Montgomery Jr, J.; Stratmann, R.; Burant, J., Gaussian 09, Gaussian, Inc., Pittsburgh, PA, 2009;.

16. Perdew, J. P.; Burke, K.; Ernzerhof, M., Generalized gradient approximation made simple. *Phys. Rev. Lett.* **1996,** 3865.

17. Lei, X.; Shang, M.; Fehlner, T. P., Clusters as Ligands. 5. Tricobalt Cluster Alkoxycarboxylates of Titanium and Zirconium Exhibiting Novel Structures and Properties. *Organometallics* **1997,** 5289-5301.

18. Mason, J. A.; Darago, L. E.; Lukens Jr, W. W.; Long, J. R., Synthesis and O2 Reactivity of a Titanium (III) Metal–Organic Framework. *Inorg. Chem.* **2015,** 10096-10104.

19. Entley, W. R.; Treadway, C. R.; Wilson, S. R.; Girolami, G. S., The Hexacyanotitanate Ion: Synthesis and Crystal Structure of [NEt4] 3 [TiIII (CN) 6]·4MeCN. *J. Am. Chem. Soc.* **1997,** 6251-6258.

20. Spannenberg, A.; Tillack, A.; Arndt, P.; Kirmse, R.; Kempe, R., Homoleptic trisaminopyridinato MIII complexes (M□Ti, V and Cr), synthesis, structure and EPR investigations. *Polyhedron* **1998,** 845-850.

21. Léonard, N. G.; Bezdek, M. t. J.; Chirik, P. J., Cobalt-Catalyzed C (sp2)–H Borylation with an Air-Stable, Readily Prepared Terpyridine Cobalt (II) Bis (acetate) Precatalyst. *Organometallics* **2016,** 142-150.

22. Léonard, N. G.; Bezdek, M. J.; Chirik, P. J., Cobalt-Catalyzed C(sp2)–H Borylation with an Air-Stable, Readily Prepared Terpyridine Cobalt(II) Bis(acetate) Precatalyst. *Organometallics* **2017,** 142-150.

23. Bowman, A. C.; Milsmann, C.; Bill, E.; Lobkovsky, E.; Weyhermüller, T.; Wieghardt, K.; Chirik, P. J., Reduced N-Alkyl Substituted Bis(imino)pyridine Cobalt Complexes: Molecular and Electronic Structures for Compounds Varying by Three Oxidation States. *Inorg. Chem.* **2010,** 6110-6123.

24. Scherer, A.; Haase, D.; Saak, W.; Beckhaus, R. d.; Meetsma, A.; Bouwkamp, M. W., Low-valent pentafulvene titanium dinitrogen complex as a precursor for cationic titanium complexes. *Organometallics* **2009,** 6969-6974.

25. Ciancanelli, R.; Noll, B. C.; DuBois, D. L.; DuBois, M. R., Comprehensive Thermodynamic Characterization of the Metal− Hydrogen Bond in a Series of Cobalt-Hydride Complexes. *J. Am. Chem. Soc.* **2002,** 2984-2992.

26. Milošv, I.; Strehblow, H. H.; Navinšek, B.; Metikoš-Huković, M., Electrochemical and thermal oxidation of TiN coatings studied by XPS. *Surf. Interface Anal.* **1995,** 529-539.

27. Durmeyer, O.; Kappler, J.; Beaurepaire, E.; Heintz, J.; Drillon, M., TiK XANES in superconducting LiTi2O4 and related compounds. *J. Phys.: Condens. Matter* **1990,** 6127.

28. WlvcnuNls, G. A., Synchrotron radiation XANES spectroscopy of Ti in minerals: Effects of Ti bonding distances, Ti valence, and site geometry on absorption edge structure. *Am. Mineral.* **1987,** 89-101.

Chapter 7. Cerium-Hydride SBUs in a Porous MOF for Catalytic Hydroboration and Hydrophosphination

7.1 Introduction

MOFs provide a unique approach to develop reusable and highly active single-site solid catalysts via direct solvothermal synthesis or post-synthetic functionalization.[1] All the structural components of MOFs, including their inorganic nodes, organic linkers, and void spaces, have been used to install catalytic species.[2-12] In particular, the previous chapters have discussed the straightforward metalation of bridging hydroxides in MOF nodes to provide an intriguing opportunity to design single-site solid catalysts that do not have homogeneous counterparts. However, the direct use MOF nodes for catalysis has been very rare and has been mostly limited to weak Lewis acid or Brønsted acid catalysts. This chapter describes one of the few examples of straightforward transformation of MOF SBU into organometallic-type of catalyst for challenging organic reactions.

Lanthanide (Ln) catalysts are used for a wide range of reactions, including polymerization, hydroamination, hydrogenation, hydroboration, Diels-Alder reactions, and Aldol reactions.[13-23] They are more favored for these reactions due to their high natural abundance, low toxicity, and better tolerance to inhibitive functional groups (*e.g.* phosphines) than precious metal catalysts.[24] While most lanthanide catalysts are based on La, Sm, and Lu, little effort has been devoted to the more abundant Ce, despite its broadly application in stoichiometric organic transformations.[25-29] Furthermore, Ln catalysts are often supported on sterically hindered ligands, notably η_5-C_5Me_5 (Cp*), to prevent catalyst disproportionation and oligomerization. These ligands restrict the

electronic and steric tuning of catalyst properties. Although some elaborately designed ligands like $Me_2Si(Cp^*)_2$ can increase the open space around Ln centers, their syntheses are typically lengthy and laborious. [30-31] We thus aimed to develop new synthetic strategies to produce Ln catalysts with low steric hindrance and unique electronic properties.

In this chapter, we explore the direct transformation of the $Ce^{IV}_6(\mu_3\text{-}O)_4(\mu_3\text{-}OH)_4(OH)_6(OH_2)_6$ nodes in a new Ce_6-BTC MOF into previously unknown metal-hydride nodes with the formula of $Ce^{III}_6(\mu_3\text{-}O)_4(\mu_3\text{-}OLi)_4(H)_6(THF)_6$ and its application in catalytic hydroboration of pyridines and alkenes as well as hydrophosphination of alkenes. The Ce_6H_6-BTC catalyst exhibits superior activity and unique regioselectivity than existing homogeneous lanthanide catalysts as a result of having low steric hindrance and unique electronic properties.

7.2 Results and Discussion

7.2.1 Ce oxidation state in Ce_6-BTC

Ce_6-BTC was synthesized in 54% yield by reacting $(NH_4)_2Ce(NO_3)_6$ with H_3BTC in a mixture of DMF and H_2O at 100 °C for 15 min (**Figure 7-1**). The Ce oxidation state of Ce_6-BTC was investigated through XANES analysis, by using $(NH_4)_2Ce^{IV}(NO_3)_6$ and $Ce^{III}Cl_3$ the tetravalent and trivalent standards. The Ce^{IV} species features a set of two peaks at the L-edge, while Ce^{III} features has only a single peak with lower edge-energy. Ce_6-BTC displayed a set of two edge peaks with the energy of 5730 and 5738 eV that are identical to the Ce^{IV} standard, indicating the tetravalent oxidation state in Ce_6-BTC (**Figure 7-2**). We attributed the stability of Ce^{IV} toward potential reductants (either DMF or water) under high temperature to the strong electron-donation of bridging oxide/hydroxide groups and the carboxylates.

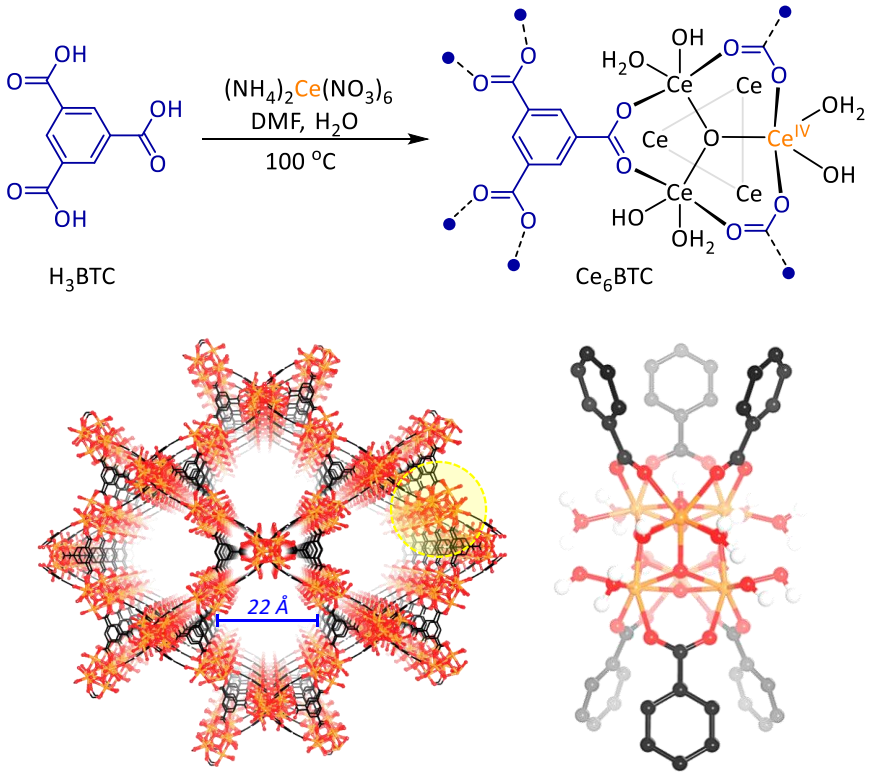

Figure 7-1. Synthesis and the structural model of Ce_6-BTC. The structure features a large uniform channel with the diameter of 22 Å.

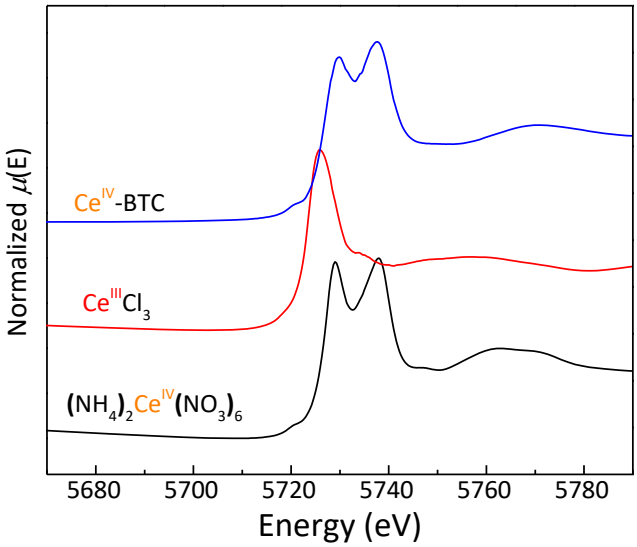

Figure 7-2. XANES analysis of Ce_6-BTC (blue) shows the Ce^{IV} oxidation state in the as prepared Ce_6-BTC MOF. XANES spectra of $CeCl_3$ and $(NH_4)_2Ce(NO_3)_6$ were shown in red and black, respectively.

^{1}H NMR of digested Ce_6-BTC in D_3PO_4/DMSO-d_6 showed only the signals of H_3BTC and adsorbed solvents, consistent with the proposed formula of $Ce^{IV}_6(\mu_3O)_4(\mu_3\text{-}OH)_4(OH)_6(OH_2)_6(BTC)_2$. The proposed Ce_6 structural model well fitted the Ce L_3 EXAFS data, with an average Ce-OH/Ce-OH_2 distance of 2.43 Å, similar with the typical Ce^{IV}-O distances (**Figure 7-3**).

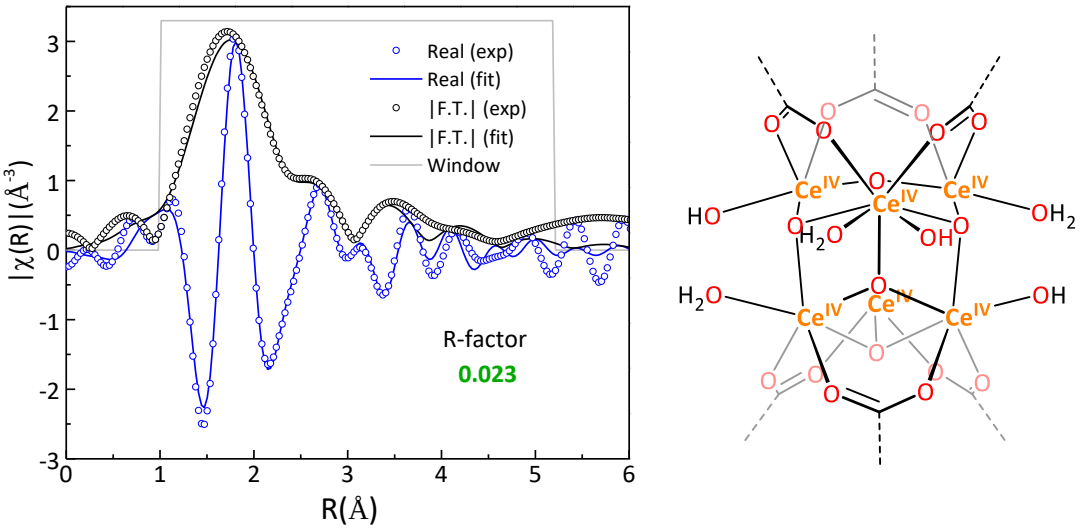

Figure 7-3. XAFS fitting on Ce_6-BTC and the chemical structure of the fitting model.

The Ce coordination environment of $[(\mu_3\text{-}O)_2(\mu_3\text{-}OH)_2(\mu_2\text{-}CO_2^-)_2]Ce(OH)(OH_2)$ in Ce_6-BTC is analogous to that of $Cp_2Ln(X)(L)$ (X = anionic ligand and L = neutral ligand) which have been widely used in many catalytic reactions. A structural model of Ce_6-BTC indicates that Ce-OH and Ce-OH_2 moieties point toward the largest channel which has the diameter of 22 Å, affording low steric hindrance around the Ce centers. We thus sought to activate the $Ce(OH)(OH_2)$ sites to prepare Ce catalysts that are readily accessible to organic substrates through the large open channels of Ce_6-BTC.

7.2.2 Synthesis of Ce_6H_6-BTC

Ce_6-BTC was activated by deprotonation with $LiCH_2SiMe_3$ followed by reduction with pinacolborane (HBpin) to generate the first MOF-supported Ce-hydride catalyst for several important organic transformations. The lithiated MOF, denoted $Ce_6(OH)_{12}$-BTC, was obtained by treating Ce_6-BTC with 10 equiv. of $LiCH_2SiMe_3$ (w.r.t. Ce) to deprotonate (μ_3-OH)Ce(OH)(OH_2) to form [(μ_3-OLi)Ce$(OH)_2$]Li, and generate $SiMe_4$ as the by-product (**Scheme 7-1**). The amount of $SiMe_4$ was used to probe the deprotonation step. After removing $Ce_6(OH)_{12}$-BTC, 1.74±0.15 equiv. of $SiMe_4$ (w.r.t. Ce) was detected in the supernatant by ^{1}H NMR, which corresponds well to the calculated result of 1.67. ICP-MS analysis of $Ce_6(OH)_{12}$-BTC gave a Li/Ce ratio of 1.69±0.05, also matching our calculated result of 1.67. Based on these quantitative studies, the formula of $Ce_6(OH)_{12}$-BTC was proposed to be $Ce^{IV}{}_6(\mu_3\text{-}O)_4(\mu_3\text{-}OLi)_4[(OH)_{12}Li_6](BTC)_2$.

Scheme 7-1. Activation of Ce_6-BTC to form $Ce_6(OH)_{12}$-BTC through lithiation with $LiCH_2SiMe_3$.

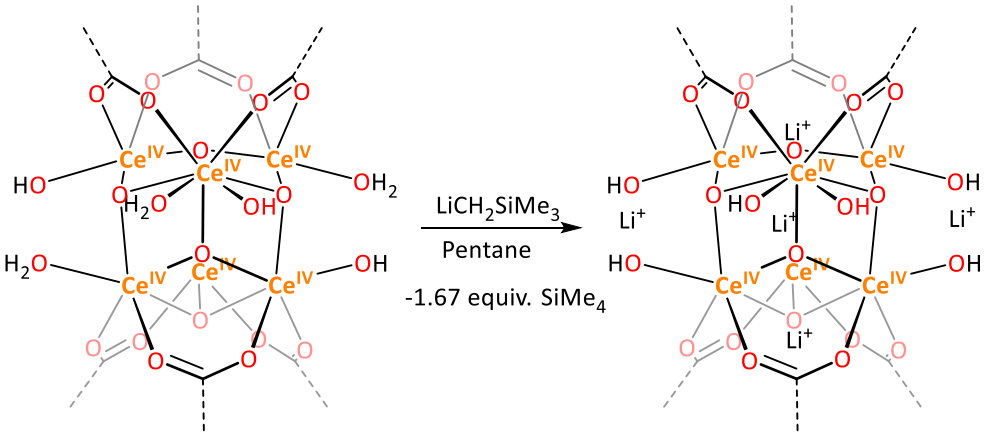

$Ce_6(OH)_{12}$-BTC was reduced to form Ce_6H_6-BTC by treatment with HBpin at 60 °C in THF for 6 h (**Scheme 7-2**). GC analysis of the head space gas indicated the production of 0.5 equiv. of H_2 w.r.t. Ce. After removal of Ce_6H_6-BTC, 2.02±0.14 equiv. of HOBpin (w.r.t. Ce) was detected in the supernatant by ^{1}H NMR, which corresponds to our calculated result of 2 equiv. The identity

of HOBpin was confirmed using ^{11}B NMR, which showed chemical shift δ of 22.7 ppm, close to literature reported value.

Scheme 7-2. Activation of Ce-OH to form Ce_6H_6-BTC using HBpin.

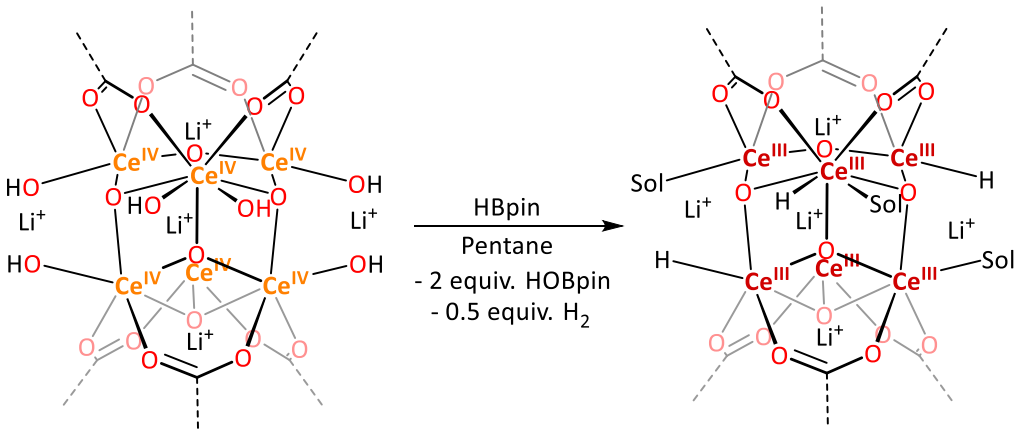

Based on the formation of 0.5 equiv. of H_2 and 2 equiv. of HOBpin, we propose that the reduction occurred via an H/OH exchange between HBpin and $Ce(OH)_2$ to form $Ce^{IV}(H)_2$ and HOBpin, followed by bimetallic reductive elimination of H_2 from neighboring $Ce^{IV}(H)_2$ species to form $Ce^{III}H(THF)$, with the concomitant formation of 0.5 equiv. of H_2 w.r.t. Ce (**Scheme 7-3**).

Scheme 7-3. Proposed bimetallic reductive elimination mechanism to generate $Ce^{III}{}_6H_6$-BTC.

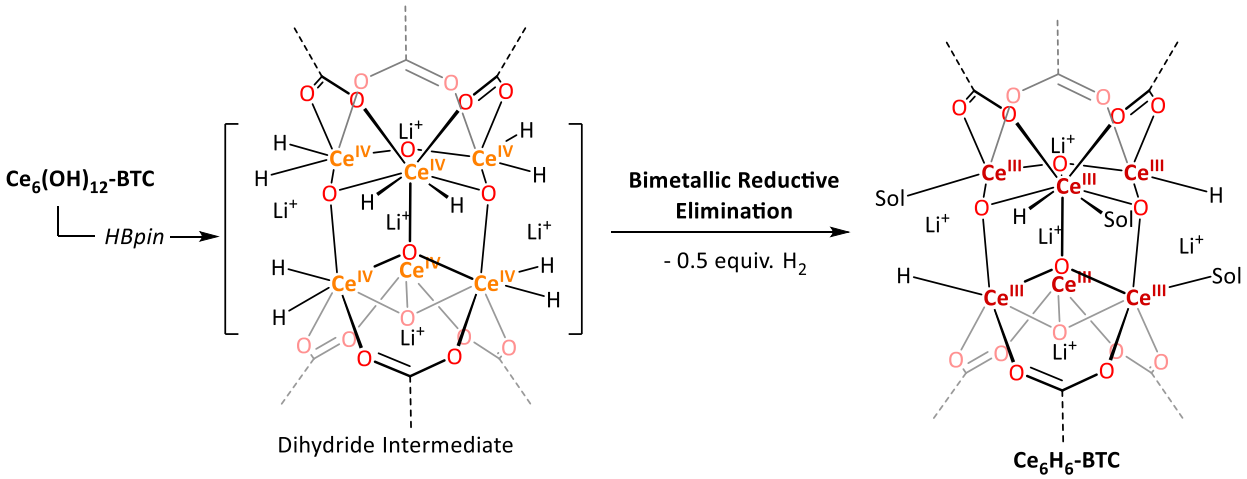

XANES of Ce_6H_6-BTC showed a single Ce peak at 5726 eV, identical to the absorption feature of $CeCl_3$ (**Figure 7-4**). The amount of hydride in Ce_6H_6-BTC was confirmed by treating Ce_6H_6-BTC with hydrochloric acid. The reaction immediately generated 0.98±0.11 equiv. of H_2, while no H_2 was observed when Ce_6-BTC or $Ce_6(OH)_{12}$-BTC was treated with hydrochloric acid.

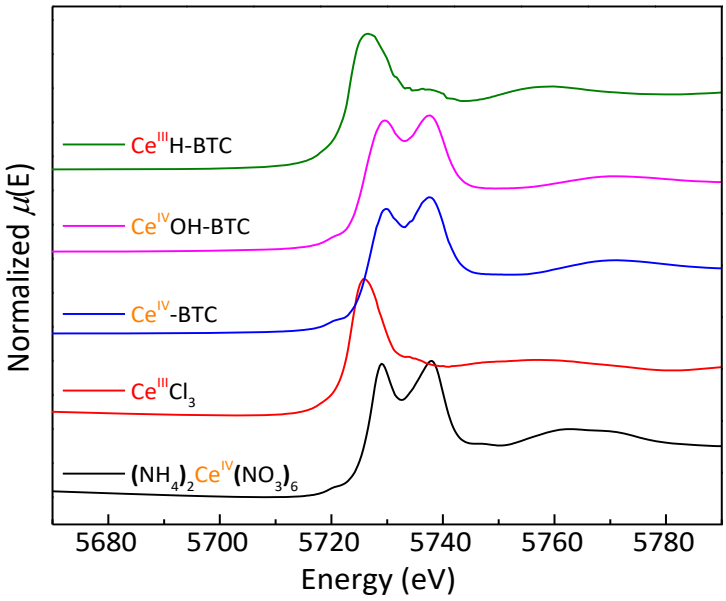

Figure 7-4. XANES analysis of Ce_6-BTC (blue), $Ce_6(OH)_{12}$-BTC (pink), and Ce_6H_6-BTC (green) shows the reduction of Ce^{IV} in $Ce_6(OH)_{12}$-BTC to Ce^{III} in Ce_6H_6-BTC.

The proposed $Ce^{III}H(THF)$ coordination model fitted well to the Ce L_3 edge EXAFS data of Ce_6H_6-BTC, with an R-factor of 0.015 (**Figure 7-5**). The fitted Ce^{III}-(μ_3-O) distance of 2.44 Å is slightly longer than the Ce^{IV}-(μ_3-O) distance of 2.25 Å in $Ce_6(OH)_{12}$-BTC, which is consistent with the larger Ce^{III} ionic radius than Ce^{IV}. The $Ce[(\mu_3\text{-}O)_2(\mu_3\text{-}OH)_2(\mu_2\text{-}CO_2^-)_2]$ moiety is expected to be more electron-deficient than other organolanthanide catalysts (*e.g.* Cp^*_2Ln), therefore potentially endowing the Ce_6H_6-BTC catalyst with better activity and unique selectivity.

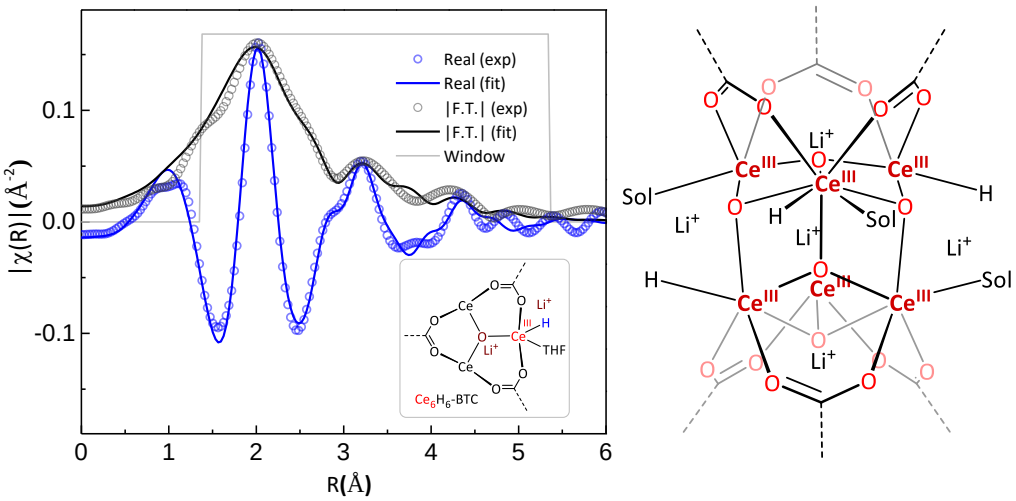

Figure 7-5. XAFS fitting on Ce_6H_6-BTC confirms the proposed structure for the catalytic species. The R factor is 0.0146.

The PXRD pattern of Ce_6H_6-BTC is identical to that of Ce_6-BTC, indicating that the framework structure remains intact after the lithiation and reduction (**Figure 7-6**). The framework porosity of is maintained after desolvation. $Ce^{III}{}_6H_6$-BTC has a BET surface area of 721 m^2/g based on N_2 sorption isotherm, which is very similar to that observed for Ce_6-BTC (**Figure 7-7**). Pore size distribution analysis of Ce_6H_6-BTC shows two types of pores at 15 Å and 19 Å.

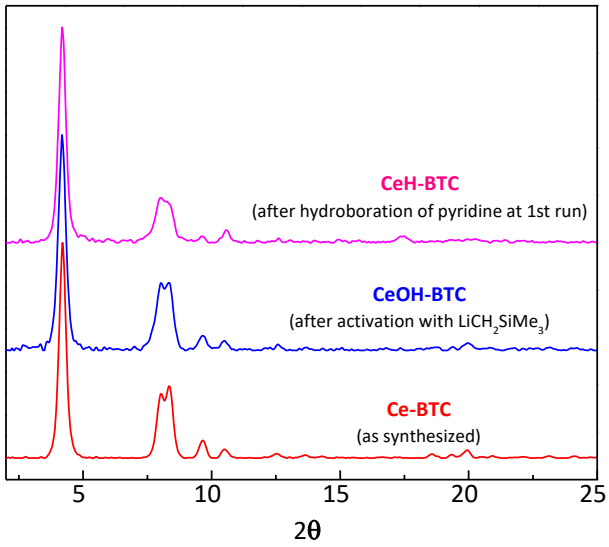

Figure 7-6. PXRD patterns of Ce_6H_6-BTC compared to that of $Ce_6(OH)_{12}$-BTC and Ce_6-BTC.

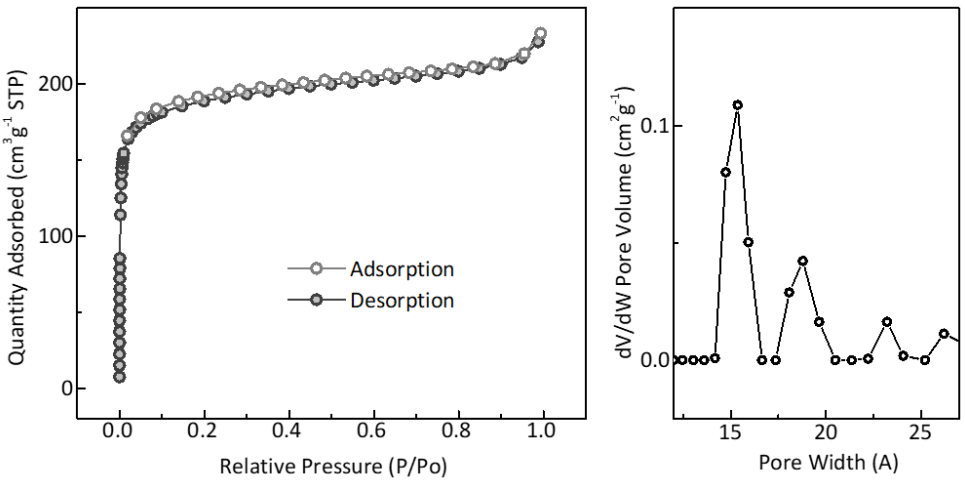

Figure 7-7. Nitrogen sorption isotherms (77 K) and the pore size distributions of Ce_6H_6-BTC.

7.2.3 Ce_6H_6-BTC catalyzed pyridine hydroboration.

Ce_6H_6-BTC is a highly active catalyst for pyridine hydroboration with high 1,4-selectivity. 1,4-dihydropyridines are an important class reducing reagents, and important building block for natural products and biologically active intermediates. Although hydroboration of pyridines provides a convenient synthetic route to 1,4-dihydropyridines, but at the time of this report, only one organoborane catalyst and one example of ruthenium catalyst were reported to effect 1,4-selective hydroboration reactions. At 4 mol% Ce_6H_6-BTC catalyst loading and 80 °C, pyridine was efficiently reduced by HBpin in 71% yield with almost exclusive 1,4-selectivity (**Table 7-1**). The 1,4-selectivity is distinct from other lanthanide catalysts which exclusively prefer 1,2-selectivity. The pyridines hydroboration by Ce_6H_6-BTC also has a broad substrate scope. At 2-4 mol% catalyst loading, Ce_6H_6-BTC converted 3-bromopyridine and 3-methylpyridine to their corresponding 1,4-addition products in high yields and only with small amounts of 1,2-addition byproducts. 3,5-disubstututed pyridines (*e.g.* 3,5-dimethylpyridine) was also hydroborated in high

yield by using 10 mol% Ce_6H_6-BTC. Ce_6H_6-BTC also exhibited good hydroboration activity for quinoline.

Table 7-1. Ce_6H_6-BTC Catalyzed 1,4-Selective Hydroboration of Pyridine Derivatives.

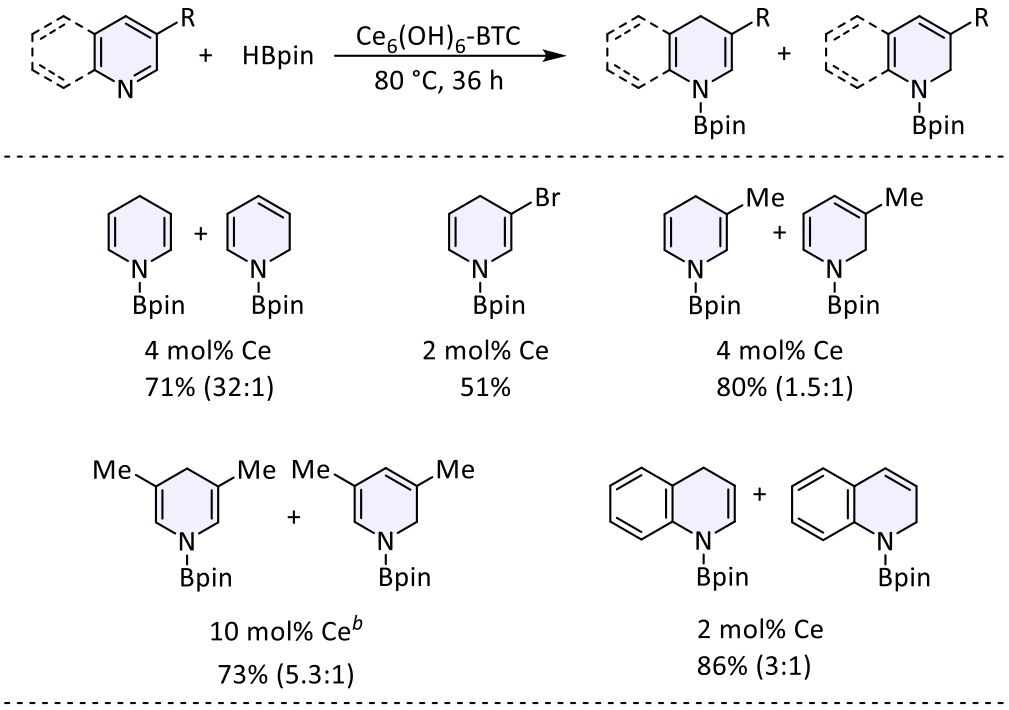

The reaction yields are based on ^{1}H NMR by using mesitylene as an internal standard.

7.2.4 Ce_6H_6-BTC catalyzed alkene hydroboration.

Ce_6H_6-BTC is also active in the hydroboration of alkenes, a useful catalytic reaction for the facile reduction of alkenes. Reacting styrene and 1.5 eq. of HBpin with 0.1 mol% Ce_6H_6-BTC catalyst loading at 80 °C for 18 h selectively gave the anti-Markovnikov addition product in 40% yield (**Table 7-2**). Increasing catalyst loading to 0.5 mol% afforded the addition product in 79% yield. The hydroboration reaction has a very broad substrate scope for alkenes. Both styrene derivatives (*e.g.* 4-fluorostyrene, α-methylstyrene) and aliphatic alkenes (*e.g.* allylbenzene, 1-octene) were effectively hydroborated in high yields.

Table 7-2. Ce_6H_6-BTC Catalyzed Hydroboration of Alkenes.

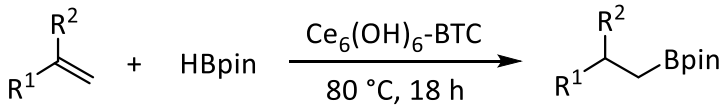

Entry	Substrate	Catalyst Loading (mol% Ce)	Yield (%)[a]
1	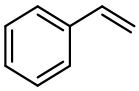	0.1	40
2		0.5	79
3	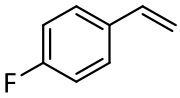	1	99
4[b]	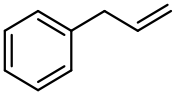	1	90
5[b]	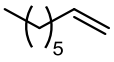	1	97
6[b,c]	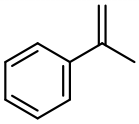	1	56

[a]NMR yield using CH_3NO_2 as an internal standard. [b]36 h. [c]100 °C.

7.2.5 Ce_6H_6-BTC catalyzed alkene hydrophosphination.

Alkene hydrophosphination is a powerful, direct, and atom-economical method to synthesize organophosphines, which is an important class of compounds for agrochemical and pharmaceutical industries. Moreover, organophosphines are among the most important ligands in homogeneous catalysis. While several examples of alkene hydrophosphination have been reported, the scope of substrates is very limited, and the examples for hydrophosphinating unactivated aliphatic olefins are rare. Ce_6H_6-BTC efficiently catalyzed the hydrophosphination of various unactivated alkenes. At 4 mol% Ce-loading, 1-octene was hydrophosphinated in 18 h to yield 74% of n-octyldiphenyl phosphine (**Table 7-3**). Prolonging the reaction to 5 d afforded the addition

product in 99% yield. The hydrophosphination reaction also proceeded for 1-decene and 6-chlorohexene. The reaction also proceeds with more hindered substrates 2-methyl-1-pentene and cis-β-methylstyrene with high activity.

Table 7-3. Ce_6H_6-BTC Catalyzed Hydrophosphination of Alkenes

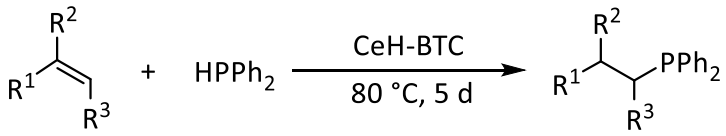

Entry	Substrate	Product	Cat. Loading (mol% Ce)	Yield (%)[a]
1[b]	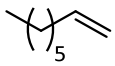	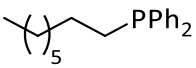	4	74
2			4	99
3	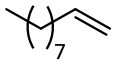	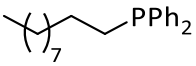	4	75
4	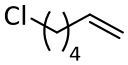	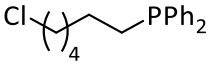	4	80
5	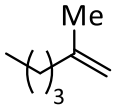	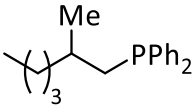	12	50
6[c]	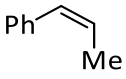	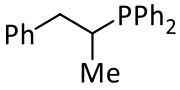	12	41

[a]^{1}H NMR yield was determined by CH_3NO_2 as an internal standard. [b]18 h. [c]100 °C.

The PXRD of Ce_6H_6-BTC recovered from hydroboration of pyridines and alkenes remained the same as that of freshly prepared Ce_6H_6-BTC, indicating the high stability under reaction conditions. We conducted several experiments to demonstrate the heterogeneity of Ce_6H_6-BTC. We used ICP-MS to show that the amounts of Ce leached into the supernatant during the hydroboration of pyridine and styrene and the hydrophosphination of 1-octene were less than 0.6%,

0.75%, and 0.03%, respectively. Moreover, the Ce_6H_6-BTC could be recovered and reused 1 to 7 times for each of the above reactions without any loss of activity (**Figure 7-8**).

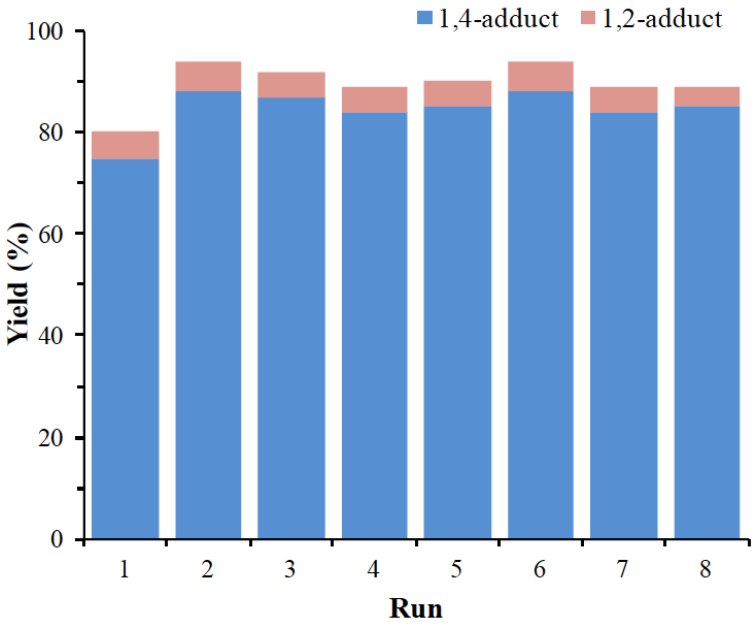

Figure 7-8. Plots of yields (%) of 1-(4,4,5,5-tetramethyl-1,3,2-dioxaborolan-2-yl)-1,4-dihydropyridine and 1-(4,4,5,5-tetramethyl-1,3,2-dioxaborolan-2-yl)-1,2-dihydropyridine at different runs in the recycling experiments of CeOH-BTC for hydroboration of pyridine with pinacolborane. The Ce-loadings were 20 mol%.

7.3 Conclusion

This chapter reports the synthesis of a new Ce_6-BTC MOF with a $Ce^{IV}_6(\mu_3\text{-}O)_4(\mu_3\text{-}OH)_4(OH)_6(OH_2)_6$ SBU, which was transformed to a $[Ce^{III}_6(\mu_3\text{-}O)_4(\mu_3\text{-}OLi)_4(H)_6(THF)_6]^{6+}$ node. The cerium hydride node is an active catalyst for the selective hydroboration of pyridine and alkenes as well as the hydrophosphination of alkenes. The Ce_6H_6-BTC catalyst is more electron-deficient and sterically open than other lanthanide catalysts, which likely accounts for the unique 1,4-regioselectivity for the pyridine hydroboration. MOF nodes thus have great potential for sustainable chemical synthesis through transformation into single-site solid catalysts without homogeneous counterparts.

7.4 Experimental

7.4.1 Material and Methods

All of the reactions and manipulations were carried out under nitrogen with the use of standard inert atmosphere and Schlenk techniques unless otherwise indicated. Tetrahydrofuran was purified by passing through a neutral alumina column under N_2. d_6-Benzene was distilled over CaH_2. Alkenes and pyridine derivatives were purchased from Fisher, distilled and then dried over 4Å molecular sieves prior to use. $(NH_4)_2Ce(NO_3)_6$ was purchased from Sigma-Aldrich and used as received. Powder X-ray diffraction data were collected on Bruker D8 Venture diffractometer using Cu Kα radiation source (l = 1.54178 Å). Nitrogen adsorption experiments were performed on a Micrometrics TriStar II 3020 instrument. TGA was performed in air using a Shimazu TGA-50 equipped with a platinum pan and heated at a rate of 3 ˚C per min. ^{1}H NMR spectra were recorded on a Bruker NMR 500 DRX spectrometer at 500 MHz or a Bruker NMR 400 DRX spectrometer at 400 MHz, and referenced to the proton resonance resulting from incomplete deuteration of the $CDCl_3$ (δ 7.26) or C_6D_6 (δ 7.14). ^{13}C NMR spectra were recorded at 125 MHz, and all of the chemical shifts were reported downfield in ppm relative to the carbon resonance of $CDCl_3$ (δ 77.00) or C_6D_6 (δ 128.00). ^{11}B NMR spectra were recorded at 128 MHz, and all of the chemical shifts were reported downfield in ppm relative to an external BF_3•OEt_2 standard. The following abbreviations are used here: s: singlet, d: doublet, t: triplet, q: quartet, m: multiplet, br: broad, app: apparent. Gas chromatography data were obtained on an Agilent 7890B Gas Chromatograph. ICP-MS data were obtained with an Agilent 7700x ICP-MS and analyzed using ICP-MS MassHunter version B01.03. Sample were diluted in a 2% HNO_3 matrix and analyzed with a ^{159}Tb internal standard against a 12-point standard curve over the range from

0.1ppb to 500ppb. The correlation was >0.9997 for all analyses of interest. Data collection was performed in Spectrum Mode with five replicates per sample and 100 sweeps per replicates.

7.4.2 Synthesis and characterization of Ce_6-BTC

Ce_6-BTC was synthesized in 54% yield by treating $(NH_4)_2Ce(NO_3)_6$ with H_3BTC in a mixture of DMF and H_2O at 100 °C for 15 min. This synthetic procedure is special compared to the synthesis of Zr-MOFs because (i) no acidic modulator were added, and (ii) the reaction time is very short. This is because the Ce_6 SBU assembly is very dynamic and efficient. Because the MOF synthesis is so quick, no crystal structure of Ce_6-BTC was obtained. Attempts to slow down the MOF growth through the addition of acidic modulators leads to the reduction of Ce^{IV} to Ce^{III}, and affording trivalent cerium-based MOFs with completely different structure and smaller channels. The structure of Ce_6-BTC was modelled using the crystal structure of Zr-BTC (MOF-808) by elongating the Zr-μ_3O distance of 2.16 Å to Ce-μ_3O distance of 2.25 Å, while maintaining the space group and M-carboxylate bond distances.

Similarities between PXRD patterns of as-synthesized Ce_6-BTC and the simulated pattern confirmed the spn topology (**Figure 7-9**). The Ce centers were believed to possess square antiprismatic geometry, with a coordination environment of $[(\mu_3\text{-}O)_2(\mu_3\text{-}OH)_2(\mu_2\text{-}CO_2^-)_2]Ce(OH)(OH_2)$, similar to the Zr coordination in MOF-808. Since Ce^{IV} has a larger ionic radius than Zr^{IV} [$r(Ce^{IV})$=0.97 Å and $r(Zr^{IV})$=0.84 Å], the Ce_6 node in Ce_6-BTC is larger than the Zr_6 node in MOF-808, with a Ce-Ce distance of 3.74 Å vs the Zr-Zr distance of 3.57 Å. This difference in SBU size leads to the shift of the first diffraction peak to lower angle than Zr-BTC MOF.

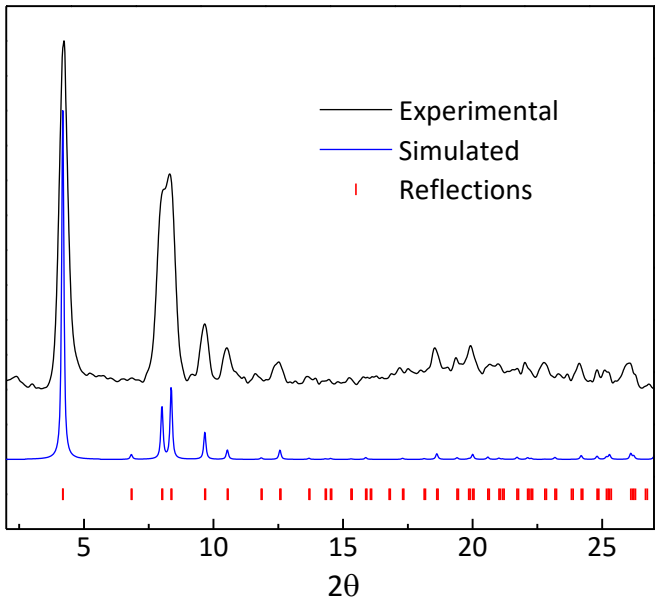

Figure 7-9. Comparison of experimental PXRD pattern (black solid line) with the simulated pattern (blue solid line).

N_2 sorption isotherms of Ce_6-BTC at 77 K gave a BET surface area of 1008 m^2/g and a largest pore size of 22 Å, which corresponds well to the size of the hexagonal pore in the simulated structure of Ce_6-BTC (**Figure 7-10**).

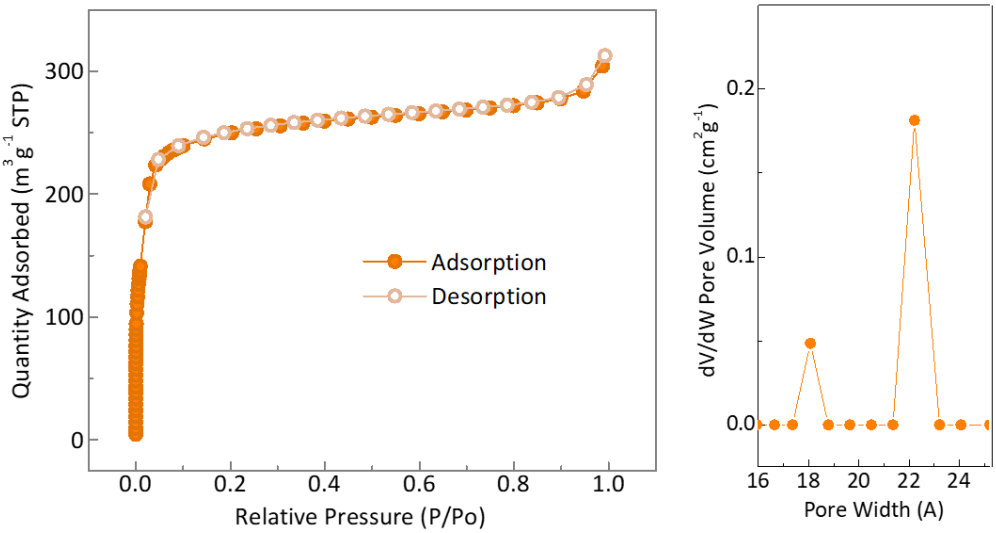

Figure 7-10. Nitrogen sorption isotherms (left) of Ce_6-BTC (77 K, which gives calculated BET surface areas of 1008 m^2/g. DFT simulated cylinder-shape pore size distribution (right) shows that Ce_6-BTC has the largest pore size of about 22Å, which is consistent with the simulated Ce_6-BTC structure.

TGA analysis was adopted to investigate the thermal stability of Ce_6-BTC, and validate the chemical composition of the material (**Figure 7-11**). The first weight loss (39.4%) in the 25–240 °C temperature range corresponds to the removal of coordinated water molecules on Ce centers and adsorbed solvents (e.g., benzene) in the pores. The second weight loss (39.8%) in the 240–800 °C temperature range corresponds to decomposition of $Ce_6O_4(OH)_{10}(OH_2)_6(BTC)_2$ to Ce_2O_3 (experimental 39.8%; calculated 38.5%).

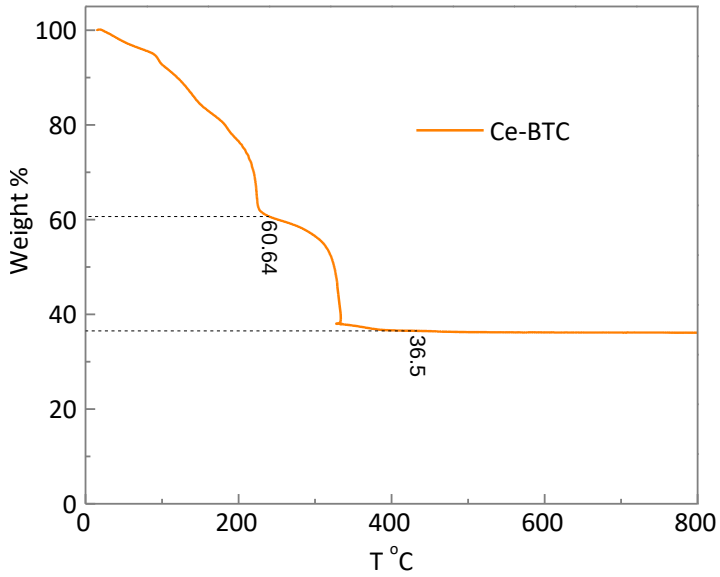

Figure 7-11. TGA curves of freshly prepared Ce_6-BTC in the 25~800 °C range.

7.4.3 Quantification of $SiMe_4$ during the Ce_6-BTC lithiation

After activation with $LiCH_2SiMe_3$ overnight using the aforementioned procedure, 5 equivalent of cyclohexane (100 μmol) was added to the suspension as internal standard for ^1H NMR. The MOF was removed by centrifugation, and one drop of supernatant was diluted with C_6D_6 and used for ^1H NMR. 1.74±0.15 equivalent of $SiMe_4$ per Ce was detected after repeating the same experiment for three runs, very close to calculated 1.67 equiv. from the proposed reaction. Pentane was introduced as a result of the addition of $LiCH_2SiMe_3$ in pentane solution.

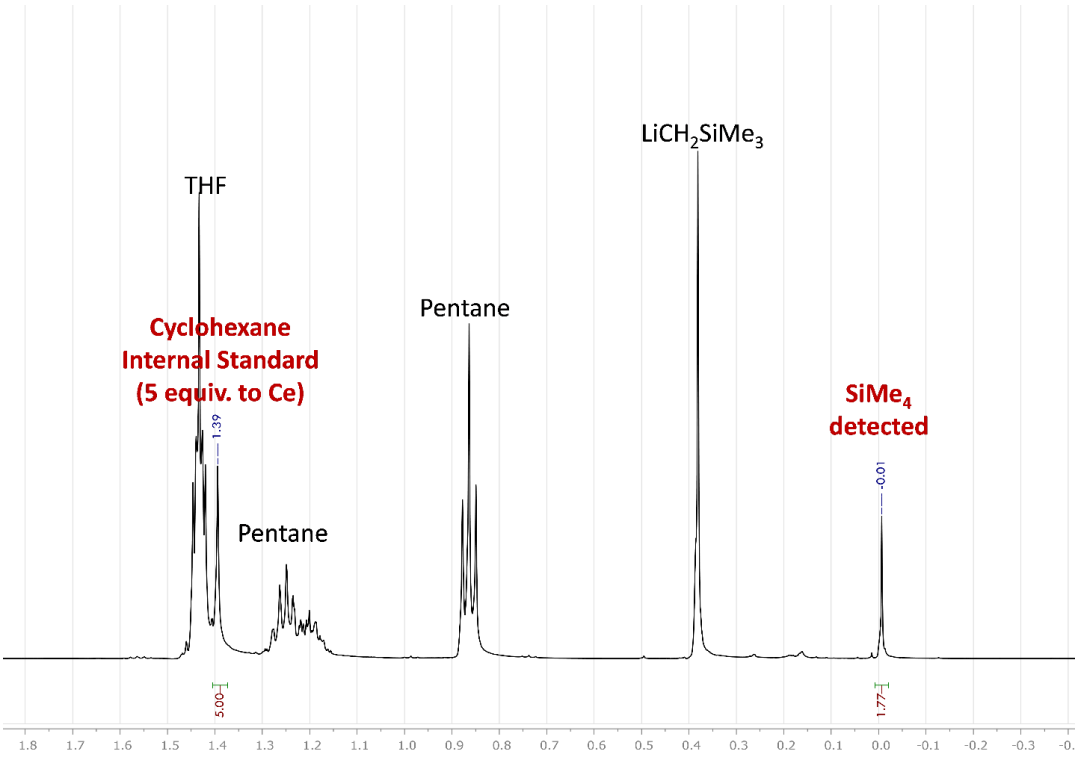

Figure 7-12. ^{1}H NMR of the liquid product from Ce_6-BTC activation with $LiCH_2SiMe_3$ showing the formation of 1.74±0.15 equiv of $SiMe_4$ per Ce.

7.4.4 Quantification of $SiMe_4$ during the Ce_6-BTC lithiation

GC was used to quantify the head-space gases in the J.Young tubes during the reduction of $Ce_6(OH)_{12}$-BTC by HBpin. The figure below shows three different runs affording consistent results. The amount of H_2, after subtraction of background, was calculated to be 10.2±0.26 μmol, which corresponds to 0.51±0.013 equiv. of H_2 w.r.t. Ce (**Figure 7-13**).

The identity of HOBpin was confirmed using ^{11}B NMR, which showed chemical shift δ of 22.7 ppm, close to literature reported value (**Figure 7-14**). The frequency of the spectrometer is 128 MHz. $MeNO_2$ (2 equiv. to Ce) was used as internal standard. 2.02± 0.14 equiv. of HOBpin was detected w.r.t. Ce. Identity of HOBpin was confirmed by ^{11}B NMR ($CDCl_3$, 128 MHz). Peak

position of detected boron species at δ 21.7 ppm matched well with the HO-Bpin standard at δ 22.7 ppm; No peak matching HBpin at δ 28.4 (green) was observed (**Figure 7-15**).

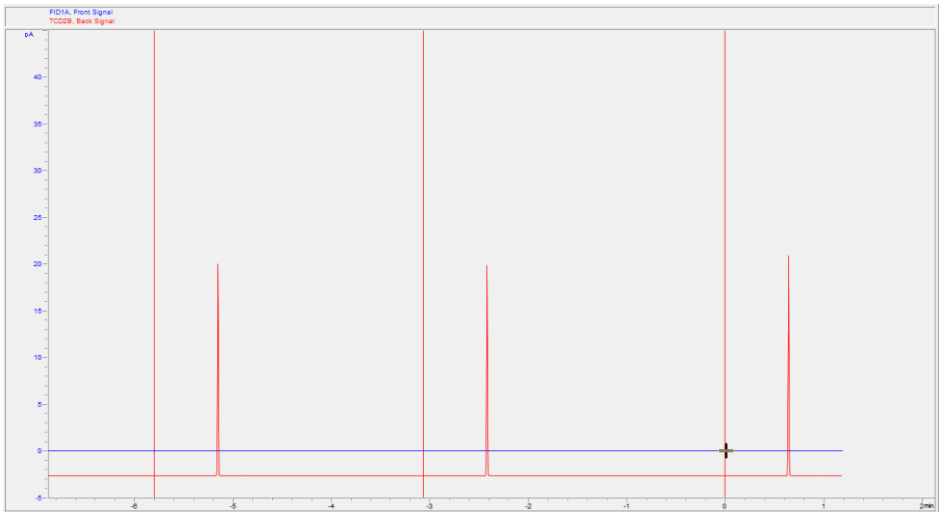

Figure 7-13. GC trace of head-space gases during the reduction of $Ce_6(OH)_{12}$-BTC by HBpin.

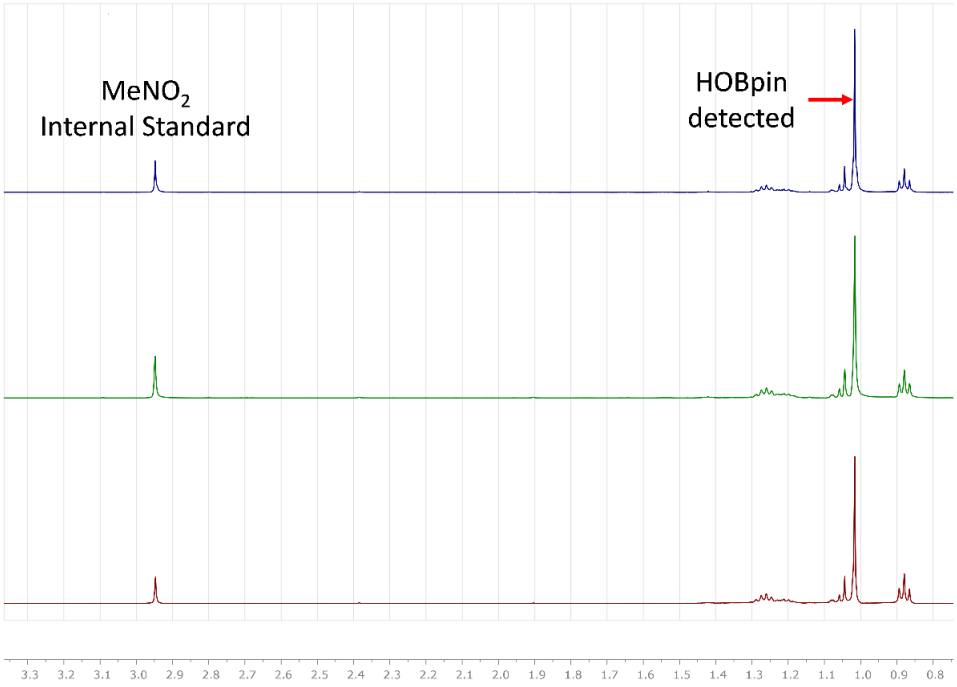

Figure 7-14. ^{1}H NMR quantification of HOBpin in three runs.

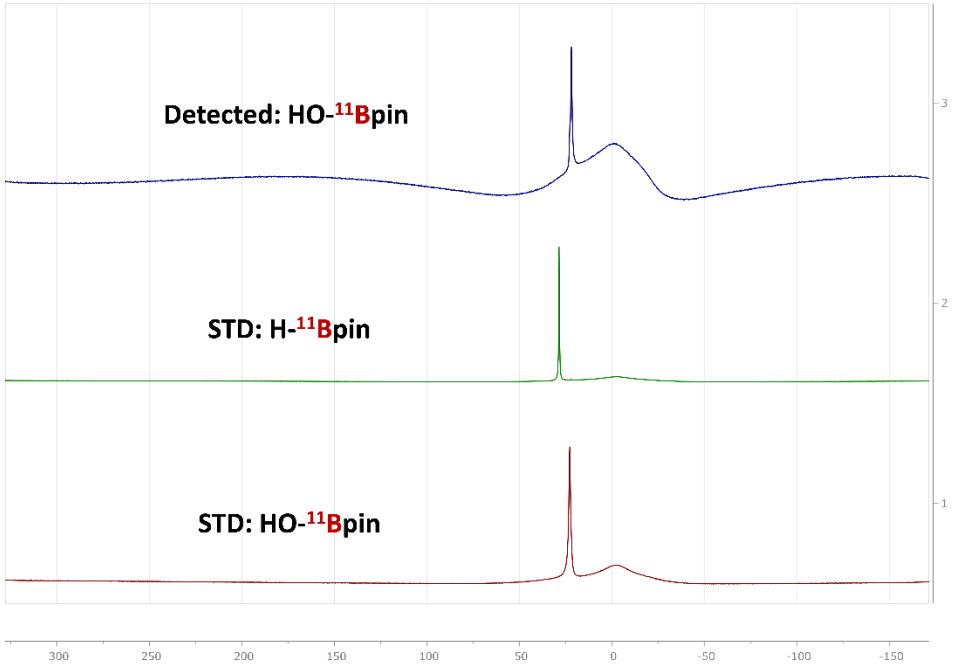

Figure 7-15. ^{11}B NMR ($CDCl_3$, 128 MHz) for identifying HOBpin species.

7.5 References

1. i Xamena, F. X. L.; Gascon, J., *Metal Organic Frameworks as Heterogeneous Catalysts*. Royal Society of Chemistry: 2013.

2. Manna, K.; Ji, P.; Greene, F. X.; Lin, W., Metal–Organic Framework Nodes Support Single-Site Magnesium–Alkyl Catalysts for Hydroboration and Hydroamination Reactions. *J. Am. Chem. Soc.* **2016,** 7488-7491.

3. Klet, R. C.; Tussupbayev, S.; Borycz, J.; Gallagher, J. R.; Stalzer, M. M.; Miller, J. T.; Gagliardi, L.; Hupp, J. T.; Marks, T. J.; Cramer, C. J.; Delferro, M.; Farha, O. K., Single-Site Organozirconium Catalyst Embedded in a Metal–Organic Framework. *J. Am. Chem. Soc.* **2015,** 15680-15683.

4. Comito, R. J.; Fritzsching, K. J.; Sundell, B. J.; Schmidt-Rohr, K.; Dinca, M., Single-Site Heterogeneous Catalysts for Olefin Polymerization Enabled by Cation Exchange in a Metal Organic Framework. *J. Am. Chem. Soc.* **2016**.

5. Zhang, T.; Manna, K.; Lin, W., Metal–Organic Frameworks Stabilize Solution-Inaccessible Cobalt Catalysts for Highly Efficient Broad-Scope Organic Transformations. *J. Am. Chem. Soc.* **2016,** 3241-3249.

6. Thacker, N. C.; Lin, Z.; Zhang, T.; Gilhula, J. C.; Abney, C. W.; Lin, W., Robust and Porous β-Diketiminate-Functionalized Metal–Organic Frameworks for Earth-Abundant-Metal-Catalyzed C–H Amination and Hydrogenation. *J. Am. Chem. Soc.* **2016,** 3501-3509.

7. Falkowski, J. M.; Sawano, T.; Zhang, T.; Tsun, G.; Chen, Y.; Lockard, J. V.; Lin, W., Privileged Phosphine-Based Metal–Organic Frameworks for Broad-Scope Asymmetric Catalysis. *J. Am. Chem. Soc.* **2014,** 5213-5216.

8. Manna, K.; Zhang, T.; Carboni, M.; Abney, C. W.; Lin, W., Salicylaldimine-Based Metal–Organic Framework Enabling Highly Active Olefin Hydrogenation with Iron and Cobalt Catalysts. *J. Am. Chem. Soc.* **2014,** 13182-13185.

9. Sawano, T.; Ji, P.; McIsaac, A. R.; Lin, Z.; Abney, C. W.; Lin, W., The first chiral diene-based metal–organic frameworks for highly enantioselective carbon–carbon bond formation reactions. *Chem Sci* **2015,** 7163-7168.

10. Genna, D. T.; Wong-Foy, A. G.; Matzger, A. J.; Sanford, M. S., Heterogenization of homogeneous catalysts in metal–organic frameworks via cation exchange. *J. Am. Chem. Soc.* **2013,** 10586-10589.

11. Choi, K. M.; Na, K.; Somorjai, G. A.; Yaghi, O. M., Chemical Environment Control and Enhanced Catalytic Performance of Platinum Nanoparticles Embedded in Nanocrystalline Metal–Organic Frameworks. *J. Am. Chem. Soc.* **2015,** 7810-7816.

12. Wang, C.; deKrafft, K. E.; Lin, W. B., Pt Nanoparticles@Photoactive Metal-Organic Frameworks: Efficient Hydrogen Evolution via Synergistic Photoexcitation and Electron Injection. *J. Am. Chem. Soc.* **2012,** 7211-7214.

13. Hou, Z.; Wakatsuki, Y., Recent developments in organolanthanide polymerization catalysts. *Coord. Chem. Rev.* **2002,** 1-22.

14. Zhang, L.; Suzuki, T.; Luo, Y.; Nishiura, M.; Hou, Z., Cationic Alkyl Rare-Earth Metal Complexes Bearing an Ancillary Bis(phosphinophenyl)amido Ligand: A Catalytic System for Living cis-1,4-Polymerization and Copolymerization of Isoprene and Butadiene. *Angew. Chem. Int. Ed.* **2007,** 1909-1913.

15. Hong, S.; Marks, T. J., Organolanthanide-catalyzed hydroamination. *Accounts Chem Res* **2004,** 673-686.

16. Hong, S.; Tian, S.; Metz, M. V.; Marks, T. J., C2-Symmetric Bis(oxazolinato)lanthanide Catalysts for Enantioselective Intramolecular Hydroamination/Cyclization. *J. Am. Chem. Soc.* **2003,** 14768-14783.

17. Conticello, V. P.; Brard, L.; Giardello, M. A.; Tsuji, Y.; Sabat, M.; Marks, T. J., Homogeneous Enantioselective Hydrogenation with Chiral Organolanthanide Complexes. *Abstr Pap Am Chem S* **1989,** 31-Inor.

18. Obora, Y.; Ohta, T.; Stern, C. L.; Marks, T. J., Organolanthanide-catalyzed imine hydrogenation. Scope, selectivity, mechanistic observations, and unusual byproducts. *J. Am. Chem. Soc.* **1997,** 3745-3755.

19. Jeske, G.; Lauke, H.; Mauermann, H.; Schumann, H.; Marks, T. J., Highly Reactive Organolanthanides - a Mechanistic Study of Catalytic Olefin Hydrogenation by Bis(Pentamethylcyclopentadienyl) and Related 4f Complexes. *J. Am. Chem. Soc.* **1985,** 8111-8118.

20. Dudnik, A. S.; Weidner, V. L.; Motta, A.; Delferro, M.; Marks, T. J., Atom-efficient regioselective 1,2-dearomatization of functionalized pyridines by an earth-abundant organolanthanide catalyst. *Nat Chem* **2014,** 1100-1107.

21. Harrison, K. N.; Marks, T. J., Organolanthanide-Catalyzed Hydroboration of Olefins. *J. Am. Chem. Soc.* **1992,** 9220-9221.

22. Kobayashi, S.; Hachiya, I.; Takahori, T.; Araki, M.; Ishitani, H., Lanthanide trifluoromethanesulfonates as reusable catalysts. Michael and Diels-Alder reactions. *Tetrahedron Lett.* **1992,** 6815-6818.

23. Shibasaki, M.; Yoshikawa, N., Lanthanide Complexes in Multifunctional Asymmetric Catalysis. *Chem. Rev.* **2002,** 2187-2210.

24. Kobayashi, S.; Anwander, R., *Lanthanides: chemistry and use in organic synthesis*. Springer Science & Business Media: 1999; Vol. 2.

25. Sridharan, V.; Menéndez, J. C., Cerium(IV) Ammonium Nitrate as a Catalyst in Organic Synthesis. *Chem. Rev.* **2010,** 3805-3849.

26. Piro, N. A.; Robinson, J. R.; Walsh, P. J.; Schelter, E. J., The electrochemical behavior of cerium(III/IV) complexes: Thermodynamics, kinetics and applications in synthesis. *Coord. Chem. Rev.* **2014,** 21-36.

27. Schelter, E. J., Cerium under the lens. *Nat. Chem.* **2013,** 348-348.

28. Nair, V.; Deepthi, A., Cerium(IV) Ammonium NitrateA Versatile Single-Electron Oxidant. *Chem. Rev.* **2007,** 1862-1891.

29. Nair, V.; Balagopal, L.; Rajan, R.; Mathew, J., Recent Advances in Synthetic Transformations Mediated by Cerium(IV) Ammonium Nitrate. *Acc. Chem. Res.* **2004,** 21-30.

30. Jeske, G.; Schock, L. E.; Swepston, P. N.; Schumann, H.; Marks, T. J., Highly Reactive Organolanthanides - Synthesis, Chemistry, and Structures of 4f Hydrocarbyls and Hydrides with Chelating Bis(Polymethylcyclopentadienyl) Ligands. *J. Am. Chem. Soc.* **1985,** 8103-8110.

31. Fendrick, C. M.; Mintz, E. A.; Schertz, L. D.; Marks, T. J., Manipulation of organoactinide coordinative unsaturation and stereochemistry. Properties of chelating bis(polymethylcyclopentadienyl) hydrocarbyls and hydrides. *Organometallics* **1984,** 819-821.

Chapter 8. Transformation of MOF SBUs into Hexanuclear Zr-Alkyl Catalysts for Ethylene Polymerization

8.1 Introduction

The last chapter discussed the activation of Ce-OH bond with HBpin to form Ce-H species as the active catalyst for multiple addition reactions. We are interested in extending this strategy of using oxo-philic reagents to cleave hydroxide groups to other MOF systems. This chapter discusses the stepwise and quantitative transformation of the $Zr_6O_4(OH)_4(HCO_2)_6$ nodes in Zr_6-BTC (MOF-808) to the $[Zr_6O_4(OH)_4Cl_{12}]^{6-}$ nodes in Zr_6Cl_{12}-BTC, and then to the organometallic $[Zr_6O_4(OLi)_4R_{12}]^{6-}$ nodes in ZrR_2-BTC (R = CH_2SiMe_3 or Me). Activation of Zr_6Cl_{12}-BTC with MMAO-12 generates Zr_6Me_6-BTC as an efficient catalyst for ethylene polymerization to produce high-molecular-weight linear polyethylene. Compared to homogeneous Zr catalysts, Zr_6Me_6-BTC displays unique electronic and steric properties with the proximity of multiple active sites. MOF nodes can thus be directly transformed into novel single-site organometallic catalysts for polymerization reactions.

Group IV metal complexes form an important class of catalysts for a broad range of reactions including olefin polymerization, [1-2] hydrogenation, [3-6] hydroboration, [7] and hydroamination. [8-11] For most of these reactions, group IV metal catalysts are advantageous over precious metals for their high natural abundance, low toxicity, and above all, unique reactivity through ionic pathway. For example, several benchmark Zr-catalysts including zirconocenes, ansa-zirconocenes, and constrained geometry catalysts (CGCs) have been developed over the past few decades as highly active catalysts for olefin polymerization (**Figure 8-1**).[2, 12] All of these catalysts

are coordinated with electron-rich Cp ligands or other ancillary ligands, including amido, amidinate, aryloxide, and imine ligands. Here we report a simple strategy to directly transform the Zr_6 SBU into a hexanuclear Zr-alkyl species that is supported by all-oxygen ligand for olefin polymerization.

Prior to this work, electrophilic Zr-benzyl species were supported on the SBUs of Hf-NU-1000 to afford active catalysts for olefin polymerization.[13] MOF-based olefin polymerization catalysts have also been generated by partial substitution of Zn centers in the Zn_5Cl_4 SBUs of MFU-4l with Ti or Cr species followed by MAO activation.[14] However, the multimetallic nature of metal cluster SBUs in MOFs has not been utilized for olefin polymerization. In homogeneous system, there has been significant interest in developing multinuclear catalysts to harness the cooperative effects of multiple metal centers to tune the molecular weight and the micro-structure of polymer products. For example, dinuclear zirconocene catalysts and CGC catalysts generate polyolefins with higher MW and branching content than their mononuclear analogs, which was ascribed to agostic interactions and the bimetallic chain transfers process (**Figure 8-1**). We hypothesize that MOFs can provide a novel strategy to access multinuclear Zr catalysts with unique electronic and steric properties than homogeneous catalysts. We illustrate this approach by transforming Zr_6-BTC to organometallic $Zr_6(O)_4(OLi)_4R_{12}Li_6$ (ZrR_2-BTC, R = CH_2SiMe_3 or Me) and $Zr_6(O)_4(OLi)_4Me_6$ (Zr_6Me_6-BTC) nodes. Zr_6Me_6-BTC efficiently catalyzes the polymerization of ethylene to generate high-MW linear polyethylene.

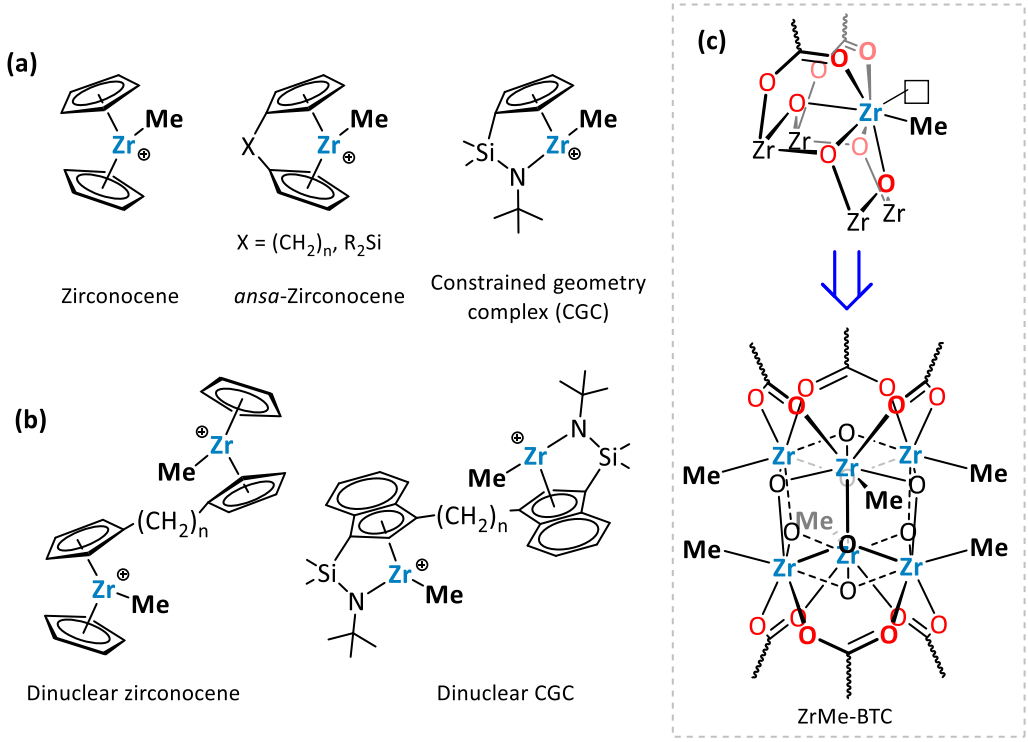

Figure 8-1. Zr coordination environments in (a) homogeneous mononuclear Zr olefin polymerization catalysts, (b) homogeneous dinuclear Zr catalysts, and (c) mononuclear versus hexanuclear view of the Zr_6Me_6-BTC catalyst.

8.2 Results and Discussion

8.2.1 Synthesis of Zr_6Cl_{12}-BTC

Scheme 8-1. Synthesis of $Zr_6(OH)_6$-BTC via formate removal from Zr_6-BTC.

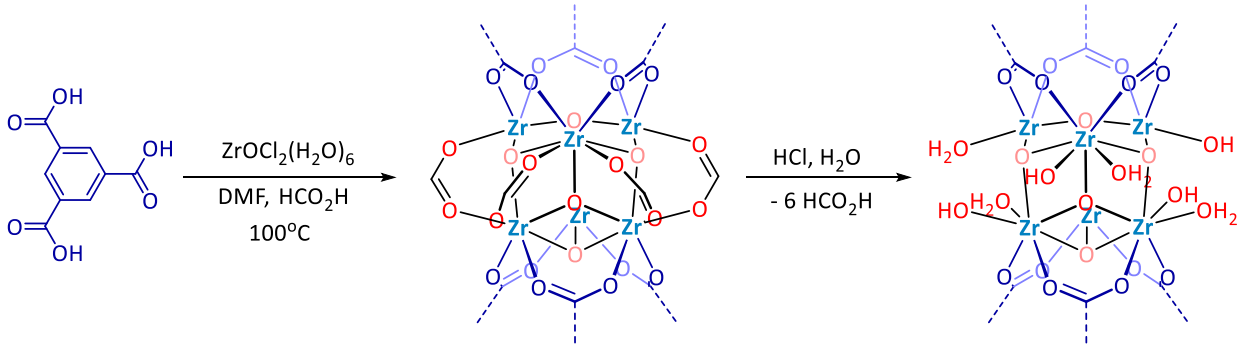

Zr_6-BTC was synthesized in 70% yield using a solvothermal reaction as described in the experimental section (**Scheme 8-1**). ^{1}H NMR analysis of digested Zr_6-BTC indicated the presence

of six formic acids per Zr_6 node. The capping formate groups were removed by stirring Zr_6-BTC in 1M aqueous solution of HCl at 90 °C for 12h to afford $Zr_6(OH)_6$-BTC. The complete removal of formate was confirmed from the ^{1}H NMR of the digested $Zr_6(OH)_6$-BTC. The inorganic node in $Zr_6(OH)_6$-BTC is therefore formulated as $Zr_6(O)_4(OH)_4[(OH)(OH_2)]_6$. Formate removal likely occurs via protonation of the Zr-formate species followed by the H_2O displacement to form a $Zr(OH_2)^{2+}$ intermediate that is deprotonated to form the $Zr(OH)(OH_2)$ species in $Zr_6(OH)_6$-BTC. The MOF crystallinity of $Zr_6(OH)_6$-BTC was maintained as indicated by its similar PXRD pattern to Zr_6-BTC.

Scheme 8-2. Synthesis of Zr_6Cl_{12}-BTC via deoxygenation of $Zr_6(OH)_6$-BTC with Me_3SiCl.

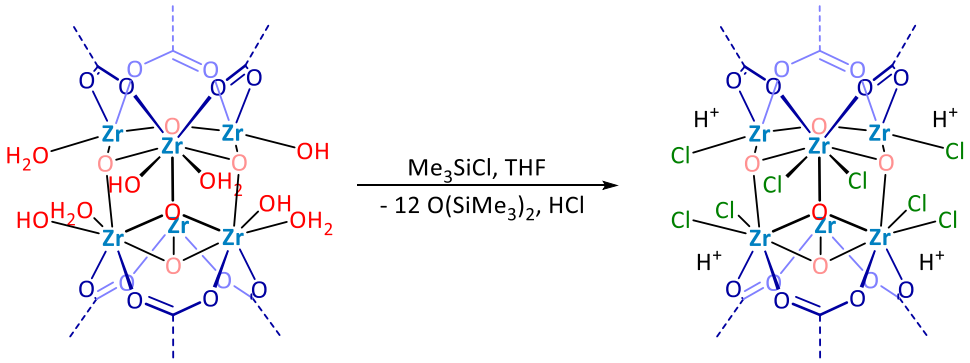

The terminal Zr-OH/-OH_2 bonds in $Zr_6(OH)_6$-BTC were cleaved with 10 equiv. of Me_3SiCl at 23 °C to generate Zr-Cl bonds in Zr_6Cl_{12}-BTC along with two equiv. of $(SiMe_3)_2O$. The formula of Zr_6Cl_{12}-BTC was therefore proposed to be $Zr_6O_4(OH)_4(Cl_{12}H_6)(BTC)_2$ (**Scheme 8-2**). $(SiMe_3)_2O$ is the only side product from the activation step. The identity of $(SiMe_3)_2O$ was confirmed by ^{29}Si and ^{1}H NMR spectroscopy, and the amount of $(SiMe_3)_2O$ was determined by ^{1}H NMR to be 1.97±0.22 equiv. w.r.t. Zr. Me_3SiCl was previously used to activate U=O and Cd-OR bonds to form U-Cl and Cd-Cl species in molecular systems. The synthesis of Zr_6Cl_{12}-BTC represents the first example of using this strategy in a MOF system.[15-16] We propose that the Zr-OH species is first silylated to generate Zr-$OSiMe_3$, which further reacts with Me_3SiCl to form a

labile [Zr-O($SiMe_3$)$_2$]Cl intermediate. The labile ($SiMe_3$)$_2$O was displaced by Cl^- to form the Zr-Cl bond. The Zr-OH_2 bond can be analogously converted to [Zr-Cl]H.

Zr_6Cl_{12}-BTC remains crystalline as indicated by PXRD studies (**Figure 8-2a**). TEM image of the MOF shows the particle size of ~200 nm, and displayed clear lattice fringes with a distance of 1.72 nm, corresponding to the d-spacing of (200) planes which was calculated to 1.75 nm (**Figure 8-2b**).

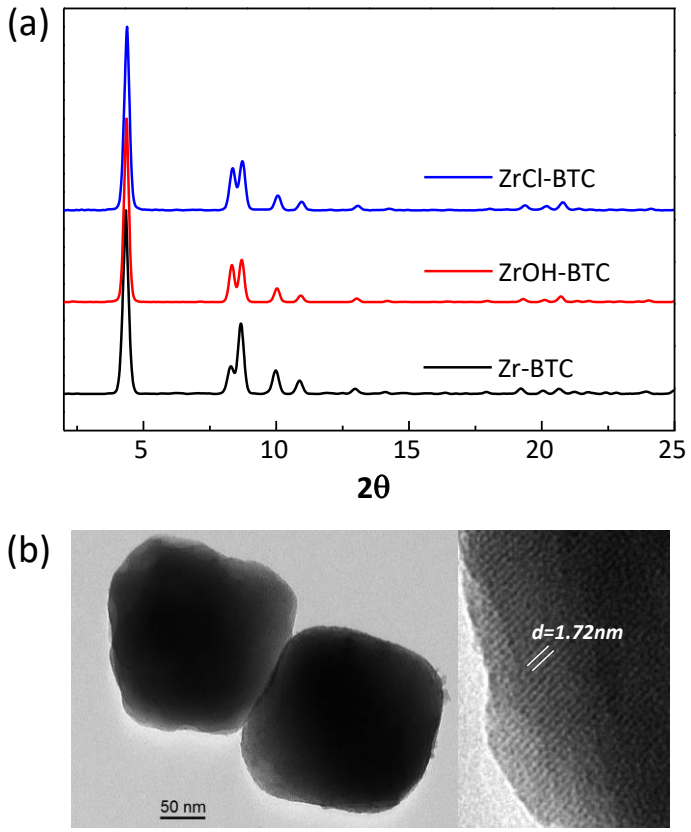

Figure 8-2. (a) PXRD patterns of Zr_6-BTC (black), $Zr_6(OH)_6$-BTC (red), Zr_6Cl_{12}-BTC (blue), and Zr(CH_2SiMe_3)$_2$-BTC (pink) indicate the retention of crystallinity through SBU transformations. (b)TEM image of Zr_6Cl_{12}-BTC.

Zr_6Cl_{12}-BTC has a BET surface area of 1693 m^2/g by measuring the N_2 sorption isotherms at 77K. The surface area is slightly lower than those of Zr_6-BTC (1843 m^2/g) and $Zr_6(OH)_6$-BTC

(1779 m^2/g), due to the increased SBU weight of Zr_6Cl_{12}-BTC (**Figure 8-3**). Pore size analysis of Zr_6Cl_{12}-BTC MOF indicates a uniform pore of 2.1 nm, which is slightly smaller than that of Zr_6-BTC (2.3 nm) as a result of having twelve chloride coordination per Zr_6 node (**Figure 8-4**).

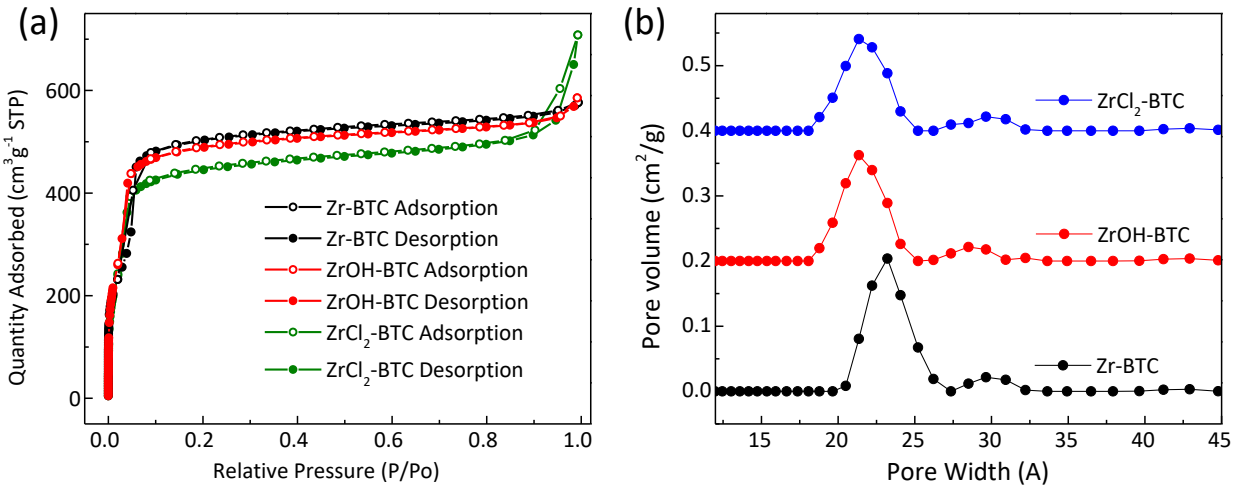

Figure 8-3. (a) N_2 sorption isotherm of Zr_6-BTC (black), $Zr_6(OH)_6$-BTC (red) and Zr_6Cl_{12}-BTC (green). (b) Pore size distribution of Zr_6-BTC (black), $Zr_6(OH)_6$-BTC (red) and Zr_6Cl_{12}-BTC (blue).

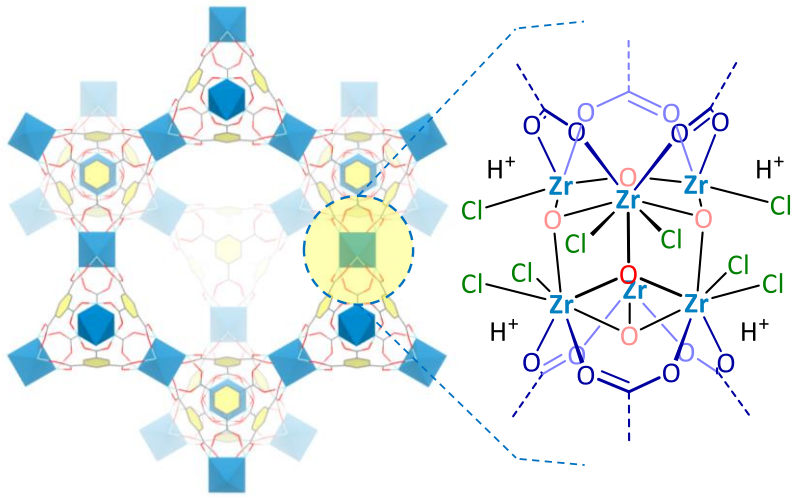

Figure 8-4. Structural model of Zr_6Cl_{12}-BTC showing large open channels of 2.1 nm in the largest dimension (left) and chemical structure of octahedral Zr_6Cl_{12} SBUs (right).

The Zr coordination environment in Zr_6Cl_{12}-BTC was studied using EXAFS. The Zr-Cl scattering pathway is evident from the second peak of Zr K-edge EXAFS spectra in the R-space, which was well separated from Zr-O scattering pathways. EXAFS fitting of the Zr coordination environment validated the proposed $[Zr_6O_4(OH)_4Cl_{12}]H_6$ model with a Zr-Cl distance of 2.50 Å, which matched well with Zr-Cl bond distances in small molecular systems (**Figure 8-5**). TGA analysis of Zr_6Cl_{12}-BTC showed a weight loss of 48.7% in the 140-800 °C range, corresponding well to the decomposition of $Zr_6O_4(OH)_4(Cl_{12}H_6)(BTC)_2$ to $(ZrO_2)_6$ (calculated 47.7%).

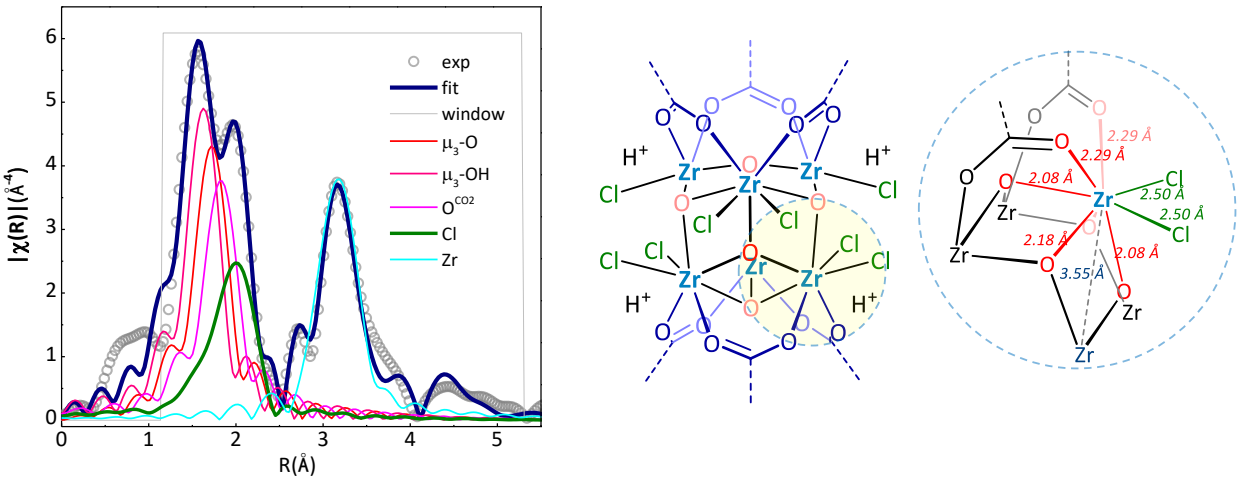

Figure 8-5. EXAFS fitting of Zr_6Cl_{12}-BTC and the bond distances obtained from the fitting result.

8.2.2 Synthesis of Zr_6R_{12}-BTC and Zr_6Me_6-BTC

The Zr-Cl bonds in Zr_6Cl_{12}-BTC can be alkylated with alkyllithium reagents. Treatment of Zr_6Cl_{12}-BTC with 10 equiv. of $LiCH_2SiMe_3$ converted the $ZrCl_2$ species into the $Zr(CH_2SiMe_3)_2$ species in the $Zr_6O_4(OLi)_4(CH_2SiMe_3)_{12}Li_6$ SBU (**Scheme 8-3**). This reaction was likely driven by the formation of LiCl as a more stable ionic compound.

Scheme 8-3. Alkylation of Zr_6Cl_{12}-BTC to form $Zr_6(CH_2SiMe_3)_{12}$-BTC.

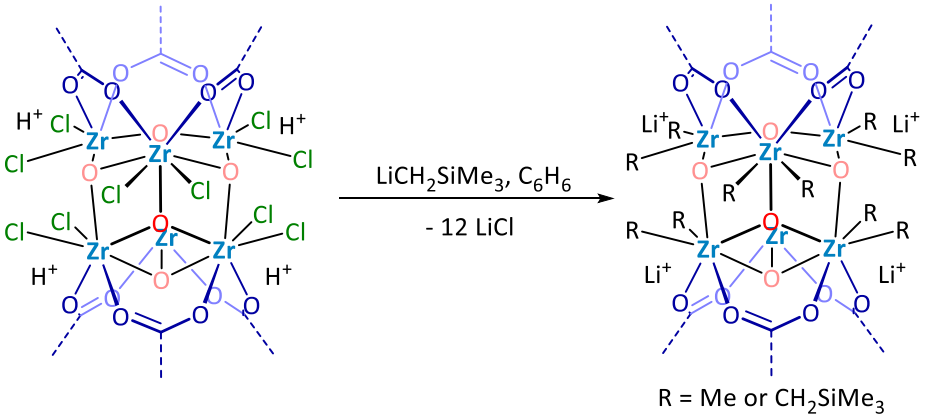

This step progressed with the release of 1.69 ± 0.17 equiv of $SiMe_4$, which matchs well with the calculated number of 1.67 equiv. The Li/Zr ratio was determined to be 1.68 ± 0.05 by ICP-MS, consistent with the calculated value of 1.67. Zr_6Me_{12}-BTC was similarly generated by treating Zr_6Cl_{12}-BTC with 10 equiv of $LiCH_3$. The formation of Zr_6R_{12} (R = CH_2SiMe_3 or Me) species was confirmed by solid-state ^{13}C-cross-polarization magic angle spinning (^{13}C-CPMAS) NMR spectroscopy. The methylene group of $Zr_6(CH_2SiMe_3)_{12}$-BTC appears at δ 73.8, which is slightly more down-field than homogeneous Zr-alkyl analogues, as a result of having more electron-deficient Zr centers in $Zr_6(CH_2SiMe_3)_{12}$-BTC. The $SiMe_3$ group appeared as a sharp peak at 25.1 ppm. As for Zr_6Me_{12}-BTC, the methyl groups of this compound appeared as a broad peak at δ 71.1. This peak position is very similar to that for the methylene group in $Zr_6(CH_2SiMe_3)_{12}$-BTC. In contrast, the Zr_6Cl_{12}-BTC control only showed ^{13}C signals from the BTC ligand, including the carboxylate peak at δ 171.4 and arene peak at δ 134 ppm (**Figure 8-6**).

The Zr K-edge EXAFS data of $Zr_6(CH_2SiMe_3)_{12}$-BTC was fitted well with $Zr(CH_2SiMe_3)_2$ dialkyl structural model, with a Zr-C bonding distance of 2.41 Å. The bond distance matched well with Zr-C bonds that are reported in small molecule systems.[12]

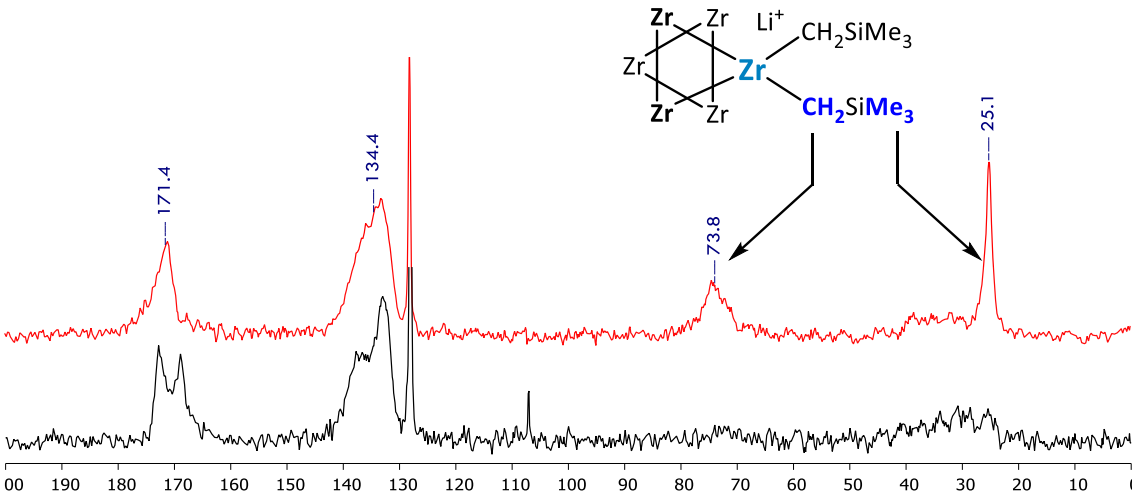

Figure 8-6. ^{13}C-CPMAS NMR spectra of $Zr_6(CH_2SiMe_3)_{12}$-BTC (red) and Zr_6Cl_{12}-BTC (black).

Because the Zr centers in Zr_6R_{12}-BTC are coordination saturated, neither of the two dialkyl compounds are active for alkene polymerization. In homogeneous systems, $LnMCl_2$ complexes are generally reacted with MAO to afford $LnMR^+$ monoalkyl species as active catalysts for olefin polymeration. Analogously, we activated Zr_6Cl_{12}-BTC with aluminum methyl compounds to generate Zr_6Me_6-BTC with node composition of $Zr_6(O)_4(OLi)_4Me_6$, which contains neutral Zr-monoalkyl species with one open coordination sites per Zr-center. Both MMAO-12 and $AlMe_3$ were good activators for transforming Zr_6Cl_{12}-BTC into Zr_6Me_6-BTC as a highly active catalyst for alkene polymerizations (**Scheme 8-4**).

Scheme 8-4. Alkylation-alumination of Zr_6Cl_{12}-BTC to form Zr_6Me_6-BTC.

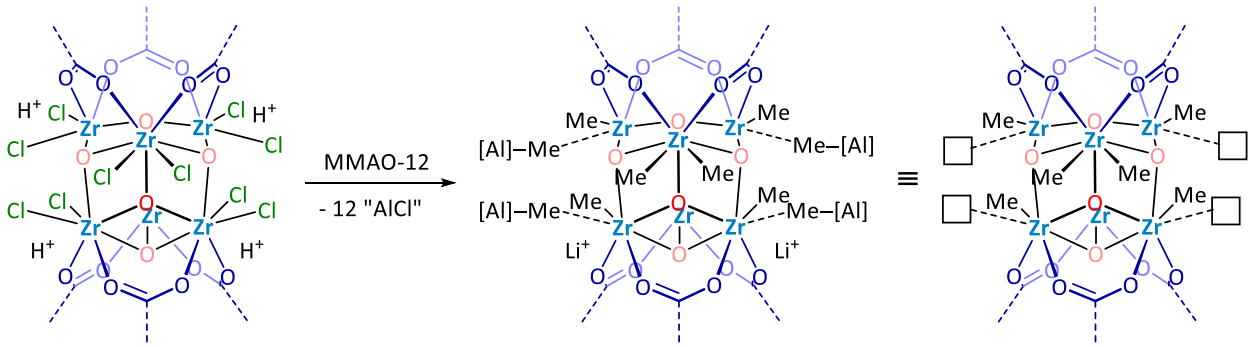

The activation of Zr-Cl bond was confirmed by comparing the EXAFS spectra of Zr_6Me_6-BTC with that of Zr_6Cl_{12}-BTC. The formation of the Zr-Me species was supported by the ^{13}C-CPMAS spectra of Zr_6Me_6-BTC which displayed Zr-Me signal at δ 73.3 (**Figure 8-7**). Furthermore, the Zr-monoalkyl model fitted well to the Zr_6Me_6-BTC EXAFS data with a Zr-C bond distance of 2.24 Å, well matching literature reported Zr-Me distance (**Figure 8-8**).

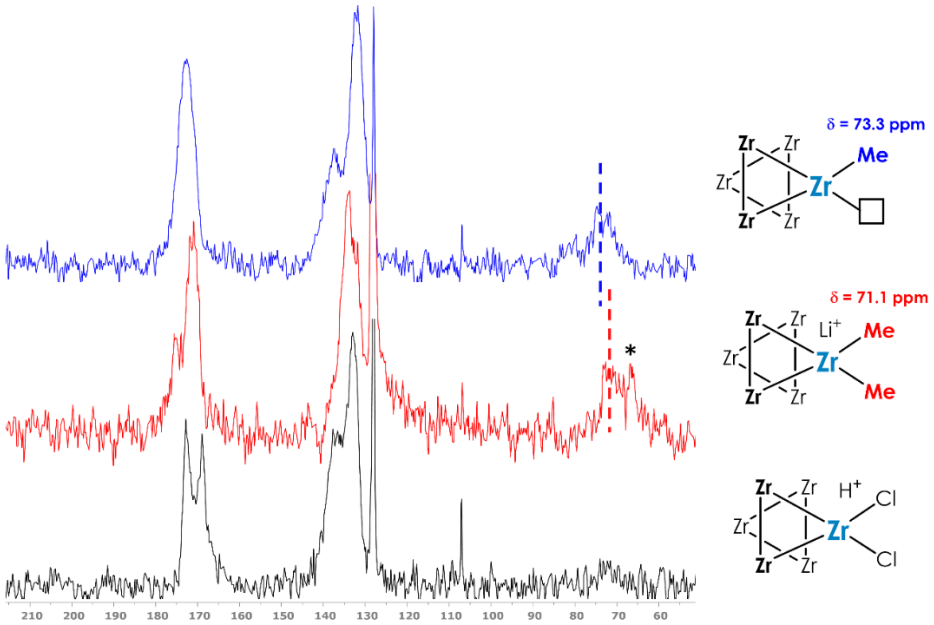

Figure 8-7. ^{13}C-CPMAS NMR spectra of Zr_6Cl_{12}-BTC (black), Zr_6Me_{12}-BTC (red) and Zr_6Me_6-BTC (blue). * signal from residual Et_2O.

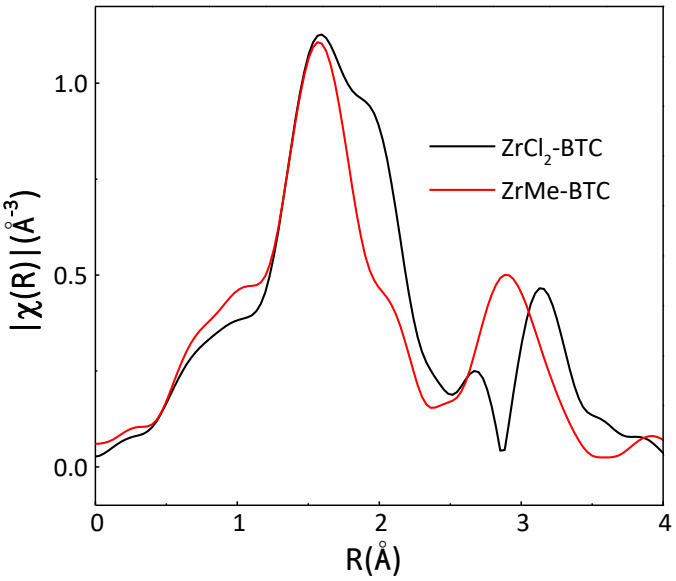

Figure 8-8. Comparison of the EXAFS spectra of Zr_6Cl_{12}-BTC and Zr_6Me_6-BTC.

8.2.3 Olefin polymerization using Zr_6Me_6-BTC

The in situ generated Zr_6Me_6-BTC is active for ethylene polymerization to produce high-MW linear PE. The activity of Zr_6Me_6-BTC increases with temperature (20-140 °C) and ethylene pressure (100-800 psi), reaching a maximum value of 658.6 kg PE·mol^{-1} Zr·h^{-1} at 100 °C and 800 psi. The maximum activity is equivalent to 3 g of PE per 1 mg of Zr-MOF within one hour. This level olefin polymerization activity compares favorably to other MOF catalysts. The effect of temperature on the catalyst activity and polymer MW agrees with well-established trends (**Table 8-1**). The effect of pressure on the catalytic performance of Zr_6Me_6-BTC varies significantly from homogenous Zr catalysts (**Table 8-2**). Typically for a homogenous Zr catalyst, polymerization activity increases linearly with respect to monomer pressure. However, we observe a 30-fold increase in activity with an 8-fold increase in ethylene pressure for the Zr_6Me_6-BTC catalyst. This effect may arise from polymer-induced fracture of the MOF particles, leading to the exposure of additional active sites.

Table 8-1. Zr_6Me_6-BTC catalyzed ethylene polymerization at different temperatures.[a]

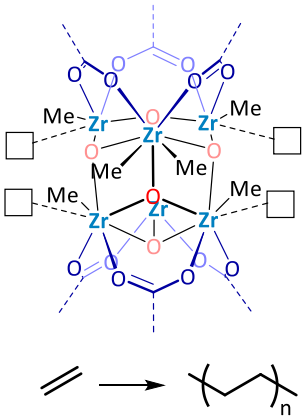

Entry	T (°C)	Yield (g)	Activity (kg×mol^{-1}×h^{-1})	M_n (×103)	M_w/M_n	T_m
1	20	0.289	2.41	158	2.69	137
2	40	0.499	4.16	189	2.62	138
3	60	1.781	14.84	191	3.55	134
4[b]	80	1.190	19.83	114	2.44	138
5[b]	100	1.431	23.85	55	4.91	134
6[b,c]	120	1.386	23.10	109	7.79	132
7[b,c]	140	1.921	32.02	47	5.78	131

[a]Fisher-Porter tube, 30 mL toluene, 0.06 mmol Zr, 12.0 mmol MMAO-12 (200 equiv.), 100 psi C2H4, 2h. [b]0.03 mmol Zr, 6.0 mmol MMAO-12 (200 equiv.) was used. [c]30 mL mesitylene.

PE samples produced by Zr_6Me_6-BTC at 20 and 40 °C have monomodal MW distributions with PDIs of 2.6, consistent with the proposed action of a single-site catalyst. At elevated temperatures, the reactor becomes filled with solvent-swollen PE and diffusion of ethylene to the active sites is limited. Broader MW distributions are observed at higher polymerization temperatures, which we ascribe to mass transport phenomena.

For control experiments, $Zr_6(OH)_6$-BTC and Zr_6-BTC were treated with MMAO-12 and are shown to be inactive for ethylene polymerization. To further demonstrate that the MOF catalyst is the only active species instead of any leached-out Zr complexes, Zr_6Cl_{12}-BTC was treated with activator in the absence of ethylene and centrifuged to collect the supernatant. The supernatant was inactive for ethylene polymerization, excluding the possibility of having leached species as the active catalyst.

Table 8-2. Zr_6Me_6-BTC catalyzed ethylene polymerization under different pressures

Entry	P (psi)	Yield (g)	Activity ($kg \times mol^{-1} \times h^{-1}$)	M_n ($\times 10^3$)	M_w/M_n	T_m
1	100	0.219	21.9	100	3.03	138
2	200	0.379	37.9	113	2.72	135
3	400	0.917	91.7	306	3.70	135
4	600	1.841	184.1	345	2.30	137
5	800	6.586	658.6	119	1.82	135

Conditions: Stainless steel Parr autoclave, 30 mL toluene, 100 °C, 0.005 mmol Zr, 1.00 mmol MMAO-12 (200 equiv.), 2 h.

Zr_6Me_6-BTC has high thermal stability and a long lifetime. Even at 100 °C, no decrease in activity was observed in 12 h. PXRD of the polymer product shows that the crystallinity of the MOF is still maintained after polymerization and acid work up, further demonstrating the robustness of the MOF catalyst. The site isolation effect of the MOF catalyst may stabilize the active species as seen in other catalytic MOFs. The lifetime of the catalytic species was probed by determining the activity for catalytic runs of 0.5 h, 2 h, and 12 h at 100 °C and 200 psi of ethylene (**Table 8-3**). The catalyst activity remains the same within that 12 h testing period.

Table 8-3. Zr_6Me_6-BTC catalyst activity during different reaction time periods.

	Activator	**C_2H_4/psi**	**Time/h**	**Yield/g**	**Activity /kg PE mol^{-1} Zr h^{-1}**	**M_n**	**M_w/M_n**	**T_m**
1	MMAO-12	200	0.5	0.101	40.4	---	---	132
2	MMAO-12	200	2	0.379	37.9	113,000	2.72	135
3	MMAO-12	200	12	2.440	40.7	---	---	134

8.3 Conclusion

In this chapter, we demonstrate that the $Zr_6O_4(OH)_4(HCO_2)_6$ nodes in Zr_6-BTC can be converted to the $[Zr_6O)_4(OH)_4Cl_{12}]^{6-}$ nodes and then to the organometallic $[Zr_6O_4(OLi)_4R_{12}]^{6-}$ or $Zr_6O_4(OLi)_4(Me)_6$ nodes. The stabilization of multimetallic active sites in Zr_6Me_6-BTC affords a robust catalyst with a long lifetime for the production of high-molecular-weight polyethylene. Notably, Zr_6Me_6-BTC is the first MOF polymerization catalyst that uses the metals of the SBUs as the active species, providing a cost-effective strategy for designing solid catalysts for olefin polymerization.

8.4 Experimental

8.4.1 Material and methods

All of the reactions and manipulations were carried out under nitrogen with the use of standard inert atmosphere and Schlenk techniques unless otherwise indicated. Tetrahydrofuran was purified by passing through a neutral alumina column under N_2. d_6-Benzene was distilled over CaH_2. Ethylene was purchased from Matheson Tri-Gas. Propylene and 1-hexene were purchased from Sigma. Alumina reagents were purchased from Sigma Aldrich. Powder X-ray diffraction data were collected on Bruker D8 Venture diffractometer using Cu Kα radiation source (l = 1.54178 Å). Nitrogen adsorption experiments were performed on a Micrometrics TriStar II 3020 instrument. Thermogravimetric analysis (TGA) was performed under air using a Shimazu TGA-50 equipped with a platinum pan and heated at a rate of 1.5 °C per min. ^{1}H NMR spectra were recorded on a Bruker NMR 500 DRX spectrometer at 500 MHz or a Bruker NMR 400 DRX spectrometer at 400 MHz, and referenced to the proton resonance resulting from incomplete deuteration of the $CDCl_3$ (δ 7.26) or C_6D_6 (δ 7.14). ^{29}Si NMR spectra were recorded at 79.5 MHz, and all of the chemical shifts were reported downfield in ppm relative to an external Me_3SiCl standard. ^{13}C cross-polarization magic angle spinning (CPMAS) solid-state NMR spectra were recorded on a Varian VXR400 (FT, 100MHz, ^{13}C). Samples were packed into 5mm cylindrical zirconia rotors in the glovebox and capped with a solid Teflon cap to avoid air exposure. ICP-MS data were obtained with an Agilent 7700x ICP-MS and analyzed using ICP-MS MassHunter version B01.03. Sample were diluted in a 2% HNO_3 matrix and analyzed with a ^{159}Tb internal standard against a 12-point standard curve over the range from 0.1 ppb to 500 ppb. The correlation was >0.9997 for all analyses of interest. Data collection was performed in Spectrum Mode with five replicates per sample and 100 sweeps per replicates.

8.4.2 Synthesis of Zr_6-BTC

$ZrOCl_2(H_2O)_8$ (680 mg) and trimesic acid (H_3BTC, 440 mg) were dissolved in DMF (40 mL) and H_2O (40 mL), and heated in a 100 °C oven for 2 days to afford Zr-BTC as a white solid (336 mg, 70% yield). The MOF was centrifuged, and then washed with 60 mL of DMF three times to remove residual metal and ligand precursors.

To quantify the amount of formate in Zr-BTC, the MOF was dried under vacuum then digested with D_3PO_4/DMSO-d_6 (0.15 mL in 0.8 mL) and analyzed by ^{1}H NMR. 0.91 equiv. of HCO_2H w.r.t. Zr was detected, corresponding to 5.5 HCO_2^- per Zr_6 node (**Figure 8-9**).

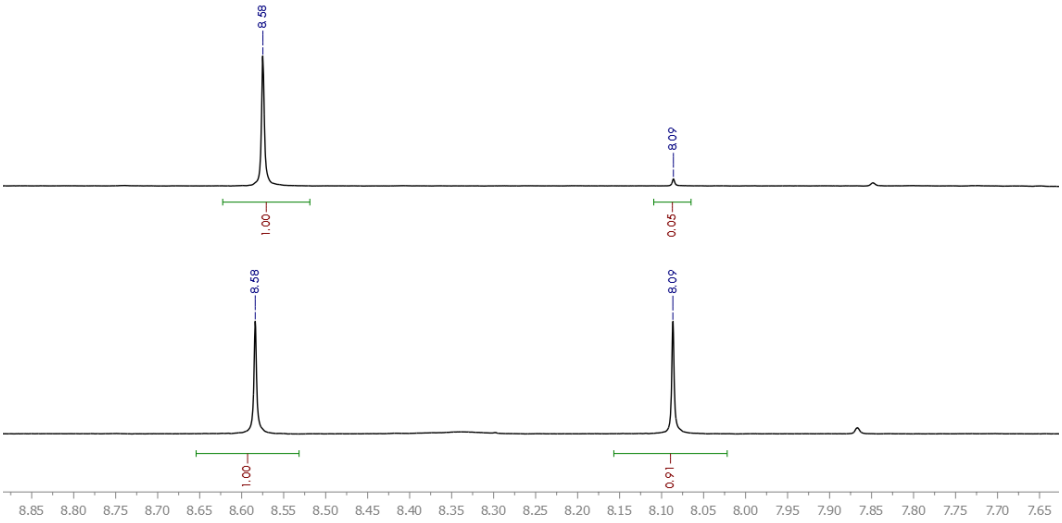

Figure 8-9. ^{1}H NMR of digested $Zr_6(OH)_6$-BTC (top) and Zr_6-BTC (bottom).

8.4.3 Synthesis of $Zr_6(OH)_6$-BTC

The experimental procedure for formate removal to access $Zr_6(OH)_6$-BTC is very straightforward. Zr_6-BTC (800 mg) in DMF was washed with 60 mL of deionized H_2O three times to remove DMF, then suspended in 80 mL of HCl (1M in H_2O) and heated in a 90 °C oven for 12 h. The mixture was centrifuged and sequentially washed with deionized H_2O three times, acetone

three times, and THF three times before freeze-drying in benzene to yield $Zr_6(OH)_6$-BTC as a white powder (650 mg, 85% yield). The $Zr_6(OH)_6$-BTC sample was stored in a nitrogen-filled glove box. The amount of formate in $Zr_6(OH)_6$-BTC was determined to be 0.05 equiv. of HCO_2H w.r.t. Zr, corresponding to 0.3 HCO_2^- per Zr_6 node (**Figure 8-9**).

8.4.4 Synthesis of Zr_6Cl_{12}-BTC

Experimental procedure for the activation is described as following. In a nitrogen-filled glovebox, $Zr_6(OH)_6$-BTC (200 mg) was dispersed in 10 mL toluene. 10 equiv. of trimethylsilyl chloride (0.78 mL) w.r.t. Zr were added to the suspension. The mixture was stirred for 6 h at room temperature, then centrifuged and washed with toluene three times, and then freeze-dried in benzene to yield Zr_6Cl_{12}-BTC as a white powder (225 mg, 96% yield).

^{29}Si NMR was taken for the supernatant from the Me_3SiCl activation of $Zr_6(OH)_6$-BTC. The chemical shifts of Me_3SiCl (red) and $(Me_3Si)_2O$ (blue) control are δ = 30.00 and 7.95 ppm, respectively. ^{29}Si NMR of the supernatant from $Zr_6(OH)_6$-BTC activation showed the formation of $(Me_3Si)_2O$ along with the unreacted Me_3SiCl starting material (**Figure 8-10**). This suggests that the conversion of Zr-OH/Zr-OH2 into Zr-Cl is driven by the formation of strong Si-O bonds. The amount of $(Me_3Si)_2O$ was monitored by ^{1}H NMR. The chemical shifts of $(Me_3Si)_2O$ control, $SiMe_3Cl$, and mesitylene CH_3 groups (as internal standard) are δ = 0.12, 0.18, and 2.16 ppm, respectively (**Figure 8-11**). The amount of $(Me_3Si)_2O$ was averaged to be 1.97±0.22 equiv. w.r.t. Zr in 3 runs, matching well with the expected value of 2.

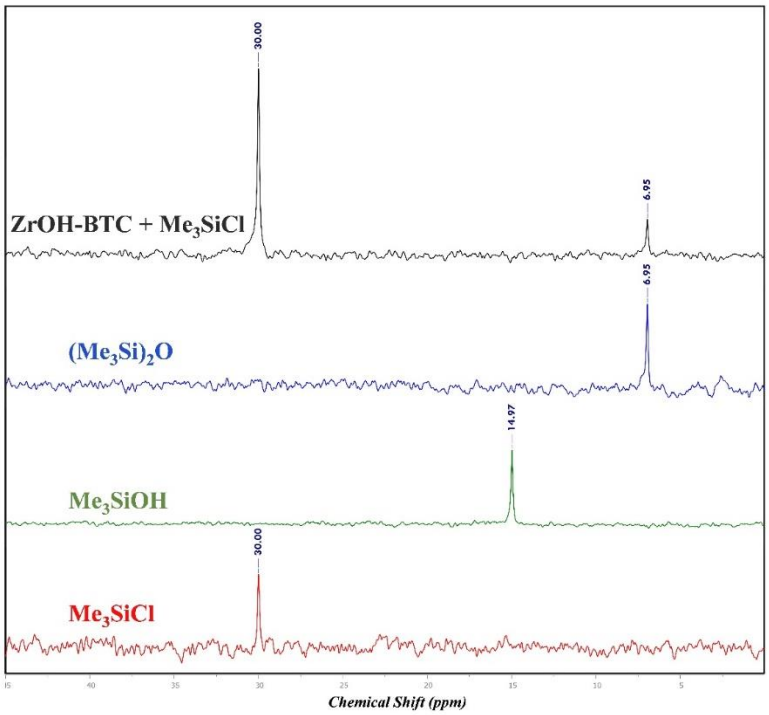

Figure 8-10. ^{29}Si NMR of the supernatant from $Zr_6(OH)_6$-BTC activation with Me_3SiCl.

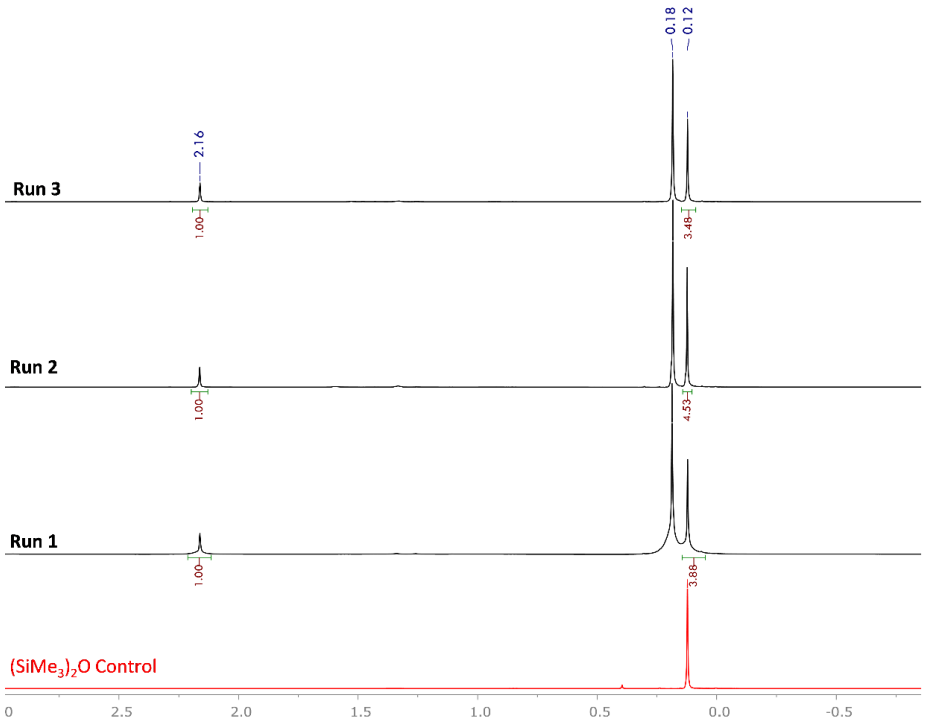

Figure 8-11. ^{1}H NMR of the supernatant from $Zr_6(OH)_6$-BTC activation with Me_3SiCl.

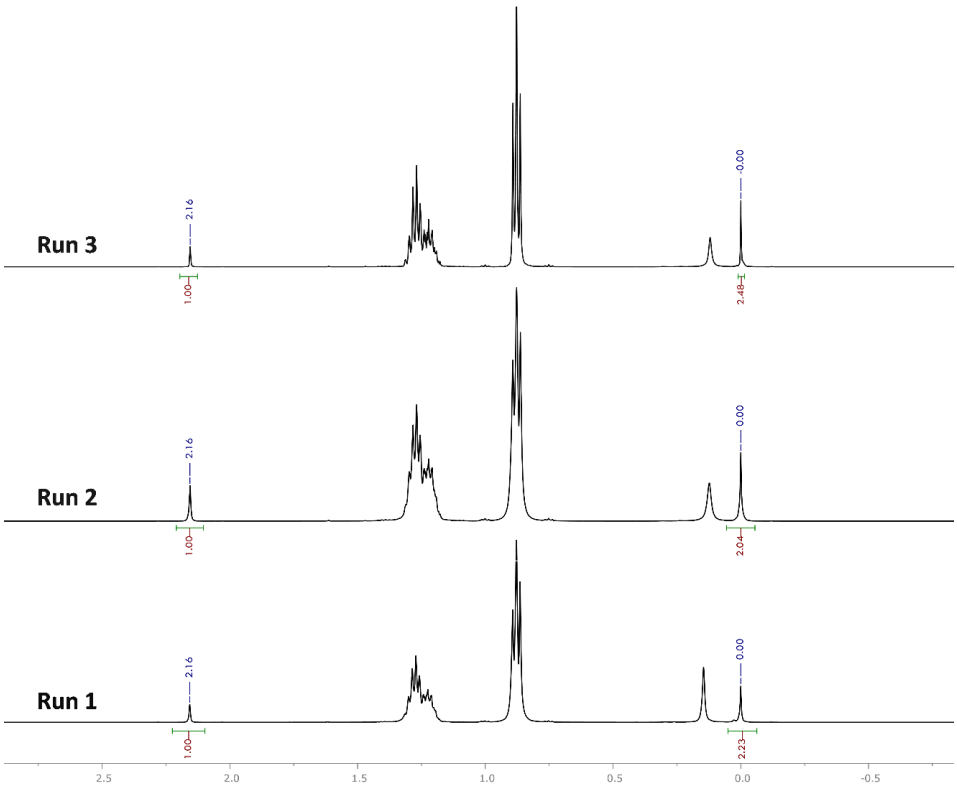

Figure 8-12. ^{1}H NMR of the supernatant from Zr_6Cl_{12}-BTC lithiation with $LiCH_2SiMe_3$ showing the formation of 1.69 ± 0.17 equiv of $SiMe_4$ w.r.t. Zr.

8.4.5 Application of Zr_6Me_6-BTC for ethylene polymerization

High pressure homopolymerizations of ethylene and lifetime experiments were performed in a 300 mL stainless steel Parr autoclave equipped with a water-cooling loop, thermocouple and magnetically coupled stirrer, and controlled by a Parr 4842 controller. In a glovebox, $ZrCl_2$-BTC was washed three times with toluene and then suspended in 30 mL of Toluene. The suspension was then transferred to a glass liner. Cocatalyst was added to the suspension and the liner was placed inside the autoclave. Then the autoclave was sealed and transferred out of the box. The autoclave was heated to the desired temperature (100 °C) and kept at that temperature for at least 10 min while the mixture was stirred at the rate of 150 rpm. The autoclave was pressurized with ethylene to the desired pressure and had a constant flow of ethylene. After the desired time the

ethylene flow was terminated and the pressure was slowly released in a fume hood. The mixture was cooled to room temperature and 100-150 mL of acidified MeOH (10% HCl) was added. The polymer was collected by filtration, washed with MeOH (3 x 20 mL). The polymer was then transferred into a tared scintillation vial and dried in a vacuum oven overnight.

For low pressure homopolymerization of ethylene that was used to screen activators and temperature, a glass Fischer-Porter bottle equipped with a magnetic stir bar was used. In a glovebox, $ZrCl_2$-BTC was washed three times with toluene and then suspended in 30 mL of Toluene. The suspension was then transferred to a Fischer-Porter bottle. The bottle was then sealed and taken out of the glovebox. The bottle was then heated in an oil bath at the desired temperature for 30 minutes (For room temperature polymerizations, the bottle was placed in a room temperature water bath). The bottle was then pressurized with ethylene to 100 psi and released to 20 psi three times. Then at 20 psi the cocatalyst was injected using a gas-tight syringe through a septum at the top of the Fischer-Porter bottle. The bottle was then charged to 100 psi with a constant flow of ethylene. After 2 h the ethylene flow was terminated and the pressure was slowly released in a fume hood. The mixture was cooled to room temperature and 100-150 mL of acidified MeOH (10% HCl) was added. The polymer was collected by filtration, washed with MeOH (3 x 20 mL). The polymer was then transferred into a tared scintillation vial and dried in a vacuum oven overnight.

Gel permeation chromatography (GPC) data were obtained on a Polymer Laboratories PL-GPC 200 instrument at 150 °C with 1,2,4-trichlorobenzene (stabilized with 125 ppm BHT) as the mobile phase. Three PLgel 10 μm Mixed-B LS columns were used. Molecular weights were calibrated using narrow polystyrene standards (ten-point calibration with Mn from 570 Da to 5670 kDa) and are corrected for linear polyethylene by universal calibration using the following

Mark−Houwink parameters: polystyrene, $K = 1.75 \times 10^{-2}$ cm^3 g^{-1} , $\alpha = 0.67$; polyethylene, $K = 5.90 \times 10^{-2}$ cm^3 g^{-1} , $\alpha = 0.69$

Melting points of the PE samples were determined using DSC. DSC measurements were collected on a TA Instruments DSC 2920 instrument. Samples (4-5 mg) were annealed by heating to 180 C at 15 °C/min, cooled to 50 C at 15 °C/min, and then analyzed while being heated to 180 °C at 15 °C/min.

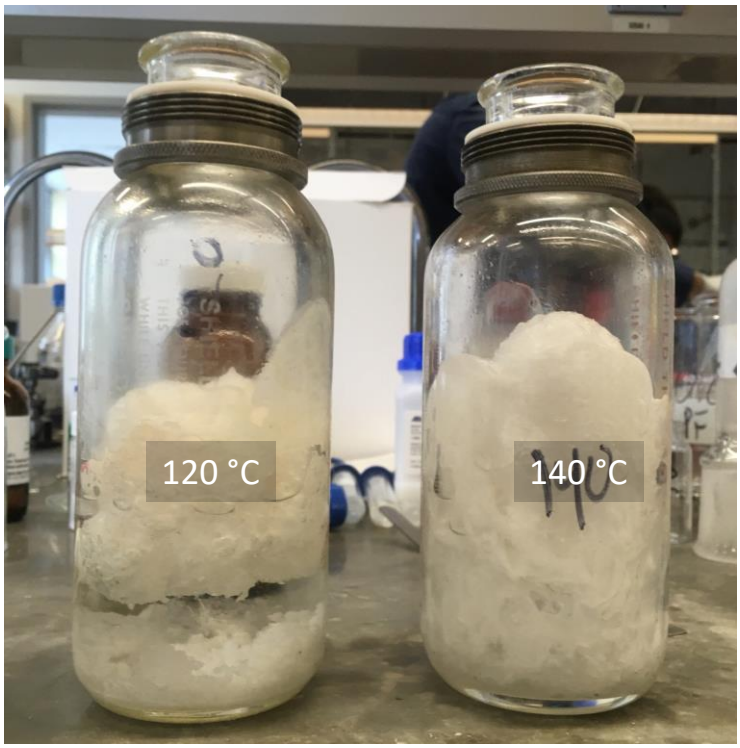

Figure 8-13. Picture of polyethylene product from Zr_6Me_6-BTC catalyzed reaction.

8.4.5 Application of Zr_6Me_6-BTC for the polymerization of propylene and 1-hexene

The Zr_6Me_6-BTC is also active for the polymerization of propylene. The activity of Zr_6Me_6-BTC for the homopolymerization of propylene was screened at low pressure. The trials were conducted in a Fisher-Porter bottle equipped with a magnetic stirring bar with Zr_6Cl_{12}-BTC

(20 mg, 0.06 mmol) suspended in 30 mL of toluene and 200 equiv. (12 mmol) of cocatalyst were added in the presence of propylene.

In a glovebox, Zr_6Cl_{12}-BTC was washed three times with toluene and then suspended in 30 mL of toluene. The suspension was then transferred to a Fischer-Porter bottle. The bottle was then sealed and taken out of the glovebox. The bottle was then heated in an oil bath at the desired temperature for 30 minutes (For room temperature polymerization, the bottle was placed in a room temperature water bath). The bottle was then pressurized with propylene to 40 psi. After 30 minutes, the pressure was released to 20 psi and the cocatalyst was injected using a gas-tight syringe through a septum at the top of the Fischer-Porter bottle. The bottle was then charged to 40 psi with a constant flow of propylene. After 2 h the propylene flow was terminated and the pressure was slowly released in a fume hood. The mixture was cooled to room temperature and 100-150 mL of acidified MeOH (10% HCl) was added. The polymer was collected by filtration, washed with MeOH (3 x 20 mL). The polypropylene (PP) was then transferred into a tared scintillation vial and dried in a vacuum oven overnight. The polymerization activity under different temperature were listed in **Table 8-4**.

Table 8-4. Zr_6Me_6-BTC catalyst activity for propene polymerization

Entry	Activator	C_3H_6 / psi	Time/h	T/°C	Yield/g	Activity/ kg PP mol^{-1} Zr h^{-1}
1	MMAO-12	40	2	20	0.025	0.21
2	MMAO-12	40	2	40	0.038	0.32

The activity of Zr_6Cl_{12}-BTC for the homopolymerization of 1-hexene was screened. The trials were conducted in a 15 mL pressure vessel equipped with a magnetic stirring bar with

Zr_6Cl_{12}-BTC (5 mg, 0.015 mmol) suspended in 2 mL of 1-hexene and 200 equiv. (3 mmol) of cocatalyst were added to the suspension.

3 mmol of MMAO-12 in toluene was added to a Schleck flask and was dried overnight at room temperature on a high vacuum manifold, yielding a white powder. The flask was then pumped into the glovebox and the white powder was then dissolved in 1.5 mL of 1-hexene, yielding a 2M solution of MMAO-12 in 1-hexene.

In a glovebox, Zr_6Cl_{12}-BTC was washed three times with 1-hexene and then suspended in 5 mL of 1-hexene. The suspension was then transferred to a pressure vessel. Then 1.5 mL of the 2M MMAO-12 in hexane solution was added and the vessel was then sealed and taken out of the glovebox. The bottle was then heated in an oil bath (For room temperature polymerization, the bottle was placed in a room temperature water bath). After 2 h, the pressure vessel was opened and 10 mL of hexanes was added to the reaction mixture, which was then transferred dropwise to 100-150 mL of acidified MeOH (10% HCl). The mixture was stirred for 2 hours and then the hexanes layer was separated from the acidified methanol layer. The hexanes layer was washed with MeOH (3 x 30 mL). The hexanes solution was added to a tared flask and then concentrated in vacuo. The resulting poly(1-hexene) (PH) was a viscous oil and was dried in a vacuum oven overnight. The polymerization activity under different temperature were listed in **Table 8-5**.

Table 8-5. Zr_6Me_6-BTC catalyst activity for 1-hexene polymerization.

Entry	Activator	Time/h	T/°C	Yield/g	Activity/ kg PH mol^{-1} Zr h^{-1}
1	MMAO-12	2	20	0.053	1.77
2	MMAO-12	2	60	0.066	2.20

Branching per 1000 carbons was determined to be 167 by following formula:

$$\frac{2I_{Me}}{3I_{total}} \times 1000$$

This suggests exclusive 1,2-enchainment of 1-hexene.

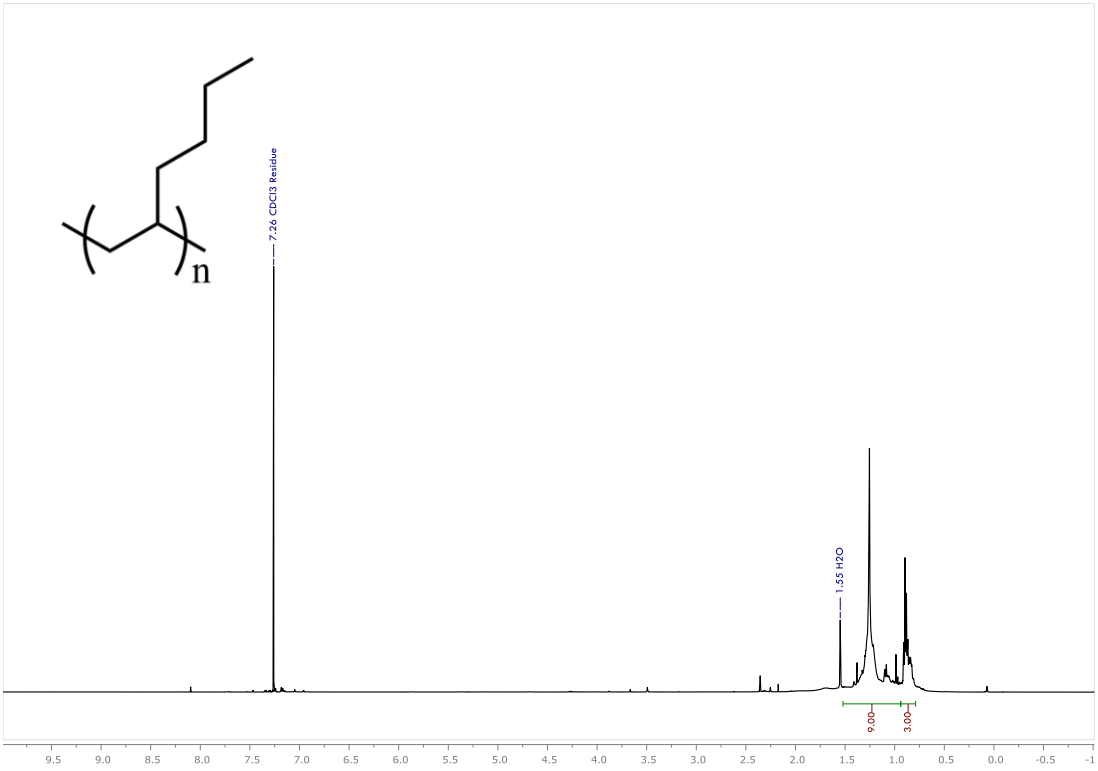

Figure 8-14. ^{1}H NMR spectrum of poly(1-hexene) in $CDCl_3$. Poly(1-hexene) sample from entry 2, table S7. Bruker NMR 500 DRX spectrometer at 500 MHz with the following parameters: aq. = 3.7, d1 = 42.2, and ns = 120.

8.5 Reference

1. Jordan, R. F.; Bajgur, C. S.; Willett, R.; Scott, B., Ethylene polymerization by a cationic dicyclopentadienyl zirconium (IV) alkyl complex. *J. Am. Chem. Soc.* **1986,** 7410-7411.

2. Chien, J. C. W., Supported metallocene polymerization catalysis. *Top. Catal.* **1999,** 23-36.

3. Troutman, M. V.; Appella, D. H.; Buchwald, S. L., Asymmetric hydrogenation of unfunctionalized tetrasubstituted olefins with a cationic zirconocene catalyst. *J. Am. Chem. Soc.* **1999,** 4916-4917.

4. Williams, L. A.; Guo, N.; Motta, A.; Delferro, M.; Fragalà, I. L.; Miller, J. T.; Marks, T. J., Surface structural-chemical characterization of a single-site d0 heterogeneous arene hydrogenation catalyst having 100% active sites. *PNAS* **2013,** 413-418.

5. Stalzer, M. M.; Nicholas, C. P.; Bhattacharyya, A.; Motta, A.; Delferro, M.; Marks, T. J., Single-Face/All-cis Arene Hydrogenation by a Supported Single-Site d0 Organozirconium Catalyst. *Angew. Chem. Int. Ed.* **2016,** 5349-5353.

6. Gu, W.; Stalzer, M. M.; Nicholas, C. P.; Bhattacharyya, A.; Motta, A.; Gallagher, J. R.; Zhang, G.; Miller, J. T.; Kobayashi, T.; Pruski, M., Benzene Selectivity in Competitive Arene Hydrogenation: Effects of Single-Site Catalyst⋯ Acidic Oxide Surface Binding Geometry. *J. Am. Chem. Soc.* **2015,** 6770-6780.

7. Eedugurala, N.; Wang, Z.; Chaudhary, U.; Nelson, N.; Kandel, K.; Kobayashi, T.; Slowing, I. I.; Pruski, M.; Sadow, A. D., Mesoporous silica-supported amidozirconium-catalyzed carbonyl hydroboration. *ACS Catal.* **2015,** 7399-7414.

8. Manna, K.; Everett, W. C.; Schoendorff, G.; Ellern, A.; Windus, T. L.; Sadow, A. D., Highly Enantioselective Zirconium-Catalyzed Cyclization of Aminoalkenes. *J. Am. Chem. Soc.* **2013,** 7235-7250.

9. Leitch, D. C.; Turner, C. S.; Schafer, L. L., Isolation of Catalytic Intermediates in Hydroamination Reactions: Insertion of Internal Alkynes into a Zirconium–Amido Bond. *Angew. Chem. Int. Ed.* **2010,** 6382-6386.

10. Walsh, P. J.; Baranger, A. M.; Bergman, R. G., Stoichiometric and catalytic hydroamination of alkynes and allene by zirconium bisamides Cp2Zr (NHR) 2. *J. Am. Chem. Soc.* **1992,** 1708-1719.

11. Sun, Q.; Wang, Y.; Yuan, D.; Yao, Y.; Shen, Q., Zirconium catalysed intermolecular hydroamination reactions of secondary amines with alkynes. *ChemComm* **2015,** 7633-7636.

12. McKnight, A. L.; Waymouth, R. M., Group 4 ansa-cyclopentadienyl-amido catalysts for olefin polymerization. *Chem. Rev.* **1998,** 2587-2598.

13. Klet, R. C.; Tussupbayev, S.; Borycz, J.; Gallagher, J. R.; Stalzer, M. M.; Miller, J. T.; Gagliardi, L.; Hupp, J. T.; Marks, T. J.; Cramer, C. J., Single-Site Organozirconium Catalyst Embedded in a Metal–Organic Framework. *J. Am. Chem. Soc.* **2015,** 15680-15683.

14. Comito, R. J.; Fritzsching, K. J.; Sundell, B. J.; Schmidt-Rohr, K.; Dincă, M., Single-Site Heterogeneous Catalysts for Olefin Polymerization Enabled by Cation Exchange in a Metal-Organic Framework. *J. Am. Chem. Soc.* **2016,** 10232-10237.

15. Kiernicki, J. J.; Zeller, M.; Bart, S. C., Facile Reductive Silylation of UO22+ to Uranium (IV) Chloride. *Angew. Chem. Int. Ed.* **2016**.

16. Chakrabarti, N.; Ruccolo, S.; Parkin, G., Cadmium Compounds with an [N3C] Atrane Motif: Evidence for the Generation of a Cadmium Hydride Species. *Inorg. Chem.* **2016,** 12105-12109.

Chapter 9. A Trivalent Zirconium MOF for Catalytic 1, 4-Dearomative Additions of Pyridines and Quinolines

9.1 Introduction

The last chapter established the stepwise transformation of Zr_6-BTC to $Zr^{IV}_6Me_6$-BTC for olefin polymerization. Spectroscopic data suggests that the $Zr^{IV}_6Me_6$-BTCis more electron-deficient than classical zirconocene alkyl compounds as a result of having weak-field and less electron-donating carboxylate/oxo ligands. We surmised that the electron-deficient nature of such complexes should facilitate the reduction of Zr^{IV} centers to Zr^{III}, affording a unique opportunity for studying the electronic properties and catalytic activities of previously elusive Zr^{III} species. This chapter describes the quantitative conversion of $[Zr^{IV}_6O_4(OH)_4Cl_{12}]^{6-}$ nodes in the Zr_6Cl_{12}-BTC MOF into the $[Zr^{III}_6O_4(ONa)_4H_6]^{6-}$ nodes in $Zr^{III}_6H_6$-BTC via bimetallic reductive elimination of H_2 from the proposed $[Zr^{IV}_6O_4(OH)_4H_{12}]^{6-}$ intermediate. The same reduction process also applies to Hf_6Cl_{12}-BTC. The coordinatively unsaturated $Zr^{III}H$ centers are highly active and selective for 1,4-dearomative hydroboration and hydrosilylation of pyridines and quinolines. The activity is 20-fold higher than the previously described Ce_6H_6-BTC catalyst. This work demonstrates the potential of SBU transformation in generating homogeneously-inaccessible hexanuclear solid catalysts with unique electronically properties for organic synthesis.

The chemistry of Ti^{III} has been the focus of intense research, leading to important applications in photocatalysis, organic synthesis, and organometallic catalysis. [1-2] In contrast, examples of Zr^{III} and Hf^{III} complexes are rare, due to their highly negative potentials and chemical instability.[3-9] Low concentrations of transient Zr^{III} species were recently proposed to exist in Zr_6

SBUs that are responsible for photocatalysis and CO_2 hydrogenation, based on low-intensity features in EPR spectra.[10-13] We report here the synthesis, spectroscopy, electron transfer properties, and catalytic applications for $M^{III}_6H_6$-BTC that composed exclusively of Zr^{III} or Hf^{III} centers. The framework rigidity and site-isolation effect can stabilize these sterically open and coordination-unsaturated Zr^{III} complexes with unique electronic properties, providing a highly effective solid catalyst for dearomative 1,4-additions of pyridines and quinolines with boranes and silanes to access useful synthons to nitrogen-containing natural products (**Figure 9-1**).[14-16]

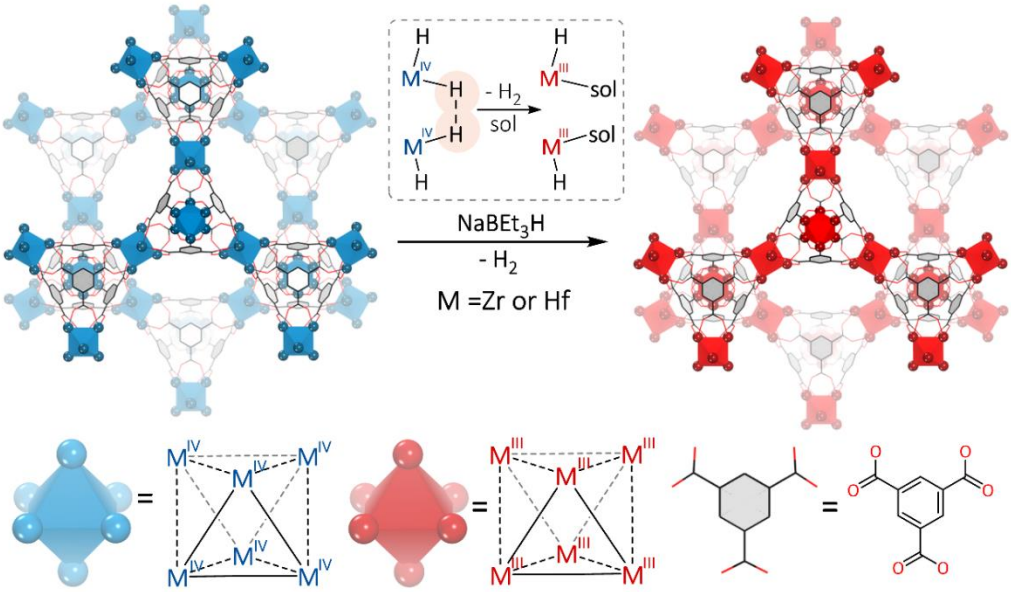

Figure 9-1. Reduction of $M^{IV}_6Cl_{12}$-BTC to $M^{III}_6H_6$-BTC (M=Zr and Hf) by $NaBEt_3H$ via bimetallic reductive elimination of H_2.

9.2 Results and Discussion

9.2.1 Synthesis and characterization of Zr_6H_6-BTC

In this work, Zr_6Cl_{12}-BTC was prepared through Me_3SiCl activation of $Zr_6(OH)_6$-BTC in toluene, and used as a precursor to synthesize $Zr^{III}_6H_6$-BTC. Treating Zr_6Cl_{12}-BTC with excess

$NaBEt_3H$ vigorously evolved H_2 through the deprotonation of μ_3-OH groups and proton counter cations on the Zr_6 SBUs, as well as the reduction of Zr^{IV} centers. The reduction process occurs with a concomitant color change from white to deep red, which is generally a characteristic color of Zr^{III} species. This reduction is proposed to go through an unusual bimetallic reductive elimination mechanism (**Scheme 9-1**).[17-19] The $[Zr_6Cl_{12}]^{6-}$ core in Zr_6Cl_{12}-BTC first undergoes chloride/hydride metathesis to afford the putative $[Zr_6H_{12}]^{6-}$ intermediate. Within this intermediate, two Zr-hydrides from two neighbouring Zr^{IV} centers reductively eliminates H_2 while supplying electrons to generate Zr^{III}.

Scheme 9-1. Synthesis of $Zr^{III}_6H_6$-BTC via chloride/hydride metathesis of Zr_6Cl_{12}-BTC followed by bimetallic reductive elimination of H_2.

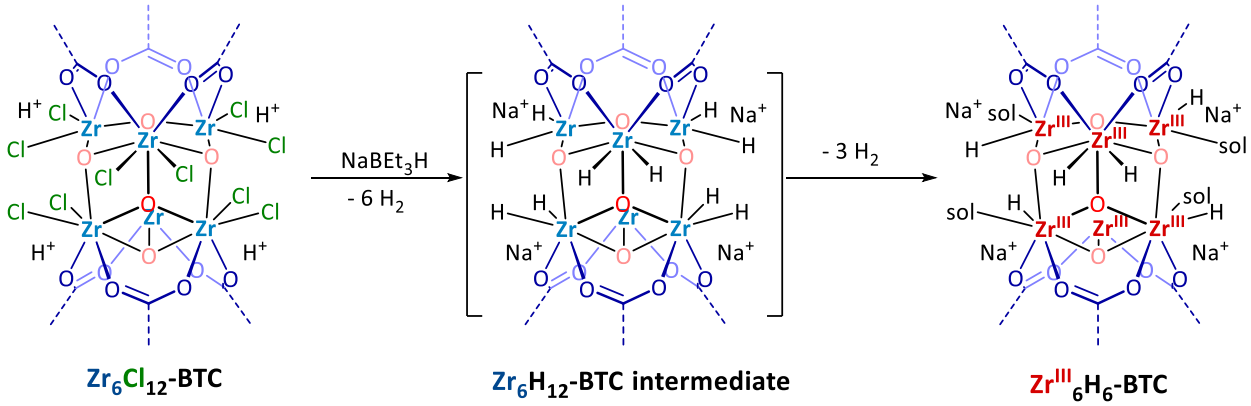

PXRD patterns of the generated $Zr^{III}_6H_6$-BTC matched well with the simulated pattern of Zr-BTC, indicating the framework structure remained intact through the stepwise transformation of Zr_6-BTC→$Zr_6(OH)_6$-BTC→Zr_6Cl_{12}-BTC→$Zr^{III}_6H_6$-BTC (**Figure 9-2**). ICP-MS analysis of the digested $Zr^{III}_6H_6$-BTC revealed an Na/Zr ratio of 1.65 ± 0.08, consistent with the expected value of 1.67 for the proposed formula $[Zr_6O_4(ONa)_4H_6]Na_6(BTC)_2$.

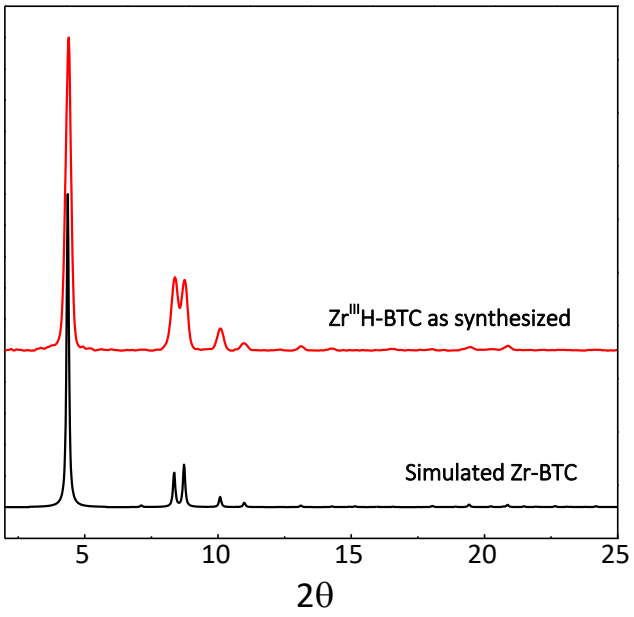

Figure 9-2. PXRD patterns of simulated Zr_6-BTC (black) and $Zr^{III}_6H_6$-BTC (red), indicating the retention of crystallinity through SBU transformations.

Several different spectroscopic methods including XPS, XANES and EPR were utilized to study the oxidation state and electronic property of Zr^{III} centers. XPS is a very useful tool to study metal oxidation states in solid material. For the Zr_6Cl_{12}-BTC control, the Zr $3d_{5/2}$ peak exhibited a binding energy of 182.9 eV, corresponding to the Zr^{IV} oxidation state. For the $Zr^{III}_6H_6$-BTC sample, however, the $3d_{5/2}$ peak binding energy is 182.6 eV, which is 0.3 eV lower than tetravalent control, indicating the reduction of Zr^{IV} to Zr^{III} in the SBU. Furthermore, $Zr^{III}_6H_6$-BTC displayed very strong shake-up features of Zr^{III} $3d_{5/2}$ and $3d_{3/2}$ peaks, which is expected for Zr^{III} centers with unpaired d electrons (**Figure 9-3**). Such shake-up features of Zr^{III} $3d_{5/2}$ and $3d_{3/2}$ peaks have never been reported due to the inability to obtain Zr samples with exclusively Zr^{III} centers.[20-21]

K-edge XANES analysis was also employed to characterize $Zr^{III}_6H_6$-BTC. Unlike the Zr_6Cl_{12}-BTC control, the pre-edge features of $Zr^{III}_6H_6$-BTC at 18003.5 eV which are generally associated with 1s-4d transitions exhibited greatly enhanced intensity. The post-edge peaks at

18021.1 eV and 18027.2 eV also changed significantly, indicating the 1s-5p and other electron transitions have change (**Figure 9-4**). As a control, the $Zr^{IV}_6H_6$-BTC sample which was obtained via oxidation of $Zr^{III}_6H_6$-BTC with $FcPF_6$ (described later), displayed almost identical XANES features to the Zr_6Cl_{12}-BTC standard, further validating that the XANES feature changes are a result of Zr reduction.

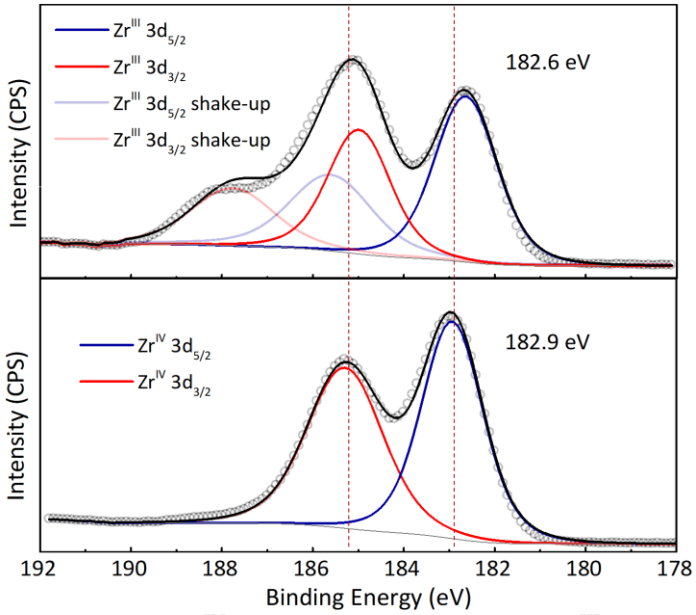

Figure 9-3. Zr 3d XPS spectra of $Zr^{IV}_6Cl_{12}$-BTC (bottom) and $Zr^{III}_6H_6$-BTC (top). Black circle, experimental data; Black solid line, fitting results.

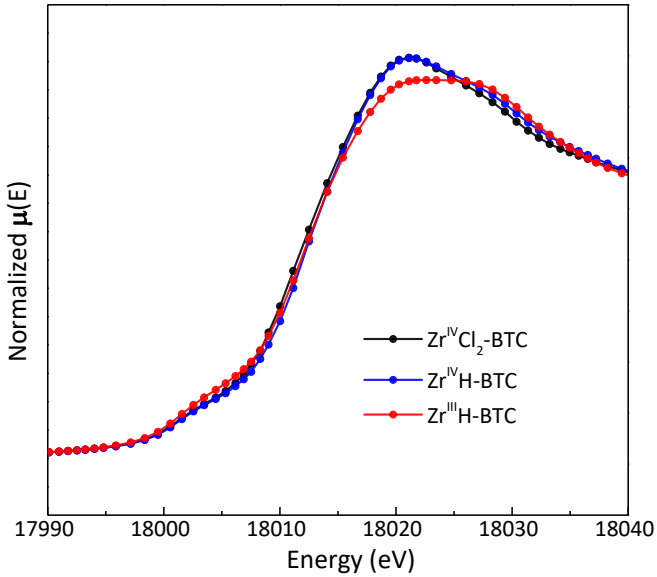

Figure 9-4. XANES analysis of $Zr^{IV}_6Cl_{12}$-BTC (black), $Zr^{III}_6H_6$-BTC (red) and $Zr^{IV}_6H_6$-BTC(blue), showing pre- and post-edge features of Zr^{III} and Zr^{IV} centers in Zr_6 SBUs.

EXAFS spectroscopy was used to study the Zr coordination environment in $Zr^{III}_6H_6$-BTC. The proposed $(\mu_3\text{-}O)_4(\mu_2\text{-}CO_2)_2ZrH(THF)$ structural model fitted well to the Zr K-edge spectrum, with an R-factor of 0.011. The fitted Zr-H and Zr-O^{THF} distances were 1.90 Å and 2.28 Å, respectively. Interestingly, the evident Zr-Zr scattering pathway in the R-space spectrum has a fitted distance of 3.35 Å, which is 0.20 Å shorter than that in Zr_6Cl_{12}-BTC, suggesting the potential Zr^{III}-Zr^{III} bonding interactions in Zr^{III}_6 SBUs (**Figure 9-5**).[22-24]

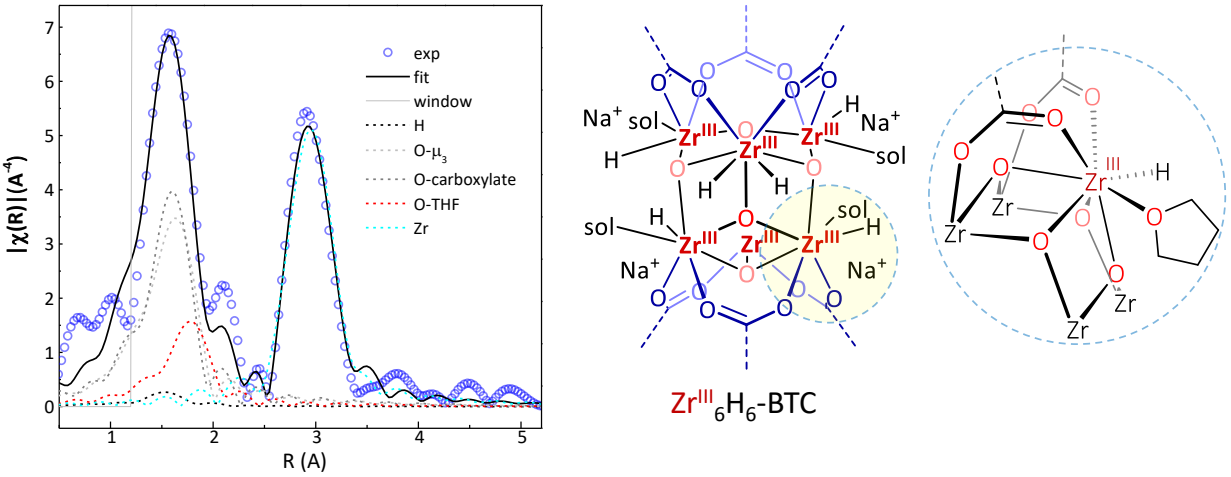

Figure 9-5. EXAFS fitting of $Zr^{III}_6H_6$-BTC, showing the Zr coordination environment as $(\mu_3\text{-}O)_4(\mu_2\text{-}CO_2)_2ZrH(THF)$.

9.2.2 Electron transfer reactions of Zr_6H_6-BTC

$Zr^{III}_6H_6$-BTC was treated with $FcPF_6$, oxygen, and quinone to establish its electron transfer properties. $FcPF_6$ was used as an oxidant to titrate the amount of Zr^{III} in $Zr^{III}_6H_6$-BTC. Upon adding to $Zr^{III}_6H_6$-BTC, the deep-blue solution of $FcPF_6$ immediately changed to orange, suggesting rapid reduction of Fc^+ to Fc and oxidation of $Zr^{III}_6H_6$-BTC to $Zr^{IV}_6H_6$-BTC (**Scheme 9-2**). The amount of ferrocene was determined by GC to be 0.99 ± 0.04 equiv. w.r.t. Zr, consistent with having exclusively reduced Zr^{III} centers in $Zr^{III}_6H_6$-BTC.

Scheme 9-2. Electron transfer from $Zr^{III}_6H_6$-BTC to $FcPF_6$ to form $Zr^{IV}_6H_6$-BTC and Fc as the side product.

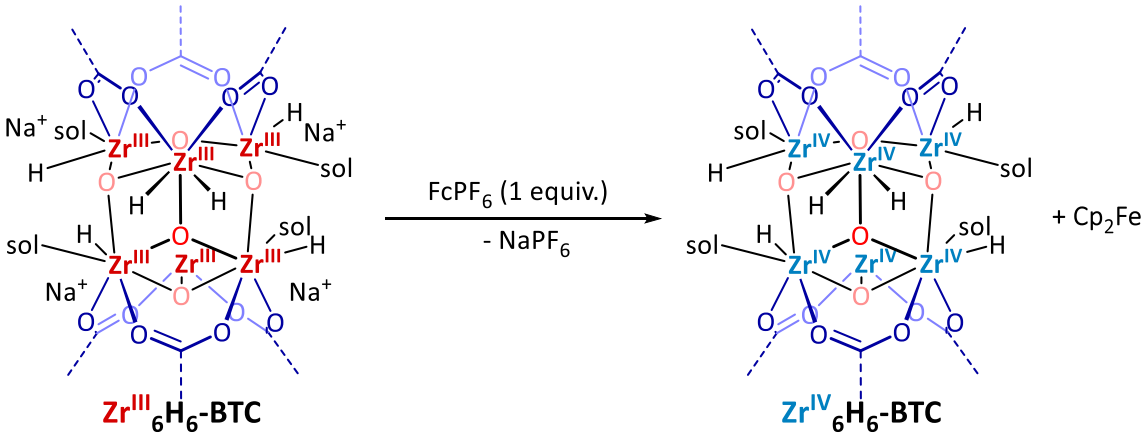

The EXAFS data of the oxidized $Zr^{IV}_6H_6$-BTC product was well fitted using the proposed $(\mu_3\text{-}O)_4(\mu_2\text{-}CO_2)_2ZrH(THF)$ coordination model. The EXAFS fitting afforded a Zr-Zr distance of 3.59 Å, which is longer than the Zr-Zr distance of 3.35 Å in $Zr^{III}_6H_6$-BTC, indicating the absence of Zr^{III}-Zr^{III} bonding interactions in the oxidized MOF (**Figure 9-6**). The significant change in Zr-Zr interactions are visibly apparent by comparing the EXAFS spectra of $Zr^{IV}_6H_6$-BTC and $Zr^{III}_6H_6$-BTC (**Figure 9-7**).

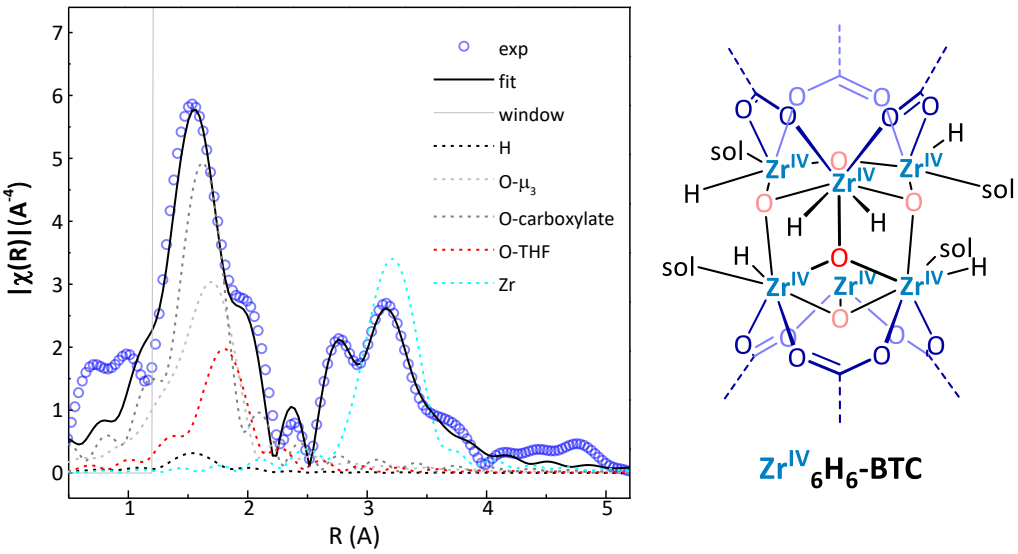

Figure 9-6. EXAFS fitting of $Zr^{IV}_6H_6$-BTC, showing the Zr coordination environment as $(\mu_3\text{-}O)_4(\mu_2\text{-}CO_2)_2ZrH(THF)$.

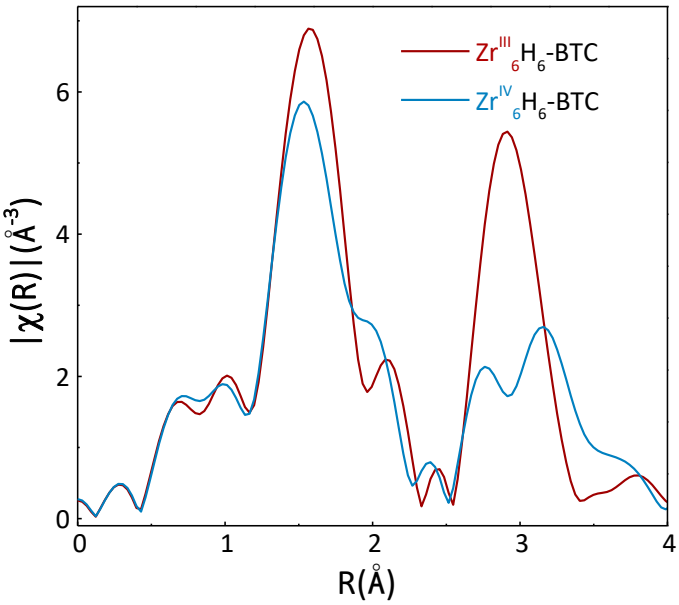

Figure 9-7. Comparison of the EXAFS spectra of $Zr^{IV}_6H_6$-BTC and $Zr^{III}_6H_6$-BTC.

$Zr^{III}_6H_6$-BTC was EPR-silent at both 200K and 20K, indicating strong antiferromagnetic coupling between the six Zr^{III} centers.[22-24] After treating with O_2, $Zr^{III}_6H_6$-BTC displayed two sets of intense signals. The first set of peaks displayed g-values of 2.029, 2.010 and 2.002, similar to the Zr^{IV}-bound superoxide radicals which has been observed on zirconia surface (**Figure 9-8**). The second set of peaks showed an isotropic signal with g-value of 1.978, which was assignable to Zr^{III} centers. The Zr^{III} signal was only observed in the partially oxidized sample because of the presence of isolated Zr^{III} centers which are not antiferromagnetically coupled with each other.

Furthermore, menadione, a quinone derivative, was reacted with $Zr^{III}_6H_6$-BTC to form Zr-bound semiquinone radical, which exhibited a strong EPR signal at a g-vale of 2.003 (**Figure 9-9**). These experiments have established $Zr^{III}_6H_6$-BTC as a very reactive electron donor to a variety of oxidants, confirming the high reactivity of the Zr^{III} centers, and pinpointed their potential role in Zr-MOF mediated photocatalytic and gas-phase reactions.

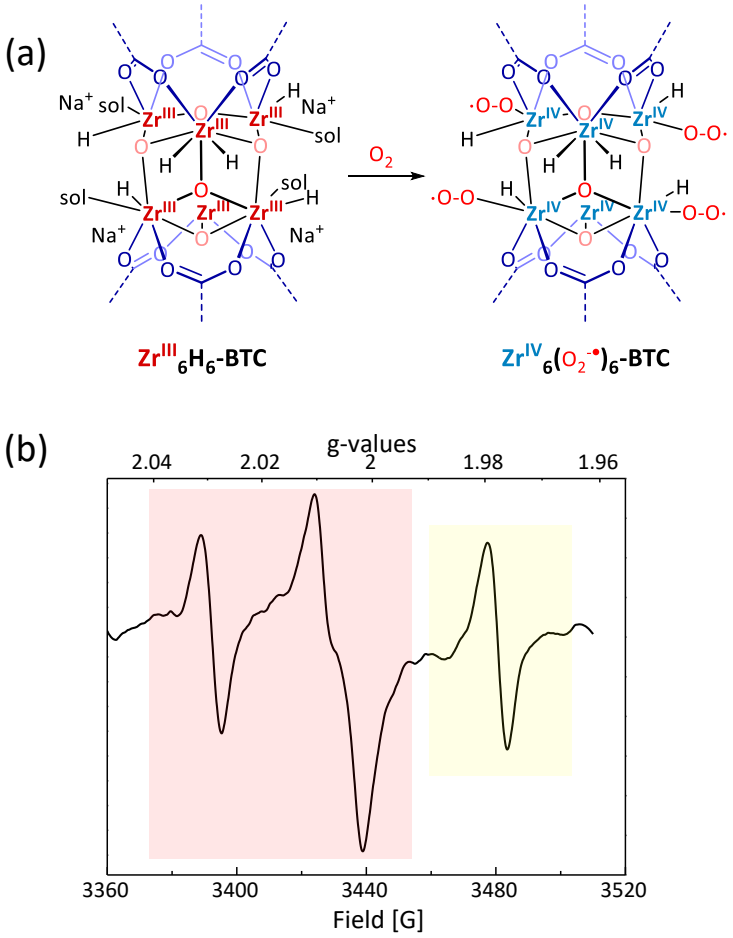

Figure 9-8. (a) Electron transfer from $Zr^{III}_6H_6$-BTC to O_2 to form Zr^{IV}-bound superoxide. (b) EPR spectrum of $Zr(O_2^{\cdot})$-BTC, showing strong superoxide and Zr^{III} signals.

To demonstrate the bimetallic reduction strategy is generally applicable to other metals, we also applied the strategy to synthesize the analogous $Hf^{III}_6H_6$-BTC. The freshly synthesized Hf-BTC was first treated with 1M aqueous HCl to form $Hf_6(OH)_6$-BTC, which was subsequently activated with Me_3SiCl to yield Hf_6Cl_{12}-BTC in quantitative yield. Although Zr and Hf have similar chemical properties due to the lanthanide contraction, Hf^{IV} is still more difficult to reduce than Zr^{IV}, evidenced by the more negative Hf/Hf^{IV} reduction potential of -1.70 V (vs. SHE) compared to that of -1.53 V for Zr/Zr^{IV}. While the reduction of Zr_6Cl_{12}-BTC with $NaBEt_3H$ was completed in less than 0.5 h at room temperature, the reduction of Hf_6Cl_{12}-BTC by $NaBEt_3H$ took 2 h to complete (**Scheme 9-3**).

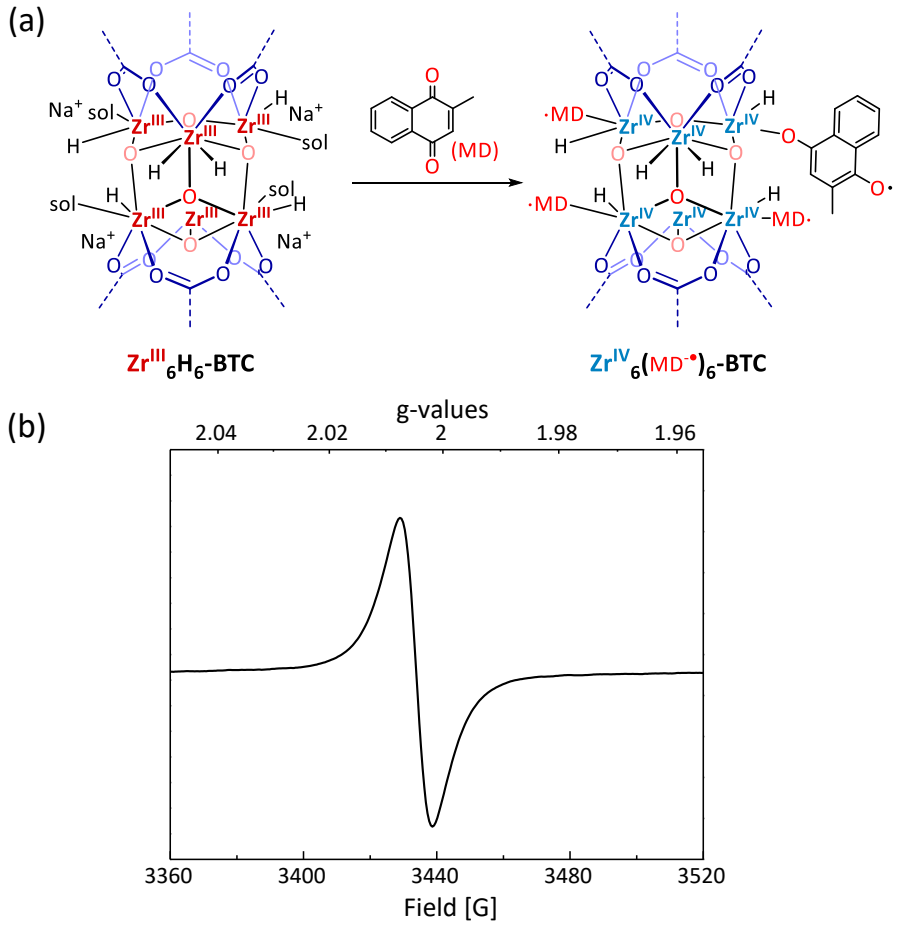

Figure 9-9. (a) Electron transfer from $Zr^{III}_6H_6$-BTC to menadione to form Zr^{IV}-bound semiquinone. (b) EPR spectrum of Zr(MD˙)-BTC, showing strong oxygen-center EPR signal.

The proposed $(\mu_3\text{-O})_4(\mu_2\text{-CO}_2)_2\text{HfH(THF)}$ structure model for the Hf centers in $Hf^{III}_6H_6$-BTC fitted well to the Hf L_3-edge EXAFS spectra. The Hf-Hf distance was determined to be 3.32 Å, which is 0.23 Å shorter than that found in $Hf^{IV}_6H_6$-BTC. This result suggests Hf-Hf bonding interactions in Hf^{III}_6 SBUs. Analogously, EPR spectrum of $Hf^{III}_6H_6$-BTC showed no signal due to strong antiferromagnetic coupling between Hf^{III} centers. Upon treatment with O_2, however, the partially oxidized $Hf^{III}_6H_6$-BTC showed two sets of intense EPR signals. One with g-values of 2.029, 2.010 and 2.001, corresponding to Hf-O_2. Species, and the other has g-value of 1.978, corresponding to isolated Hf^{III} centers. $Hf^{III}_6H_6$-BTC could also reduce 1 equiv. of menadione to

form Hf^{IV}-bound semiquinone with a strong EPR signal at a g-vale of 2.003. These experiments represent the first study of electron transfer properties and EPR signatures of Hf^{III} compounds.

Scheme 9-3. Synthesis of $Hf^{III}_6H_6$-BTC via chloride/hydride metathesis of Hf_6Cl_{12}-BTC followed by bimetallic reductive elimination of H_2.

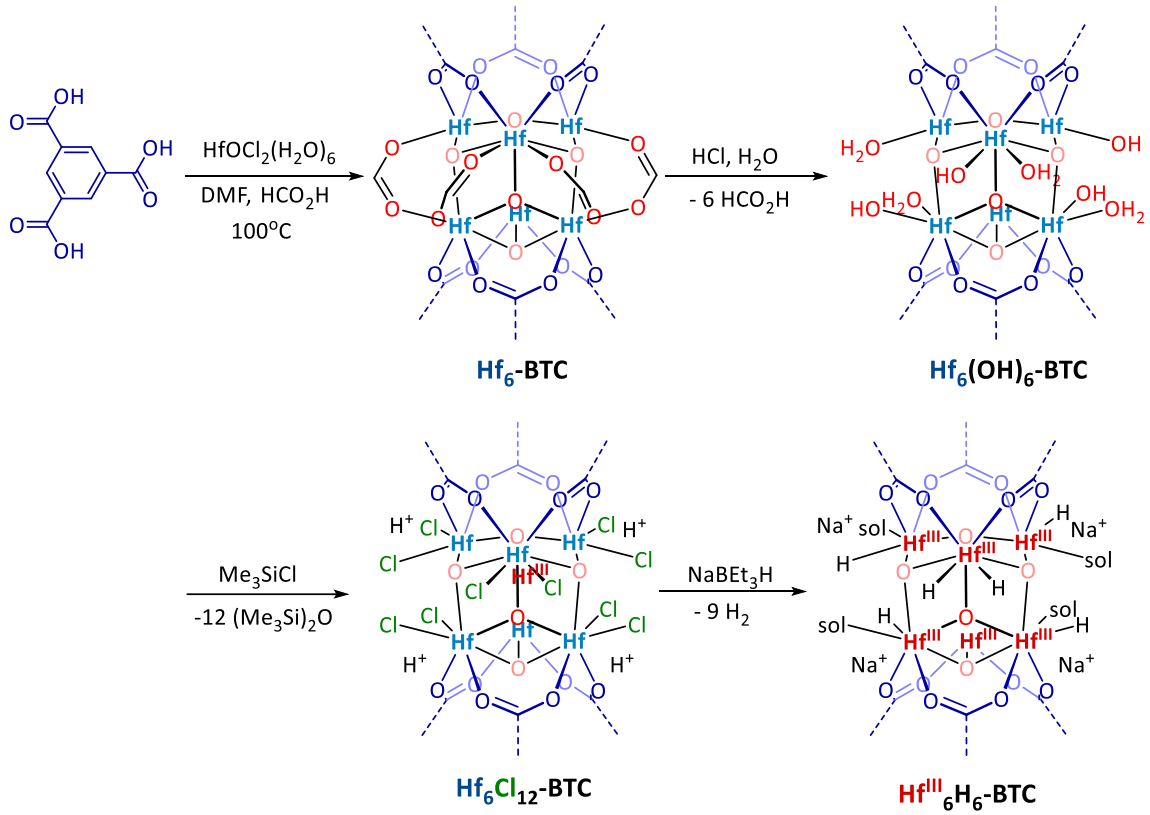

9.2.3 Zr_6H_6-BTC catalyzed pyridine hydroboration.

Zr^{IV} complexes have found applications in catalyzing a broad scope of reactions including alkene polymerization and hydroelementation reactions. In contrast, little is known about the catalytic properties of Zr^{III} complexes. This is because all homogeneous Zr^{III} compounds are difficult to prepare, chemically unstable, and coordinatively saturated. But the $Zr^{III}H$ species is expected to have strong hydridic character for readily insertion into unsaturated bonds and enable novel catalytic reactions. $Zr^{III}_6H_6$-BTC thus offers a unique platform to stabilize the coordinatively

unsaturated Zr^{III} centers with unusual electronic properties, and allowed for exploring the catalytic activity of Zr^{III} metal centers.

$Zr^{III}_6H_6$-BTC is a highly active catalyst for the 1,4-selective hydroboration of pyridines and quinolines. The selective dearomative addition of pyridines affords the partially reduced azacyclic compounds as important precursors for synthesizing bioactive alkaloids. Although several catalysts have recently been reported for the 1,4-hydroboration of pyridines, most of them suffer from low activities (up to 20 mol% catalyst loading) and/or low chemoselectivity.[15-16, 25] The $Zr^{III}_6H_6$-BTC MOF is so far the most productive catalyst for pyridine hydroboration. At only 0.2 mol% $Zr^{III}_6H_6$-BTC loading, pyridine was reacted with HBpin at 90 °C to afforded the 1,4-addition product in 73% yield within 18 h, with a TON of 365 (**Table 9-1**).

Table 9-1. $Zr^{III}_6H_6$-BTC catalyzed 1,4- hydroboration of pyridines and quinolines

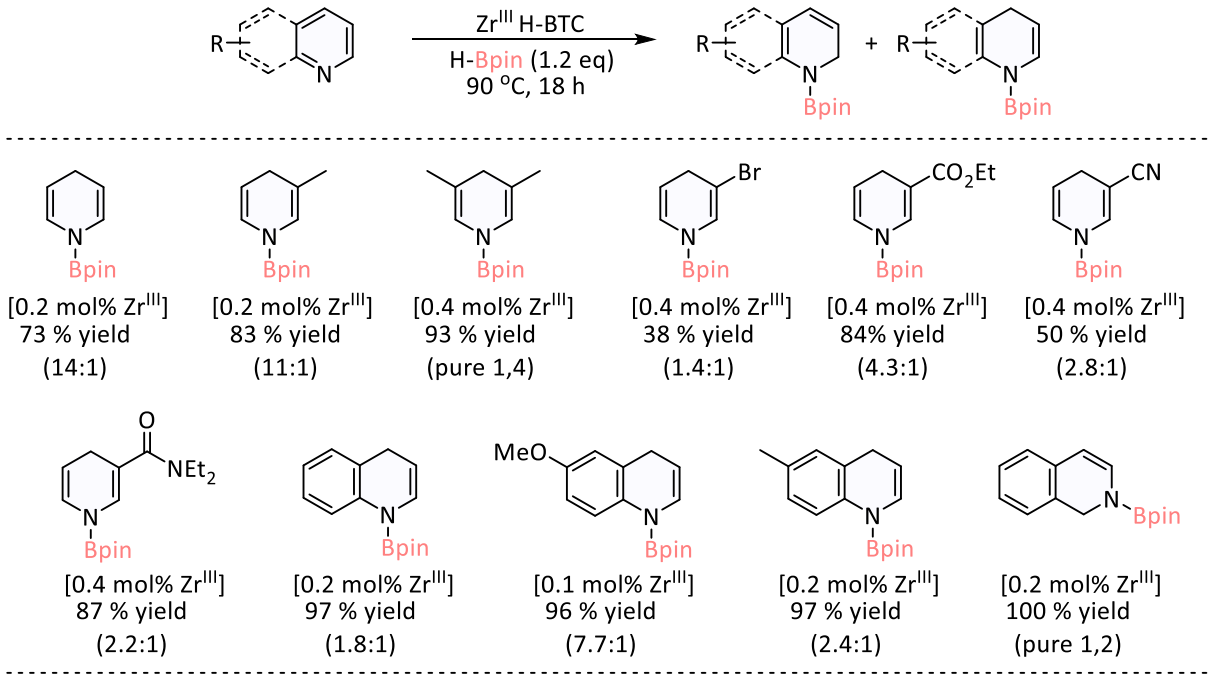

Yield was determined by 1H NMR using mesitylene as internal standard. The ratio of 1,4 product vs 1,2 product was shown in the parenthesis.

$Zr^{III}_6H_6$-BTC also catalyzed the hydroboration of a broad scope of pyridine derivatives, including more hinder pyridines (*e.g.* 3-methylpyridine, 3,5-dimethylpyridine) and pyridines with reducible functionalities (*e.g.* bromo, nitrile, ester, and amide groups). The reactions all proceeded with high TONs and 1,4-selectivities. Moreover, quinolines and derivatives (*e.g.* 6-methoxyquinoline, 6-methylquinoline) were also hydroborated with high TONs and 1,4-selectivities. For substrates that cannot undergo 1,4-addition, such as isoquinoline, $Zr^{III}_6H_6$-BTC catalyzed the 1,2-hydroboration of the substrate with high activity. $Hf^{III}_6H_6$-BTC is a less active catalyst for pyridine 1,4-hydroboration. At 0.2 mol% catalyst loading, pyridine was converted in 57% yield.

$Zr^{III}_6H_6$-BTC was reused 5 times for 1,4-hydroboration of 6-methoxyquinoline without any significant drop in yield or selectivity (**Figure 9-10**), indicating the robustness and recyclability of the catalyst. Interestingly, the tetravalent form of the catalyst, $Zr^{IV}_6H_6$-BTC, showed no activity for the hydroboration of pyridine or 6-methoxyquinoline. This experiment demonstrates the unique reactivities of Zr^{III}-H species toward substrate insertion.

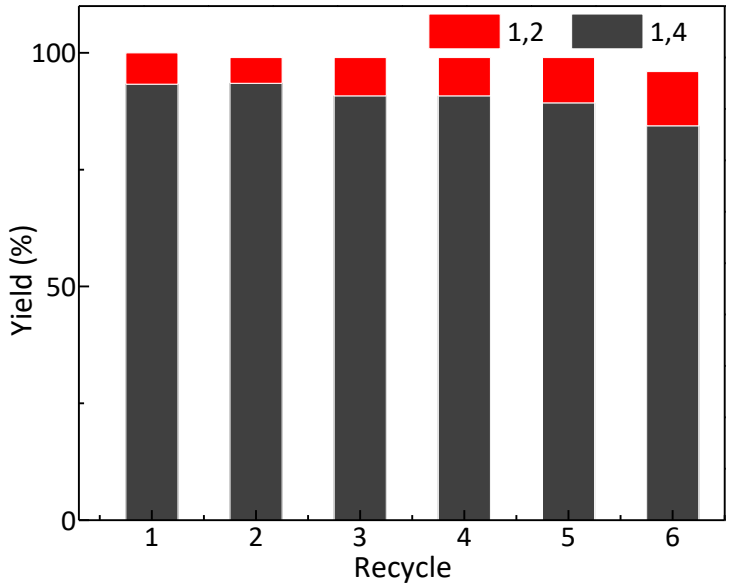

Figure 9-10. Plots of yields (%) for the 6-methoxyquinoline hydroboration products in six runs. The loading of $Zr^{III}_6H_6$-BTC catalyst were 1 mol%.

Besides recycle experiments, additional experiments were performed to exclude the possibility of having leached-out species catalyzing the reactions, therefore validate the heterogeneity of $Zr^{III}_6H_6$-BTC catalyst. By examining the space-filling model of the MOF, a large tetraquinoline substrate which cannot easily diffuse through MOF channels was designed. The substrate was synthesized through Suzuki-Miyaura coupling of tetrabromo precursor with quinoline boronic acid in high yield. The structure model in **Figure 9-11** displayed the largest channel of the MOF, which is smaller than the size of the tetraquinoline substrate (1,1,2,2-tetrakis(4-(quinolin-6-yl)phenyl)ethene). Therefore, the large substrate cannot diffuse into the channel and access catalytic Zr^{III} metal centers, and displayed almost no conversion.

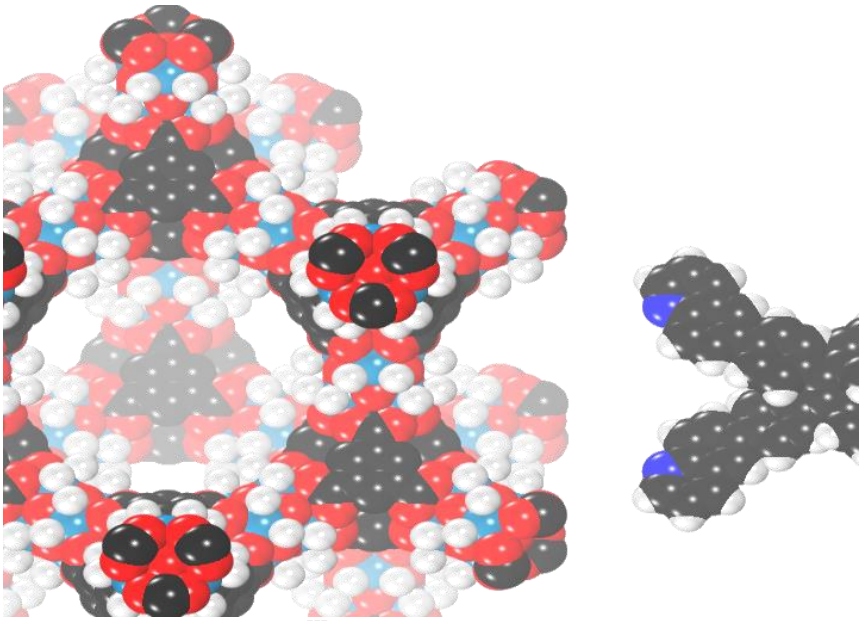

Figure 9-11. Space-filling model of $Zr^{III}_6H_6$-BTC (left) and the large tetraquinoline substrate.

9.2.4 Zr_6H_6-BTC catalyzed pyridine hydrosilylation.

Silanes are generally more diverse and easily available than boranes. Therefore, the hydrosilylation of pyridines and quinolines presents an even more versatile and practical method to synthesis azacyclic compounds. However, only a handful of catalysts were reported to effect

pyridine hydrosilylation reactions. $Zr^{III}_6H_6$-BTC is a highly active and selective catalyst for 1,4-hydrosilylation of pyridines and quinolines with triethoxysilane (**Table 9-2**). At 2 mol% loading, $Zr^{III}_6H_6$-BTC hydrosilylated pyridine in 72% yield with exclusive 1,4-selectivity. At 0.2 mol% loading of $Zr^{III}_6H_6$-BTC, a broad scope of pyridines and quinoline with various substituents are hydrosilylated in high yields and selectivity. For substrate that cannot undergo 1,4-addition (*e.g.* isoquinoline), $Zr^{III}_6H_6$-BTC effected the 1,2-addition of triethoxysilane with a high activity. Similar to hydroboration reactions, the oxidized form $Zr^{IV}_6H_6$-BTC showed no activity for the hydrosilylation of pyridines and quinolines, likely a result of sluggish substrate insertion of Zr^{IV}-H functionality.

Table 9-2. $Zr^{III}_6H_6$-BTC catalyzed 1,4-hydrosilylation of pyridines and quinolines

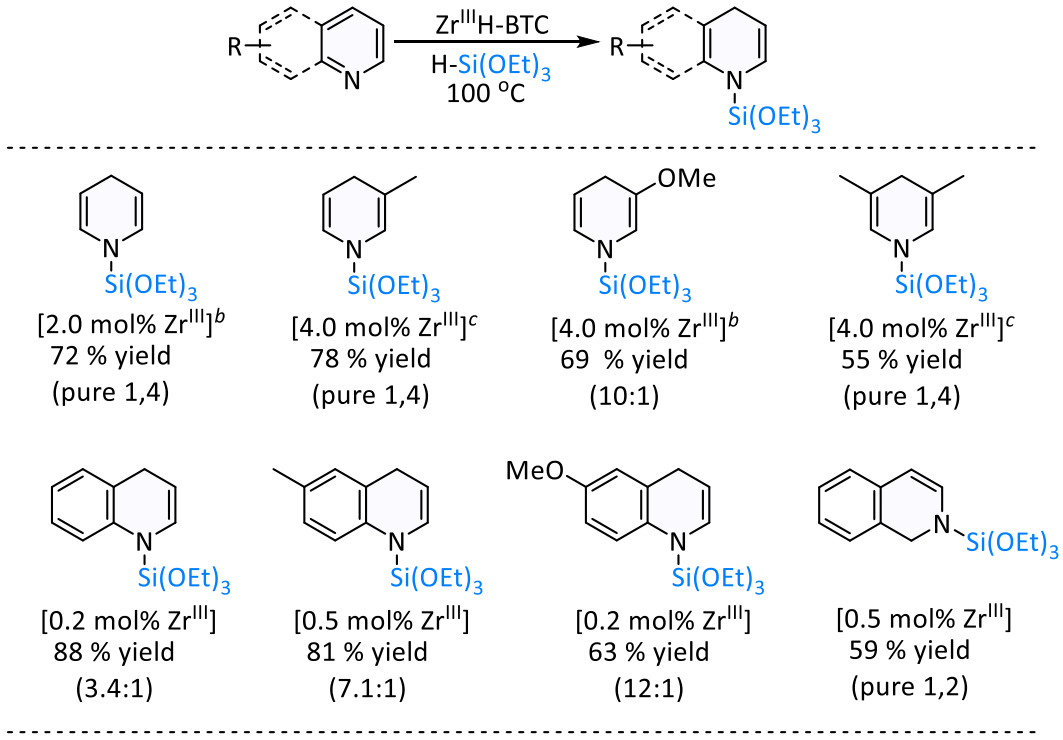

1 equiv. of $HSi(OEt)_3$ w.r.t. pyridine or quinoline was used unless otherwise indicated. Yield was determined by ^1H NMR using mesitylene as internal standard. The ratio of 1,4 product vs 1,2 product was shown in parenthesis.

9.3 Conclusion

In this chapter, we demonstrate the quantitative conversion of $[M^{IV}_6O_4(OH)_4Cl_{12}]^{6-}$ nodes in M_6Cl_{12}-BTC to the $[M^{III}_6O_4(ONa)_4H_6]^{6-}$ nodes (M = Zr, Hf) via a novel bimetallic reductive elimination process. The bridging oxo/carboxylate ligands and the site-isolation effect of the MOF framework stabilize coordinatively unsaturated $M^{III}H$ centers to afford highly active and selective catalysts for dearomative 1,4-hydroboration and 1,4-hydrosilylation of pyridines and quinolines. This work demonstrates SBU transformation as a general and powerful strategy to create homogeneously inaccessible, and coordinately unsaturated single-site MOF catalysts with unique electronic properties for organic synthesis.

9.4 Experimental

9.4.1 Material and methods

All of the reactions and manipulations were carried out under N_2 with the use of a glove box or Schlenk technique, unless otherwise indicated. Tetrahydrofuran and toluene were purified by passing through a neutral alumina column under N_2. Benzene and d_6-benzene were distilled over CaH_2. Pyridine and quinoline derivatives were purchased from Fisher, distilled, and then dried over 4Å molecular sieves prior to use. Pinacolborane and silanes were purchased from Sigma-Aldrich and used as received. Powder X-ray diffraction (PXRD) data was collected on Bruker D8 Venture diffractometer using Cu Kα radiation source (l = 1.54178 Å). N_2 sorption experiments were performed on a Micrometrics TriStar II 3020 instrument. Thermogravimetric analysis (TGA) was performed in air using a Shimazu TGA-50 equipped with a platinum pan and heated at a rate of 1.5 °C per min. Electron paramagnetic resonance (EPR) spectra were collected with a Bruker Elexsys 500 X-band EPR spectrometer at 20 K. X-ray photoelectron spectroscopy

(XPS) data was collected using an AXIS Nova spectrometer (Kratos Analytical) with monochromatic Al Kα X-ray source; Al anode was powered at 10 mA and 15 kV, and the instrument work function was calibrated to give an Au $4f_{7/2}$ metallic gold binding energy (BE) of 83.95 eV. Instrument base pressure was ca. 1×10^{-9} Torr. The analysis area size was 0.3×0.7 mm^2. For calibration purposes, the binding energies were referenced to the C 1s peak at 284.8 eV. Survey spectra were collected with a step size of 1 eV and 160 eV pass energy. ICP-MS data was obtained with an Agilent 7700x ICP-MS and analyzed using ICP-MS MassHunter version B01.03. Samples were diluted in a 2% HNO_3 matrix and analyzed with a ^{159}Tb internal standard against a 12-point standard curve over the range from 0.1ppb to 500ppb. The correlation was >0.9997 for all analyses of interest. Data collection was performed in Spectrum Mode with five replicates per sample and 100 sweeps per replicate.

9.4.2 Synthesis of a large quinoline substrate

Scheme 9-4. Synthesis of large quinoline substrate through Suzuki-Miyaura coupling.

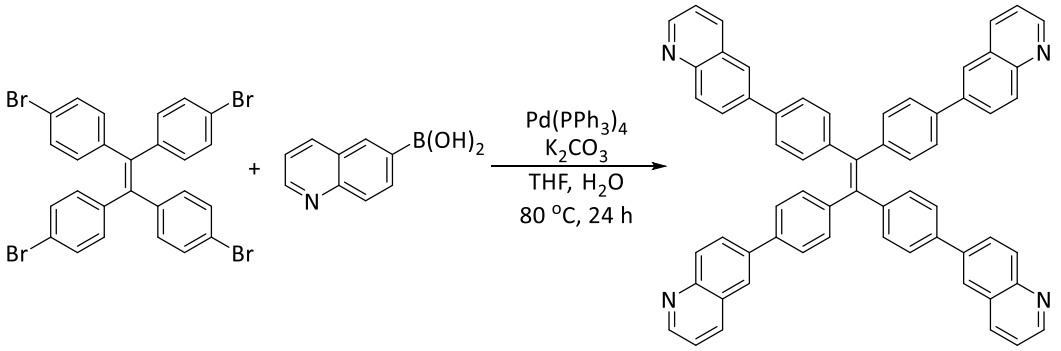

1,1,2,2-tetrakis(4-(quinolin-6-yl)phenyl)ethene

1,1,2,2-tetrakis(4-(quinolin-6-yl)phenyl)ethene was synthesized by a Suzuki coupling reaction. 1,1,2,2-tetrakis(4-bromophenyl)ethene (318 mg g, 0.5 mmol), quinoline boronic acid (519 mg, 3 mmol), tetrakis (triphenylphosphine) palladium (116 mg, 0.1 mmol) and K_2CO_3 (691 mg, 5 mmol) were charged into a heavy-walled glass tube and dried under vacuum for 10 min. Degased THF (10 mL) and H_2O (4 mL) were then added to the glass tube via cannula transfer.

The glass tube was sealed with a Teflon cap and heated at 80 ˚C for 24 h. After cooling to room temperature, the crude product was extracted with CH_2Cl_2, and recrystallized from THF to obtain 1,1,2,2-tetrakis(4-(quinolin-6-yl)phenyl)ethene product as a bright yellow powder (192 mg, 47% yield).

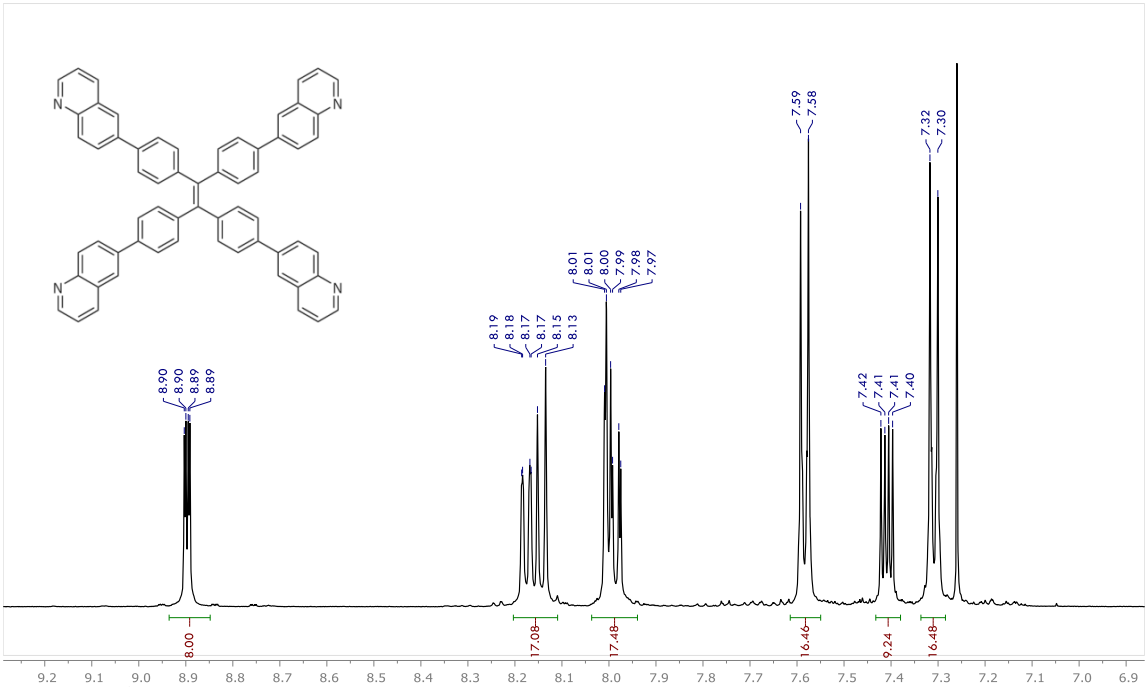

Figure 9-12. ^{1}H NMR of 1,1,2,2-tetrakis(4-(quinolin-6-yl)phenyl)ethene in $CDCl_3$.

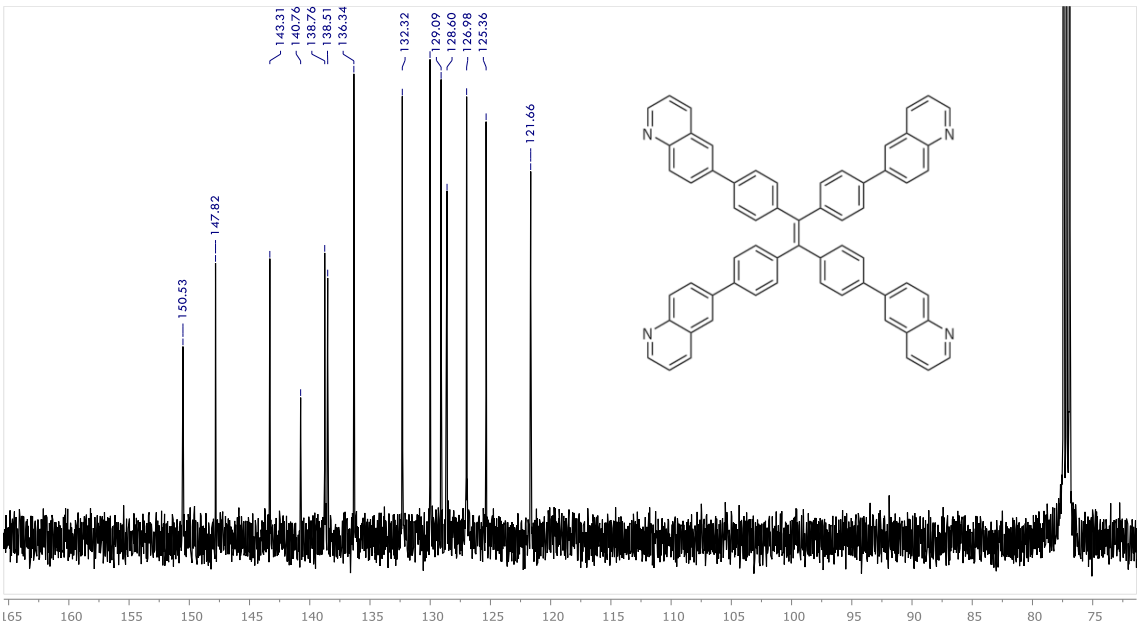

Figure 9-13. ^{13}C NMR of 1,1,2,2-tetrakis(4-(quinolin-6-yl)phenyl)ethene in $CDCl_3$.

9.4.3 Synthesis of $Zr^{III}_6H_6$-BTC

In a N_2-filled glove box, Zr_6Cl_{12}-BTC (20.0 μmol of Zr) was weighed out in a 1.5 mL centrifuge tube and dispersed in 1.0 mL of toluene. $NaBEt_3H$ (0.2 mL, 0.2 mmol, 1.0 M solution in toluene) was then added dropwise to the suspension. The color of the MOF immediately changed from white to deep red while vigorously evolving H_2 gas. The resulting suspension was kept at room temperature for 30 min to ensure complete reduction. The red solid was then centrifuged out of the suspension and washed with toluene 3 times to remove excess $NaBEt_3H$ and side products (NaCl, BEt_3).

9.4.4 Typical procedure for $Zr^{III}_6H_6$-BTC catalyzed pyridine 1,4-hydroboration

$Zr^{III}_6H_6$-BTC (2.2 μmol Zr) was prepared as described above. 6-methoxyquinoline (300 μL, 2.17 mmol) was then added to a solution of $Zr^{III}_6H_6$-BTC and pinacolborane (378 μL, 2.60 mmol). The reaction mixture was stirred under N_2 at 90 °C for 18 h. The MOF was removed from the solution by centrifugation. The supernatant was transferred to a vial, and the MOF was washed with Hexanes. The combined organic extracts were concentrated in vacuo to afford a mixture of 6-methoxy-1-(4,4,5,5-tetramethyl-1,3,2-dioxaborolan-2-yl)-1,4-dihydroquinoline (1.84 mmol, 85% NMR yield based on mesitylene as an internal standard) and 6-methoxy-1-(4,4,5,5-tetramethyl-1,3,2-dioxaborolan-2-yl)-1,2-dihydroquinoline (0.24 mmol, 11% NMR yield based on mesitylene as an internal standard). 0.4% of Zr leaching was determine by ICP-MS analysis of the organic extract, indicating minimal MOF decomposition during catalysis.

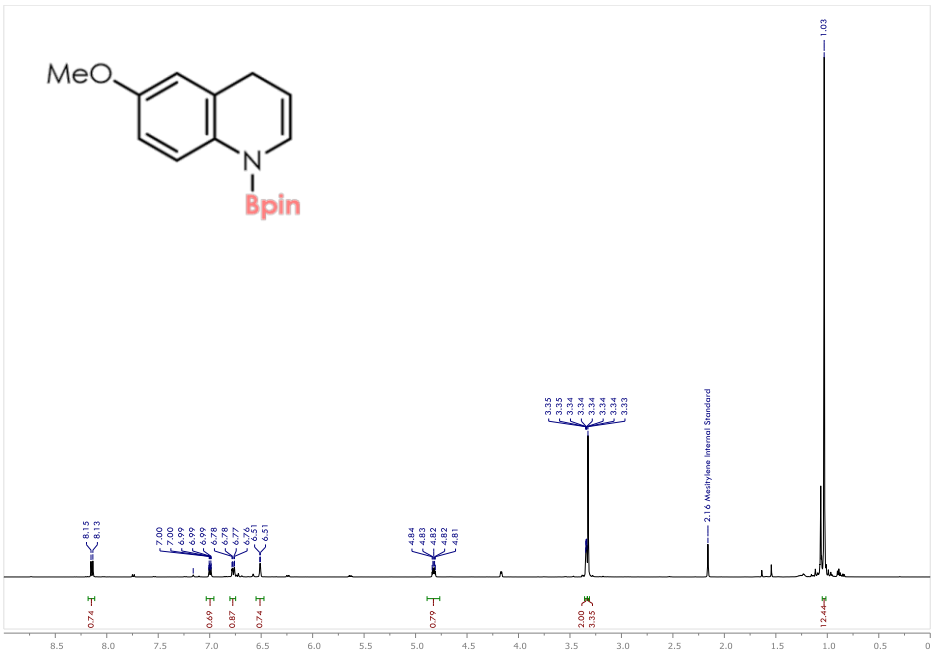

Figure 9-14. ^{1}H NMR of hydroborated 6-methoxyquinoline.

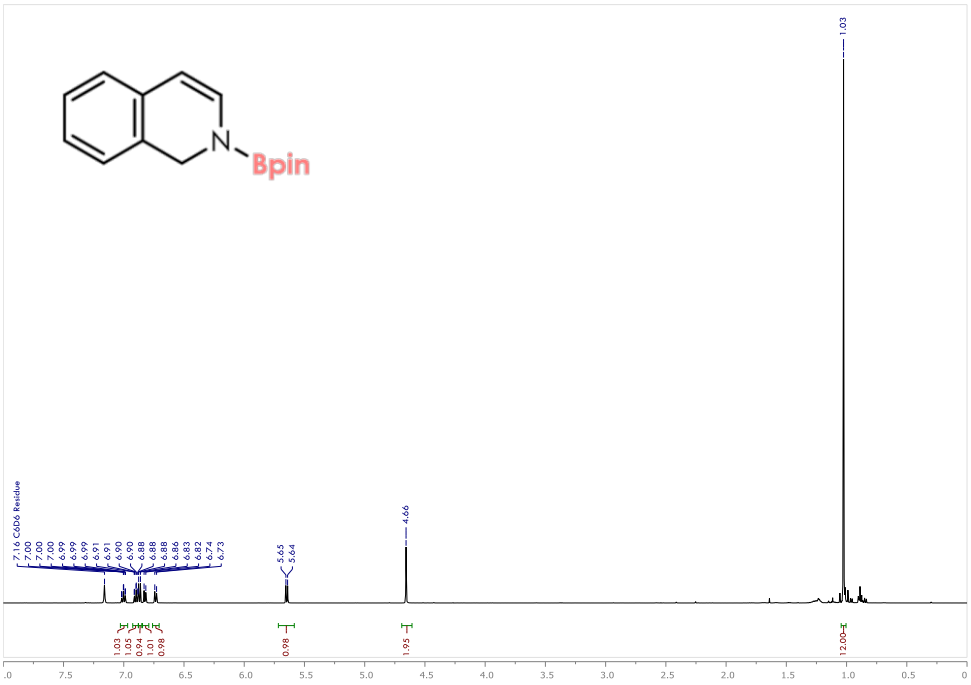

Figure 9-15. ^{1}H NMR of hydroborated isoquinoline.

9.4.5 Typical procedure for $Zr^{III}_6H_6$-BTC catalyzed pyridine 1,4-hydrosilylation

$Zr^{III}_6H_6$-BTC (11 μmol Zr) was prepared as described above. 6-methylquinoline (291 μL, 2.17 mmol) was added to a solution of $Zr^{III}_6H_6$-BTC and triethoxysilane (480 μL, 2.60 mmol). The reaction mixture was stirred under N_2 at 90 °C for 18 h. The MOF was removed from the solution by centrifugation. The supernatant was transferred to a vial, and the MOF was washed with Hexanes. The combined organic extracts were concentrated in vacuo to afford a mixture of 6-methyl-1-(triethoxysilyl)-1,4-dihydroquinoline (1.54 mmol, 71% NMR yield based on mesitylene as an internal standard) and 6-methyl-1-(triethoxysilyl)-1,2-dihydroquinoline (0.22 mmol, 10% NMR yield based on mesitylene as an internal standard).

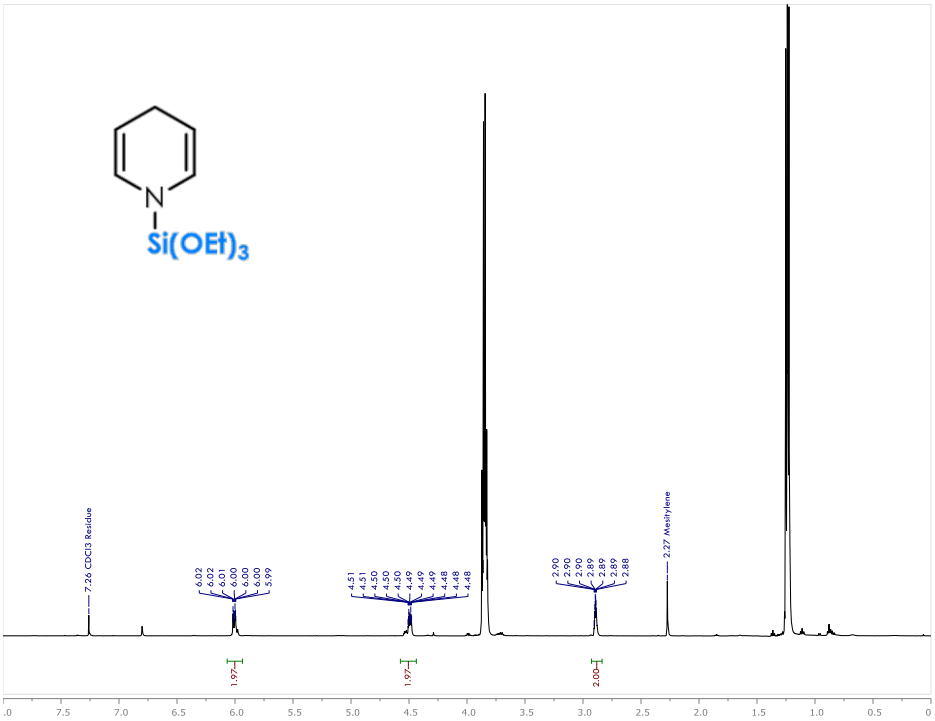

Figure 9-16. ^{1}H NMR of hydrosilylated pyridine with almost exclusive 1,4-selectivity.

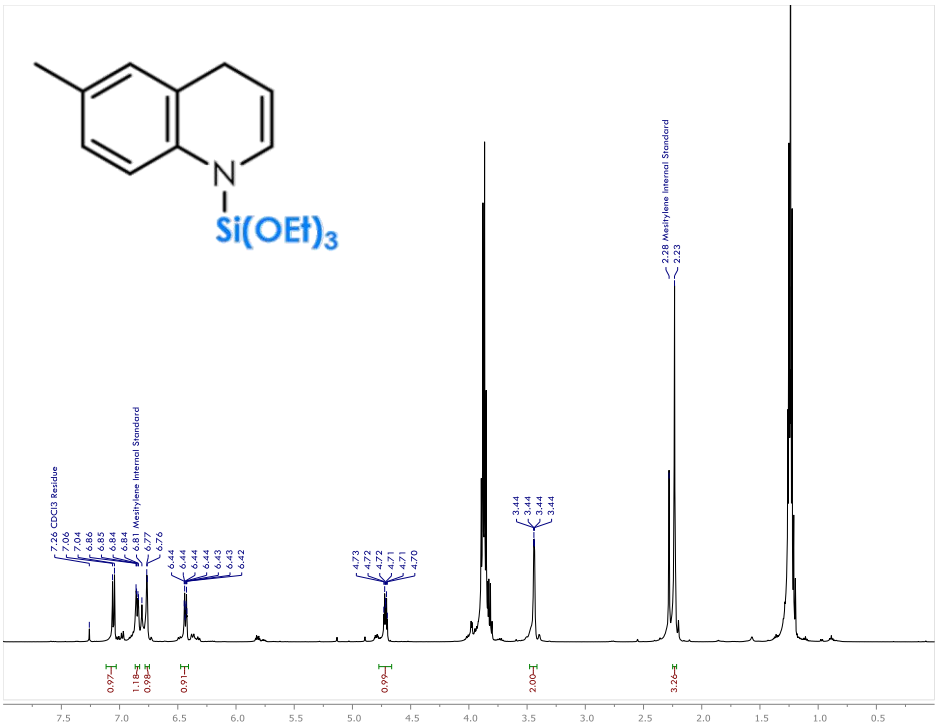

Figure 9-17. ^{1}H NMR of hydrosilylated 6-methylquinoline.

9.5 References

1. Mason, J. A.; Darago, L. E.; Lukens, W. W.; Long, J. R., Synthesis and O2 Reactivity of a Titanium(III) Metal–Organic Framework. *Inorg. Chem.* **2015,** 10096-10104.

2. Mountford, P.; Hazari, N., 4.04 - Complexes of Titanium in Oxidation State iii A2 - Mingos, D. Michael P. In *Comprehensive Organometallic Chemistry III*, Crabtree, R. H., Ed. Elsevier: Oxford, 2007; pp 281-322.

3. Cam, D.; Sartori, F.; Maldotti, A., Reduction of bis(η5-cyclopentadienyl)zirconium dichloride in the presence of methylalumoxane. *Macromol. Chem. Phys.* **1994,** 2817-2826.

4. Lenton, T. N.; Bercaw, J. E.; Panchenko, V. N.; Zakharov, V. A.; Babushkin, D. E.; Soshnikov, I. E.; Talsi, E. P.; Brintzinger, H. H., Formation of Trivalent Zirconocene Complexes from ansa-Zirconocene-Based Olefin-Polymerization Precatalysts: An EPR- and NMR-Spectroscopic Study. *J. Am. Chem. Soc.* **2013,** 10710-10719.

5. Brand, H.; Arnold, J., Facile Reduction of a Dialkyl Zirconium(IV) Octaethylporphyrin (OEP) Complex by H2: Crystal Structure and Spectroscopic Characterization of [(OEP)ZrCH2SiMe3]. *Angew. Chem. Int. Ed.* **1994,** 95-97.

6. Lancaster, S. J., 4.07 - Complexes of Zirconium and Hafnium in Oxidation State iii A2 - Mingos, D. Michael P. In *Comprehensive Organometallic Chemistry III*, Crabtree, R. H., Ed. Elsevier: Oxford, 2007; pp 741-757.

7. Cotton, F. A.; Kibala, P. A.; Wojtczak, W. A., A simple compound containing the first hafnium(III) to hafnium(III) bond. *Inorg. Chim. Acta* **1990,** 1-3.

8. Morse, P. M.; Wilson, S. R.; Girolami, G. S., A compound with a hafnium-hafnium bond. The first structurally characterized hafnium (III) complex: hexachlorobis (1, 2-bis (diisopropylphosphino) ethane) dihafnium. *Inorg. Chem.* **1990,** 3200-3202.

9. Visser, C.; van den Hende, J. R.; Meetsma, A.; Hessen, B., Polynuclear Hafnium Polyhydrides with a 1,3-Butadiene-1,4-diyl Fragment from Hydrogenolysis of a Butadiene Alkyl Complex. *Organometallics* **2003,** 615-617.

10. Xu, H.-Q.; Hu, J.; Wang, D.; Li, Z.; Zhang, Q.; Luo, Y.; Yu, S.-H.; Jiang, H.-L., Visible-Light Photoreduction of CO2 in a Metal–Organic Framework: Boosting Electron–Hole Separation via Electron Trap States. *J. Am. Chem. Soc.* **2015,** 13440-13443.

11. Long, J.; Wang, S.; Ding, Z.; Wang, S.; Zhou, Y.; Huang, L.; Wang, X., Amine-functionalized zirconium metal-organic framework as efficient visible-light photocatalyst for aerobic organic transformations. *Chem. Commun.* **2012,** 11656-11658.

12. Rungtaweevoranit, B.; Baek, J.; Araujo, J. R.; Archanjo, B. S.; Choi, K. M.; Yaghi, O. M.; Somorjai, G. A., Copper Nanocrystals Encapsulated in Zr-based Metal–Organic Frameworks for Highly Selective CO2 Hydrogenation to Methanol. *Nano Lett.* **2016,** 7645-7649.

13. An, B.; Zhang, J.; Cheng, K.; Ji, P.; Wang, C.; Lin, W., Confinement of Ultrasmall Cu/ZnOx Nanoparticles in Metal–Organic Frameworks for Selective Methanol Synthesis from Catalytic Hydrogenation of CO2. *J. Am. Chem. Soc.* **2017,** 3834-3840.

14. Hao, L.; Harrod, J. F.; Lebuis, A.-M.; Mu, Y.; Shu, R.; Samuel, E.; Woo, H.-G., Homogeneous Catalytic Hydrosilylation of Pyridines. *Angew. Chem. Int. Ed.* **1998,** 3126-3129.

15. Arrowsmith, M.; Hill, M. S.; Hadlington, T.; Kociok-Köhn, G.; Weetman, C., Magnesium-Catalyzed Hydroboration of Pyridines. *Organometallics* **2011,** 5556-5559.

16. Dudnik, A. S.; Weidner, V. L.; Motta, A.; Delferro, M.; Marks, T. J., Atom-efficient regioselective 1,2-dearomatization of functionalized pyridines by an earth-abundant organolanthanide catalyst. *Nat Chem* **2014,** 1100-1107.

17. Powers, D. C.; Geibel, M. A. L.; Klein, J. E. M. N.; Ritter, T., Bimetallic Palladium Catalysis: Direct Observation of Pd(III)−Pd(III) Intermediates. *J. Am. Chem. Soc.* **2009,** 17050-17051.

18. Collman, J. P.; Hutchison, J. E.; Wagenknecht, P. S.; Lewis, N. S.; Lopez, M. A.; Guilard, R., An unprecedented, bridged dihydrogen complex of a cofacial metallodiporphyrin and its

relevance to the bimolecular reductive elimination of hydrogen. *J. Am. Chem. Soc.* **1990,** 8206-8208.

19. Ji, P.; Sawano, T.; Lin, Z.; Urban, A.; Boures, D.; Lin, W., Cerium-Hydride Secondary Building Units in a Porous Metal–Organic Framework for Catalytic Hydroboration and Hydrophosphination. *J. Am. Chem. Soc.* **2016,** 14860-14863.

20. Lee, W.-J.; Lee, Y.-S.; Rha, S.-K.; Lee, Y.-J.; Lim, K.-Y.; Chung, Y.-D.; Whang, C.-N., Adhesion and interface chemical reactions of Cu/polyimide and Cu/TiN by XPS. *Appl. Surf. Sci.* **2003,** 128-136.

21. Chusuei, C. C.; Brookshier, M. A.; Goodman, D. W., Correlation of Relative X-ray Photoelectron Spectroscopy Shake-up Intensity with CuO Particle Size. *Langmuir* **1999,** 2806-2808.

22. Gambarotta, S.; Chiang, M. Y., Synthesis of a diamagnetic fulvalene zirconium(III) derivative. The crystal structure of (.eta.5:.eta.5-C10H8)[(.eta.5-C5H5)Zr(.mu.-Cl)]2. *Organometallics* **1987,** 897-899.

23. Hoffman, D. M.; Lee, S., Synthesis of pyridine complexes of zirconium(III) chloride and the apparent oxidation to zirconium(IV) by a nitrile. *Inorg. Chem.* **1992,** 2675-2676.

24. Cotton, F. A.; Feng, X.; Shang, M.; Wojtczak, W. A., Empty Octahedral Hexazirconium Clusters with Only Ten Electrons, [Zr6X14(PR3)4]. *Angew. Chem. Int. Ed.* **1992,** 1050-1053.

25. Fan, X.; Zheng, J.; Li, Z. H.; Wang, H., Organoborane Catalyzed Regioselective 1,4-Hydroboration of Pyridines. *J. Am. Chem. Soc.* **2015,** 4916-4919.

Chapter 10. Tuning Lewis Acidity of MOFs via Perfluorination of Bridging Ligands: Spectroscopic, Theoretical, and Catalytic Studies

10.1 Introduction

MOF Lewis acidity has attracted broad research interest in recent years. This chapter describes the development of two quantitative methods for determining MOF Lewis acidity through either the EPR spectroscopy of MOF-bound superoxide ($O_2^{\bullet-}$) or the fluorescence spectroscopy of MOF-bound NMA. The techniques were used to quantitatively measure the enhanced Lewis acidity of perfluorinated MOFs. Two novel perfluorinated MOFs, Zr_6-fBDC and Zr_6-fBPDC, were shown to be significantly more Lewis acidic than non-substituted UiO-66 and UiO-67 MOFs as well as the nitrated MOFs Zr_6-BDC-NO_2 and Zr_6-BPDC-$(NO_2)_2$. Zr_6-fBDC was therefore used as a highly active solid Lewis acid for catalyzing the Diels-Alder and arene C-H iodination reactions.

Early demonstrations of MOF catalysis utilized the metal-connecting points as Lewis acidic sites, but these MOFs only displayed limited catalytic activities (**Figure 10-1**). The advent of highly stable MOFs based on Group IV metals with d^0 electronic configurations brought about porous solid catalysts with greatly enhanced Lewis acidity, and have been used for a number of catalytic reactions including isomerization, hydrolysis, and dehydrations.[1-8]

Despite recent progress, existing MOFs still exhibit much lower Lewis acidity than the benchmark homogeneous systems (*e.g.* $Sc(OTf)_3$).[9-15] The Lewis acidity of homogeneous catalysts can be precisely measured. In contrast, no techniques are currently available to quantitatively assess the MOF Lewis acidity, mainly due to the insolubility and structural complexity of MOFs.

Although notable efforts were made to probe Lewis acidity using reaction kinetics, but such measurements are convoluted with the varied substrates/products diffusion rates through different MOFs, and the partition of substrates/products between different MOF channels. The objectives of this work are to develop quantitative methods to determine MOF Lewis acidity and to discover effective strategies to enhance their Lewis acidity, with the goal of making porous solid catalysts with much larger channels than zeolites for fine chemical synthesis.

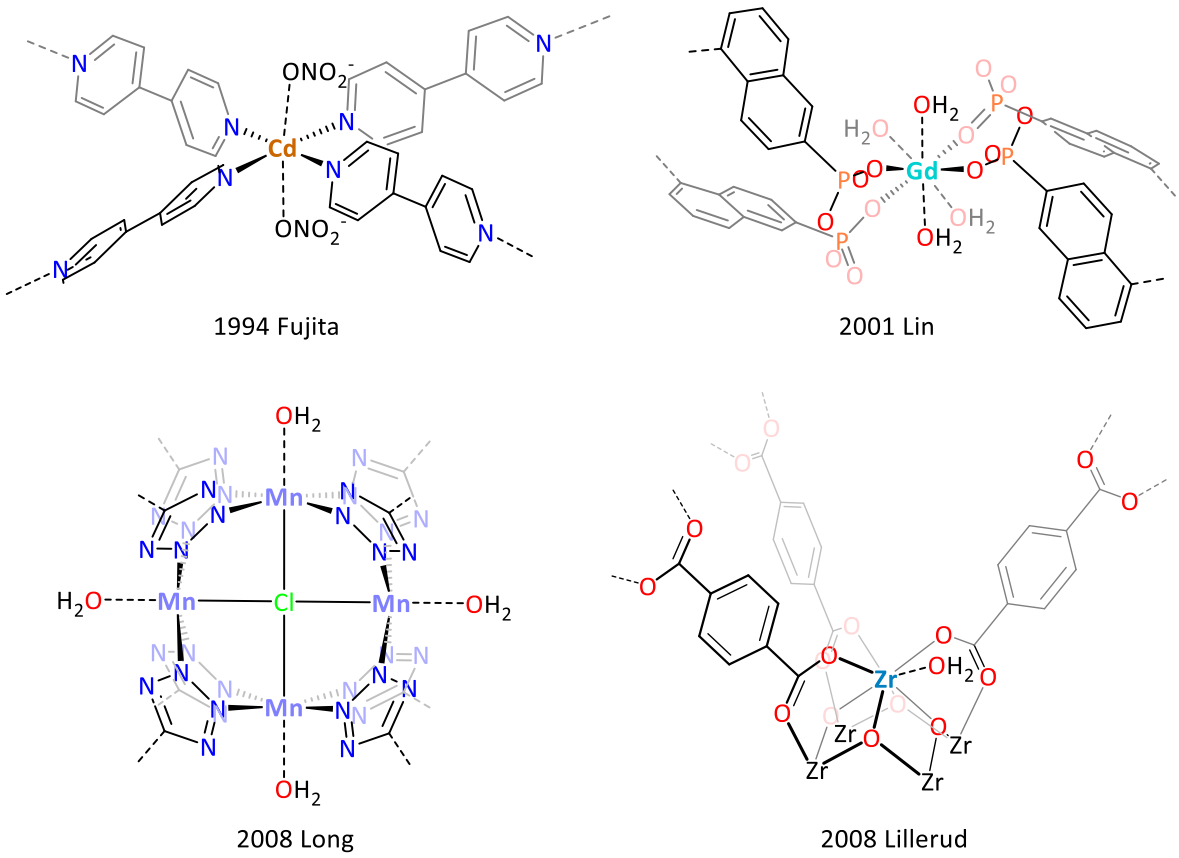

Figure 10-1. Notable examples of MOF Lewis acids.

This chapter describes a series of UiO MOFs featuring defect $Zr_6O_4(OH)_4$ inorganic nodes with missing linkers and unsaturated coordination around Zr centers.[16-21] EPR and fluorescence methods were applied to measure a variety of Lewis acidic MOFs to unveil a strong correlation

between dicarboxylate electron density and $Zr_6O_4(OH)_4$ Lewis acidity. Based on this insight, we have significantly enhanced the Zr-MOF Lewis acidity using perfluorinated bridging ligands to afford porous solid catalysts for challenging transformations that typically effected by strongly Lewis acidic homogeneous catalysts (**Figure 10-2**).

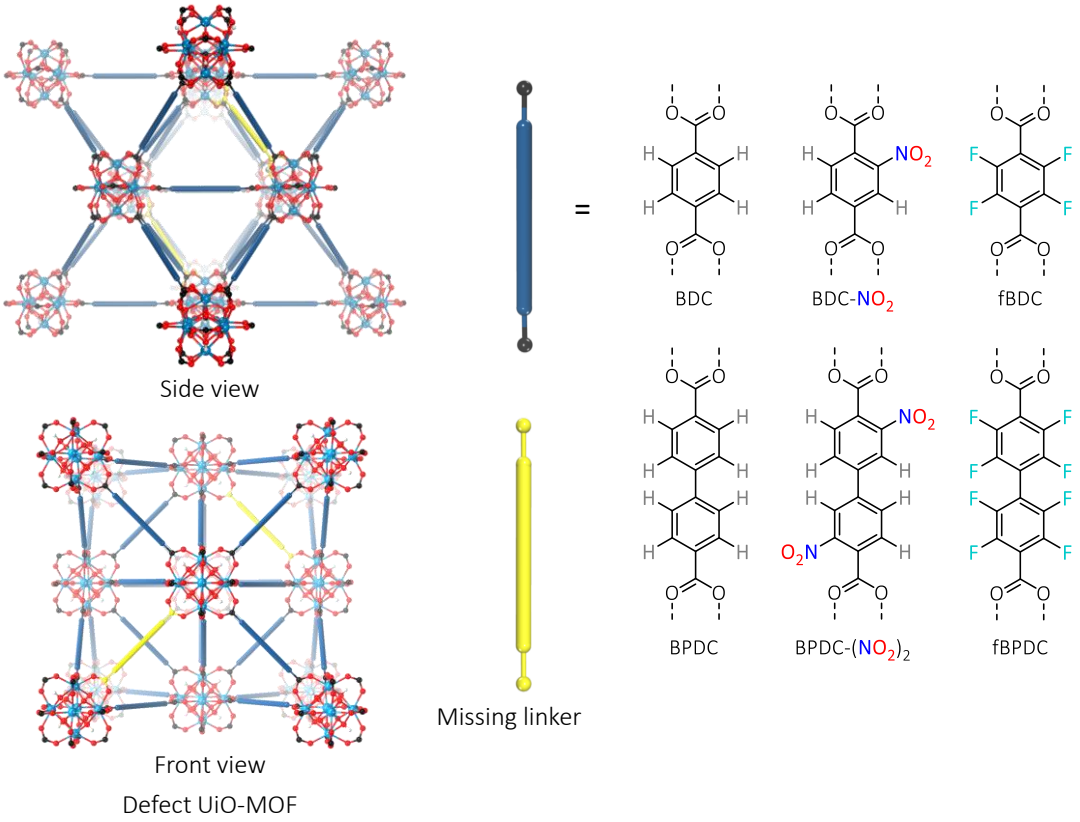

Figure 10-2. Framework structures and bridging ligands of two series of MOFs isostructural to UiO-66 and UiO-67 with defect $Zr_6O_4(OH)_4$ nodes.

10.2 Results and Discussion

10.2.1 EPR method for measuring Lewis acidity

Two perfluorinated UiO-MOFs, Zr_6-fBDC and Zr_6-fBPDC were synthesized. The structure of these two MOFs can be viewed as replacing BDC in UiO-66 and BPDC in UiO-67 with fBDC

and fBPDC ligands, respectively (**Figure 10-2**). These two MOFs were synthesized by heating a mixture of $ZrOCl_2 \cdot 8H_2O$ and fluorinated linkers in acidic THF at 80 °C.

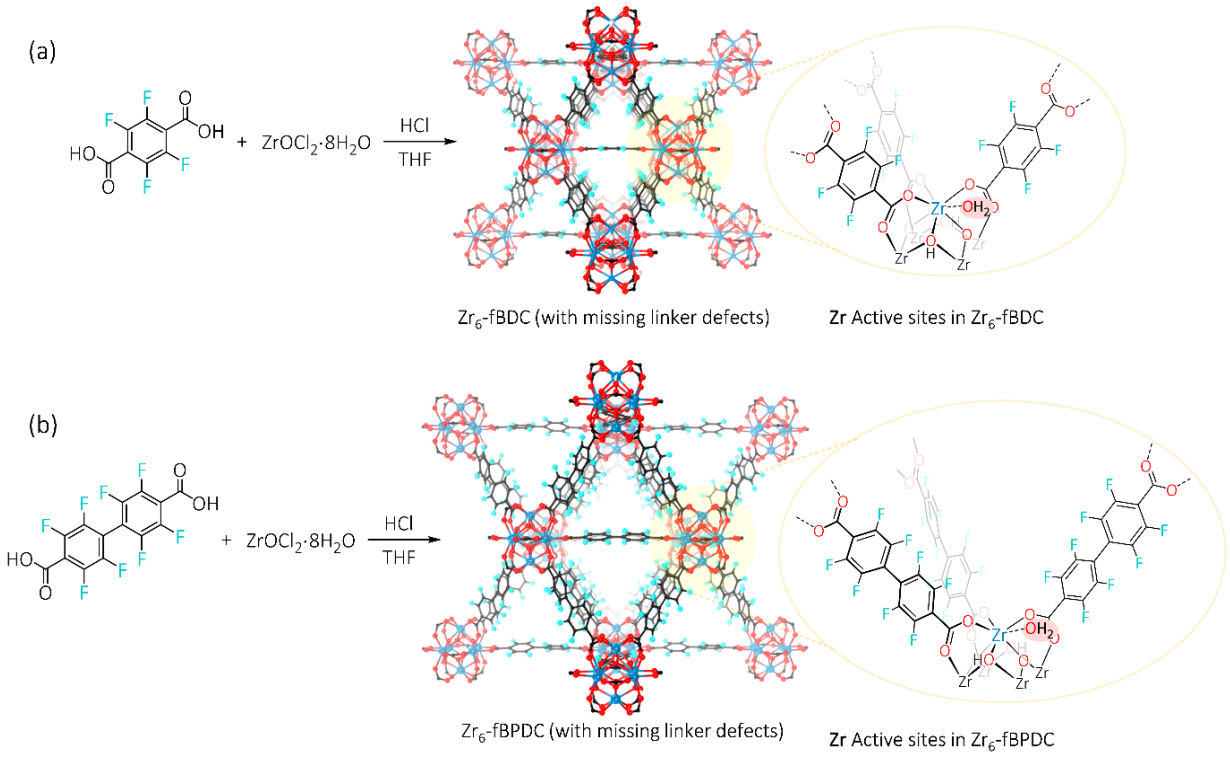

Figure 10-3. Synthesis of defect Zr_6-fBDC (a) and Zr_6-fBPDC (b) from $ZrOCl_2 \cdot 8H_2O$ and perfluorinated linkers. The missing organic linkers give rise to unsaturated coordination around the Zr_6 nodes. The coordination environments of the Zr active sites are approximately $Zr(\mu_3\text{-}O)_2(\mu_3\text{-}OH)_2(L)_3(OH_2)$ in these two MOFs (L is fBDC or fBPDC).

Spectroscopic measurements of MOFs using UV-vis, fluorescence or EPR have been challenging. The signals tend to be weak and noisy because MOFs are poorly dispersed in solvents and scatter photons very strongly. One solution to this problem is to utilize probes that have high sensitivity toward photon excitations. We have chosen $O_2^{\bullet-}$ and NMA as two sensitive probes to assess the Lewis acidity of MOFs. Superoxide ions display strong EPR signals and NMA is a highly emissive fluorescent dye. More importantly, their signals are sensitive to the Lewis acidity

of metal ions. In this work, we show for the first time that EPR of MOF-bound superoxide and fluorescence of MOF-bound NMA provide sensitive indicators for the Lewis acidity of MOFs.

$O_2^{\bullet-}$ can be in situ generated by the 1 e^- reduction of O_2 using $(BNA)_2$ as the photo-reductant. $O_2^{\bullet-}$ is very small and easily diffuses through the MOF channel before quenching. Moreover, $O_2^{\bullet-}$ is very electron-rich and strongly binds to the Zr defect sites in UiO-MOFs by displacing the weakly coordinating H_2O molecule to form the EPR-active $Zr(O_2^{\bullet-})$ species (**Scheme 10-1**).

Scheme 10-1. Proposed mechanism for the superoxide binding to the defect Zr sites in Zr_6-fBDC.

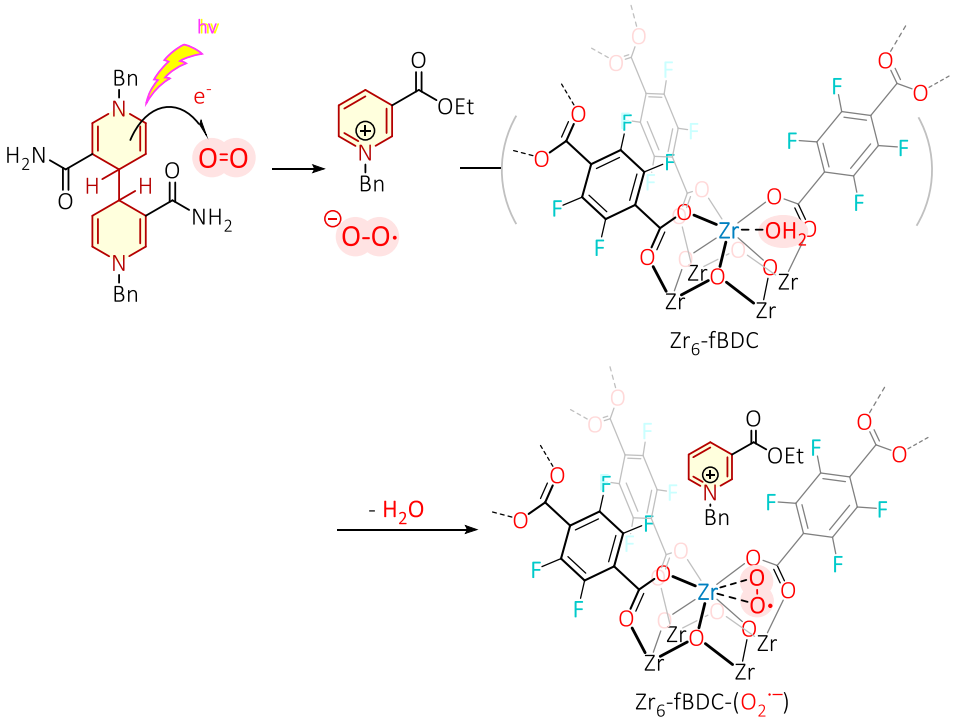

The coordination to Lewis acids significantly changes the EPR signature of $O_2^{\bullet-}$. The rhombic g-tensor of the EPR spectrum, most evidently the g_{zz} component, is diagnostic of the binding strength between $O_2^{\bullet-}$ and the Lewis acid. This effect is due to coordination of the electron pair in the HOMO of the $O_2^{\bullet-}$ (π_g^y), which increases the energy splitting (ΔE) between the HOMO and the SOMO of the $O_2^{\bullet-}$ (π_g^x). The ΔE is related to the g_{zz} value following the Känzig-Cohen

equation. More Lewis acidic metal centers would split the π* orbitals to a greater extent to give larger ΔE values.

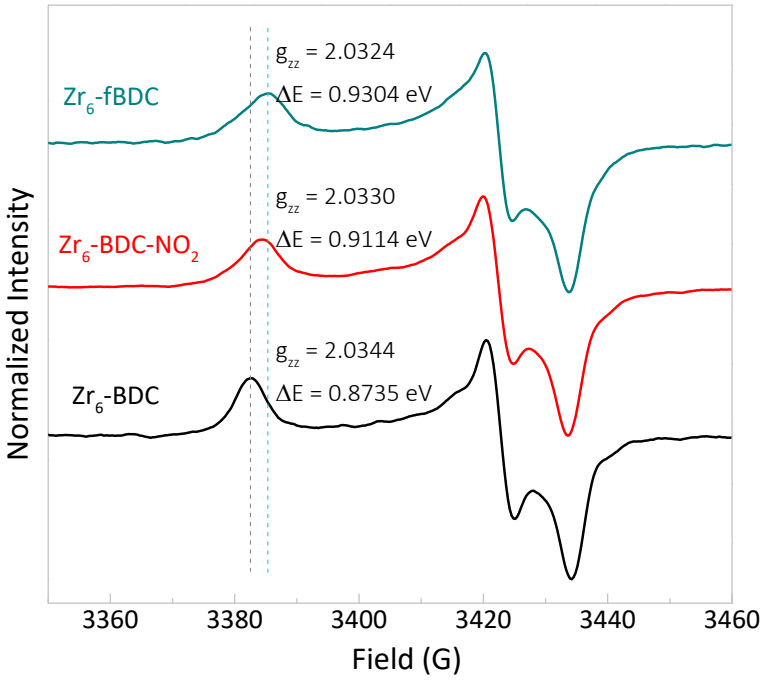

Figure 10- 4. Zr($O_2^{\bullet-}$) EPR spectra of Zr_6-BDC (black), Zr_6-BDC-NO_2 (red), and Zr_6-fBDC (blue).

The EPR spectra of a variety of UiO MOF-bound superoxide ions were measured at 100 K, and the measured g_{zz} values displayed a clear trend. UiO MOFs grown from more electron-deficient dicarboxylates, namely those with electron-withdrawing groups, showed smaller g_{zz}, indicating larger ΔE values. For example, Zr_6-BDC produced a g_{zz} value of 2.0344, corresponding to a ΔE of 0.8735 eV. The Zr_6-BDC-NO_2 MOF, which has more Lewis acidic Zr centers, showed a smaller g_{zz} value of 2.0330, corresponding to a larger ΔE of 0.9114 eV. In contrast, the Zr_6-fBDC MOF exhibited a g_{zz} of 2.0324 and a ΔE of 0.9304 eV, making it the most Lewis acidic MOF in the UiO-66 series (**Figure 10-4**).

To validate the trend observed for the UiO-66 series, three MOFs of the UiO-67 series were prepared and measured for EPR spectra. Zr_6-BPDC showed a g_{zz} of 2.0343, corresponding to ΔE of 0.8743 eV, similar to that of Zr_6-BDC. Zr_6-BPDC-$(NO_2)_2$ gave a g_{zz} of 2.0334 and a ΔE of 0.9014 eV. The perfluorinated Zr_6-fBPDC is much more Lewis acidic than the other two MOFs, with a g_{zz} of 2.0326 and a ΔE of 0.9246 eV. These experiments established that perfluorination is an effective way to enhance Lewis acidity of defect $Zr_6O_4(OH)_4$ nodes in UiO-MOFs (**Figure 10-5**).

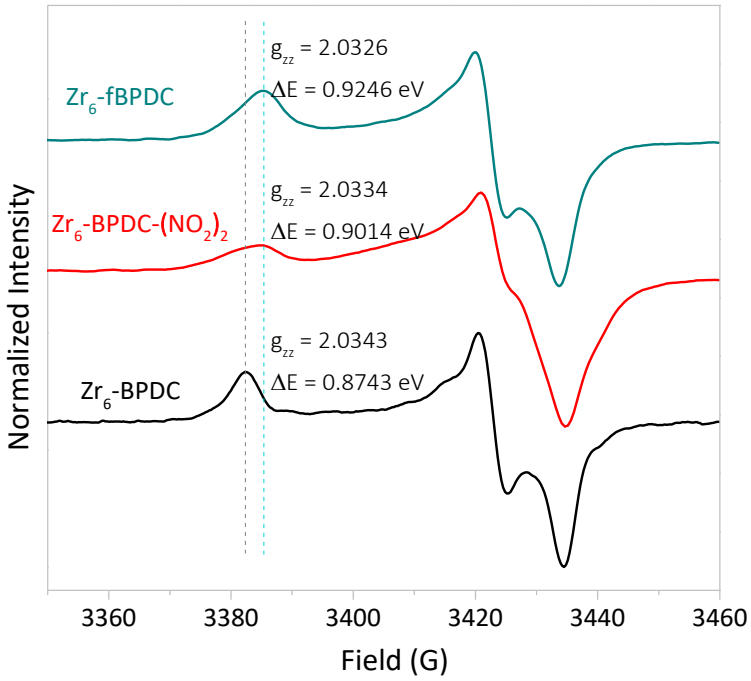

Figure 10-5. $Zr(O_2^{\bullet-})$ EPR spectra of Zr_6-BPDC(black), Zr_6-BPDC-$(NO_2)_2$ (red), and Zr_6-fBPDC (blue).

10.2.2 DFT calculations to validate the EPR method

DFT calculations were carried out to gain insight into the coordination mode and electronic structure of $O_2^{\bullet-}$ bound to Zr_6 nodes. The optimized structures for the models of all six MOFs showed a side-on binding mode of the $O_2^{\bullet-}$ on the Zr_6 node (**Figure 10-6**). [29] The side-on coordination is analogous to that proposed for superoxide ions bound to a zirconia surface. For the

Zr_6-fBDC-$O_2^{\bullet-}$ model structure, the O-O distance at the Zr($O_2^{\bullet-}$) site is 1.301 Å, longer than the O-O distance in a free $O_2^{\bullet-}$ species (1.28 Å). This is presumably due to the weakening of the O-O bond by the coordination to Zr centers. The Zr-O bond distances in Zr_6-fBDC-($O_2^{\bullet-}$) are 2.18 and 2.21 Å, with a small degree of binding asymmetry. Comparing the Zr($O_2^{\bullet-}$) bond distances in the Zr_6-BDC and Zr_6-fBDC models offered insight into the binding strength of $O_2^{\bullet-}$ to different Zr centers. Indeed, the Zr-O distances in Zr_6-fBDC are 2.18 and 2.21 Å, shorter than those in Zr_6-BDC (2.19 and 2.23 Å). These computational results therefore verified that electron withdrawing groups on the organic linker increase the Lewis acidity of Zr sites in defect UiO-MOFs.

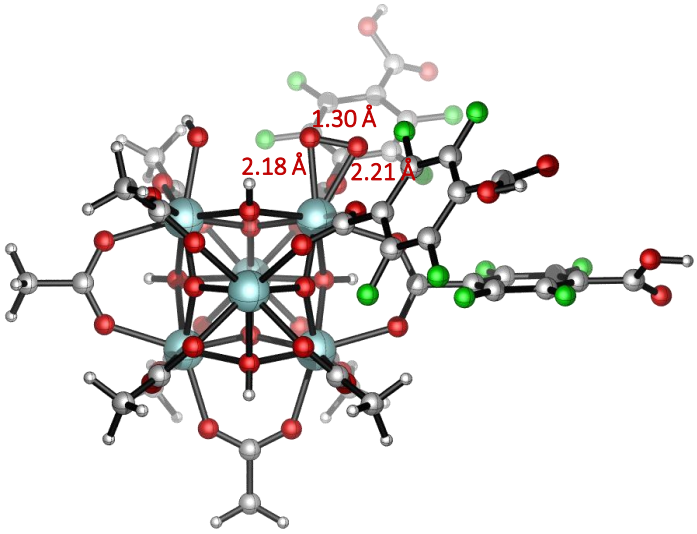

Figure 10-6. DFT optimized superoxide binding mode on Zr_6-fBDC-$O_2^{\bullet-}$.

The enhancement of MOF Lewis acidity by installing electron withdrawing groups on the linker was also verified by DFT through calculation of ΔE values. The molecular orbital diagram of a Zr($O_2^{\bullet-}$) fragment in the Zr_6-BDC model structure was analyzed using biorthogonalization method. The bonding orbitals for the $O_2^{\bullet-}$ significantly overlap with the Zr^{4+} orbitals, indicating strong binding of $O_2^{\bullet-}$ onto the Zr center instead of simply electro-static attachment. The energy

gaps between the HOMO and SOMO were calculated using restricted open shell methods, and are correlated to the EPR-measured ΔE values. (**Figure 10-7a**).

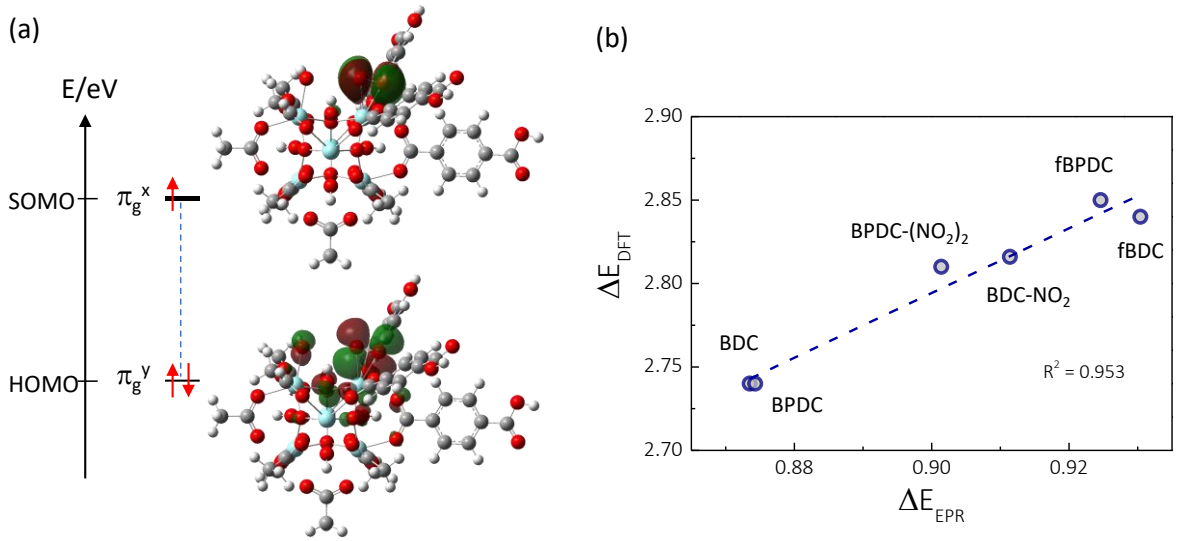

Figure 10-7. (a) Molecular orbital diagram for $Zr(O_2^{\bullet-})$ in the model structure. The HOMO-SOMO gap for Zr_6-BDC-$O_2^{\bullet-}$, indicated by the dotted line, is 2.74 eV. (b) The linear relationship be-tween ΔE values calculated by DFT, ΔE_{DFT}, and ΔE values measured by EPR, ΔE_{EPR}, with an adjusted R^2 of 0.953.

We have observed that the HOMO-SOMO energy gaps increase in the following order: Zr_6-BDC ≈ Zr_6-BPDC < Zr_6-BDC-NO_2 < Zr_6-BPDC-$(NO_2)_2$ < Zr_6-fBPDC < Zr_6-fBDC (**Figure 10-7b**). A linear relationship between the calculated ΔE_{DFT} with the EPR measured ΔE was observed with an adjusted R^2 of 0.953. Therefore, DFT calculations support the proposal that electron-withdrawing groups on the MOF ligand significantly increase the binding strength of superoxide on the MOF node.

10.2.3 DFT calculations to compare Zr_6 nodes with multiple defect sites.

DFT calculations have also been utilized to elucidate the impact of defect density on the MOF Lewis acidity. For Zr_6-fBDC, two additional models for the superoxide-bound MOF nodes,

one with two missing carboxylate defects (Zr_6-fBDC-2def- $O_2^{\bullet-}$) and another with three missing carboxylate defects (Zr_6-fBDC-2def- $O_2^{\bullet-}$), were optimized and analyzed for SOMO-HOMO gaps. The open Zr sites generated from linker removal were capped with H_2O and OH (**Figure 10-8, 10-10**). The superoxide moieties in the optimized doubly or triply defected models adopt identical coordination modes as the singly defected model and produced identical SOMO-HOMO gaps of 2.84 eV (**Figure 10-9**, **10-11**). Unlike the change of carboxylates, the inclusion of more defects does not alter the primary coordination environment around the Lewis acidic Zr centers.

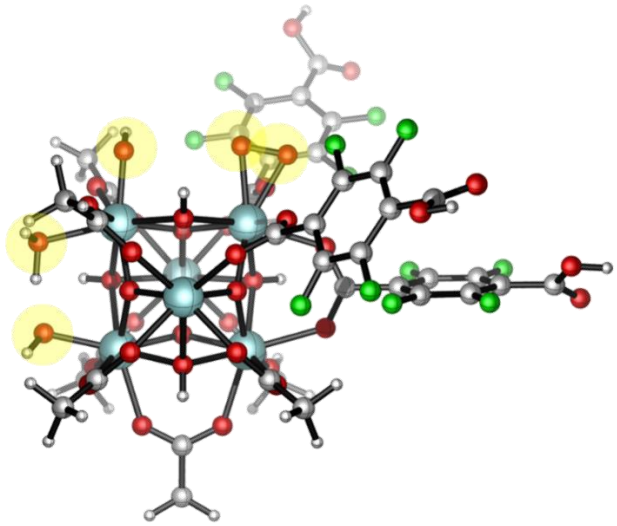

Figure 10-8. DFT optimized structure for Zr_6-fBDC-2def-$O_2^{\bullet-}$ with two defects. The missing carboxylate defect sites are highlighted in yellow.

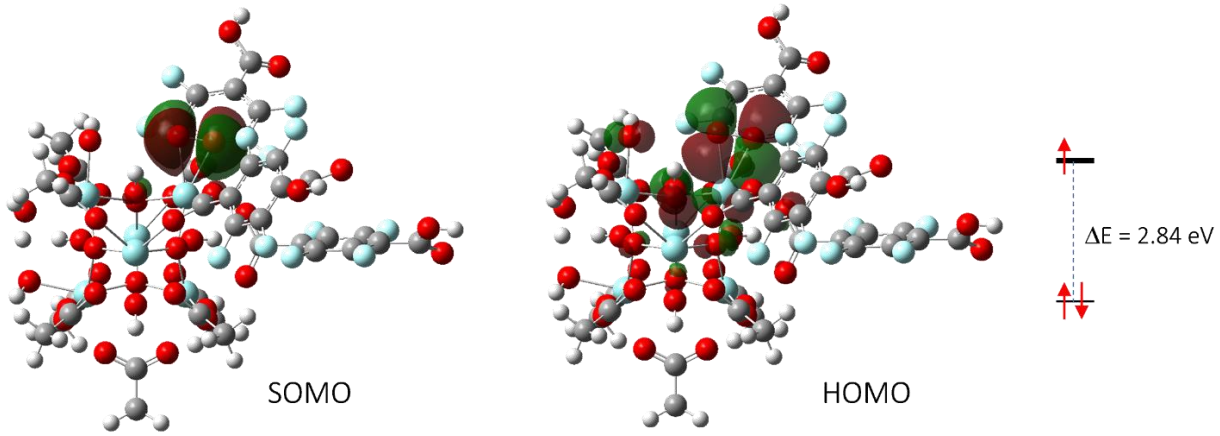

Figure 10-9. Molecular orbital diagrams for Zr_6-fBDC-2def-$O_2^{\bullet-}$. The SOMO-HOMO gap for superoxide in this model is 2.84 eV.

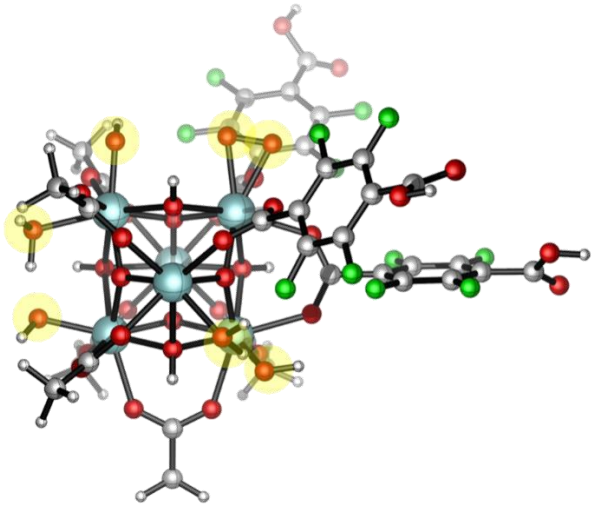

Figure 10-10. DFT optimized structure for Zr_6-fBDC-3def-$O_2^{\bullet-}$. The missing carboxylate defect sites are highlighted in yellow.

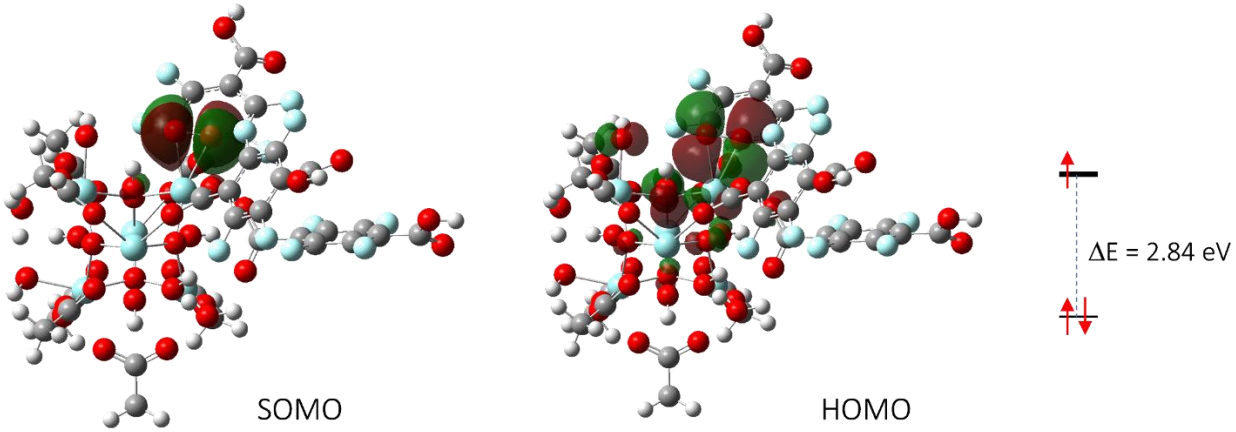

Figure 10-11. Molecular orbital diagrams for Zr_6-fBDC-3def-$O_2^{\bullet-}$. The SOMO-HOMO gap for superoxide in this model is 2.84 eV.

10.2.4 Fluorescence method for measuring Lewis acidity

Although $O_2^{\bullet-}$ is an accurate indicator of MOF Lewis acidity, the experimental procedures for superoxide generation and EPR measurement are lengthy and tedious. Therefore, we have also used NMA fluorescence to probe Lewis acidity of MOFs. NMA is a commercially-available

fluorescent dye, which features lone pairs of electron that can effectively bind to vacant metal sites (**Figure 10-12**).

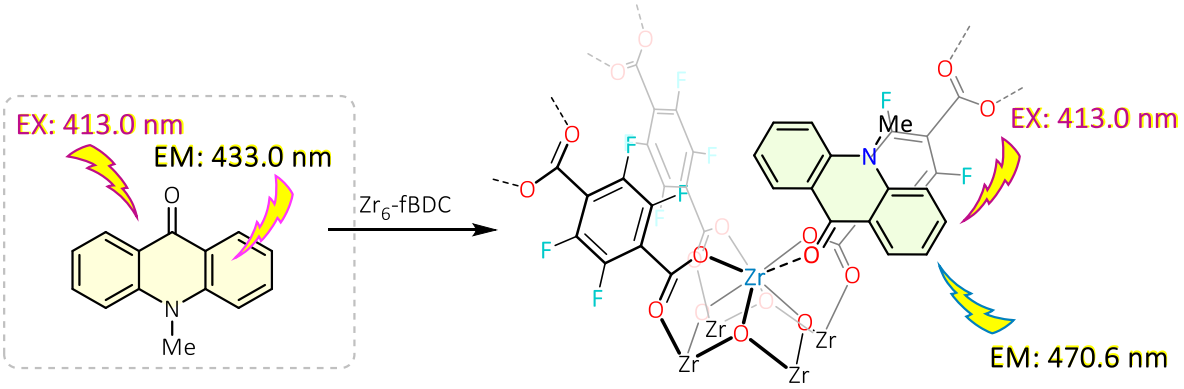

Figure 10-12. The coordination of NMA dye to the Zr defect sites in Zr_6-fBDC, leading to a dramatic shift in the emission maxima.

The fluorescence maxima (λ_{max}) of NMA shifts significantly upon binding to metal centers (**Figure 10-13**). These shifts are indicative of the binding affinity of the probe to the metals and thus can be used as a measure of Lewis acidity. A large excess of Lewis acids is typically used with respect to NMA to avoid the emission of non-coordinated NMA molecules. The fluorescence spectra of NMA coordinated to three different UiO-66 MOFs are shown in **Figure 10-14**. In the case of Zr_6-BDC and Zr_6-BDC-NO_2, the λmax of NMA changed dramatically from 433.0 nm to 466.4 nm and 469.0 nm, respectively, upon coordination of the dye to defect Zr sites. Zr_6-fBDC shifted the NMA emission wavelength the most, with a λ_{max} of 470.6 nm. The same trend was observed for the three UiO-67 MOFs, where the Zr_6-fBPDC shifted the NMA emission wavelength the most, with a λ_{max} of 469.6 nm.

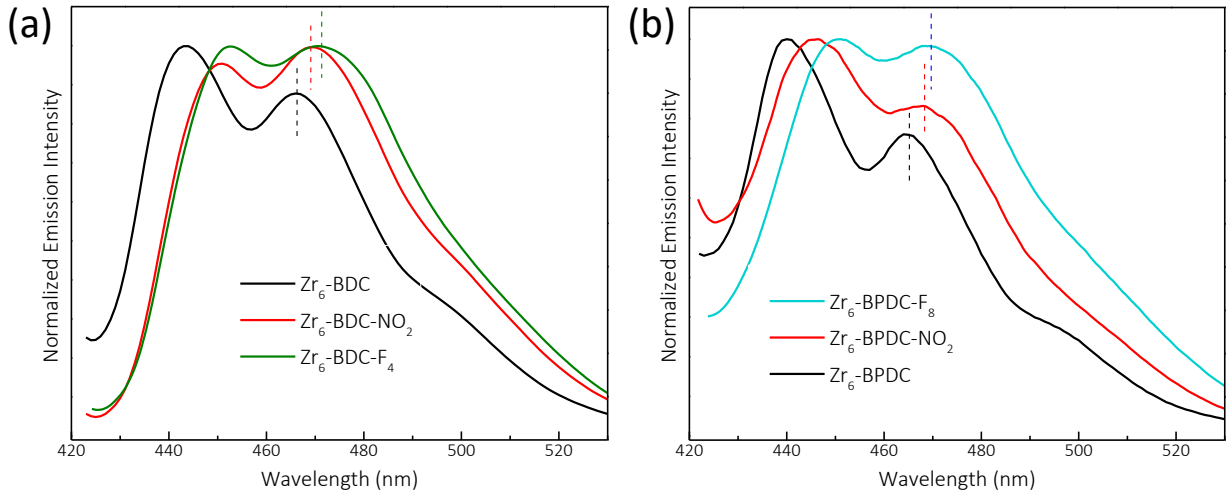

Figure 10-13. (a) Fluorescence spectra of NMA binding to Zr_6-BDC (black), Zr_6-BDC-NO_2 (red), and Zr_6-fBDC (blue) in MeCN at 298 K. (b) Fluorescence spectra of NMA binding to Zr_6-BDPC (black), Zr_6-BPDC-$(NO_2)_2$ (red), and Zr_6-fBPDC (blue) in MeCN at 298 K.

We also found that the λ_{max} of Zr-bound NMA was linearly related to the ΔE measured from the EPR method, with an adjusted R-squared value of 0.954. A fitted empirical relationship (**Figure 10-23b**) between the λ_{max} and ΔE was used to calculate the NMA fluorescence-derived ΔE values (ΔE_{NMA}) for every MOF. The ΔE_{NMA} values were compared with the EPR-measured ΔE values to check the reliability of the fluorescence method. The λ_{max}, ΔE_{NMA} and ΔE for each of the six different MOFs are summarized in **Figure 10-15a**. The ΔE_{NMA} consistently reproduces the EPR-measured ΔE, indicating that the fluorescence dye is a convenient probe for assessing Lewis acidity in MOFs.

(a)

MOFs	λ_{max} (nm)	ΔE_{NMA} (eV)	ΔE_{EPR} (eV)
Zr_6-BDC	466.4	0.8788	0.8735
Zr_6-BDC-NO_2	469.0	0.9121	0.9114
Zr_6-fBDC	470.6	0.9326	0.9304
Zr_6-BPDC	465.5	0.8673	0.8743
Zr_6-BPDC-$(NO_2)_2$	468.4	0.9044	0.9014
Zr_6-fBPDC	469.6	0.9200	0.9246

(b)

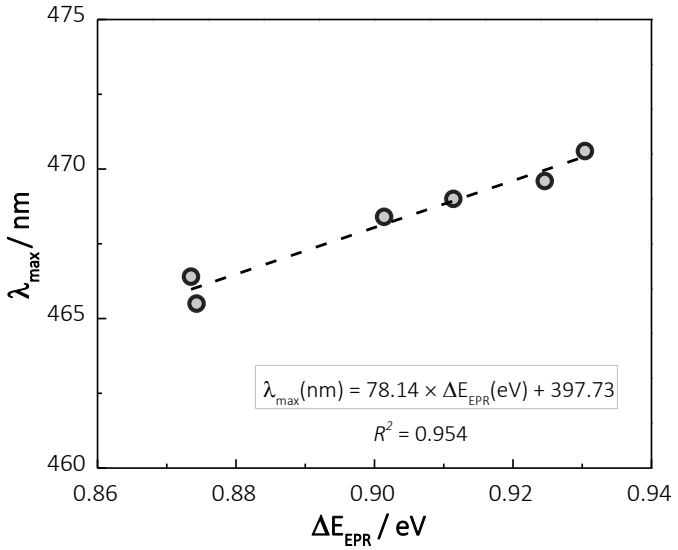

Figure 10-14. (a) Linear relationship between the EPR measured ΔE_{EPR} and the DFT calculated ΔE_{DFT}. (b) List of the fluorescence maxima (λmax), calculated ΔE_{NMA} from NMA λ_{max}, and ΔEEPR measured from Zr-($O_2^{\bullet-}$) EPR spectra.

The coordination mode and electronic structure of NMA bound to the Zr_6 node was also studied by DFT. The optimized structure showed that the carbonyl group (instead of the aryl or nitrogen) is coordinated to the vacant site of the Zr_6 node, adopting a side-on coordination mode (**Figure 10-16**). Molecular orbital calculations of the NMA fluorescent dye revealed the electronic structure of the HOMO orbital, which is proposed to be responsible for the NMA coordination to Zr.

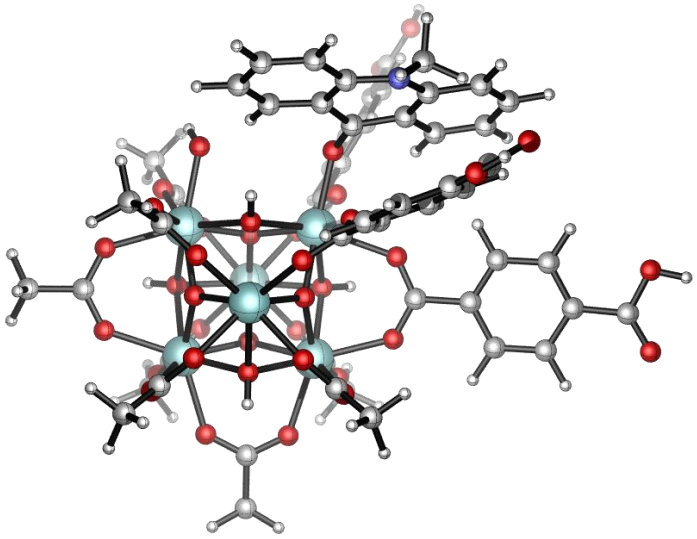

Figure 10-15. Coordination mode of NMA on Zr_6 node of defect UiO-66.

10.2.5 Zr_6-fBDC catalyzed Diels-Alder reactions.

We first tested Zr_6-fBDC for Diels-Alder reactions. The Diels-Alder reaction is of great synthetic value to the organic chemistry community and has been widely applied to the synthesis of six-member ring structures with high regioselectivity and stereoselectivity. However, the reaction generally requires high temperatures and long reaction times when performed without the addition of an acid catalyst. Unlike classical Lewis acidic metal complexes, MOF catalysts benefit from having uniform active sites which can lead to better reaction selectivity. The solid nature of MOFs offers additional advantages, including easy separation from reaction mixtures and catalyst reusability.

For the cyclization of 1,4-benzoquinone with 2,3-dimethylbuta-1,3-diene, only 4% yield of product was observed in the absence of catalyst at 25 °C after 2 h (**Table 10-1**). In the presence of Zr_6-BDC and Zr_6-BDC-NO_2, the product yields increased to 14% and 25% respectively. In contrast, Zr_6-fBDC afforded the cycloaddition product in 78% yield at the same reaction condition. Elongation of the reaction time from 2 h to 8 h further increased the yield to 98%. Considering Zr_6-fBDC has a higher density of defect sites, additional control experiments were performed by

increasing the catalyst loading of Zr_6-BDC and Zr_6-BDC-NO_2 to the same loading of defect sites as Zr_6-fBDC. However, the yields of product are still much lower than that of Zr_6-fBDC catalyzed entries. The reaction is proposed to be initiated by the coordination of the lone pair electrons of the quinones to the Zr centers. This coordination is expected to lower the energy of the LUMO orbital to enhance the overlap with the HOMO orbital of the dienes.

Table 10-1. Catalyst evaluation of Zr_6-fBDC catalyzed Diels-Alder reactions.

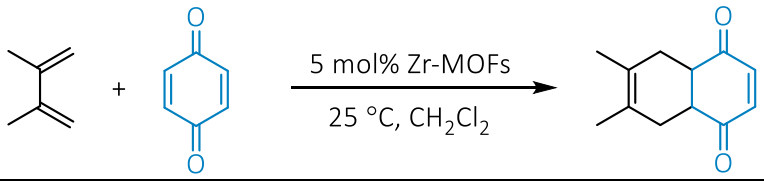

Entry	Product	Catalyst	Time	Yield
1	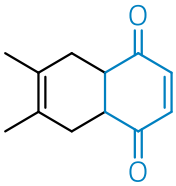	No catalyst	2 h	4 %
2		MOF-5	2 h	8 %
3		HKUST	2 h	46 %
4		Zr_6-BDC	2 h	14 %
5		Zr_6-BDC-NO_2	2 h	25 %
6		Zr_6-fBDC	2 h	78 %
7		Zr_6-fBDC	8 h	98 %

Reaction conditions: dienophile (1 equiv., 1 mmol), diene (1.2 equiv.), Zr MOFs (5 mol%, 0.05 mmol), CH_2Cl_2 (3.0 mL), 25 °C. Reaction yields were determined from ^{1}H NMR using mesitylene as an internal standard.

The MOF-catalyzed Diels-Alder reaction displayed a broad substrate scope (**Table 10-2**). Cyclohexa-1,3-diene, a less reactive diene than cyclopentadiene or 2,3-dimethylbuta-1,3-diene, was cyclized with 1,4-benzoquinone in 94% yield in 12h in the presence of 5 mol% Zr_6-fBDC. Quinone substrates containing electron-donating groups, such as the 2-methyl-1,4-benzoquinone, are generally less reactive in Diels-Alder reactions due to their much higher LUMO energy and increased steric hindrance. Impressively, in the presence of 5 mol% Zr_6-fBDC, 2-methyl-1,4-benzoquinone efficiently reacted with cyclohexa-1,3-diene and 2,3-dimethylbuta-1,3-diene at

25 °C to afford cycloaddition products in 74% and 84% yields, respectively. Moreover, Zr_6-fBDC was reused for at least three runs without significant loss of catalytic activity (**Figure 10-17**).

Table 10-2. Catalyst evaluation and substrate scope of Zr_6-fBDC catalyzed Diels-Alder reactions.

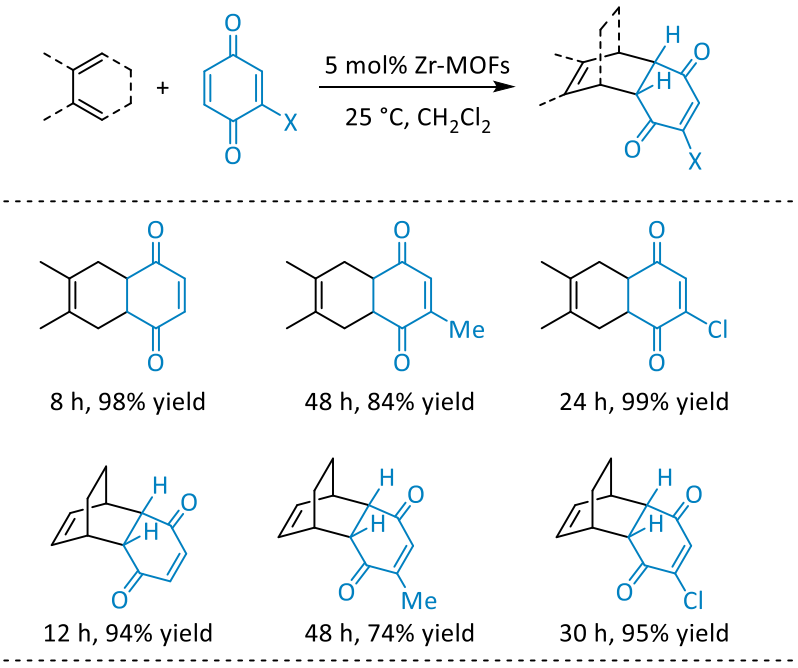

Reaction conditions: dienophile (1 equiv., 1 mmol), diene (1.2 equiv.), Zr MOFs (5 mol%, 0.05 mmol), CH_2Cl_2 (3.0 mL), 25 °C. Reaction yields were determined from 1H NMR using mesitylene as an internal standard.

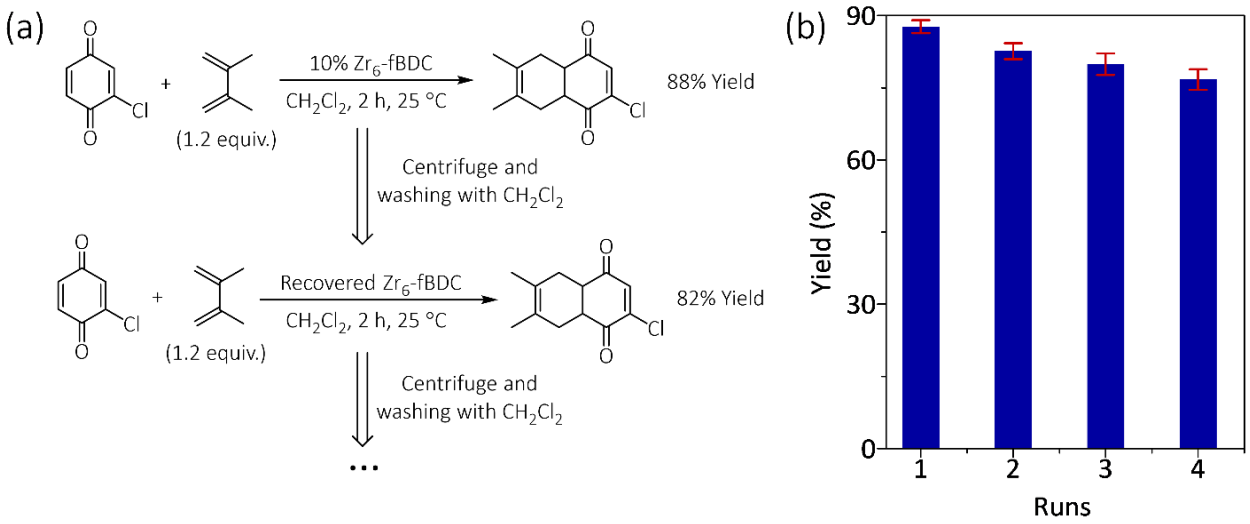

Figure 10-16. (a) Experimental procedure for the recycling experiment of Zr_6-fBDC catalyzed Diels-Alder reactions. (b) Plots of yields (%) and error bars for Diels-Alder reaction products in four consecutive runs.

10.2.6 Zr_6-fBDC catalyzed arene C-H iodination reactions.

Aryl iodides are very useful building blocks in organic synthesis. The C-I bonds of arenes readily undergo cross-coupling reactions and nucleophilic substitutions. There are multiple synthetic methods to access these compounds, including the Sandmeyer reaction, halide exchange reactions, and electrophilic substitutions. The most straightforward method is the direct C-H iodination using iodine or N-iodosuccinimide (NIS). Many acid catalysts have been developed to perform such reactions, notably the BF_3-H_2O system reported by Olah and co-workers which could iodinate very challenging electron-deficient arenes. For electron-rich arenes, however, many catalysts suffer from poor regioselectivity, leading to the formation of multi-iodinated products. Zr_6-fBDC was tested for the iodination of anisole at 25°C using MeCN as the solvent. These conditions afforded exclusively the mono-idodination product in 96% yield after 30 h. Other arene substrates, such as 2-methoxynaphthalene, aniline, and N-methylaniline, were also iodinated in high yields with excellent regioselectivity (**Table 10-3**).

Table 10-3. Substrate scope of Zr_6-fBDC catalyzed C-H iodination reactions.

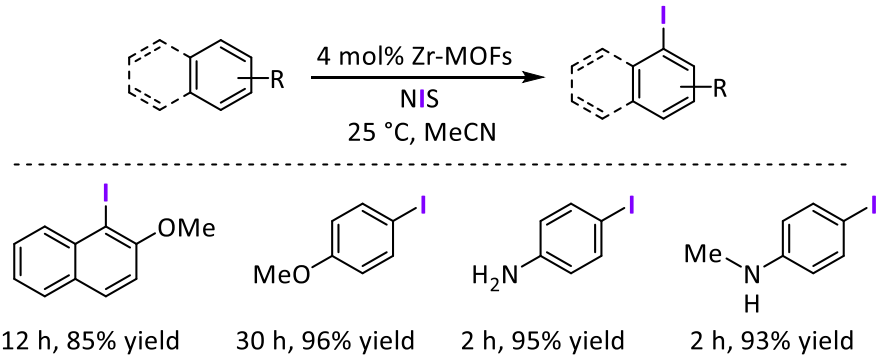

Reaction conditions: arenes (1 equiv., 0.5 mmol), N-iodosuccinimide (1.1 equiv.), Zr MOFs (4 mol%, 0.02 mmol), MeCN (1.5 mL), 25 °C. Reaction yields were determined from ^{1}H NMR using mesitylene as an internal standard.

The catalytic performance of Zr_6-fBDC was compared to other MOFs to show the importance of ligand perfluorination. At identical reaction conditions and catalyst loading, Zr_6-BDC and Zr_6-BDC-NO_2 only iodinated 2-methoxynaphthalene in 16% and 28% yield, respectively, while Zr_6-fBDC gave 85% yield of the 3-iodinated product. Other Lewis acidic MOF catalysts, i.e. MOF-5 and HKUST-1, also displayed much lower catalytic performance than Zr_6-fBDC (**Table 10-4**). Impressively, Zr_6-fBDC could be recycled at least 6 times without a significant drop in catalytic activity, illustrating the robustness of the solid Lewis acid catalyst (**Figure 10-19**).

Table 10-4. Catalyst evaluation and substrate scope of Zr_6-fBDC catalyzed C-H iodination reactions.

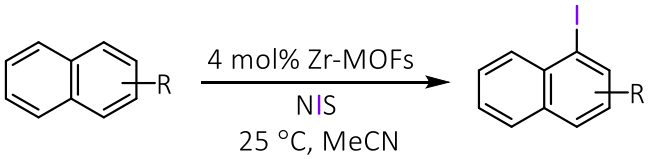

	Product	Catalyst	Time	Yield
1	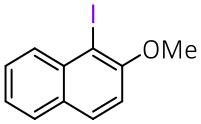	No catalyst	12 h	10 %
2		MOF-5	12 h	32 %
3		HKUST-1	12 h	16 %
4		Zr_6-BDC	12 h	16 %
5		Zr_6-BDC-NO_2	12 h	28 %
6		Zr_6-fBDC	12 h	85 %

Reaction conditions: arenes (1 equiv., 0.5 mmol), N-iodosuccinimide (1.1 equiv.), Zr MOFs (4 mol%, 0.02 mmol), MeCN (1.5 mL), 25 °C. Reaction yields were determined from ^{1}H NMR using mesitylene as an internal standard.

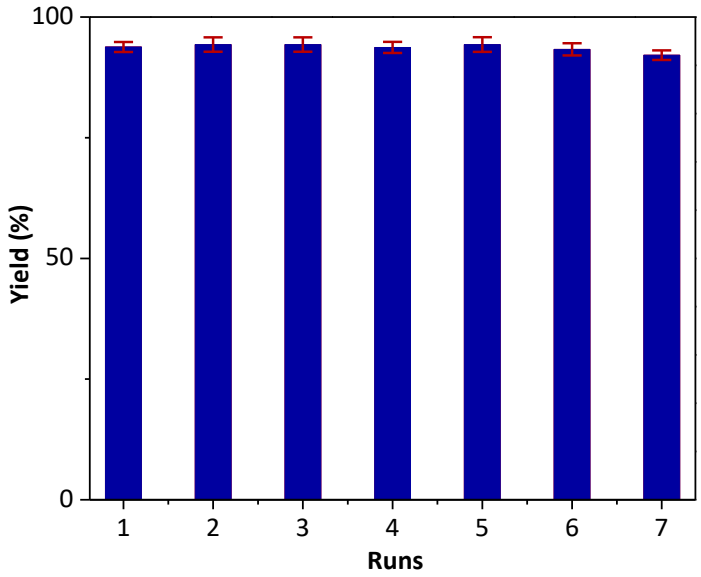

Figure 10-17. Plots of yields (%) and error bars of 4-iodoaniline in seven consecutive runs of Zr_6-fBDC catalyzed iodination of aniline with N-iodosuccinimide. The Zr-loadings were 10 mol% (total Zr w.r.t. to aniline). The catalyst loading of defective site w.r.t. aniline is 4.33 mol%.

10.3 Conclusion

In this chapter, we developed two general methods quantify the Lewis acidity of MOFs by measuring the changes in superoxide EPR signals and shifts of NMA fluorescence peaks upon their coordination to MOFs. We prepared a series of UiO-MOFs featuring defect $Zr_6O_4(OH)_4$ nodes with missing linkers and unsaturated coordination around Zr active sites. The application of the EPR and fluorescence methods to a variety of MOFs unveiled a strong correlation between dicarboxylate electron density and $Zr_6O_4(OH)_4$ Lewis acidity, leading to the discovery of significantly enhanced Lewis acidity within Zr-MOFs containing per-fluorinated bridging ligands. The new perfluorinated MOFs, Zr_6-fBDC and Zr_6-fBPDC, are significantly more Lewis acidic than non-substituted UiO-66 and UiO-67 as well as the nitrated MOFs Zr_6-BDC-NO_2 and Zr_6-BPDC-$(NO_2)_2$. Zr_6-fBDC was shown to be a highly active Lewis acid catalyst for Diels-Alder and arene C-H iodination reactions. This work therefore establishes the important role of ligand

perfluorination in enhancing MOF Lewis acidity and the potential of designing novel MOFs with high Lewis acidity as porous solid catalysts for fine chemical synthesis.

10.4 Experimental

10.4.1 Synthesis and characterizations of Zr_6-fBDC and Zr_6-fBPDC.

I have synthesized two perfluorinated UiO-MOFs, Zr_6-fBDC and Zr_6-fBPDC, by replacing BDC in UiO-66 and BPDC in UiO-67 with fBDC and fBPDC ligands, respectively (**Figure 10-2**). Zr_6-fBDC was synthesized in 86% yield by heating a mixture of $ZrOCl_2 \cdot 8H_2O$ and H_2fBDC in acidic THF at 80 °C. PXRD studies indicated that Zr_6-fBDC is isostructural to UiO-66 (**Figure 10-20**).

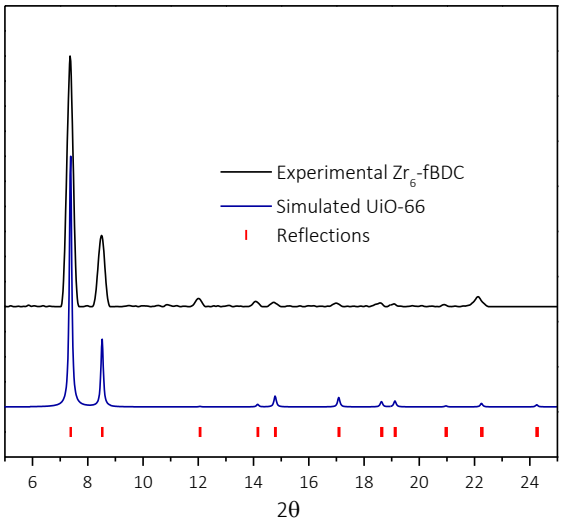

Figure 10-18. PXRD pattern of Zr_6-fBDC (black) matched well with that simulated for UiO-66 (navy). The diffraction peaks of Zr_6-fBDC matched those expected for a UiO-type of MOF.

The porosity of Zr_6-fBDC was confirmed by N_2 sorption isotherms, which displayed a BET surface area of 1021 m_2/g. DFT fitting of the N_2 sorption isotherms of Zr_6-fBDC gave pore sizes

of ~6 and ~8 Å that are attributable to the tetrahedral and octahedral cages of the UiO structure, respectively, in addition to a larger pore at ~12 Å due to the missing fBDC ligands (**Figure 10-21**).

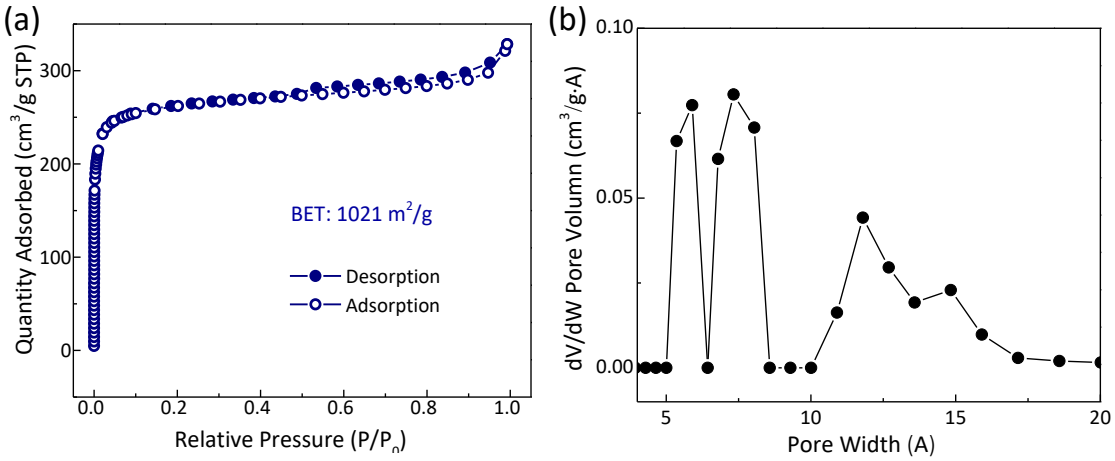

Figure 10-19. (a) N_2 sorption isotherms of Zr_6-fBDC with a BET surface area of 1021 m^2/g. (b) Pore size distribution of Zr_6-fBDC calculated from DFT.

The surface area of Zr_6-fBDC is lower than that of UiO-66 due to the increased formula weight in the perfluorinated MOF (1875 Da for Zr_6-fBDC vs 1664 Da for UiO-66). Unlike previously reported perfluorinated MOFs, Zr_6-fBDC features high thermal stability with a decomposition temperature of 380 °C as measured TGA. [22-26] A combination of ^{19}F NMR and ICP-MS techniques showed the number of missing linkers to be 1.33 per Zr_6 node (**Figure 10-22**). Based on this information, the formula of Zr_6-fBDC is calculated to be $Zr_6O_4(OH)_4(fBDC)_{4.67}$-$[(OH)(OH_2)]_{2.66}$.

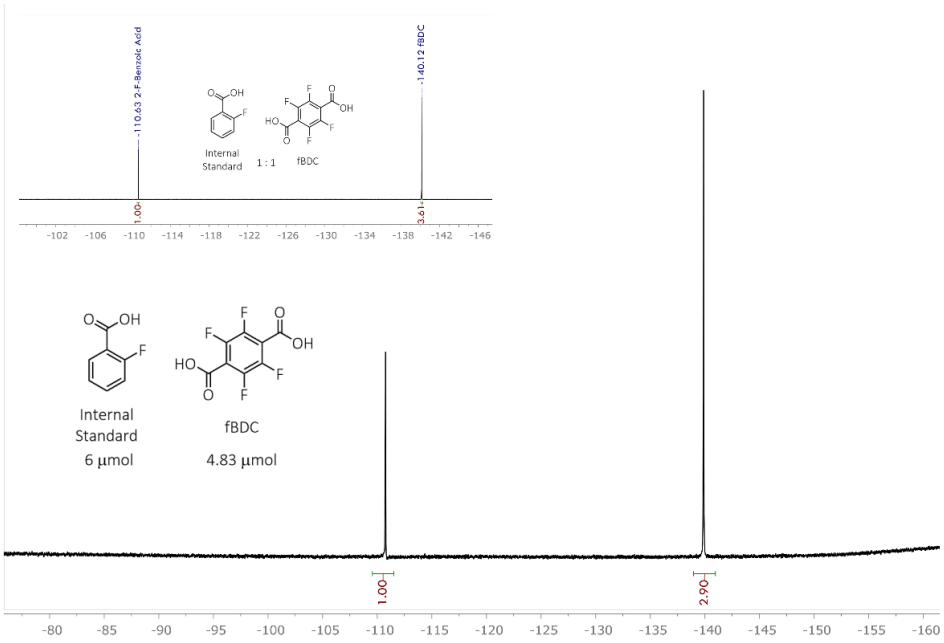

Figure 10-20. ^{19}F NMR of Zr_6-fBDC (2.0 mg) digested in D_3PO_4/DMSO-d_6. The amount of fBDC was quantified to be 4.83 μmol by using 6 μmol 2-fluorobenzoic acid as an internal standard. The amount of Zr was quantified by ICP-MS to be 6.2 μmol, thus affording 4.67 ligands per Zr_6 node.

The defect density of Zr_6-fBDC is slightly larger than that of defect UiO-66, which was reported to be 0.7 missing linkers per Zr_6 node, presumably due to the relatively weaker coordination strength of the fBDC ligand to the Zr_6 node.61 The structure of Zr_6-fBDC was unaltered after desolvation and catalysis based on the retention of the Zr_6-fBDC PXRD patterns.

Zr_6-fBPDC, a UiO-67 analogue of Zr_6-fBDC with larger channels, was prepared similarly. The H_2fBPDC linker was synthesized by $CuCl_2$-mediated oxidative aryl-aryl coupling of the methyl tetrafluorobenzoate organozinc reagent followed by ester hydrolysis. Zr_6-fBPDC was synthesized in 90% yield by heating a mixture of $ZrOCl_2 \cdot 8H_2O$ and H_2fBPDC in acidic THF at 80 °C. The PXRD pattern of Zr_6-fBPDC matched well with the simulated pattern for UiO-67, indicating their isostructural nature (**Figure 10-23**).

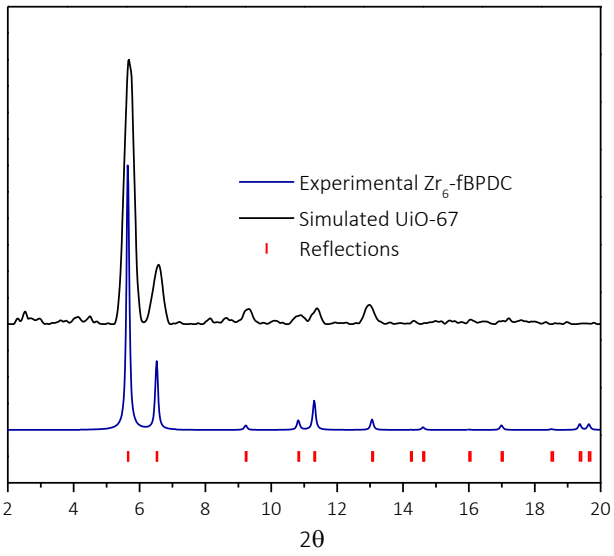

Figure 10-21. PXRD pattern of Zr_6-fBPDC (black) matched well with that simulated for UiO-67 (navy). The diffraction of Zr_6-fBPDC displayed all the expected reflections for a UiO-type of MOF.

Compared to Zr_6-fBDC, Zr_6-fBPDC has a larger BET surface area of 1148 m^2/g while maintaining high thermal stability with a decomposition temperature of 310 °C as measured by TGA. Zr_6-fBPDC displayed two types of pores at ~12 and ~15 Å, corresponding to the tetrahedral and octahedral cages, respectively, and a larger pore at ~22 Å due to the missing fBPDC ligands (**Figure 10-24**).

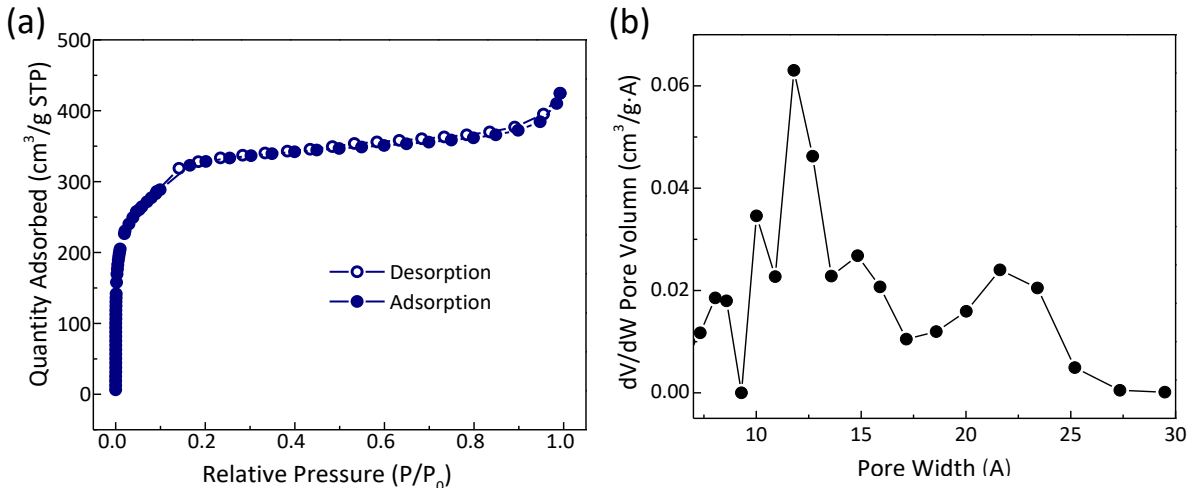

Figure 10-22. (a) N_2 sorption isotherms of Zr_6-fBPDC with a BET surface area of 1148 m^2/g. (b) Pore size distribution calculated from DFT showed that Zr_6-fBPDC possesses tetrahedral and octahedral pores at 10-17 Å. The larger pore at ~22 Å is caused by the missing linkers.

The number of missing linkers per Zr_6 node was determined by ^{19}F NMR and ICP-MS to be 1.73 per Zr_6 node, giving the formula $Zr_6O_4(OH)_4$(fBPDC)4.27[(OH)(OH2)]3.46 for Zr_6-fBPDC (**Figure 10-25**).

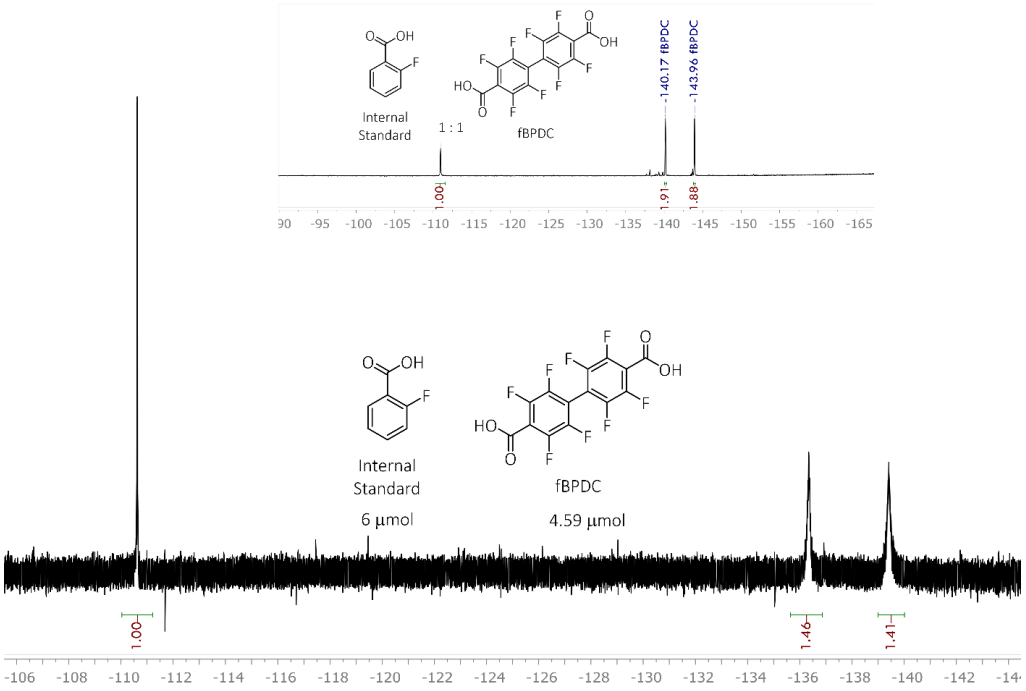

Figure 10-23. ^{19}F NMR of Zr_6-fBPDC (2.4 mg) digested in D_3PO_4/DMSO-d_6. The amount of fBPDC was quantified to be 4.59 μmol by using 6 μmol 2-fluorobenzoic acid as an internal standard. The amount of Zr was quantified by ICP-MS to be 6.45 μmol, thus affording 4.27 ligands per Zr_6 node.

10.4.2 Synthesis and characterizations of Zr_6-BDC-NO_2 and Zr_6-BPDC-$(NO_2)_2$.

Zr_6-BDC-NO_2 and Zr_6-BPDC-$(NO_2)_2$ were synthesized to compare their Lewis acidity with those of perfluorinated MOFs. Zr_6-BDC-NO_2 was prepared from H_2BDC-NO_2 and $ZrOCl_2 \cdot 8H_2O$ in acidified DMF. PXRD studies indicated its isostructural nature with UiO-66. N_2 sorption isotherms of Zr_6-BDC-NO_2 afforded a BET surface area of 960 m^2/g and pore diameters of ~6, ~8, and ~12 Å. The similar porosity of Zr_6-BDC-NO_2 and Zr_6-fBDC makes them a good

pair to study the impact of Lewis acidity on catalytic performance without the complication of varying diffusion kinetics through MOF channels. The number of missing linkers was determined by ^{1}H NMR and ICP-MS to be 0.94 per Zr_6 node, thus giving Zr_6-BDC-NO_2 the formula $Zr_6O_4(OH)_4(BDC\text{-}NO_2)_{5.06}[(OH)(OH_2)]_{1.88}$. The defect density of Zr_6-BDC-NO_2 is essentially the same as that of Zr_6-fBDC.

Zr_6-BPDC-$(NO_2)_2$ with larger channels was synthesized in 85% yield by heating a mixture of H_2BPDC-$(NO_2)_2$ and $ZrOCl_2 \cdot 8H_2O$ in acidified THF at 80 °C. The H_2BPDC-$(NO_2)_2$ ligand was synthesized in high yield using the Pd-catalyzed Suzuki-Miyaura cross-coupling reaction followed by ester hydrolysis. Zr_6-BPDC-$(NO_2)_2$ is isostructural to UiO-67 based on the similarity of their PXRD patterns. The porosity of The Zr_6-BPDC-$(NO_2)_2$ was confirmed by N_2 sorption isotherms, affording a BET surface area of 1205 m^2/g and pore diameters of ~12, ~15, and ~22 Å.

10.4.3 EPR measurement of MOF Lewis acidity

EPR spectra were recorded on a Bruker Elexsys 500 X-band EPR spectrometer under irradiation of a white-light lamp (Fiber-Lite MI-150) by focusing the lamp on the sample cell in the ESR cavity at 100 K (**Figure 10-26**). The sample was loaded into the cavity and held for 10 minutes to ensure superoxide generation and coordination to the MOF and the freezing of the dispersion. The EPR spectrum was collected at 9.63 GHz.

For Zr_6-fBDC, the coordinated superoxide showed a typical anisotropic signal with g_{zz} = 2.0324, g_{yy} = 2.0105 and g_{xx} = 2.0038. The superoxide binding energy to Zr centers can be calculated using the following equation adopted from literature reports:[27-28]

$$g_{zz} = g_e + 2\sqrt{\frac{\lambda^2}{\lambda^2 + \Delta E^2}}$$

where the free spin value $g_e = 2.0023$, λ is the spin-orbit coupling constant of oxygen known to be 0.014 eV, and ΔE is the energy splitting of π_g levels due to superoxide coordination to Zr.

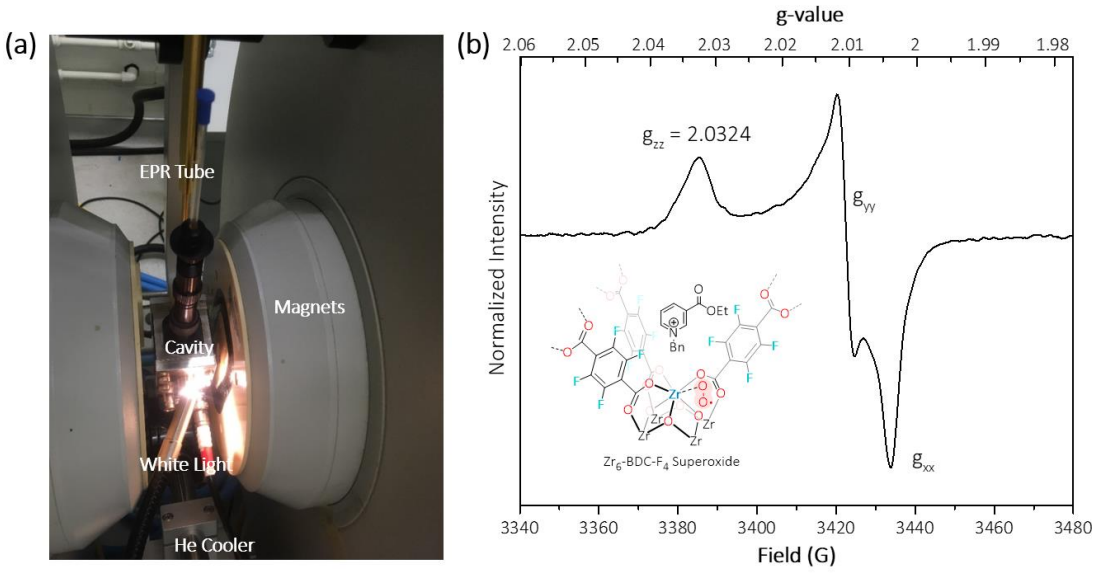

Figure 10-24. (a) EPR experiment setup for the characterization of Zr-bound superoxides. An EPR tube loaded with a Zr MOF, $(BNA)_2$, and oxygen was irradiated with intense white light. (b) EPR spectrum (100 K) of superoxide bond to Zr_6-fBDC measured in MeCN/toluene mixed solvents.

10.4.4 Fluorescence measurement of MOF Lewis acidity

For the measurement of MOF Lewis acidity, 0.8 mmol of Zr MOF (w.r.t. Zr) was added to a 2-dram vial in an N_2-filled glovebox. 4 mL of NMA solution (10 μM in MeCN) was then added to the vial. The resulting mixture was sonicated for 2 min until the MOF was well suspended, and then the suspension was transferred to a fluorescence cuvette for measurement using an excitation wavelength of 413 nm. The fluorescence of NMA-bound Zr_6-fBDC is shown as an example. The incident violet light (413 nm) was adsorbed by the Zr-bound NMA and emitted as blue/cyan light (452.6 nm and 470.6 nm). Both spectra were measured using an excitation wavelength of 413 nm. The emission peaks of NMA at 413.0 nm and 433.0 nm shifted to 452.6 nm and 470.6 nm, respectively, upon binding to Zr_6-fBDC.

To exclude the possibility that the Brønsted acidic μ_3-OH (pKa ~ 3.52) might have caused the shift in the NMA emission, a series of Brønsted acids (trifluoroacetic acid, benzoic acid, acetic acid, and 4-aminobenzoic acid) covering the pKa range of -0.25 ~ 4.86 were mixed with NMA in MeCN to measure fluorescence. None of the four acids caused any shift in the NMA emission spectra, indicating Brønsted acids are not responsible for the shifts in NMA fluorescence in the UiO series.

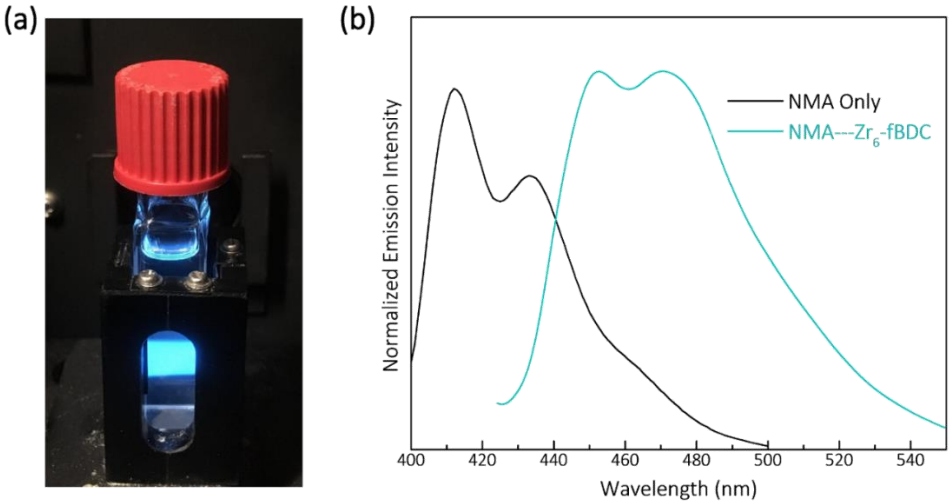

Figure 10-25. (a) Tyndall effect of Zr_6-fBDC fine suspension in MeCN. (b) The fluorescence spectra of NMA in MeCN (black) and NMA bound to Lewis acidic sites in Zr_6-fBDC (cyan).

10.4.5 DFT calculation

DFT calculations were carried out to gain insight into the coordination mode and electronic structure of $O_2^{\bullet-}$ bound to Zr_6 nodes. To reduce the computational expense, only the three ligands that were directly connected to the $Zr(O_2^{\bullet-})$ species were allowed to fully relax. The corresponding linkers and clusters were optimized at the M06 level of theory. All other dicarboxylate ligands were replaced with acetates and held fixed. The optimized structures for the models of all six MOFs showed a side-on binding mode of the $O_2^{\bullet-}$ on the Zr_6 node.[29]

10.4.6 Typical procedure for Zr_6-fBDC catalyzed C-H iodination

Zr_6-fBDC was prepared as described above and stored in an N_2-filled glove box. To a 15 mL Teflon-sealed tube were added 2-methoxynaphthalene (79 mg, 0.5 mmol), N-iodosuccinimide (123 mg, 0.55 mmol, 1.1 equiv.), Zr_6-fBDC (20 μmol Zr), and acetanitrile (1.5 mL). The reaction mixture was sealed with a Teflon cap and stirred in the dark at 25 °C for 12 h. The reaction was monitored by ^{1}H NMR and GC, which gave a yield of iodination product of 98%. The reaction mixture was centriguged to remove MOF catalyst. The supernatant was condensed under rotavap, then purified with chromatography using hexane as eluent to give the pure product (128 mg, 90% isolated yield).

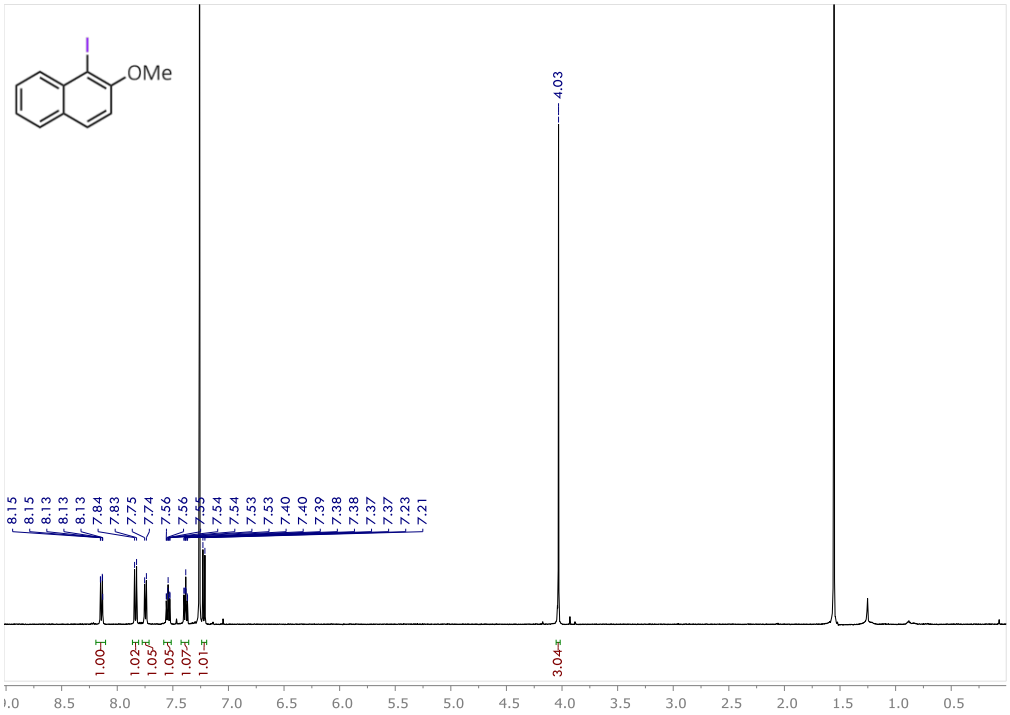

Figure 10-26. ^{1}H NMR of pure 1-iodo-2-methoxynaphthalene product isolated by column chromatography.

10.5 References

1. Vermoortele, F.; Vandichel, M.; Voorde, B. V. d.; Ameloot, R.; Waroquier, M.; Speybroeck, V. V.; Vos, D. E. D., Electronic Effects of Linker Substitution on Lewis Acid Catalysis with Metal–Organic Frameworks. *Angew. Chem. Int. Ed.* **2012,** 4887-4890.

2. Vermoortele, F.; Bueken, B.; Le Bars, G.; Van de Voorde, B.; Vandichel, M.; Houthoofd, K.; Vimont, A.; Daturi, M.; Waroquier, M.; Van Speybroeck, V.; Kirschhock, C.; De Vos, D. E., Synthesis Modulation as a Tool To Increase the Catalytic Activity of Metal–Organic Frameworks: The Unique Case of UiO-66(Zr). *J. Am. Chem. Soc.* **2013,** 11465-11468.

3. Mondloch, J. E.; Katz, M. J.; Isley Iii, W. C.; Ghosh, P.; Liao, P.; Bury, W.; Wagner, G. W.; Hall, M. G.; DeCoste, J. B.; Peterson, G. W.; Snurr, R. Q.; Cramer, C. J.; Hupp, J. T.; Farha, O. K., Destruction of chemical warfare agents using metal–organic frameworks. *Nat. Mater* **2015,** 512.

4. Yang, D.; Ortuño, M. A.; Bernales, V.; Cramer, C. J.; Gagliardi, L.; Gates, B. C., Structure and Dynamics of Zr6O8 Metal–Organic Framework Node Surfaces Probed with Ethanol Dehydration as a Catalytic Test Reaction. *J. Am. Chem. Soc.* **2018,** 3751-3759.

5. Beyzavi, M. H.; Klet, R. C.; Tussupbayev, S.; Borycz, J.; Vermeulen, N. A.; Cramer, C. J.; Stoddart, J. F.; Hupp, J. T.; Farha, O. K., A Hafnium-Based Metal–Organic Framework as an Efficient and Multifunctional Catalyst for Facile CO2 Fixation and Regioselective and Enantioretentive Epoxide Activation. *J. Am. Chem. Soc.* **2014,** 15861-15864.

6. Rasero-Almansa, A. M.; Iglesias, M.; Sanchez, F., Synthesis of bimetallic Zr(Ti)-naphthalendicarboxylate MOFs and their properties as Lewis acid catalysis. *RSC Adv.* **2016,** 106790-106797.

7. Sang, X.; Zhang, J.; Xiang, J.; Cui, J.; Zheng, L.; Zhang, J.; Wu, Z.; Li, Z.; Mo, G.; Xu, Y.; Song, J.; Liu, C.; Tan, X.; Luo, T.; Zhang, B.; Han, B., Ionic liquid accelerates the crystallization of Zr-based metal–organic frameworks. *Nat. Commun.* **2017,** 175.

8. Ly, H. G. T.; Fu, G.; Kondinski, A.; Bueken, B.; De Vos, D.; Parac-Vogt, T. N., Superactivity of MOF-808 toward Peptide Bond Hydrolysis. *J. Am. Chem. Soc.* **2018,** 6325-6335.

9. Zou, R.-Q.; Sakurai, H.; Han, S.; Zhong, R.-Q.; Xu, Q., Probing the Lewis Acid Sites and CO Catalytic Oxidation Activity of the Porous Metal−Organic Polymer [Cu(5-methylisophthalate)]. *J. Am. Chem. Soc.* **2007,** 8402-8403.

10. Horike, S.; Dincă, M.; Tamaki, K.; Long, J. R., Size-Selective Lewis Acid Catalysis in a Microporous Metal-Organic Framework with Exposed Mn2+ Coordination Sites. *J. Am. Chem. Soc.* **2008,** 5854-5855.

11. Henschel, A.; Gedrich, K.; Kraehnert, R.; Kaskel, S., Catalytic properties of MIL-101. *Chem. Commun.* **2008,** 4192-4194.

12. Shultz, A. M.; Farha, O. K.; Hupp, J. T.; Nguyen, S. T., A Catalytically Active, Permanently Microporous MOF with Metalloporphyrin Struts. *J. Am. Chem. Soc.* **2009,** 4204-4205.

13. Tanabe, K. K.; Cohen, S. M., Modular, Active, and Robust Lewis Acid Catalysts Supported on a Metal−Organic Framework. *Inorg. Chem.* **2010,** 6766-6774.

14. Srirambalaji, R.; Hong, S.; Natarajan, R.; Yoon, M.; Hota, R.; Kim, Y.; Ho Ko, Y.; Kim, K., Tandem catalysis with a bifunctional site-isolated Lewis acid-Bronsted base metal-organic framework, NH2-MIL-101(Al). *Chem. Commun.* **2012,** 11650-11652.

15. Jiang, Z. R.; Wang, H.; Hu, Y.; Lu, J.; Jiang, H. L., Polar Group and Defect Engineering in a Metal–Organic Framework: Synergistic Promotion of Carbon Dioxide Sorption and Conversion. *Chemsuschem* **2015,** 878-885.

16. Katz, M. J.; Brown, Z. J.; Colon, Y. J.; Siu, P. W.; Scheidt, K. A.; Snurr, R. Q.; Hupp, J. T.; Farha, O. K., A facile synthesis of UiO-66, UiO-67 and their derivatives. *Chem. Commun.* **2013,** 9449-9451.

17. Wu, H.; Chua, Y. S.; Krungleviciute, V.; Tyagi, M.; Chen, P.; Yildirim, T.; Zhou, W., Unusual and Highly Tunable Missing-Linker Defects in Zirconium Metal–Organic Framework UiO-66 and Their Important Effects on Gas Adsorption. *J. Am. Chem. Soc.* **2013,** 10525-10532.

18. Shearer, G. C.; Chavan, S.; Ethiraj, J.; Vitillo, J. G.; Svelle, S.; Olsbye, U.; Lamberti, C.; Bordiga, S.; Lillerud, K. P., Tuned to Perfection: Ironing Out the Defects in Metal–Organic Framework UiO-66. *Chem. Mater.* **2014,** 4068-4071.

19. A., T. C.; J., G. K.; Seungkyu, L.; Felipe, G.; Hans-Beat, B.; M., Y. O., Definitive Molecular Level Characterization of Defects in UiO-66 Crystals. *Angew. Chem. Int. Ed.* **2015,** 11162-11167.

20. Cai, G.; Jiang, H. L., A Modulator-Induced Defect-Formation Strategy to Hierarchically Porous Metal–Organic Frameworks with High Stability. *Angew. Chem. Int. Ed.* **2017,** 563-567.

21. Stefano, D.; Konstantin, E.; R., H. W.; Gregor, K.; A., F. R., Defective Metal-Organic Frameworks. *Adv. Mater.* 1704501.

22. Yang, C.; Wang, X.; Omary, M. A., Fluorous Metal−Organic Frameworks for High-Density Gas Adsorption. *J. Am. Chem. Soc.* **2007,** 15454-15455.

23. Yang, C.; Wang, X.; Omary, M. A., Crystallographic Observation of Dynamic Gas Adsorption Sites and Thermal Expansion in a Breathable Fluorous Metal–Organic Framework. *Angew. Chem. Int. Ed.* **2009,** 2500-2505.

24. Chen, T.-H.; Popov, I.; Zenasni, O.; Daugulis, O.; Miljanic, O. S., Superhydrophobic perfluorinated metal-organic frameworks. *Chem. Commun.* **2013,** 6846-6848.

25. Noro, S.-i.; Nakamura, T., Fluorine-functionalized metal–organic frameworks and porous coordination polymers. *Npg Asia Materials* **2017,** e433.

26. Cheplakova, A. M.; Kovalenko, K. A.; Samsonenko, D. G.; Lazarenko, V. A.; Khrustalev, V. N.; Vinogradov, A. S.; Karpov, V. M.; Platonov, V. E.; Fedin, V. P., Metal-organic frameworks based on octafluorobiphenyl-4,4[prime or minute]-dicarboxylate: synthesis, crystal structure, and surface functionality. *Dalton Trans.* **2018,** 3283-3297.

27. Ohkubo, K.; Menon, S. C.; Orita, A.; Otera, J.; Fukuzumi, S., Quantitative Evaluation of Lewis Acidity of Metal Ions with Different Ligands and Counterions in Relation to the Promoting Effects of Lewis Acids on Electron Transfer Reduction of Oxygen. *J. Org. Chem.* **2003,** 4720-4726.

28. Sobańska, K.; Krasowska, A.; Mazur, T.; Podolska-Serafin, K.; Pietrzyk, P.; Sojka, Z., Diagnostic Features of EPR Spectra of Superoxide Intermediates on Catalytic Surfaces and Molecular Interpretation of Their g and A Tensors. *Top. Catal.* **2015,** 796-810.

29. Bedilo, A. F.; Plotnikov, M. A.; Mezentseva, N. V.; Volodin, A. M.; Zhidomirov, G. M.; Rybkin, I. M.; Klabunde, K. J., Superoxide radical anions on the surface of zirconia and sulfated zirconia: formation mechanisms, properties and structure. *PCCP* **2005,** 3059-3069.

30. De Vos, A.; Hendrickx, K.; Van Der Voort, P.; Van Speybroeck, V.; Lejaeghere, K., Missing Linkers: An Alternative Pathway to UiO-66 Electronic Structure Engineering. *Chem. Mater.* **2017,** 3006-3019.